Surface Engineering of Mesoporous Silica for Ti-Based Epoxidation Catalysts

Lin Fang

ENS DE LYON

N° d'order:

N° attribué par la bibliothèque:

Thèse

En vue d'obtenir le garde de

Docteur de l'Ecole Normale Supérieure de Lyon – Université de Lyon

et

l'Université Normale de l'Est de La Chine

Discipline: Chimie

Laboratoire de Chimie

Ecole Doctorale de Chimie de Lyon

Présentée et soutenue publiquement le 9 Novembre 2012

Par Madame Lin FANG

Titre:

Surface Engineering in Mesoporous Silica for Ti-Based Epoxidation Catalysts

---

Directeur de thèse: *M. Laurent BONNEVIOT (ENS), M. Peng WU (ECNU)*

Après l'avis de: *Chargé de Recherches Marc PERA-TITUS*
Professeur Yanqin WANG,

Devant la commission d'Examen formée des membres suivants :

Chargé de Recherches Marc PERA-TITUS, membre/rapporateur
Professeur Yanqin WANG, membre/rapporateur
Professeur Mingyuan HE, membre
Professeur Dongyuan ZHAO, membre
Maître de conférences Belén ALBELA, membre
Professeur Peng WU, membre
Professeur Laurent BONNEVIOT, membre

2012th Doctoral Thesis

School Code: 10269

Student ID: 52090906052

East China Normal University

Surface Engineering in Mesoporous Silica for Ti-Based Epoxidation Catalysts

Academy:	*Department of Chemistry*
Major:	*Physical Chemistry*
Direction:	*Catalysis and Green Chemistry*
Supervisor:	*Prof. WU Peng*
Supervisor:	*Prof. BONNVIOT Laurent*
Doctor:	*FANG Lin*

November 2012, Shanghai

学位论文独创性声明

本人所呈交的学位论文是我在导师的指导下进行的研究工作及取得的研究成果。据我所知，除文中已经注明引用的内容外，本论文不包含其他个人已经发表或撰写过的研究成果。对本文的研究做出重要贡献的个人和集体，均已在文中作了明确说明并表示谢意。

作者签名：　　日期：

学位论文授权使用声明

本人完全了解华东师范大学有关保留、使用学位论文的规定，学校有权保留学位论文并向国家主管部门或其指定机构送交论文的电子版和纸质版。有权将学位论文用于非赢利目的的少量复制并允许论文进入学校图书馆被查阅。有权将学位论文的内容编入有关数据库进行检索。有权将学位论文的标题和摘要汇编出版。保密的学位论文在解密后适用本规定。

学位论文作者签名;　　导师签名

日期;　　日期：

方林博士学位论文答辩委员会成员名单

姓名	职称	单位	备注
王艳芹	教授	华东理工大学	主席
Marc PERA-TITUS	研究员	**Le laboratoire Produits et Procédés Eco-Efficients (E2P2), Shanghai**	委员
赵东元	教授	复旦大学	委员
何鸣元	院士	华东师范大学	委员
Belén ALBELA	教授	里昂高等师范学院	委员
张坤	副教授	华东师范大学	秘书
Laurent BONNEVIOT	教授	里昂高等师范学院	导师
吴鹏	教授	华东师范大学	导师

Acknowledgment

First, and foremost, I would like to express my great appreciations to the cooperation program «JORISS» between Ecoles Normales Supérieures (ENS) and East China Normal University (ECNU) in the education and training of graduate students. It offered me the opportunity to study in ENS-Lyon and ECNU. I am sincerely grateful to the Shanghai Key Laboratory of Green Chemistry and Chemical Process, directed by Prof. Ming-Yuan HE, who has always delivered the full support. Also, I would like to give my thanks to the administratives for managing this program, particularly Mme Yun-Hua QIAN and Mme Julie MOLUT, who have made big effort to resolve the problems appearing at any time.

Then the great gratitude I would like to express to my two supervisors, Prof. Laurent BONNEVIOT (ENS-Lyon, France) and Prof. Peng WU (ECNU, China). To be more independent, to be more precise, to be more professional, guided by the three main research disciplines from Prof. Laurent BONNEVIOT, sometimes I feel the truth is closing but the more unknown is following. "Shorter, but more

difficult" , to my most impression is the saying that when M. BONNEVIOT corrects the publication in a short communication, word by word, he shows the great respect to the research results and the readers who will read it.

Prof. Peng WU is ready to back up me at any time although I have just stayed and worked in the lab in Shanghai less than two months. Prof. WU always replied the emails containing problems and questions as soon as he could, like a fireman. As a famous expert in porous material and green catalysis, he is able to give the constructive proposals to the progress and point a right direction.

I am also grateful to my advisor, Dr. Bélen ALBELA of ENS, for her specific guidance throughout my researching, and writing stages. Bélen also influenced me imperceptibly by her nice personality. Never, I could feel the frustration when she stands beside me with energetic and optimistic encouragement.

I would like to thank my other colleagues both in ENS-Lyon and in ECNU for their help during my PhD study. Many thanks to Sandrine DENIS-QUANQUIN for her assistance with solid state NMR and Delphine PITRAT for her professional management of the

chemicals. Also, the other colleagues in ECNU, Yu-Ting ZHENG, Bo-Ting YANG, Le XU, Li CHEN and so on deserve my thanks.

Last, but not least, I would like to thank my families and friends. I am deeply indebted to my parents for their deepest love and unqualified moral support. And finally I would also like to give my thanks to the friends in Lyon who have ever brought the happiness and support to my life in France.

Abstract

Silica supported titanium are often reported as heterogeneous catalyst for oxidation reaction and particularly for epoxidation of alkenes where isolated titanium sites are known to be the active species. However, site isolation on a refractory surface like silica remains a challenge since most metals like titanium tend to aggregate into oxide clusters. The strategy adopted here consists to graft titanium isopropoxide by reaction with surface silanol groups, the quantity of which has been decreased at low temperature by chemical capping instead of high temperature thermal condensation. The originality resides in the molecular control of such operation using the so-called molecular stencil patterning (MSP) specifically developed for cationic templated silicas in the laboratory. Indeed, these silicas presents very high surface areas and very well calibrated cylindrical 1D nanochannel in the range 2.5 to 10 nm that is favorable for high metal dispersion and for post organic modification without loss of accessibility for reactants. Indeed, MSP overcome the diffusion problem for metal dispersion using a surface masking method based on the templating surfactant kept at a controlled filling factor inside the channels. After the removal of the masking surfactant, the silanol left available are located on isolated spots where in principle any metal can be grafted.

It is shown here that MSP can be applied to graft metal directly to these isolated silanol spots. The use of a dipodal organosilazane capping agent, leading to more stable grafted 1-2-ethanebis(dimethylsilyl) moieties (EBDMS) than the monopodal

trimethylsilyl moieties (TMS) was tested and found applicable but less convenient for surface coverage control. Nonetheless, the templated mesoporous silicas capped with dipodal organosilyl EBDMS groups contain as planned more isolated sites than the unmodified silica. This advantage depends on the titanium loading and it is more pronounced at low Ti loading where site isolation is at the best. A drastic blue shift of the ligand to metal UV transition attest for a profound effect on Ti dispersion in strongly correlated with the epoxidation activity as expected. Quantitative ^{29}Si NMR and FT-IR reveal that EBDMS are mostly bigrafted. After Ti grafting part of EBDMS are directly linked to grafted Ti sites likely via the formation of a direct Ti-O-Si bridge.

The organosilazane precursor of the quite stable grafted EBDMS is much more expensive and less convenient than HMDS. Therefore stabilization of the grafted monopodal TMS moieties was studied using a thermal treatment. The goal was to convert TMS into di-or trigrafted species using TGA profile as an indicator for the best choice of temperature. Thanks to a quantitative ^{29}Si NMR monitoring, the highest temperature to avoid a loss of grafted organosilyl moieties was determined (500 °C). The so-obtained ultra-stable organically modified surface are shown also to keep their properties of metal dispersion at least for Ti according to UV characteristic of the solids.

To quantify the grafted Ti species that are always present as a mixture, it was necessary to determine their molar coefficient of extinction. It was found that five different Gaussian only were necessary to simulate the quite large number of UV spectra obtained from the different syntheses. Each Gaussian was assigned to different groups of species: isolated tetra coordinated, penta-coordinated and hexa-coordinated Ti species with also small and large clusters of TiO_2. It was found for the first time on a surface that this coefficient decreases by two order of magnitude along the above series over representing isolated and tetrahedral species by far.

These studies required a panel of physical techniques such as X-ray diffraction (XRD), Nitrogen adsorption, thermogravimetry analysis (TGA), Diffuse reflectance UV (DR-UV), Fourier transformed Infrared (FT-IR) as well as ^{29}Si and ^{13}C magic angle solid state nuclear magnetic resonance (MAS-NMR) techniques. The epoxidation properties were tested on cyclohexene using tert-butyl hydroperoxide (TBHP) as oxydant.

摘要

钛负载的氧化硅基材料作为一种非均相催化剂在烃类选择氧化反应尤其是烯烃的环氧化反应中显示出了优越的性能，其中处于高分散状态的钛物种被认为是催化的活性中心。然而，大多数活泼金属如 Ti 在负载的过程中倾向团聚成氧化物多聚体，因此如何在固体材料如硅基材料表面负载高分散的金属物种仍然是一个极富挑战的课题。本论文在较低温度下将钛的前躯体通过与介孔材料表面的硅羟基发生缩合从而负载到其表面。介孔材料作为一种优良的载体，具有高的表面积和规整有序的一维纳米孔道，孔径分布在 2.5 nm 到 10 nm,既有利于负载高分散的金属物种或有机基团，又能保证反应物的扩散不受限制。本文通过“分子复刻”技术控制此负载过程中金属物种的高度分散性。“分子复刻”技术充分利用介孔材料中丰富的阳离子模板剂，从分子层面上控制负载的效果。在材料制备过程中，首先部分阳离子模板剂被去除，使部分羟基质子化作为第一种功能基团的嫁接点。通过控制模板剂去除的量，可以间接地调变有机官能团的嫁接量。然后去除介孔硅材料中剩余的阳离子模板剂，被其保护的硅羟基暴露出来并被此前负载的功能基团有效隔离，处于分散状态。此时第二种功能基团如金属有机化合物与处于分散状态的硅羟基发生缩合

并嫁接到介孔硅材料的表面。因此，最后被负载到介孔硅材料表面的金属物种在理论上也应处于分散状态，从而很好地解决了金属化合物负载过程中容易团聚的问题。

论文的第一部分详述了如何利用分子复刻法在介孔硅材料上负载高分散的 Ti 物种。此过程中第一种功能基团选用的是双齿有机硅烷化试剂，与硅羟基缩合后在表面上形成 1-2-乙二（二甲基硅烷）基团。双齿硅烷基与载体之间的作用力较之单齿硅烷基更强且实用性也更强，但是其嫁接量无法通过控制模板剂的去除量得到有效的调节。尽管如此，相对于未经修饰的介孔硅母体，被双齿硅烷化试剂部分负载的介孔硅材料仍具有较多的处于分散状态的硅羟基。但是当采用双齿有机硅烷化试剂作为第一种功能基团，“分子复刻”技术的优势只有在 Ti 负载量低的情况下才能得到体现，即钛负载量越低其分散性越好。紫外吸收光谱的明显蓝移现象以及催化剂在环氧化反应中的优异的性能证明了钛物种处于高分散的四配位状态。经 ^{29}Si 核磁共振技术和红外光谱的表征，双齿硅烷基大多数以双齿嫁接的形式存在，而 Ti 与 Si 成键以四配位的状态存在。

三甲基硅烷化试剂与载体的结合力较弱导致其稳定性较差，但是与价格昂贵且嫁接量不易控制的双齿有机硅烷化试剂相比，具有价格低廉，应用广泛且嫁接量可控等特点。基于此，论文的第二部分利用热处理的方式提高三甲基硅烷基的稳定性，将其从单齿配位的方式转化成双齿甚至是三齿配位方式。通过热重分析法和

^{29}Si 核磁共振光谱确定热处理的最佳温度为 500 ℃，既避免了有机功能团的流失，又能保证随后高分散的钛负载过程。

论文的第三部分对每种配位状态的钛物种的吸光系数进行了计算。以往的报道中，钛的配位方式只有定性的描述，因此有必要对其进行定量分析。本文采用首次采用 5 个高斯分布曲线来拟合各种不同方法合成得到的钛硅材料的紫外光谱图。这 5 个高斯曲线分别归属于孤立的四配位 Ti，五配位 Ti，六配位 Ti，小团簇 TiO_x 多聚物以及大团簇 TiO_2 纳米颗粒。当紫外吸收光谱发生红移现象，其配位状态的系数降低：四配位 Ti 的吸光系数约是团簇 TiO_x 或者 TiO_2 的两个数量级。

本文利用了一系列的物理表征手段研究材料的结构和形态以及金属的配位状态，如X-射线衍射（XRD），N_2 吸附脱附等温线（N_2 sorption），差热热重法（TGA），固体紫外漫反射（DR-UV），傅立叶红外（FT-IR）以及^{29}Si和^{13}C魔角固态核磁共振（29Si MAS-NMR & 13C MAS-NMR）。此外，催化剂的催化活性通过叔丁基过氧化氢作为氧化剂的环己烯环氧化反应来表征。

Résumé

Les sites actifs de l’époxydation des alcènes dans les catalyseurs au titane supporté sur silice sont des ions Ti(IV) isolés. La stratégie d’isolation de site adoptée ici consiste à

greffer l'isopropoxyde de titane par réaction avec les groupements silanol de surface dont la densité est diminuée par « capping » chimique remplaçant le traitement thermique usuel, très énergivore. La technique du pochoir moléculaire à motifs périodiques (PMP) a été appliquée pour forcer l'isolation de site. Dans les silices poreuses mesostructurées par un tensio-actif, c'est ce dernier, partiellement extrait, qui génère l'effet PMP lors du capping. Son élimination à l'étape suivante libère des îlots de groupements silanol sur les quels sont greffés les ions Ti(VI). Une étude spectroscopique quantitative menée en parallèle par FT-IR et par RMN du solide du ^{29}Si démontre que le pochoir organique inverse formé de groupement organosilyls greffés est conservé à toutes les étapes de synthèse. La spectroscopie UV en corrélation avec l'activité catalytique en époxydation du cyclohexene montent que ces surfaces originales favorisent un nombre beaucoup plus grand de sites mononucléaires isolés que les surfaces de silice non modifiées. La démonstration est faite avec une fonction de capping dipodale, 1-2-ethanebis(dimethylsilyl) (EBDMS), beaucoup plus stable que le monopodal classique, trimethylsilyl (TMS). Par ailleurs, le pochoir organique inverse issu du TMS ou de EBDMS voit sa stabilité augmentée par traitement thermique tout en préservant son effet dispersant pour le titane. Pour ce faire, un suivi quantitatif de la décomposition des organosilanes greffés a été réalisé par RMN du solide du ^{29}Si. Finalement, une description affinée et quantitative du mode de greffage du titane a été réalisée par simulation des spectres UV sur une série de catalyseurs supposant 5 types d'espèces comprenant les sites isolés et les clusters, les derniers se différenciant par leur gamme de taille.

Contents

Chapter I Introduction *1*

1.1 General introduction *1*

1.2 Reference *5*

Chapter II Literature Survey *7*

2.1 Mesoporous materials *7*

2.1.1 Definition and history *7*

2.1.2 Mesoporous materials *9*

2.1.2.1 Types and Composite of mesopore wall *9*

2.1.2.2 Synthesis *9*

2.1.2.3 Mechanism *14*

2.1.2.4 Structural characterization of Hexagonal mesophase *16*

2.2 Modification of the internal mesopores surface *19*

2.2.1 Chemical properties of the internal surface *19*

2.2.2 Chemical modification *20*

2.2.2.1 Direct synthesis *20*

2.2.2.2 Post-grafting *23*

2.3 Ti-substituted mesostructured silica materials *29*

2.3.1 Synthesis *30*

2.3.2 Characterization *32*

2.3.2.1 FTIR *32*

2.3.2.2 Solid ^{29}Si & ^{13}C MAS NMR *35*

2.3.2.3 UV & UV-raman spectroscopy *37*

2.3.2.4 XAS *41*

2.3.2.5 EPR *42*

2.3.3 Enhancement of catalytic activity *44*

2.4 Reference *47*

Chapter III Experimental and Characterization *54*

3.1 Experimental *54*

3.1.1 Chemicals and gases *54*

3.1.2 Preparation of products *55*

3.1.2.1 LUS-CTA & LUS-TMA *55*

3.1.2.2 LUS-Cx & LUS-Tx *57*
3.1.2.3 LUS-Cx-E & LUS-Tx-E *59*
3.1.2.4 LUS-Cx-E-OH & LUS-Tx-E-OH *61*
3.1.2.5 LUS-E-Ti-n, LUS-Ti-n & LUS-Ti-E *61*
3.1.2.6 LUS-xTMS *64*
3.1.2.7 LUS-xE-cal & LUS-xTMS-cal *64*
3.1.2.8 LUS-xE-cal-E & LUS-xTMS-cal-TMS *65*
3.1.2.9 LUS-xE-cal-Ti & LUS-xTMS-cal-Ti *65*
3.2 Characterization *66*
3.3 Catalytic Reaction *69*
3.4 Reference *70*
Chapter IV Titanium Dispersion Control using Organic patterning of the silica surface *71*
4.1 Introduction *71*
4.2 Masking the surface by TMA^+ or CTA^+ *73*
4.2.1 Characterization of template free LUS capped with EBDMS *73*
4.2.2 EBDMS Grafting in the presence of surface masking ammonium agent..*77*
4.2.2.1 Monitoring of the grafting sequence using FT-IR *77*
4.2.2.1.1 Preparation of the ammonium mask: LUS-Cx & LUS-Tx *78*
4.2.2.1.2 EBDMS grafting in the presence of the mask: LUS-Cx-E & LUS-Tx-E *80*
4.2.2.1.3 Elimination of masking ammonium layer: LUS-Cx-E-OH & LUS-Tx-E-OH *81*
4.2.2.2 Complementary investigations using various techniques *84*
4.2.2.2.1 Structure of LUS-Cx-E-OH & LUS-Tx-E-OH *84*
4.2.2.2.2 Chemical analysis *87*
4.3 Masking by CTA^+ and TMA^+ at room temperature (rt) *96*
4.3.1 FT-IR for monitoring the grafting sequence *97*
4.3.2 Chemical characterization *98*
4.4 Incorporation of Ti into mesoporous silica (LUS-E-Ti-n & LUS-Ti-n) *107*
4.4.1 Charaterization *107*
4.4.2 Catalytic reaction *115*
4.5 Conclusion *118*

4.6 Reference *120*

Chapter V Thermal Treatment of Organically Patterned surface and effect on subsequent grafting *122*

5.1 Introduction *122*

5.2 Temperature of thermal treatment *123*

5.3 Characterization *124*

5.3.1 Structure of materials *124*

5.3.2 Chemical properties *128*

5.3.2.1 LUS-T100-E-cal & LUS-T100-E-cal-E *128*

5.3.2.2 LUS-T100-TMS-cal & LUS- T100-TMS-cal-TMS *136*

5.3.2.3 LUS-Tx-TMS-cal & LUS- Tx-TMS-cal-TMS *142*

5.4 Ti post-grafting and catalytic reaction *146*

5.5 Conclusion *150*

5.6 Reference *152*

Chapter VI Assignment and quantification of grafted Ti species using UV-Visible Spectroscopy *153*

6.1 Introduction *153*

6.2 Calculation of extinction coefficient constant *155*

6.2.1 DR-UV spectroscopy for Ti deposits on the surface of silica *155*

6.2.2 Simulation of UV spectra *157*

6.2.3 Extinction coefficient constant (ε) of different Ti sites *164*

6.2.4 DFT simulation *166*

6.3 Active Ti sites in the epoxidation of cyclohexene and the real TON *169*

6.4 Conclusion *171*

6.5 Reference *172*

Chapter VII Conclusion and Perspective *175*

Chapter I

Introduction

1.1 General Introduction

Alcohol, ketone, or carboxylic functions are the most important functions in organic chemistry and are related to the capacity of the chemists to add an oxygen atom at any places required in a given molecule. Such a type of transformations are classified among oxidation reactions and lead to more and more thermodynamically stable molecules with the deeper oxidation. For instance, a di-alcohol (diol) is more stable than a mono-alcohol, or a ketone is more stable than the corresponding alcohol. Eventually the more stable and oxidized form of carbon is CO_2. This is one of the fundamental reasons why selective oxidation reactions will remain the most challenging for the chemist. In addition, the classical inorganic oxydants (chromates, permanganates etc…) based on metal are very polluting and should be recycled or merely suppressed for cleaner one. Organic peroxides or even better hydrogen peroxides are excellent alternatives. Nonetheless, they are very difficult and dangerous to use at the industrial scale and necessitate very soft condition that cannot be met without the help of a catalyst. The role of the latter is to maintain the reaction media far from the reactive conditions except at the so-called the catalytic site (or center). The latter may accelerate one of the many possible reactions and provide the selectivity towards the desired product. As far as oxidation reactions are concerned, transition metal ion complexes are the best choice. In addition, for economic and environmental concerns, the separation of the catalysts from the products and even better its regeneration for other catalytic runs (recycling) prompts us to prefer solid catalysts operating in gas or liquid reaction media, i. e., the so-called heterogeneous catalysts. Therefore, the search for novel heterogeneous catalysts for oxidation reactions is mandatory to develop cleaner and safer valuable chemical processes. This is the topic of this thesis concerning particularly the reaction that consists to add a single oxygen atom onto a double C=C bond leading to a three member CCO ring. The latter molecules called epoxides are important industrial intermediates.

Among heterogeneous catalysts, titanium substituted zeolites such as TS-1, Ti-beta and Ti-MWW are reported to be efficient oxidation catalysts, in particular for small olefin epoxidation due to the very small micropores where the catalytic site are located (< 1.2 nm).[1-3] The discovery of mesoporous templated materials with much larger pores (2 to 10 nm) and their titanium modifications, namely, Ti-MCM-41, Ti-HMS, Ti-MCM-48 and Ti-SBA-15, expanded the capability to catalyze bulky reactant molecules that were not able to access the Ti sites embedded in the zeolites framework.[4-9] Unfortunately, the

activity and selectivity of such materials are lower than that of TS-1 so far. In particular, in the case of olefin epoxidation, adsorption of the epoxide on the hydrophilic silica surface often leads to ring opening and therefore to the formation of diols.[10-11]

Modification of Ti-containing mesoporous materials with organic groups can both increase the stability of the material and modify the catalytic activity (Figure 1). These functions can be introduced either by post-grafting using organosilanes functions[12-15] or by direct synthesis where the organic function and the titanium precursors are added in the initial gel.[16-18]

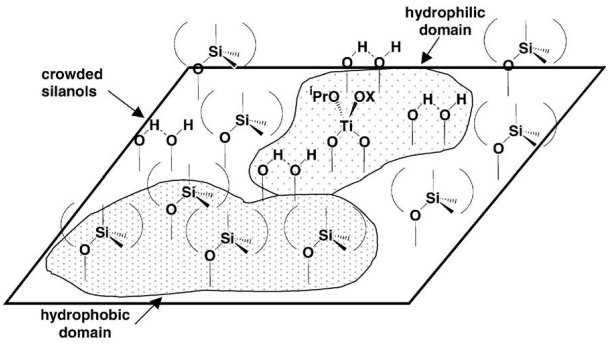

Figure 1 Proposed distribution of hydrophilic and hydrophobic domains on silica-supported titanium catalysts.[14]

Direct synthesis presents the advantage of affording a homogeneous distribution of both Ti species and hydrophobic functions in the material. In addition, the pore size is not obstructed affording higher molecular diffusion. However, the coordination environment of the Ti sites is difficult to control. Indeed, Ti species with 4-, 5-, and 6-fold coordination as well as TiO_2 oligomers may coexist depending on the experimental conditions.[18-19]

The post-grafting approach is proposed as a viable alternative although titanium oxide clusters either on the internal channel or on external silica surface are sometimes formed when unstable titanium alkoxydes or titanium chloride are used as precusors.[20-21] Several attempts have been reported to optimize both the synthesis protocol[22-24] and the titanium precursors[25-27] in order to favour isolated tetrahedral Ti sites, which are the active species, to improve the catalytic performance of the material.

However, in comparison to the co-condensation route, there are three features that had to be controlled prudently since: i) Ti site isolation mostly depends on the optimization of the Ti source or the additives during the synthesis to avoid localized condensation that may lead to inhomogeneous ‘patches’ of functions, ii) most often, the post-capping hydrophobic functions are monopodal such as trimethylsilyl (TMS) i. e., they react onto a single silanol leading to a fragile single Ti-O-Si bridge easy to cleave during a multistep synthesis or to leach out during a catalytic run and, iii) the number of effective Ti active centre in the material involved in the catalytic reaction is difficult to

determine leading to an underestimate of the true turnover number (TON) of the effective Ti catalytic centres.

To tackle the problem of site isolation, a novel technique, so-called molecular stencil patterning (MSP) has been developed to achieve an homogeneous distribution of two functions inside the nano-channels of templated mesoporous silicas by cationic surfactant (Figure 2).[28-29] It is based on a periodic patterning of self-repulsing quaternary ammonium cations acting as a protecting mask during the capping of the unprotected silanol groups using organosilanes. The role of the first capping is to fix the "latent image of the mask" by a covalently graft negative image. The removal of the mask (i.e. the residual ammonium cations) leaves behind patches of silanol islands of about the size of a hydrated ammonium head (Figure 2). This is just enough to graft a single function, F1, on these islands. Then, it is expected that a second function, F2, will be isolated one to another depending on the coverage F1. The role of the latter is to dilute the former at full surface coverage as described in previous experiments.[29] The question remains whether or not MSP site isolation technique might be applied to isolated transition metal by directly reacting them with the remaining silanol of such isolated islands. The challenge is to prove that the molecular control is kept at each step of the synthesis.

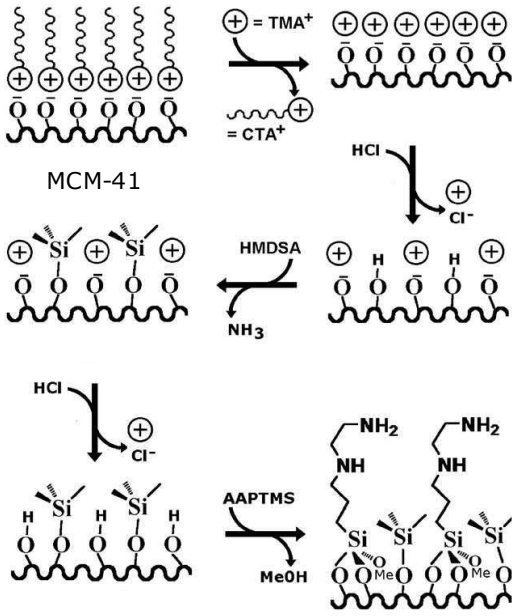

Figure 2 Example of stepwise built up of a bifunctional surface obtained via MSP technique. HMDSA is hexamethyldisilazane and AAPTMS is N-(2-aminoethyl)-3-amino-propyltrimethoxysilane. The mask is held electrostatically onto the surface by silanolate counter-charges. The surface covered by such a mask is controlled by extraction of CTA^+ or TMA^+ via partial neutralization of silanolate. The mask is made of the remaining cationic templating surfactant it-self (cetyltrimethylammonium, CTA^+) or an ersatz of it, i.e., the tetramethyl ammonium (TMA^+) mimicking the surfactant positively charged head. The capping function, F1, is here a monopodal trimethyl silyl moieties (TMS). In the present example the second function, F2, is the N-(2-aminoethyl)-3-amino-propylsilyl mieties (AAPS).

Such questions are fundamental for the design of heterogeneous catalysts where the nuclearity of the catalytic site is at stake. In this context, the main objective of the thesis appears clearly to answer such general questions in the particular case of titanium (IV) ions where isolated mononuclear species are known to be the active in the catalytic epoxidation of alkenes. This proof of concept implies the study of the organic coverage stability at different steps of the surface elaboration. The characterization of each different Ti surface species or type of species will be necessary to identify and eventually quantity the isolated ones among them. The latter is based mainly on the electronic spectra obtained from diffuse reflectance UV spectroscopy, Kubelka Munk data transformation and signal deconvolution. The catalytic activity in epoxidation of cyclohexene by terbutyl hydroperoxide (TBHP) has been used also to probe the isolated Ti sites. The same effort is also brought on the organic part with FT-IR and ^{29}Si solid state NMR deconvolution and quantification as been applied. A special effort has been made also to improve the quality of the covalently fixed organic mask using either a dipodal organosilane or a controlled thermal stabilization step.

The first part of the thesis is the present one followed by six other chapters. The second one is a survey on the actual background and development on this kind of catalyst including synthesis, characterization and application. The third part is the experimental section that includes the description of the primary matter, the material for synthesis, some typical recipes and the techniques used to collect the data. Chapters four to six report on the results and discussion: the fouth is devoted to the use of a dipodal capping function, 1-2-ethanebis(dimethylsilyl) (-$SiMe_2CH_2CH_2Me_2Si$-, EBDMS)[30-32] applied to our knowledge the first time in a heterogeneous catalysis.[33] The fifth treats the thermal stabilization treatment of the organic modified silica material. The sixth reports on the first tentative to our knowledge of quantifying Ti species from electronic spectra and on finding the true TON of the isolated Ti species in silica grafted by Ti. The seventh and last chapter provides the general conclusion of this thesis.

1.2 Reference

1 B. Notari, *Adv. Catal.*, **1996**, 41, 253.

2 P. Wu, T. Tatsumi, T. Komatsu, T. Yashima, *J. Catal.*, **2001**, 202, 245.

3 L. Wang, Y. Liu, W. Xie, H. Zhang, H. Wu, Y. Jiang, M. He, P. Wu, *J. Catal.*, **2007**, 246, 205.

4 P.T. Tanev, M. Chibwe, T.J. Pinnavia, *Nature*, **1994**, 368, 321.

5 A. Corma, M.T. Navarro, J.P. Pariente, *J. Chem. Soc., Chem. Commun.*, **1994**, 147.

6 W. Zhang, J. Lu, B. Han, M. Li, J. Xiu, P. Ying, C. Li, *Chem. Mater.*, **2002**, 14, 3413.

7 T. Maschmeyer, F. Rey, G. Sankar, J.M. Thomas, *Nature*, **1995**, 378, 159.

8 M.S. Morey, S. O'Brien, S. Schwarz, G.D. Stucky, *Chem. Mater.*, **2000**, 12, 898.

9 M. Guidotti, I. Batonneau-Gener, E. Gianotti, L. Marchese, S. Mignard, R. Psaro, M. Sgobba, N. Ravasio, *Microp. Mesop. Mater.*, **2008**, 111, 39.

10 T. Blasco, A. Corma, M.T. Navarro, J.P. Pariente, *J. Catal.*, **1995**, 156, 65.

11 A. Corma, M. Domine, J.A. Gaona, J.L. Jordá, M.T. Navarro, F. Rey, J. Pérez-Pariente, J. Tsuji, B. McCulloch, L.T. Nemeth, *Chem. Commun.*, **1998**, 2211

12 T. Tatsumi, K.A. Koyano, N. Igarashi, *Chem. Commun.*, **1998**, 3, 325.

13 P. Wu, T. Tatsumi, T. Komatsu, T. Yashima, *Chem. Mater.*, **2002**, 14, 1657

14 N. Igarashi, K. Hashimoto, T. Tatsumi, *Microp. Mesop. Mater.*, **2007**, 104, 269.

15 R.R. Sever, R. Alcala, J.A. Dumesic, T.W. Root, *Microp. Mesop. Mater.*, **2003**, 66, 53.

16 A. Bhaumik, T. Tatsumi, *J. Catal.*, **2000**, 189, 31.

17 A. Bhaumik, T. Tatsumi, *Catal. Lett.*, **2000**, 66, 181.

18 N. Igarashi, S. Kidani, R. Ahemaito, K. Hashimoto, T. Tatsumi, *Microp. Mesop. Mater.*, **2005**, 81, 97.

19 W. Zhang, M. Fröba, J. Wang, P.T. Tanev, J. Wong, T.J. Pinnavaia, *J. Am. Chem. Soc.*, **1996**, 118, 9164.

20 D. Zhao, J. Sun, Q. Li, G.D. Stucky, *Chem. Mater.*, **2000**, 12, 275.

21 M. Iwamoto, Y. Tanaka, J. Hirosumi, N. Kita, S. Triwahyono, *Micropor. Mesopor. Mater.*, **2001**, 48, 217.

22 L. Barrio, J.M. Campos-Martín, M.P. de Frutos-Escrig, J.L.G. Fierro, *Micropor. Mesopor. Mater.*, **2008**, 113, 542.

23 F. Bérubé, A. Khadhraoui, M.T. Janicke, F. Kleitz, S. Kaliaguine, *Ind. Eng. Chem. Res.*, **2010**, 49, 6977.

24 S.Y. Chen, C.Y. Tang, J.F. Lee, L.Y. Jang, T. Tatsumi, S. Cheng, *J. Mater. Chem.*, **2011**, 21, 2255

25 L. Marchese, E. Gianotti, V. Dellarocca, T. Maschmeyer, F. Rey, S. Coluccia, J.M. Thomas, *Phys. Chem. Chem. Phys.*, **1999**, 1, 585.

26 A. Tuel, L.G. Hubert-Pfalzgraf, J. Catal., **2003**, 217, 343.

27 F. Bérubé, B. Nohair, F. Kleitz, S. Kaliaguine, *Chem. Mater.*, **2010**, 22, 1988.

28 S. Calmettes, B. Albela, O. Hamelin, S. Ménage, F. Miomandre, L. Bonneviot, *New J. Chem.*, **2008**, 32, 727.

29 K. Zhang, B. Albela, M. He, Y. Wang, L. Bonneviot, *Phys. Chem. Chem. Phys.*, **2009**, 11, 2912.

Chapter II

Literature Survey

2.1 Mesoporous material

2.1.1 Definition and history

Porous solids have been attracted numerous scientific and technological interests because of their ability to interact with atoms, ions and molecules not only at their surfaces, but throughout the bulk of the material. According to the definition of IUPAC, mesoporous materials are those that have pore diameters between 2 nm to 50 nm while the pore sizes in the range of 2 nm and below are microporous and those above 50 nm are macroporous.

The discovery of porous materials can trace back to 1756 that the zeolite was found by the Swedish scientist Cronstedt when he heated an unidentified silicate mineral in a blowpipe flame it fused readily with marked fluorescence, thus he called this mineral 'zeolite' actually in Greek meaning 'boil (zeo) stone (litho)'. In fact, zeolites are crystalline aluminosilicates belonging to the term molecular sieve. The latter is commonly denominated for a kind of porous material which has a property of selective adsorption of molecules smaller than 5 Å in diameter. Nonetheless, it also includes the porous materials with pore size >5 Å like the ultra large porous VPI-5, etc. since the success of synthetic crystalline has been achieved aiming at realizing the desired functional porous materials (Table 1).[1,2]

Indeed, the distribution of pores sizes, shapes and volumes of the void spaces in porous materials directly affect their performance for a particular application. The traditional applications derived from the porous materials involve ion exchange, adsorption and catalysis can be achieved in microporous molecular sieves. The structural capabilities at the scale of a few nanometres can hardly meet the demands of the growing applications in processes involving large molecules, for example, biological and petroleum products. Thus, these motivations sparked the development the 1980s that the first report of a crystalline microporous material with uniform pores larger than 1.0 nm appeared[1] and pillared clays (PLS), which possess mesopore sizes, was extensively investigated.[2] However, the former one including VPI-5,[3] cloverite,[4] etc. has the limit in pore size no more than 1.5 nm although they are perfect inorganic crystals on the molecular scale with 3D framework structures, while the latter is ill in its widely distributed pore sizes and disordered pores arrangement seeming the significance of "template" was not realized that had used to function in the crystalline of zeolite.

Table 1 Representative examples of porous materials development

Year reported	Material	Definition	Ring size/Pore size	TEM image
1997	Macro. Mater.	*Macropore (> 50 nm)*	0.15-1 μm	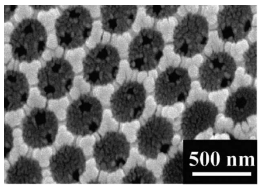 Hierarchical Macroporous Silica with Mesoporous Frameworks[5]
1992	MCM-41	*Mesopore (2-50 nm)*	4.0 nm	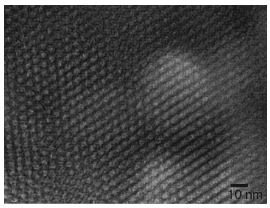 MCM-41[6]
1991 1990 1990 1988 1984	cloverite $AlPO_4$-8[7] ZSM-5[8] VPI-5 SAPO-34[9]	*Micropore (< 2 nm)*	20 MR, 6.0 * 13.2 Å 14 MR, 7.9 * 8.7 Å 10 MR, 5.3 * 5.6 Å 18 MR, 12 Å 8 MR, 4.3 Å	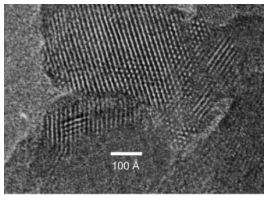 VPI-5[3]
1756	Zeolite		< 5.0 Å	—

In the early 1990s, the concept of "template" was first postulated in the synthesis of mesoporous silicate materials was reported by the separate report from Japanese scientists and Mobil scientists. Using the supramolecular templates to enhance pore size, the success of synthesis of meso-structured material characteristic of MCM-41 (M41S) more or less on the base of researches about the extra-large pore crystalline materials such as VPI-5, cloverite, etc.[10] Fllowing the discovery of a new family of mesoporous molecular sieves, MCM-48,[11] SBA-15[12] and FDU-n[13,14] such typical mesoporous materials had been explored and opened a new field of industrial and fundamental application studies.[15,16] In a board sense, the mesoporous materials are also molecular sieve. It possesses a periodic

arrangement of a moiety and gives well-defined diffraction spots on the mesoscale 2-50 nm.

And till 1997, O. D. Velev et al. used a method in which modified colloidal crystals of close-packed uniform microspheres such as polystyrene and poly(methyl methacrylate) (PMMA) are benefited as templates for silica polymerization that yields products with highly uniform and structured pores of tuneable size in the submicrometre region (0.15-1 μm), so-called 3D macroporous material. These macroporous materials are of importance in the research fields of photonic crystals, sensor devices, and catalysts.[17,18]

2.1.2 Mesoporous material

2.1.2.1 Types and composite of mesopore wall

Despite of past several decades' discussion about advanced materials applications on inclusion of electro-, photo- and bio-active guest molecules in porous host materials, few of these materials led to practical success. Nonetheless, when facing our understanding of the structure of ordered porous materials and how to control and tune, it has increased considerable advances leading to the promising future for the uses of ever more sophisticated versions of these materials.

The development of ordered mesoporous materials broadened a series of novel materials that possess uniform mesopore sizes (1.5-10 nm), highly ordered nanochannels with liquid-crystal structures, and huge surface areas (~1500 m^2/g). Since then, various types of mesoporous materials have been found and designed depending on the different meso-structures mainly including two-dimensional (2D) hexagonal with space group *p*6*mm*, three-dimensional (3D) hexagonal ($P6_3/mmc$), 3D cubic (*Pm*3*m*, *Pm*3*n*, *Fd*3*m*, *Fm*3*m*, *Im*3*m*), bicontinuous cubic (*Ia*3*d*), etc.[12,13,19,20,21]

Concomitantly, a variety of different framework compositions has been synthesized since the 1990s when the MCM-41 mesoporous silica and aluminumsilicate materials were first reported and synthesized.[12,20] They also cover metals and metal compounds such as platinum,[22] zirconium-based materials, vanadium (phosphorus) oxide, niobium oxide, tantalum oxide, etc,[23,24,25,26,27] as well as the polymers like phenolic resin, and carbons derivatives developed over the last ten years.[13,14,21,28,29,30,31]

2.1.2.2 Synthesis

The periodic arrangements of inorganic-organic composite nanoarrays have been synthesized by novel approaches based on the mechanistic idea that is mainly concerned with "building mesopores". A general synthesis route to form inorganic mesoporous materials is in a simple binary system of solvent-surfactant that the organic template molecules usually a kind of supramoleculars are used in different assembly processes or textural templates, around which the inorganic precursor can condense. It is established on the basis of the interactions between the inorganic precursor and organic template (Figure 1, A-B).

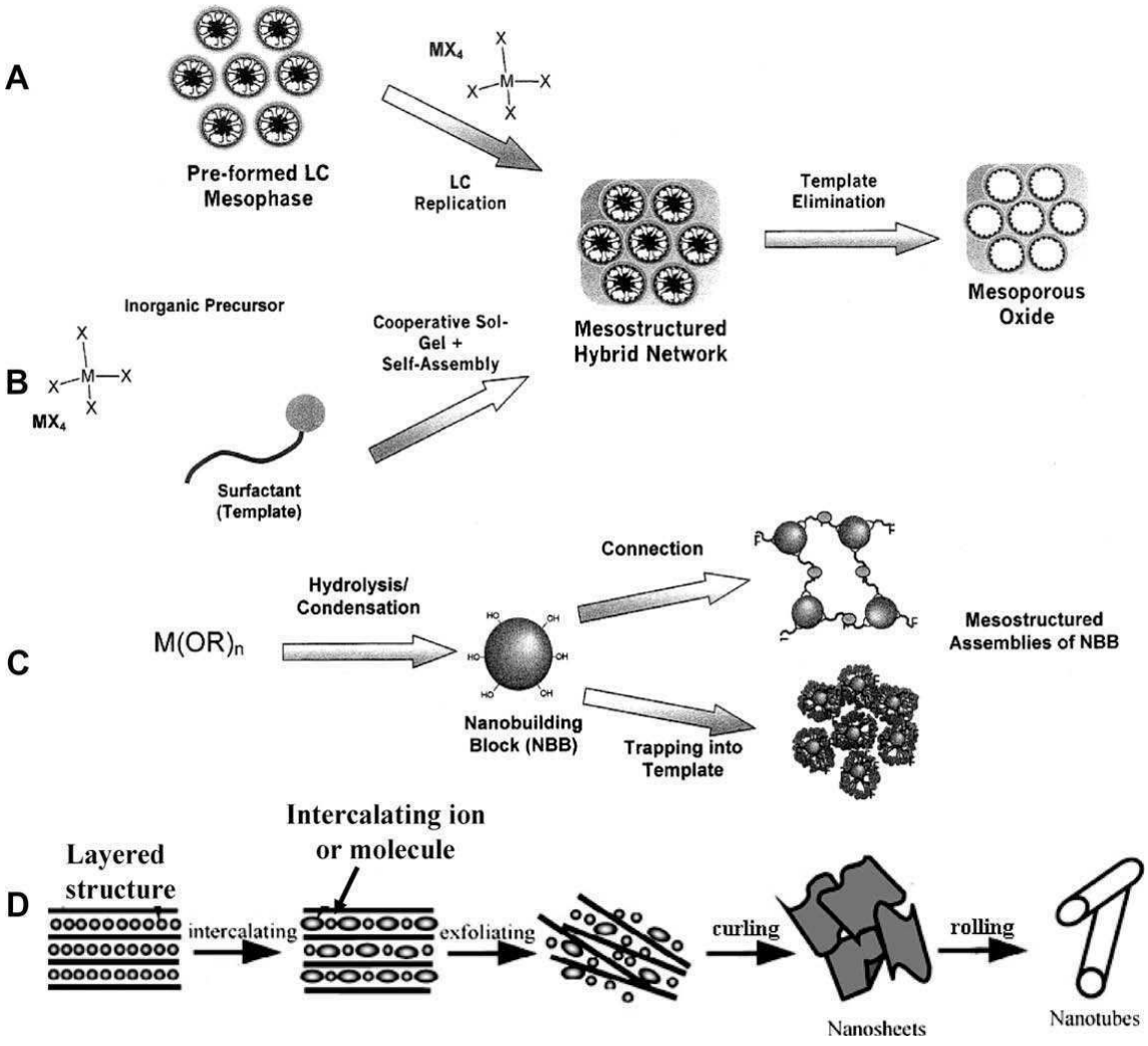

Figure 1 Schematic overview of the main synthetic approaches to mesostructured materials. (A) Liquid crystal templating, (B) self-assembly and cooperative self-assembly, (C) nanometric building blocks, and (D) sheet-folding mechanism.[32]

In addition, the template-free synthesis mechanisms like the nanobuilding block (NBB) mechanism and other approaches e.g. folded sheet nanotubes have been also reported. The NBB route applies nanoparticle which can form in solution or in micelle interiors, emulsions, or vesicles. These NBB can be subsequently assembled and linked by organic connectors or by taking advantage of organic functions dangling on the particle surface (Figure 1, C).[33] While the sheet-folding method can be applied especially in the synthesis of titanate and titania nanotubes (Figure 1, D).[34]

The first ordered mesoporous materials M41S family including MCM-48 and MCM-50 as well were synthesized in a typical way that a S^+I^- direct interaction between an ionic surfactant and a negatively charged silica source in a basic environment. The template molecules are dissolved firstly in the solvent which is usually affected by pH, temperature, additives, co-solvents etc, and then the silica source is added in. The template is usually quaternary ammonium salts ($C_nH_{2n+1}(C_mH_{2m+1})_3NX$ with n = 6-22, m = 1-4 and X = OH/Cl, OH, Cl, Br or HSO_4) or gemini surfactants ($[C_mH_{2m+1}(CH_3)_2N$-C_sH_{2s}-$N(CH_3)_2C_nH_{2n+1}]Br_2$ with m and n = 16-18 and s = 2-12). After a stirring period at a certain temperature to allow hydrolysis and pre-condensation, the temperature will be increased. Here sometimes it combines with the process enhancement such as hydrothermal treatment, microwave radiation, the addition of additives or pH changes etc, in order to optimize the condensation. Then next, the products is recovered, washed and dried. Finally, the mesoporous silica solid is obtained by removing the template via calcination or extraction.

In 1994, mesoporous silicas SBA-1 was prepared as the first one under a strongly acidic conditions which was regarded a breakthrough compared to the normally basic routes.[35] The synthesis uses cetyltriethylammonium bromide ($C_{16}H_{33}$-$N(CH_2CH_3)_3Br$, C_{16}TEABr) as a template and TEOS as a silica precursor. Thereafter, until 1998 other members of the new SBA (the acronym for Santa Barbara acids) family have been developed in an acid medium typically by the use of commercial non-ionic poly(alkylene-oxide) block copolymer or oligomeric alkyl poly(ethylene oxide) as template. The most representative template used are Pluronic® non-ionic triblock copolymers ($EO_nPO_mEO_n$) such as P123, F127, etc., which consists of large hydrophilic polyethyleneoxide $(EO)_n$ and hydrophobic polypropyleneoxide $(PO)_m$ blocks (Figure 2).[36]

The hydrophobic part gathers as the core of the meso-channel and the pore diameter can reach 8-10 nm due to its large block size. While the hydrophilic part has strong affinity with the silica source via the hydrogen bonding and it goes through the wall of silica as the branches during the condensation. Thus after removing the surfactant, it leaves the micropores in the pore wall with considerable stability which shows the novel application potentials.

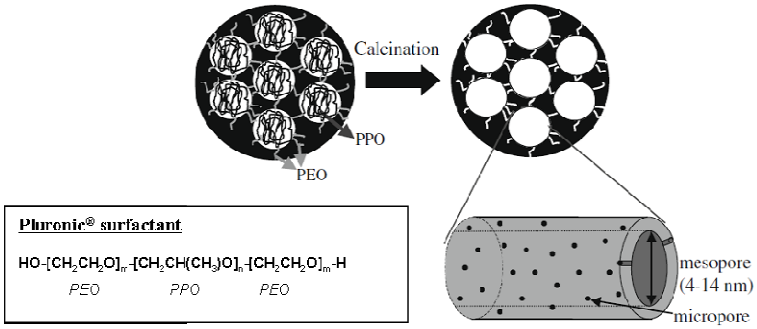

Figure 2 Schematic representation of SBA-15 before and after calcination[32]

Obviously, the template acting as an important role in the synthesis has been reported in various forms that include organic compounds like surfactant molecules, amphiphilic block copolymers, dendrimers etc which are also divided into ionic and non-ionic (Table 2), as well as biomolecules, forming micellar assemblies and/or liquid crystal mesophases. In the same way, the silica source can be derived from tetraethyl orthosilicate (TEOS), metasilicate, fumed silica etc.

Table 2 Synthesis Routes to Mesoporous Materials with the Emphasis on Silicates[37]

route	interactions	symbols	conditions	classical products
S^+I^-	electrostatic Coulomb force	S^+, cationic surfactants (frequently used cationic surfactants are shown in Figure 2); I^-, anionic silicate species	basic	MCM-41,[6] MCM-48,[6] MCM-50,[6] SBA-6,[73] SBA-2,[92] SBA-8,[93] FDU-2,[94] FDU-11,[74] FDU-13,[74] etc.
S^-I^+	electrostatic Coulomb force	S^-, anionic surfactants, $C_nH_{2n+1}COOH$, $C_nH_{2n+1}SO_3H$, $C_nH_{2n+1}OSO_2H$, $C_nH_{2n+1}OPO_2H$; I^+, transition metal ions, such as Al^{3+}	aqueous	mesoporous alumina, etc.[8]
$S^+X^-I^+$	electrostatic Coulomb force, double layer H bond	S^+, cationic surfactants (Figure 2); I^+, silicate species; X^-, Cl^-, Br^-, I^-, SO_4^{2-}, NO_3^-	acidic	SBA-1,[8] SBA-2,[95] SBA-3[92]
$S^-N^+-I^-$	electrostatic Coulomb force	S^-, anionic surfactants (lab-made) (Figure 3); N^+, cationic amino group of TMAPS or APS; I^-, anionic silicate species	basic	AMS-n[76,96–100]
$S^-X^+I^-$	electrostatic Coulomb force, double layer H bond	S^-, anionic phosphate surfactants $C_nH_{2n+1}COOH$, $C_nH_{2n+1}SO_3H$, $C_nH_{2n+1}OSO_2H$, $C_nH_{2n+1}OPO_2H$; I^-, transition metal ions, WO_4^{2-}, $Mo_2O_7^-$; X^+, Na^+, K^+, Cr^{3+}, Ni^{2+}, etc.	basic	W, Mo oxides[8,51]
S^0I^0 (N^0I^0)	H bond	S^0, nonionic surfactants, oligomeric alkyl PEO surfactants, and triblock copolymers; N^0, organic amines, $C_nH_{2n+1}NH_2$, $H_2NC_nH_{2n+1}NH_2$; I^0, silicate species, aluminate species	neutral	HMS, MSU, disordered worm-like mesoporous silicates[101,102]
$S^0H^+X^-I^+$	electrostatic Coulomb	S^0, nonionic surfactants (Figure 3); I^+, silicate species;	acidic, pH < ~2	SBA-n (n = 11, 12, 15, and 16),[31,78] FDU-n (n =

For non-siliceous materials first reported in 1995-1996, special attention has to be paid to hydrolysis rates, redox reactions, phase transformations etc in addition to those important parameters that control the formation of the structure.[27] Consequently, another novel approaches have been developed like evaporation-induced self-assembly (EISA), with which the synthesis of mesoporous phenolic polymer FDU-14,15 and mesostructured silica-polymer have been achieved,[14,28] and the "nanocasting" technique, allowing the replica of ordered mesoporous carbons and metals[38] from the molds of mesoporous silica such as MCM-48, MSU-1, and SBA-15, etc.

The synthesis of mesoporous polymer FDUs was achieved by Zhao and co-workers for the first time in 2005 as a breakthrough in the mesoporous world. A resol synthesized from the reaction of formaldehyde with phenol or the derivatives such as resorcinol, pholorglucinol [13,14,39,40] as building blocks in a weak basic aqueous medium. The resol oligomers contain a large number of hydrophilic hydroxyl groups which form hydrogen bonding with the hydrophilic PEO block of the Pluronic surfactant. Undergoing further thermal polymerization, the resols cross-link into polymers in the same meaning as silicate condensation (Figure 3).

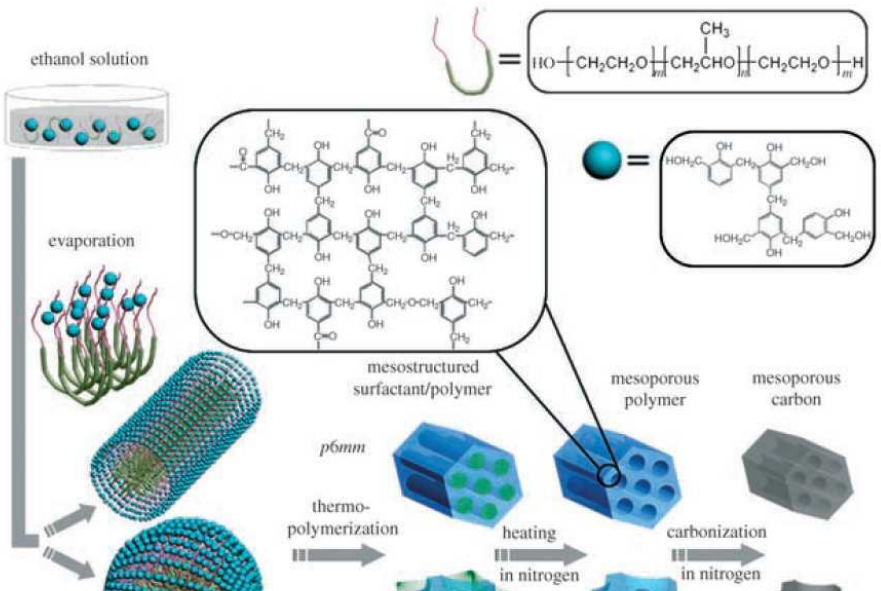

Figure 3 Schematic representation of the procedure used to prepare mesoporous polymers and carbon frameworks.[14]

PH value plays a key role during the synthesis since strong basic condition will destroy the hydrogen bond interaction, and neutral or acid media prolongs the polymerization time of resol. Therefore, the structures of assembled framework of mesoporous polymers can be tuned by controlling the copolymer/resol ratio or choosing different template from ordered 2D hexagonal (*p6mm*) FDU-15, to 3D cubic (*Im3m*) FDU-16, (*Ia3d*) FDU-14, face-Centered-Cubic *Fd3m* FDU-17 or lamellar polymer.

2.1.2.3 Mechanism

The synthesis mechanism for mesoporous materials, compared to that of microporous one, especially the templating effect used to remain a question. Three types of mechanisms, liquid crystal templating, self-assembly and cooperative self-assembly had been suggested for the synthesis of M41S materials based on the applied synthesis conditions.[2,41] In fact, the mesostructured materials derive depending on pore geometry and diameter are remarkably influenced by the concentration of surfactant in solution and processing conditions. Hence, the formation mechanism of ordered porous silica phases have been proposed so far through two typical synthetic strategies that one is called true liquid-crystal template mechanism (LCT) and the other is cooperative liquid-crystal template mechanism (Figure 4).[11,42] They include basically the possible pathways of mesostructure growth, accompanied by other modified routes.[10,43,44,45,46] The former mechanism is related to the presence of templates in the synthesis media at the very beginning and then the self-assembly process of the templates is followed by the

formation of the mineral network, which occurs at accessible interfaces built by pre-organized or self-assembled templates, creating the mesostructure in the material. While in the latter case the templates and the mineral network precursors present in the same mediate and a cooperative self-assembly is considered to take place in situ between the two yielding an organized architectures.

Therefore, the primarily rational control of surfactant-silica will determine the organic-inorganic interactions and the subsequent cooperative assembly (Figure 4, middle section). Correspondingly, the packing parameter (g value) or the hydrophilic/hydrophobic volume ratio (V_H/V_L) of template molecule is diagrammed as the decisive factors to the final mesostructures (Figure 4, upper section). Packing parameters $g = V/a_0l$ are widely used in predicting and explaining the final mesostructures in the hydrothermal synthesis, templated by the surfactant with cationic ion as head group.[47] Hence, as a derivation organic cosolvents have been applied during the synthesis to control the phase of mesoporous solid, which in fact, change the total volume of surfactant hydrophobic chains V. Penetrating into the centre of hydrophobic chain-compositing part of micelle, a polar additive acted as a swelling agent will raise V letting g decrease, and non-polar additive will increase g.[48] The expected mesophase sequence as a function of g value resumed that cubic ($Pm3n$, etc.) and 3D hexagonal ($P6_3/mmc$) with $g < 1/3$, 2D hexagonal ($p6mm$) with $1/3 < g < 1/2$, cubic ($Ia3d$) with $1/2 < g < 2/3$, and lamellar with $g \approx 1$.[41]

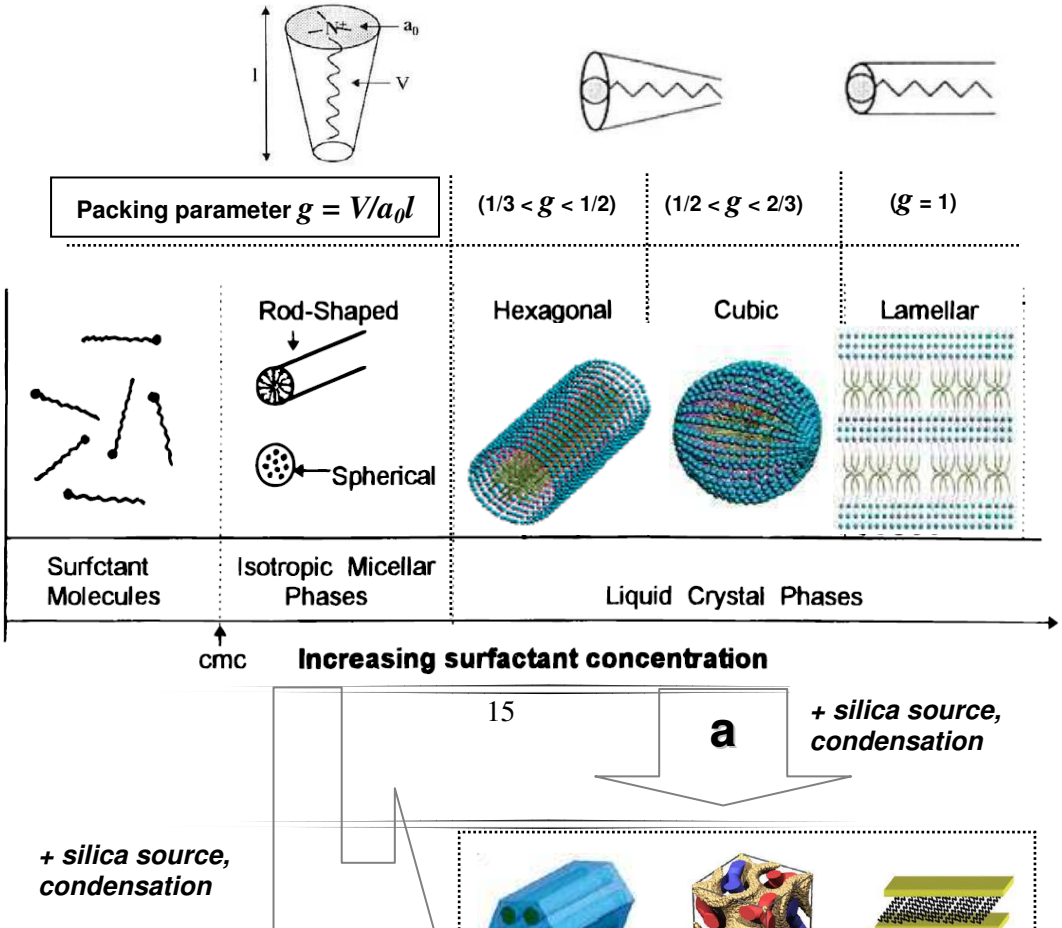

Figure 4 Formation mechanism of typical silica materials with hexagonal, cubic and lamellar meso-structures. (Upper: packing parameter of cationic surfactant and its relevance with meso-structure. Middle: phase sequence of surfactant-water binary system. Lower: two typical synthetic routes to generate meso-structure: a, true liquid-crystal template; b, cooperative liquid-crystal template)

2.1.2.4 Structural characterization of hexagonal mesophase

Among three main mesophases having been identified, the hexagonal mesophase represented by MCM-41, is the firstly reported in 1992 followed by the lamellar in 1993 and cubic phases in 1994 sequently. Compared to the two latters, the hexagonal mesophase possesses highly regular arrays of uniform-sized channels whose diameters are in the range of 1.5-10 nm depending on the templates used, the addition of auxiliary organic compounds, and the reaction parameters. By changing the synthesis conditions, it is possible to alter the types of structures among the three materials in the M41S family.[49,50]

The pores of this hexagonal mesostructured material are nearly as regular as, yet considerably larger than those present in crystalline materials such as zeolites, thus offering new opportunities for applications in catalysis. Furthermore, the hexagonal mesostructure retains when the pore wall consisting amorphous silica is replaced by another heteroelements such as Al,[51] Ti, [5,52] Co,[53] Zr,[54] Fe, Zn, Cu,[55] organic groups,[56] etc.

The classic MCM-41 material shows a typical characteristic of 2D hexagonal structure with *p6mm* space group in the X-ray diffraction pattern (XRD) (Figure 5, A). The XRD pattern contains four main reflection peaks, [100], [110], [200], and [210] at low angles ($0.5 < 2\theta < 10°$) associated with *p6mm* hexagonal symmetry.

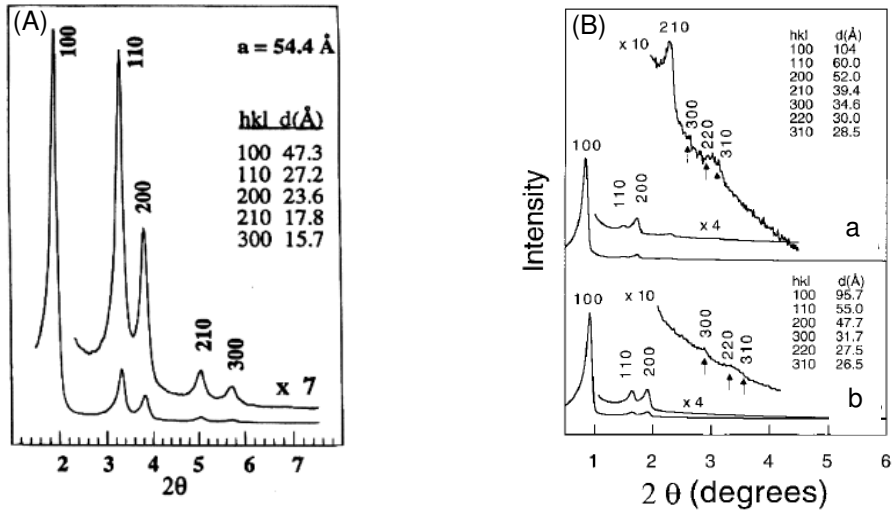

Figure 5 XRD pattern with indices of the diffraction planes of (A) MCM-41[47] and (B) SBA-15 by (a) as-synthesized and (b) calcined.[12]

A broad feature arises between 17° and 30°, similar with that of silica gel rather than the sharp Bragg reflections given by quartz crystalline, revealing the amorphous silica mesopore wall. Moreover, these reflections would only be very weak in any case, owing to the strong decrease of the structure factor at high angles.

As to another typical hexagonal mesoporous silica SBA-15, the XRD pattern also shows four well-resolved indexable reflections that are the same as those of MCM-41 indicating the periodic arrays of meso-channel (Figure 5, B). Three additional weak peaks related to the [300], [220], and [310] scattering reflections in the 2.5° to 3.5° 2θ range, indicating that as-synthesized SBA-15 has a high degree of hexagonal mesoscopic organization.[47] The intense [100] peak reflects a *d* spacing of 104 Å corresponding to a unit-cell parameter a_0 = 120 Å which is twice larger than that of MCM-41 (a_0 = 54.4 Å), indicating an enlarged meso-channel in the copolymer template material.

As well, the transmission electron microscopy (TEM) images suggest more detailed information about the overview of the two classic mesoprous silica (Figure 6, A). Both of them show uniform 2D channels of a long range with 3-4 nm mesopores for MCM-41 and about 8-9 nm for SBA-15. Note that it is difficult to image the disordered micropores in the mesopore wall of SBA-15 by the high resolution transmission electron microscope (HRTEM) technique. A 3D SBA-15 synthesized by Fan et al. using a swollen agent to expand micropore region, leaving a 2-8 nm connection that can be traced by TEM[57]

(Figure 6, B, right).

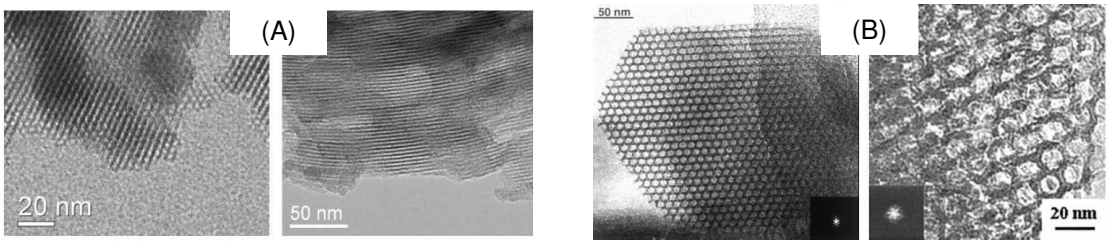

Figure 6 Transmission electron microscopy (TEM) images of (A) MCM-41[32] and (B) SBA-15[37] (left: traditional SBA-15; right: 3D SBA-15).

The N_2 adsorption/desorption measurement for both of MCM-41 and SBA-15 attributes a typical type-IV isotherms. MCM-41 has the same capillary condensation of adsorption and desorption at P/P_0 = 0.35 that indicates the uniformly cylindrical meso-channel in the material (Figure 7, A). While SBA-15 exhibits the type-H1 hysteresis loop and the capillary condensation occurs at a higher relative pressure P/P_0 = 0.75 (Figure 7, B). They both possess nearly 1000 $m^2 \cdot g^{-1}$ BET specific surface area and 1.0 $cm^3 \cdot g^{-1}$ total pore volume, and the corresponding sharp pore diameter distribution shows around 3.2 nm mesopores in the classic MCM-41 (Figure 7, A, insert) and 8.0 nm for SBA-15, which matches well with the TEM profile.

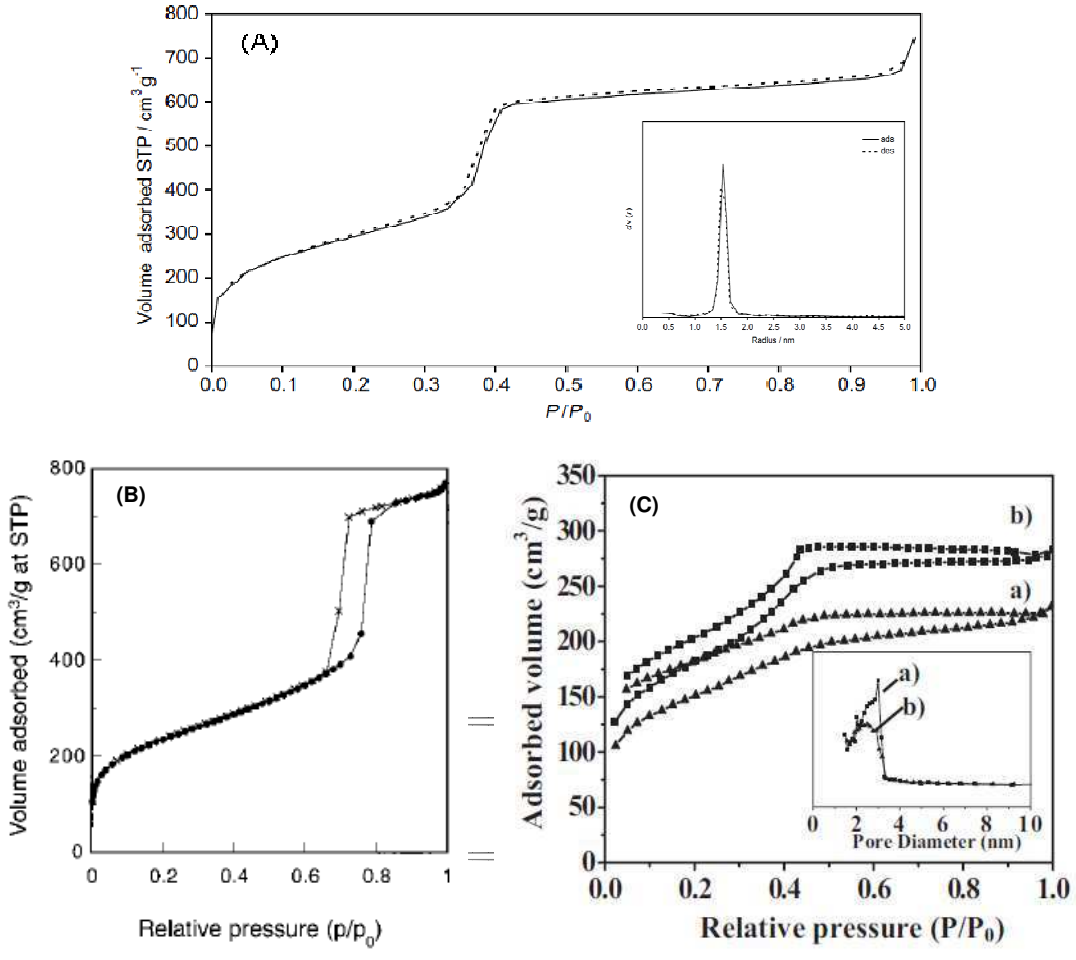

Figure 7 Nitrogen sorption isotherm and the corresponding pore radius distribution of (A) MCM-41,[32] (B) SBA-15[12] and (C) FDU-15 (a: FDU-15; b: FDU-15-SO_3H).[58]

As characterized by XRD, the pore wall of the mesoporous silica materials is amorphous compared the strictly tetrahedral constructed networks of zeolites, and not all SiO_4 units in the wall are four-connected, instead, three-connected and even two-connected SiO_4 units can be detected by ^{29}Si NMR, which generate a hydrophilic surface with more hydroxyl groups Si-OH. Although many efforts have been made to the synthesis of mesostructured silica with zeolite-type walls, there has been no major success in reproducibility. Nonetheless, increasing the thickness of pore wall can enhance the hydrothermal stability of the mesoporous silica.

For another hexagonal *P6mm* mesostructured material, FDU-15 is best known for its phenolic polymer matrix, which performs the superior application in the heterogeneous phase reaction.[58] Its nitrogen sorption isotherm, despite of a typical IV type confirming the characteristic of uniform mesostructure, the adsorption and desorption branches does not overlap completely in the region of low relative pressure, due to a typical nature of these polymer material (Figure 7, C).[14] Nevertheless, the mesopolymer possesses highly specific surface area (c.a. 600 m^2/g), narrow pore size distribution (c.a. 7 nm) and large pore volume (c.a. 0.6 cm^3/g). It has highly hydrothermal stability and is inert to base or acid (Figure 7, C, b). Furthermore, an ordered mesoporous carbon can also be obtained directly by inert gas-calcination at 900 °C to the as-made material, with consequent structure's shrink.[13,14,21]

2.2 Modification of the internal mesopores surface

2.2.1 Chemical properties of the internal surface

In comparison with the strictly constructed (TO_4) networks by aluminosilicate tetrahedron in the zeolite, the pore walls of mesoporous materials such as SBA-15,

MCM-41 etc, are amorphous ($SiO_{2+n/2}H_n$, n = 0-1). And not like the low number of surface hydroxyl groups in zeolites, three-connected and two-connected Si-O_4 units ($SiO_{2+n/2}H_n$, n = 1-2) can be detected in mesoporous silica materials, which generate a characteristic of hydrophilic nature and reactivity with more hydroxyl groups Si-OH or Si-$(OH)_2$ reaching the Si-OH density of ca. 1-2 nm^{-2}, related to Q^3 and Q^2 in the ^{29}Si NMR spectra.[59]

Different types of silanol groups (Figure 8, A) are always present on the surface and their relative ratios depend on the surface pre-treatment procedures employed. During the procedure of removing the surfactant in pores for obtaining pure mesoporous silica, mainly two ways are developed: calcination and extraction. Calcination in the high temperature (500 °C-600 °C) condenses the silanol group at the same time making the inner surface more Si-O_4 structure, more hydrophobic (Figure 8, A) which generates more Q^4 silica species and less Q^3 as shown in ^{29}Si NMR spectra (Figure 8, B); surfactant extracted by ethanol solution containing acid such as HCl, HNO_3, etc. that provides proton to the negative charged Si-O^- countered with surfactant cation, thus leaves more Si-OH group on the surface profiting the Si-OH used functionalization. For the same reason in the silylation, the conditions of pre-treatment to the surface of silica are reported important, where the dehydration occurs to change the environment of silanol groups to be modified by silylating reagents.[60]

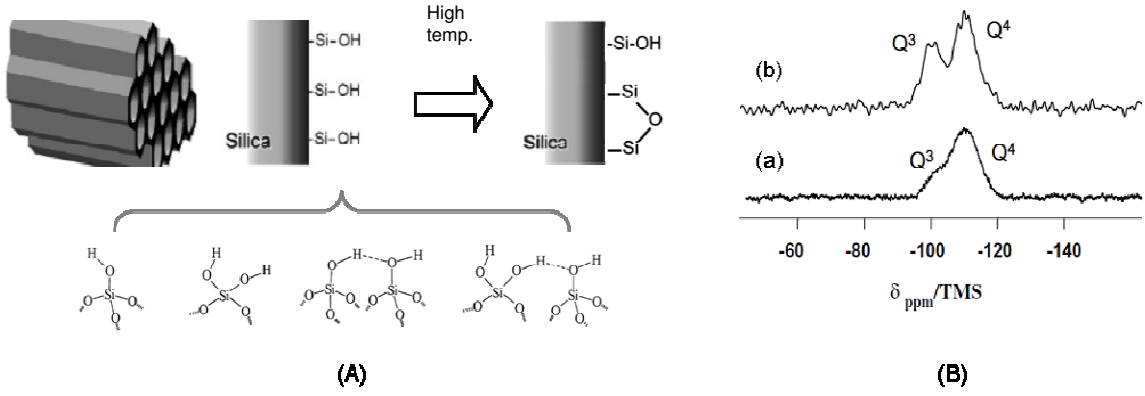

Figure 8 (A) Simplified description and (B) ^1H proton decoupled ^{29}Si MAS NMR spectra of MCM-41 materials post-treated by (a) calcined, (b) extracted.[61]

2.2.2 Chemical modification

Modifications of the mesoporous framework wall, and the pore interior have led to facile accommodation of organic,[15,56] organometallic[62,63] or even biologically active functional groups,[64,65] which give enormous impetus to the field of novel inorganic-organic hybrid solid materials with distinct physical properties or chemical functions. In general, two complementary strategies: direct route and post-grafting route, are pursued to tailor the chemical environment of mesoporous materials (Figure 9).

2.2.2.1 Direct synthesis

In the direct route, so-called one-pot synthesis, an organosilane $(R'O)_3Si\text{-}R$ or bridged silsesquioxane precursors of the type $(R'O)_3Si\text{-}R\text{-}Si(OR')_3$ (R: organic bridging group, R': methyl or ethyl) is hydrolytically condensed with conventional organosilica sources such as tetramethyl orthosilicate (TMOS) or tetraethyl orthosilicate (TEOS), etc.[66,67,68] Such mesoporous hybrids have been classified as periodic mesoporous organosilica (PMO). PMO hybrids are created firstly in 1999 by applying the concept as that for the surfactant directed synthesis of ordered mesoporous silica to covalently bonded organic-silica scaffolds (Figure 9, B).

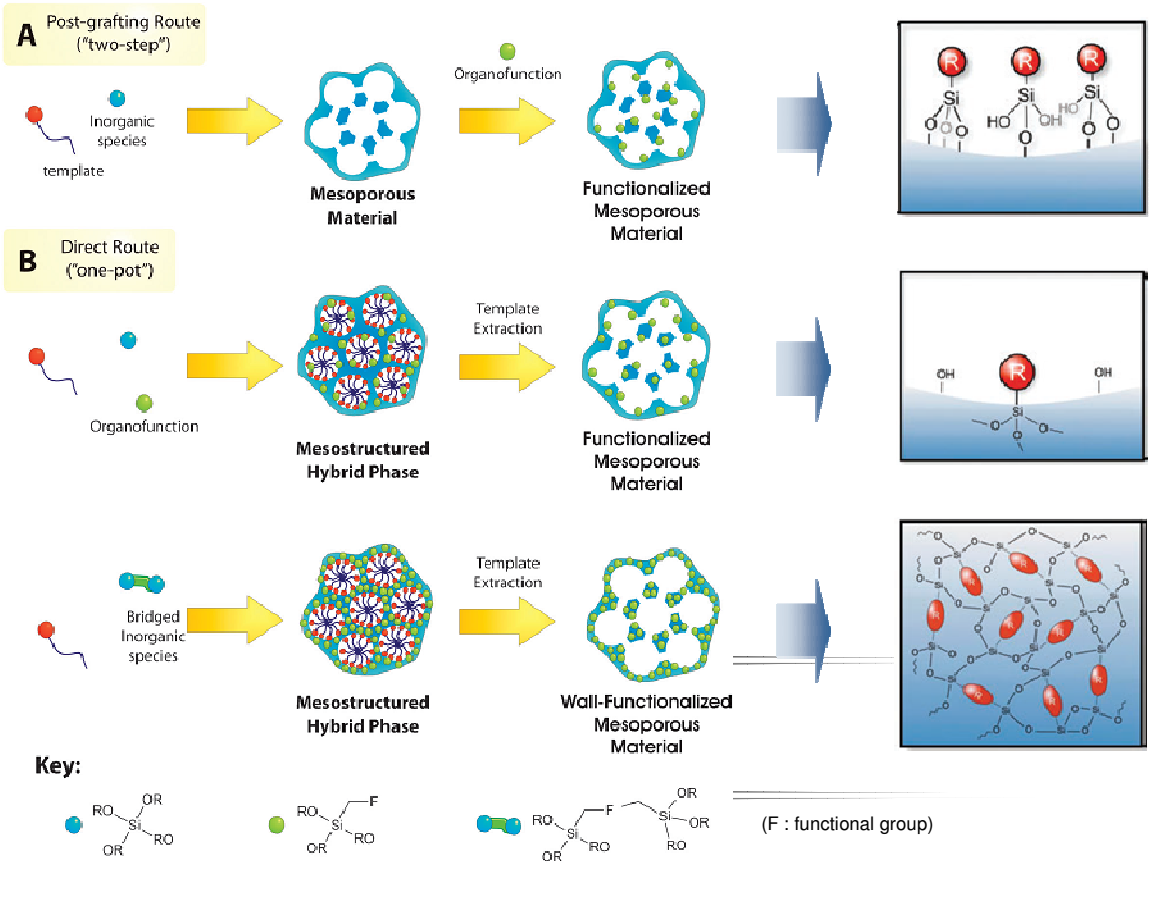

Figure 9 Outline of organo-functionalization for the mesoporous material.[69,70]

The functional group R can range from simple hydrocarbons or heteroaromatics bridges such as ethylene, ethenylene, phenylene, thiophene etc. to metal complexes.[71,72] The allylorganosilane compounds like $R[Si(CH_2CH{=}CH_2)_m(OR')_{3-m}]_n$ (m = 2, 3) can be processed in an additional hydrolysis or condensation as an alternate route.[73] As well, the template can both be ionic surfactant and amphiphilic block copolymer. The former is preferably used to prepare conventional PMOs and the latter usually results in large-pore with different symmetry of mesostructures. PMOs can be controlled in the diameter range of 1.5-30 nm by the appropriate selection of template surfactants and additives used in the polycondensation process. The one-pot synthesis takes the advantages of homogeneous distribution of the functional groups and short preparation time, etc.[74,75,76,77]

Some efforts have been taken to satisfy the common criteria of co-condensation reaction system as well as the predict models people want. The factors are the type of surfactant pathway (Figure 10),[78] the adding amount of functional precursor, the variety of organic group, the surfactant-extraction condition, etc.[68]

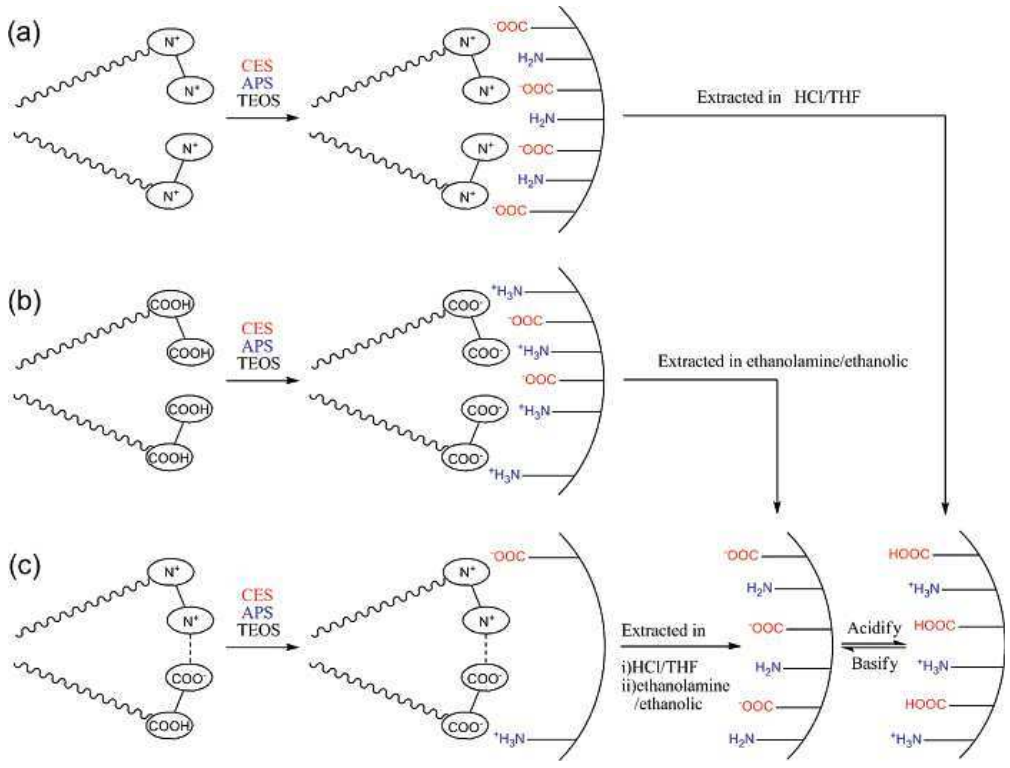

Figure 10 Direct synthesis of bifunctional mesoporous silicas based on self-assembly in the system of surfactant of (a) cationic, (b) anionic, and (c) a mixture of cationic and anionic surfactants.

All the choices are needed to avoid phase separation of the precursors to obtain uniform distributions of functional groups and avoid Si-C bond cleavage during the sol-gel reaction and during surfactant removal. Successful examples have been given, for example like the $[(R'O)_3Si\text{-}R\text{-}Si(OR')_3]$ and $[(R'O)_3SiR]$ can be combined in a mixture for the co-condensation reaction with TEOS/TMOS. The resulting bi-functional PMOs then consist of a combination of bridging organic units inside the framework and terminal organic groups whose ends point mainly into the channels (Figure 11).[79]

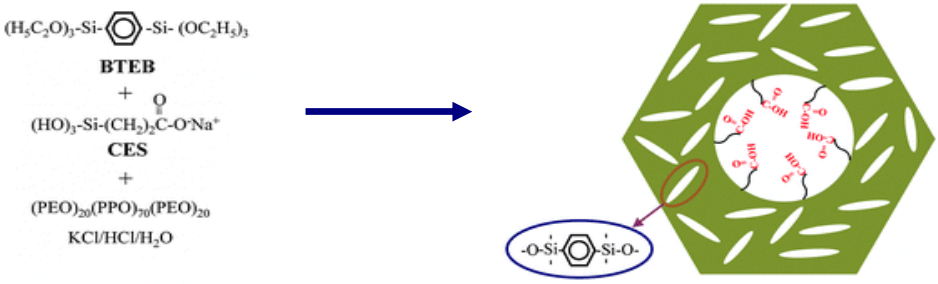

Figure 11 Co-condensation of 1,4-bis(triethoxysilyl)-benzene (BTEB) and carboxyethylsilanetriol sodium salt (CES) in a typical one-pot synthesis system solution containing KCl and P123.

2.2.2.2 Post-grafting

Surfaces of mesoporous silica with different philicity due to the silanol groups allow to incorporating a wealth of chemical species, such as inorganic cations or anions, or organo-functional molecules such as silanes, silazanes, diones, phosphates, carboxylates, etc. The post-grafting route can be used to tailor the accessible pore sizes of mesoporous solids, increase the surface hydrophobicity, passivate silanol groups, and thereby protect the framework towards hydrolysis (Figure 9, A). The porous materials tend to strongly adsorb species in solution, leading to partition and preconcentration of reagents in the pore networks. Molecules can remain just adsorbed, or react with the Si-

OH from the dehydrated pore surfaces to functionalized pore surfaces, which will present a modified behaviour (Eq. 1-3).[15]

$$\equiv Si\text{-}OH + Cl\text{-}SiR_3 \xrightarrow{\text{base, room temp.}} \equiv Si\text{-}OSiR_3 + HCl\cdot base \quad (1)$$

$$\equiv Si\text{-}OH + R'O\text{-}SiR_3 \xrightarrow[\text{room temp.}]{\text{80-100 °C}} \equiv Si\text{-}OSiR_3 + HOR' \quad (2)$$

$$\equiv Si\text{-}OH + HN\text{-}(SiR_3)_2 \rightarrow \equiv Si\text{-}OSiR_3 + NH_3 \quad (3)$$

The reactions of organosilanes primarily based on the direct bonding to the surface silanol groups by condensation reactions. Organoalkoxysilanes ($R'O\text{-}SiR_3$) or organochlorosilanes ($Cl\text{-}SiR_3$) have been widely used, as well as the silazanes $HN\text{-}(SiR_3)_3$ (R = functional organic group; R' = Me, Et). A number of the organosilanes, with their functional group R such as olefins, nitriles, alkylthiols, alkyl amines, alkyl halides, and epoxides, etc, are reactive, permitting further functionalization.

Among these, the trimethylsilylation of silanol groups ($\equiv SiO\text{-}Si(CH_3)_3$) is considered a convenient and widely applied post-grafting approach to improve the internal surface hydrophobicity of the porous silica (Figure 9, A). Reactions with or without solvent of various silane reagents have been reported such as hexamethyldisilazane (HMDZ), trimethylchlorosilane (TMCS), N-methyl-N-(trimethylsilyl)trifluoroacetamide (MSTFA), trimethylsilylimidazole, and hexamethyldisiloxane (HMDS). The degree of trimethylsilylation is affected by the reactivity of silane itself, the anhydrous environment in the pores, and reaction temperature, etc.[80]

Although the post-grafting leads to the distribution of functional groups sometimes non-uniformly that decorates mostly on the surface rich in silanol group, and causes a reduction in the porosity of the hybrid material, it preserves the framework structure of the parent mesoporous materials with ignorable harmfulness. Moreover, a functional surface environment can be designed via several chemical steps by benefit of abundant surface silanol groups, uniform ordered mesochannel and large space area (Figure 12).[81,82] The functionalization on the solid materials supplys a favorable route for the generation of highly reactive entities in several processes such as catalysis, adsorption, selective membranes, optical materials, biointerfaces, new electronics, etc. through tailoring the meso-, micro- and local environment of active surface sites.[56,65,83] Both the

microenvironment and meso-environment can affect the selectivity of a catalytic transformation and the stability of highly reactive intermediates, respectively.

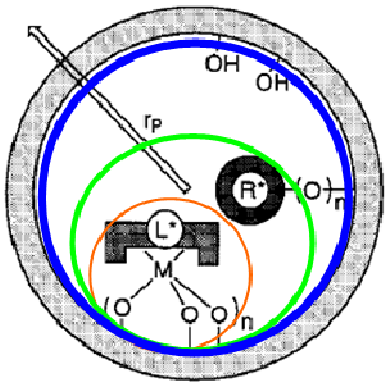

Figure 12 Schematic presentation of various surface organometallic environments in the porous materials. Left: ($2r_p$) pore diameter; (L*) ancillary ligand; (R*) surface-attached group; (n) the podality of the metal center M; (OH) residual surface silanol groups; the blue, green, and orange ring covering areas indicate the target metal's meso-, micro-, and local- environment, respectively.[62,63]

Heterogeneous catalysis reactions have a wide range to apply the organic modified mesoporous solids especially using the post-grafting method. The hybrid material provides a means of introducing steric selectivity and thus greater specificity to a reaction. And as the catalyst it can be retained and easily separated from the liquid phase by filtration. Furthermore, a followed regeneration will help it recycling. The catalytic reactions that have been studied using functionalized mesoporous solids include acid catalysis, base catalysis, oxidations, reductions, enantioselective catalysis, stereospecific polymerizations, and other catalytic reactions that produce fine chemicals.[66,80]

In one case of catalytic study applied Ti-loaded MCM-41 as catalyst, the materials was silylated TMS groups after Ti species deposition. The catalyst is highly hydrophobized on the Ti incorporated silica surface (*Chp. I*, Figure 1). Thus it can become readily available in the completely separated organic phases with TBHP even a little H_2O introduced into the reaction system, and show remarkably superior catalytic activities for the oxidation of cyclododecene (Figure 13).[84]

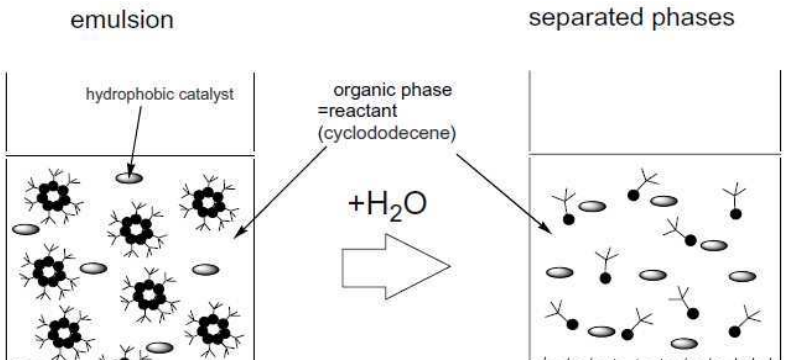

Figure 13 Oxidation of cyclododecene using heterogeneous catalyst.

However in comparison to the co-condensation route, the grafting procedure is usually related to the fact that it can be difficult to achieve a homogeneous distribution of one or more organic groups. Since there are three features had to be controlled prudently: (a) tuning the philicity and reactivity of the surface with the organo-function to avoid localized condensation that leads to the formation of function ‘‘patches’’; (b) avoiding competition of the anchoring group with other nucleophiles species in solution such as water, etc; (c) avoiding auto condensation of the functional molecules that can lead to pore blocking or a complete closure in the pore entrances due to the formation of $(R\text{-}SiO)_x$ polymers.

Therefore, precise control of the organic modification via post-synthetic sequence has been developed in order to meet the application requirement. The best known case is the molecular imprinting technique that aims to create solid materials containing chemical functionalities that are spatially organized by covalent1 or non-covalent interactions with imprint (or template) molecules during the synthesis process. Subsequent removal of the imprint molecules leaves behind designed sites for the recognition of small molecules, making the material ideally suited for applications such as separations, chemical sensing and catalysis.

M. Davis *et al.* have reported in 2000 the imprinting of bulk amorphous silicas with single aromatic rings carrying up to three 3-aminopropyltriethoxysilane side groups. This generates and occupies microporosity and attaches functional organic groups to the pore walls in a controlled fashion. The triethoxysilane part of the molecules' side groups is

incorporated into the silica framework during sol-gel synthesis, and subsequent removal of the aromatic core creates a cavity with spatially organized aminopropyl groups covalently anchored to the pore walls.[85]

Applying the new route, a pair of designed bis-silane precursor such as acid/thiol, can be grafted at two points on the surface, followed by link cleavage with an acid wash, resulting in the deprotected two functional sites within certain fixed distance (Figure 14). Tuned by the linker in the precursor, the distance can be greater uniform when using a more rigid linker. The modified material acts as a bi-functional catalyst in a cooperatively catalytic reaction, increasing the dynamic and outperforms the randomly distributed catalyst.[86]

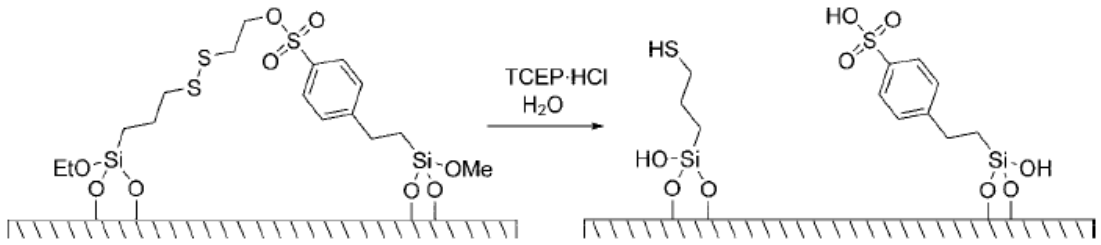

Figure 14 Synthesis of paired acid/thiol catalyst by deprotection from grafted disulfide/sulfonate ester intermediate. (TCEP·HCl: tris(2-carboxyethyl)phosphine hydrochloride)

However, the molecular imprinting technique can control the distribution of a paired function rather than the vicinity of each function one to another. Different approaches have been described in the literatures to generate site-isolation or site-to-site distance control in porous materials.[87,88,89,90] Among these, Y. Shin *et al.* synthesized a hierarchical porous material containing a rigid mesoporous oxide frame coated by a soft 'microporous' molecular monolayer (Figure 15, A). The 'microporous' is generated by template molecules that are embedded in the long-chain molecular monolayers as cavities. The template molecule can be systematically varied by tripod or dipod silane that tunes the size and shape of the cavities (Figure 15, B).

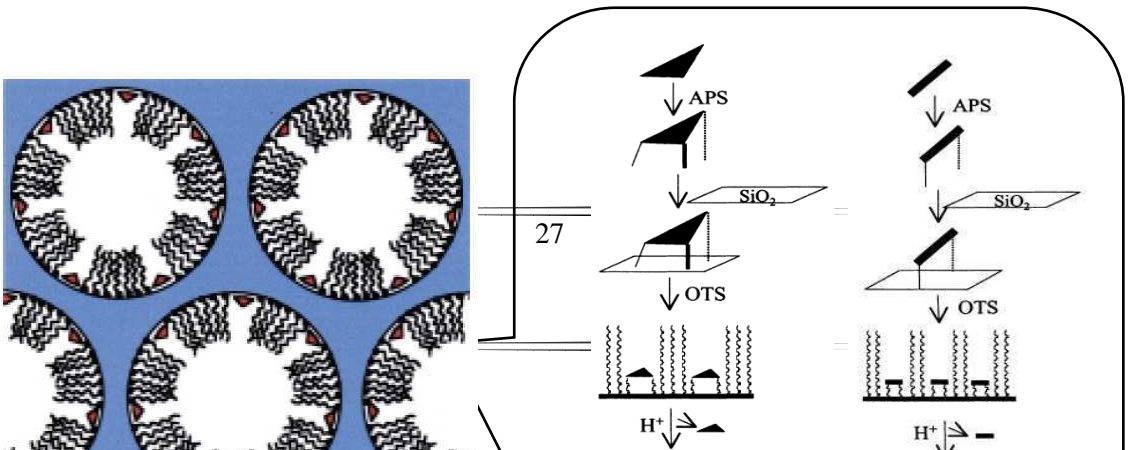

Figure 15 (A) Scheme representation of hierarchical porous material containing a rigid mesoporous oxide frame coated by a soft 'microporous' molecular monolayer by (B) varying the template molecules with tripod or dipod. The triangular shape represents the template molecules, or the idealized shape of cavity; APS: aminopropyltrimethoxysilane; OTS: octadecyltrimethoxysilane.

Lately, Jones *et al.* proposed a technique applied in mesoporous MCM-41 that takes advantage of the amino group protection-deprotection sequence to introduce steric hindrance for distance control between amino groups. Firstly, the amino group is direct bonded with the large trityl groups, which prevents incorporation of the function silane on the surface at sites immediately adjacent to each other. Then, with the functionalization of the designed aminosilane on the surface, the rest unreacted silanols are covered by trimethylsilyl group. A selective hydrolysis can remove the trityl groups giving the isolated amino group and a further capping is able to consume the additional silanol group generated in the hydrolysis (Figure 16). The latter technique allows the function group to work at full coverage in comparison to the other techniques. However, it does not provide control of the vicinity between two different species in comparison to pure molecular.

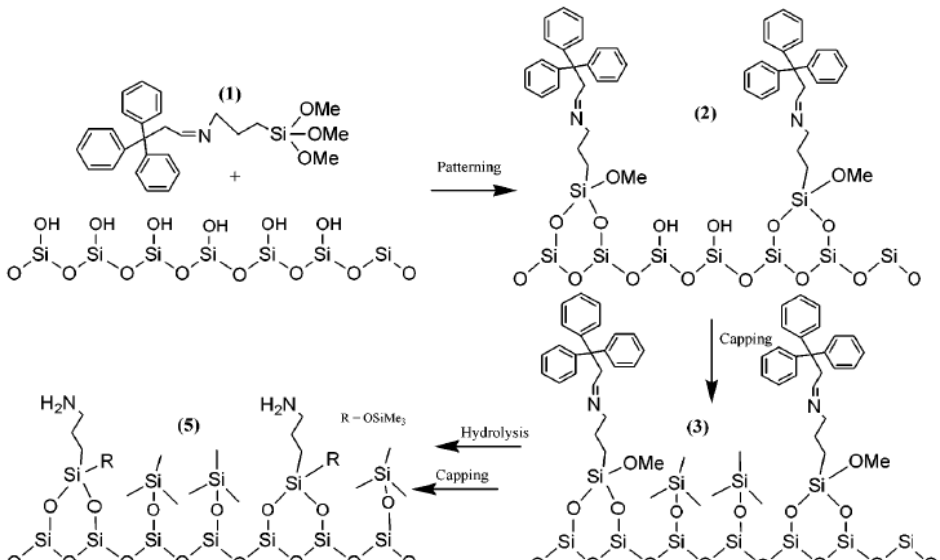

Figure 16 Scheme representation of a molecule patterning technique for the effective spacing of aminosilane groups on a silica surface.[90]

As a novel technique, it has been developed especially for the homogeneously positioned bi-functional post-grafting by L. Bonneviot *et al*, so-called molecule stencil patterning (MSP). It follows the sequences that a monolayer of template molecules are coated on the surface of mesoporous silica, soon afterwards some of them are selectively removed and it gives rise to cavitated patterns within the coated material, which refers to the free silanol groups. Subsequently, the first grafted funtion are deposited on the unoccupied surface of the silica substrates via condensation with silanol groups. Finally, the residual template molecules are removed from the surface with a mild acid wash, leaving the cavities for the eventual grafting of second functional group (Figure 17). Note that, the role of the first grafted function is to dilute the second function in order to avoid close molecular proximity between the functions of the second type even at full surface coverage.

Usually, the template molecules refer to the cation of surfactant used in the synthesis of mesoporous silica like cetyltrimethylammonium (CTA^+). After partial removal, a self-repulsion between the positively charged cations is meant to provide a regular pattern cavities homogeneously distributed all through the channel. The masking cation molecules are bulky with their long alkyl chains and may affect the distribution of the functions grafted at first (Figure 17). Thus, the template cation can be replaced by a smaller one like trimethylammonium (TMA^+) that the grafting of the first function is promoted with a controlled coverage tuning the concentration of the masking cation (*Chp. 1*, Figure 2).

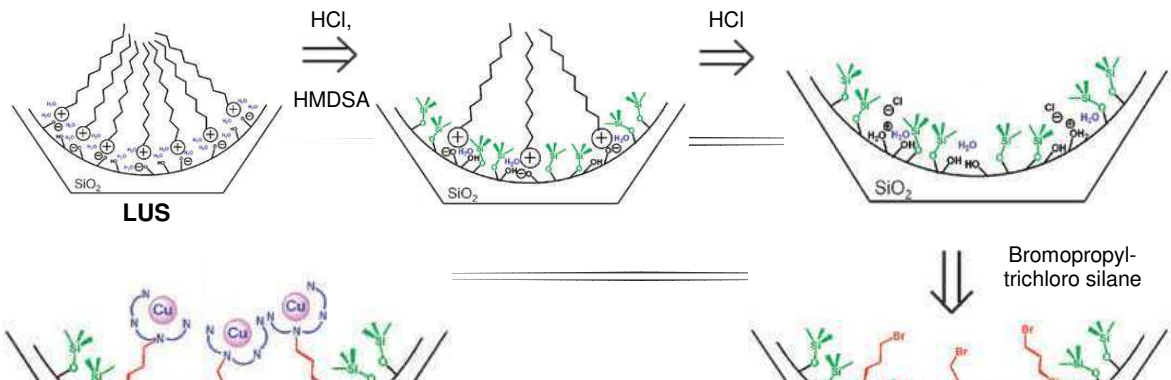

HCl

Figure 17 Synthetic steps of MSP technique using long alkyl chain cation CTA^+ as masking template.[91,92]

2.3 Ti-substituted mesostructured silica materials

Titanium is often called as the element of the 21st century because of its excellently thermodynamical reactivity, as well as its compounds, especially the extremely broad range of industrial applications of titanium-based materials.

The Ti-based porous silica materials have been famous for a long time as an efficient catalyst in oxidation reactions in the liquid phase using hydrogen peroxide or alkyl hydroperoxides as oxygen donors. The preliminary catalysts TiO_2-SiO_2, obtained by dispersing a titanium precursor on the surface of silica, have showed interesting activities and selectivities in the epoxidation of 1-octene with *tert*-butyl hydroperoxide (TBHP). In 1983, the first synthesis of titanium-substituted silicalite, TS-1 zeolite was reported, which was particularly active and selective in the oxidation and hydroxylation of small substrates with dilute H_2O_2 solutions. These properties promoted the development of new catalytic systems, based on zeolitic or amorphous materials. However, the small pores of TS-1 zeolite (0.7 nm) with the MFI topology limits its application to relative small molecules and imposes mass transport limitations.

Considerable effort has been devoted in the later more than twenty years to the synthesis of large pore Ti-incorporated zeolites, such as Ti-β (6.4 × 7.6 Å), ITQ-7 (6.1 × 6.5 Å), and Ti-MWW (7.1 × 18.2 Å), Ti containing mesoporous silicas like Ti-MCM-41 (~3.5 nm), Ti-MCM-48, Ti-SBA-15 (7~10 nm), and Ti-containing hierarchical

macroporous silica with mesoporous framework, etc.[5,93,94,95,96,97,98,99] In particular, the discovery of Ti(IV) contained mesoporous materials which possess the wider pore sizes (2~10 nm) and high surface area as reaction space opened new opportunities in various organic reactions with bulky substrates.

2.3.1 Synthesis

The titanium ion can be immobilized in the framework of mesoporous silica matrix via two ways as those for synthesizing mesoporous silica: one-pot synthesis and post-synthesis. During the hydrothermal one-pot synthesis, Ti precursor is usually added in the initial mixture solution, hydrolyzing with the silica source to form a homogeneous gel. However, the solubility of titanium source used to be a problem, which is partly solved by application of titanium tetrachloride $TiCl_4$ or different titanium alkoxides $Ti(OR)_4$ easily subjected to hydrolysis and form a homogeneous precursors solution. Titanium consequently exists in the bulk silica lattice and anchored on the wall randomly like the framework substituted type and grated type in Figure 18. Additionally a hydrolysis retarding agent related to the complexing polyalcohol such as 2,2',2"-nitriletriethanol, glycerol are added used for stabilizing the titanium species due to its high viscosity.[100,101]

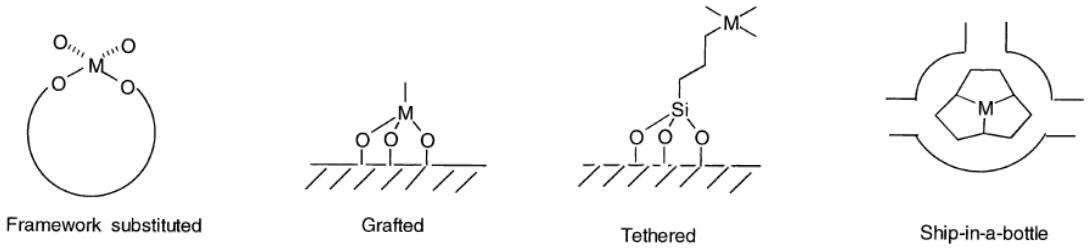

Figure 18 Schematic representation of strategies for heterogenization of Ti centre (M).[102]

The titanium alkoxides are also applied commonly in the post-synthesis of Ti-mesoporous Si, instead of titanium tetrachloride to avoid damage the Si framework from the corrosive by-product HCl. However, there is a marked tendency that the titanium alkoxides sometimes lead to oligomeric titano-oxo species or/and some anatase in the channels or on the external surface of the catalysts during the grafting. To result in high titanium dispersion on the silica surface, the use of chemically modified titanium precursors with lower reactivity were therefore explored, like titanocene dichloride

($TiCp_2Cl_2$),[103,104,105] titanium chelates,[106,107] titanosilicate molecular,[108,109] sub-nanometric multinuclear titanium cluster [110] (Figure 19) and so forth. And with different titanium precursors, the metal ion centres will differ as tethered branch on the silica surface by grafting dimeric titanosilicate complex or ship-in-a-bottle in the mesopores by using titanium cluster or the normal grafting species on the wall surface by applying the titanium alkoxides or titanocene compounds (Figure 18).

The Ti(IV) substituted porous silicas have been one of the most heavily studied heterogeneous catalysts in recent years since they exhibit a remarkably high catalytic efficiency and selectivity in olefin epoxidation,[111,112,113] phenol hydroxylation, and secondary alcohol dehydrogenation,[114] etc[115,116] using H_2O_2 or TBHP as conventional oxidants.[117] However, the structure of the active Ti site has not been definitively identified due to the extremely low concentration of the titanium site in the framework, even the catalyst materials have been extensively characterized by various techniques aiming to discovering the relation between microenvironment of active Ti sites and reactive phenomenon.

Several experimental and computational results demonstrate that the substitution of Si by Ti is isomorphous in well-prepared samples. In zeolites, the activity has been attributed to isolated, generally tetrahedrally coordinated, framework Ti species.[118,119]

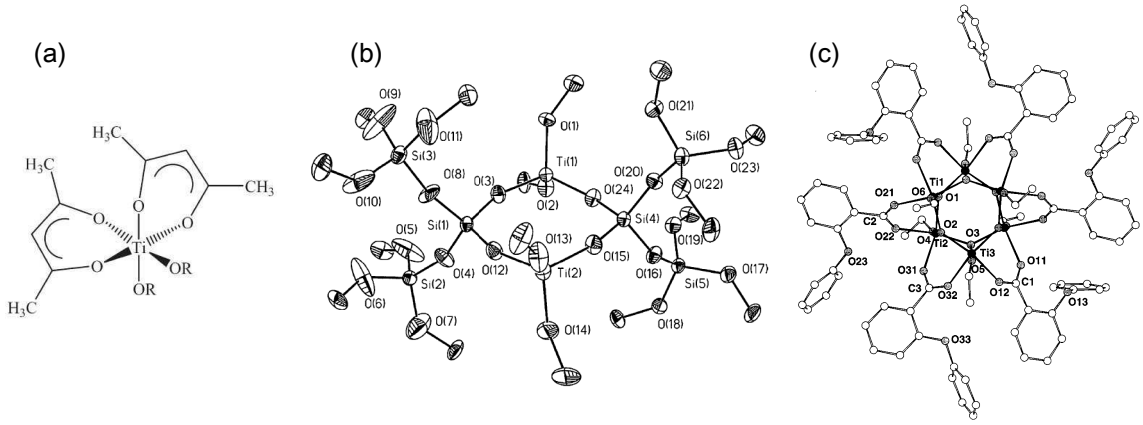

Figure 19 Scheme of chemically modified titanium precursors: (a) acetylacetone chelated titanium alkoxide, (b) dimeric titanosilicate complex, and (c) hexanuclear titanium oxo carboxylato alkoxide cluster with a size of ca. 8 Å.

However, the situation in mesoporous silicas is generally believed that the distribution of Ti over the available framework sites is at least partially disordered. It is

reported that Ti-MCM-41 or Ti-HMS materials actually contain Ti species with 4-, 5-, and 6-fold coordinations.[120] The higher coordination sites most likely result from hydration of tetrahedrally coordinated Ti species, as well as the TiO_2 nano-particles inside the mesopores due to the presence of excess titanium precursor.

2.3.2 Characterization

A variety of techniques have been developed able to detect and discriminate tetra-coordinated framework titanium from extra framework titanium atoms with higher coordination in the solid silica matrix. They are related to diffuse reflectance UV spectrum (UV), UV resonance Raman spectroscopy (UV-Raman), X-ray absorption spectroscopy (XAS), and electron paramagnetic resonance spectroscopy (EPR)/electron spin resonance spectroscopy (ESR) and so on, besides to the conventionally physic-chemical characterizations for mesoporous silica and its functionalized materials: powder X-ray diffraction (XRD), transmission electron microscopy (TEM), nitrogen adsorption isotherms, Fourier transform infrared spectra (FTIR), solid-state ^{29}Si magic angle spinning nuclear magnetic resonance (^{29}Si MAS NMR), ^{13}C cross-polarization magic angle spinning nuclear magnetic resonance (^{13}C CPMAS NMR) and elemental analysis (EA).

2.3.2.1 FTIR

The peak assignments of the pure mesoporous silica can be made on the basis of early studies on various silicates. In the basic photoacoustic-FTIR spectrum of MCM-48 (Figure 20), which proves an excellent comparison for mesoporuos silica since its peaks are clearly resolved, the sharp band at 3745 cm^{-1} is assigned to isolated SiO-H stretches and a broad band accompanies from 3400 to 3700 cm^{-1} assigned to stretching frequencies of hydrogen bound silanols. Associated with the isolated SiO-H stretches there is a band observed at 978 cm^{-1} which is assigned to the $Si\text{-}O^{\delta-}$ stretching, as well as the band in the 910-830 cm^{-1} region for Si-OH stretching (not shown). The relative narrowness of this peak at 978 cm^{-1} can be explained by the contribution from the predominance of isolated silanols on the silica surface.

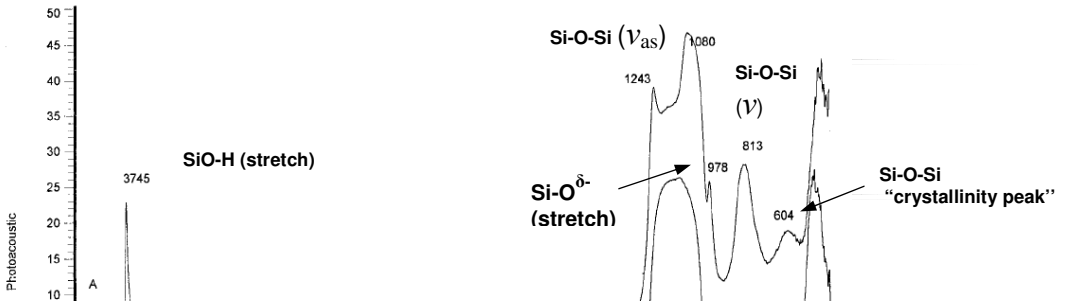

Figure 20 Photoacoustic-FTIR spectra of (A) pure silica MCM-48 and (B) Aerosil-600 amorphous silica.

Three framework bands are observed at lower frequencies for the Si-O-Si asymmetric vibration (ν_{as}) at 1243 and 1083 cm^{-1} with a weak peak at about 1195 cm^{-1}, and a strong peak at 817 cm^{-1} is attributed to Si-O-Si symmetric vibration (ν_{sym}). As to its bend mode, the peak appears at 470~500 cm^{-1}, which is commonly used as the reference for semi-quantitative of certain peaks.[91] The band at 604 cm^{-1} can be ascribed to the "crystallinity peak" resulting from the formation of silica 5-rings during hydrothermal treatment as formed in zeolite synthesis. The presence of this peak, which is notably absent in the spectrum of Aerosil-600 amorphous silica, is evidence for some intermediate range order within the walls of mesoporous silica materials.[121]

The organic species show the natural FTIR characteristic after anchored on the silica matrix only when the band is overlapped by that from silica. For example, when the amine group and carboxylic group are both grafted by the relative silanes on the SBA-15, the FTIR spectra displays all the peaks corresponding to the functional groups (Figure 21, A). The bands at 1330 cm^{-1}, 1480 cm^{-1}, and 1590 cm^{-1} correspond to the C-N stretching, the stretching and deformation frequencies of $N\text{-}H_3^+$ and N-H respectively, belonging to the amino group. While the bands at 1400 cm^{-1} and 1620 cm^{-1}, are assigned to the typical asymmetric and symmetric frequencies of ionic carbonyl ($O{=}CO^-$) which confirming the successful grafting of carboxylic group on the silica. Moreover the absence of bands in the 1754-1720 cm^{-1} range due to the C=O stretching from -COOH reveals a co-existence of carboxylic acid group in the acid-base bifunctionalized hybrid solid material.[122]

In the high region of FTIR spectra, the silanol group band at 3700 cm^{-1} disappearing in functionalized samples with silanes (Figure 21, B), is a clear indication of the chemical reaction between the organo-silane reagent and the terminal and geminal silanol groups. Furthermore, the bands appear between 3000-2800 cm^{-1} range due to the typical C-H stretching vibration that proves the formation of -CH_3 groups during the silylation process, accompanied by a Si-C stretch at 850 cm^{-1} (no shown in the Figure).[91]

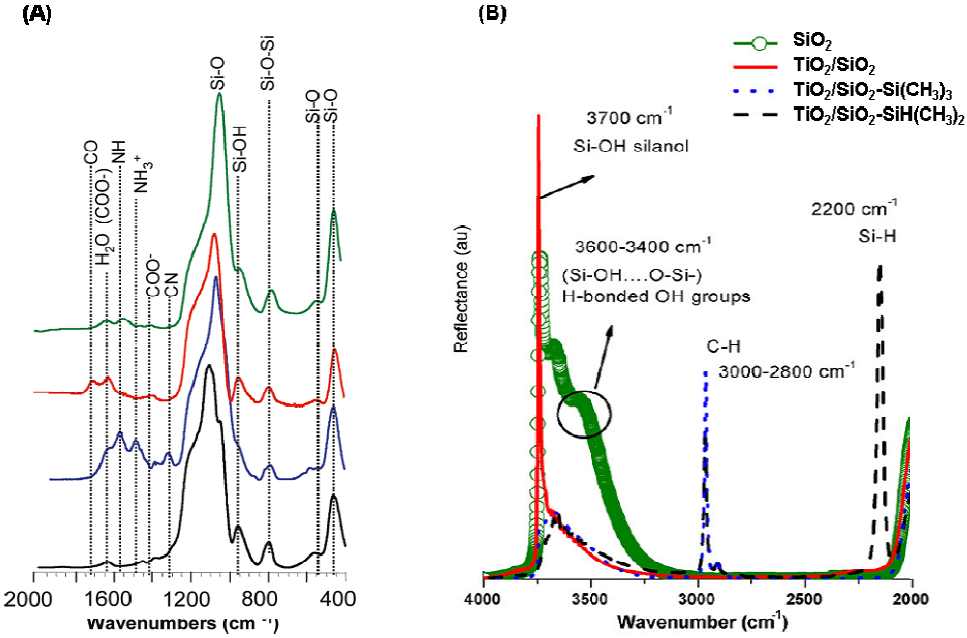

Figure 21 FTIR spectra of organic goup modified (A) SBA-15 and (B) dehydrated TiO_2/SiO_2 and it silylated samples.[122,123]

However, as to the Ti containing silica material like TiO_2/SiO_2, Ti-MCM-41, and Ti-SBA-15, the IR spectra showing a SiO-Ti stretching band centered in the 950~960 cm^{-1} range without any other featured peaks in the high region, is generally attributed to the overlapping of antisymmetric SiO-Ti stretching and Si-OH stretching.[124] But Wu *et al.* have reported that the band could split into two bands after evacuation at 573 K and turned out to be a new band with a maximum adsorption at 948 cm^{-1} when evacuation was done at 773 K (Figure 22, A). The results suggest the 948 cm^{-1} band could be assigned to purely the tetrahedral Ti species in Ti- mesoporous silica. Since the intensity of band at 948 cm^{-1} could hardly change with the evacuation temperature and gradually increased with increasing Ti content, the findings could be obtained through the dependence illustrated in the Figure 22 (B) that Ti species are incorporated into the silica

framework to occupy initially the tetrahedral sites and then partially the octahedral sites with a gradual increase in Ti incorporation.[101]

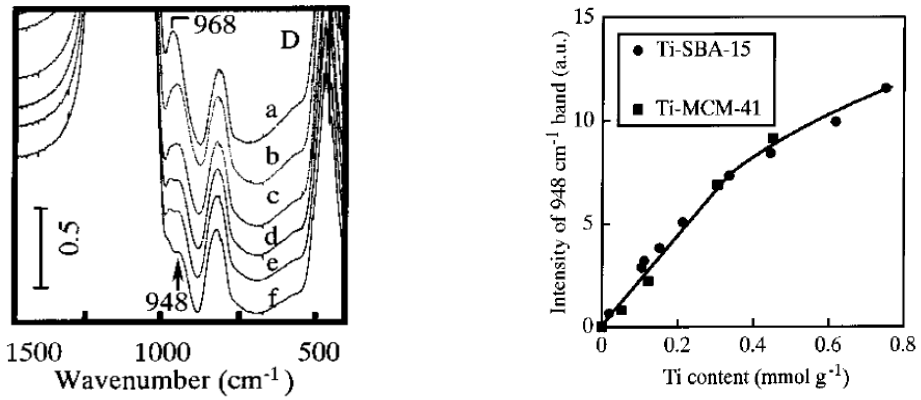

(A) (B)

Figure 22 IR spectra for (A) Ti-SBA-15 (Si/Ti=36) without evacuation (a) and after evacuation at (b) 373 K, (c) 473 K, (d) 573 K, (e) 673 K, and (f) 773 K each for 1 h and (B) dependence of the intensity of the 948 cm^{-1} band on the Ti content of Ti-SBA-15 and Ti-MCM-41.

2.3.2.2 Solid ^{29}Si & ^{13}C NMR

The basic structural units of organic-inorganic moiety in the mesoporous silica materials can be confirmed by solid state magic-angle spinning nuclear magnetic resonance (MAS NMR) technique. The technique can remove line broadening from the dipolar interaction, first-order quadrupolar interaction and the chemical shift anisotropy by fast rotation of the sample about an axis inclined at a certain angle (magic angle) to the direction of the external magnetic field.

The pure mesoporous silica functionalized by silanes to hybrid material is confirmed the inorganic Si environments by the presence of typical chemical shifts assigned to the signals Q_4 (-110 ppm), Q_3 (-100 ppm), and Q_2 (-90 ppm). Si in the siloxane networks give the distinct signals of T_2 (-57 ppm) and T_3 (-65 ppm) which is formed from *n*-alkyltrimethoxysilanes, D_1 (-10 ppm) and D_2 (-16 ppm) formed from *n*-alkylmethyldimethoxysilanes, and M_1 (13 ppm), M_0 (18 ppm), and M_1-M_1 (7 ppm) formed from *n*-alkyldimethylmethoxysilanes (Figure 23).[89,125]

The populations of these silicon environments can be calculated quantitatively using the integrated intensities supported by ^{29}Si NMR spectra and the signals T_n, D_n or M_n assigned to the organic species are indicative quantification of the organosilyl groups

in the hybrid silica materials. Assuming that all Q_4, Q_3, and Q_2 sites are accounted the composition of inorganic surface and interior walls, normalized by which the organic moieties (Si_{org}) related to the surface coverage are estimated as $Si_{org}\%$ = $(T_2+T_3)/(Q_2+Q_3+Q_4)*100\%$ for example if it's only derived from *n*-alkyltrimethoxysilane. As well, the silanol group can be proportional by Si-OH% = $(2*Q_2+Q_3)/(Q_2+Q_3+Q_4)*100\%$ to the whole silica matrix system.[122,126]

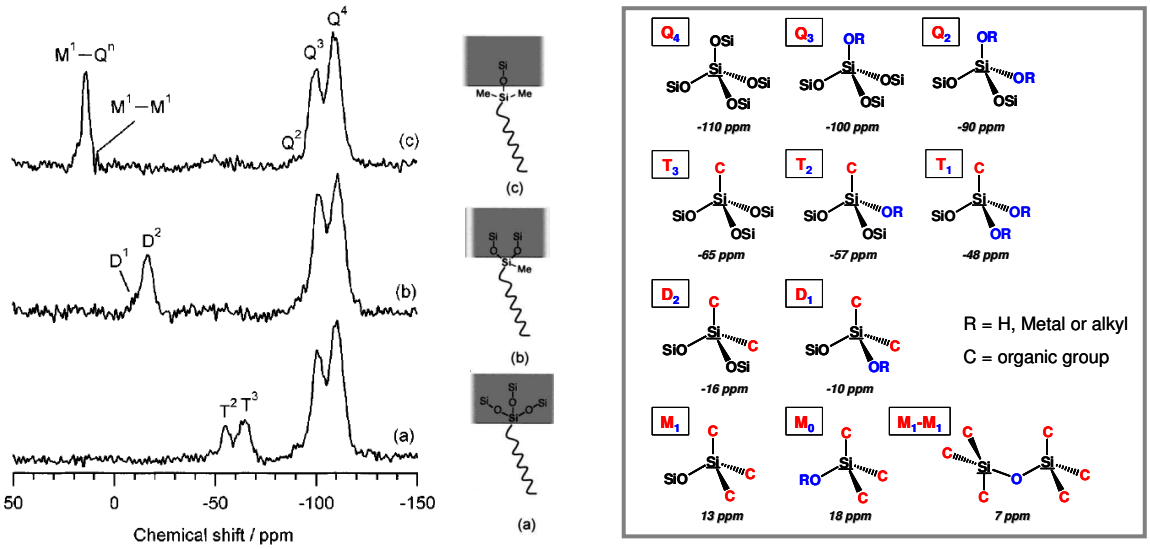

Figure 23 ^{29}Si MAS NMR spectra of silica modified by (a) *n*-Alkyltrimethoxysilanes, (b) *n*-alkylmethyldimethoxysilanes and (c) *n*-alkyldimethylmethoxysilanes

Covalently bonded to the immobilized patterning Si species, the carbon atoms are showed the characteristic signals in the solid state ^{13}C cross-polarization (CP) NMR spectrum. However, the signals for the same carbon position demonstrate different chemical shift when in the different type of silanes. For example, an ethane fragment sandwiched by silicons (Si-CH_2CH_2-Si), the chemical shifts of methylene carbon (-**C**H_2-) vary 2.0 ppm, 5.4 ppm, and 9.3 ppm when the "sandwiches" form as $(OH)_3$Si-**C**H_2**C**H_2-Si$(OH)_3$, $(OSi)_3$Si-**C**H_2**C**H_2-Si$(OSi)_3$, and $(CH_3)_2(OSi)$Si-**C**H_2**C**H_2-Si$(OSi)(CH_3)_2$, respectively.[127,128] According to the theory of NMR, the chemical shift is effected by the adjacent group which is electron donor or withdraw, more electron donor, higher chemical shift, as the comparison between -NH_2 and -Cl noted in Table 3, entries a-d. Normally the carbon shift is similar as that in the liquid phase for the Si atom acts like a

prone (Table 3, entries e-f).

Table 3 ^{13}C NMR resonances of organic patterning agent functionalized on the silica.[89,129]

Entry	Assignment	Resonance (ppm)
a	-Si-CH_2-**C**H_2-CH_2-Cl	26
b	-Si-CH_2-**C**H_2-CH_2-NH_2	22
c	-CH_2-**C**H_2-Cl	46
d	-CH_2-**C**H_2-NH_2	42
e	-**C**H=N-	165
f	-CH_2-**C**-$(Ph)_3$	145
g	-Si-**C**H_3	0
h	-Si-**C**H=CH_2	137
i	-Si-CH=**C**H_2	132
j	-Si-**C**$_6H_5$	128
k	-Si-O**C**H_3	49

2.3.2.3 UV & UV-raman spectroscopy

The influence of Ti containing silica solids on the catalytic properties is quite difficult to estimate due to the simultaneous presence of Ti species with different coordination states. The in situ X-ray absorption spectroscopy establishes unequivocally the averaged structure of the Ti site of surface-grafted Ti-MCM-41 is tetrahedral containing around three Ti-O-Si bonds.[74] And most commonly, UV-vis spectroscopic and catalytic studies have revealed that the surface Ti sites which gives the best activity/selectivity performance corresponds to the isolated and tetrahedral, while the presence of titanium dimers or oligomers is thought to accelerate decomposition of the peroxide and octahedrally coordinated titanium is inactive for the epoxidation of alkenes since it lacks free coordination sites.[52,96 ,97 ,101]

UV-vis spectroscopy is proved a very useful tool as it gives direct information on the chemical events occurring in the first coordination sphere of Ti(IV). Bands at 48000 cm^{-1} are assigned to Laporte allowed ligand to metal charge transfer (LMCT) transitions in [TiO_4] and [O_3TiOH] tetra-coordinated structures. New bands appearing as an optical transition in the 40000~30000 cm^{-1} range is assigned to LMCT bands in $[TiO_2]_n$ clusters,

or from a direct interaction of incoming adsorbate ligands with the Ti(IV) atoms, leading the coordination number of Ti(IV) increases (Figure 24).

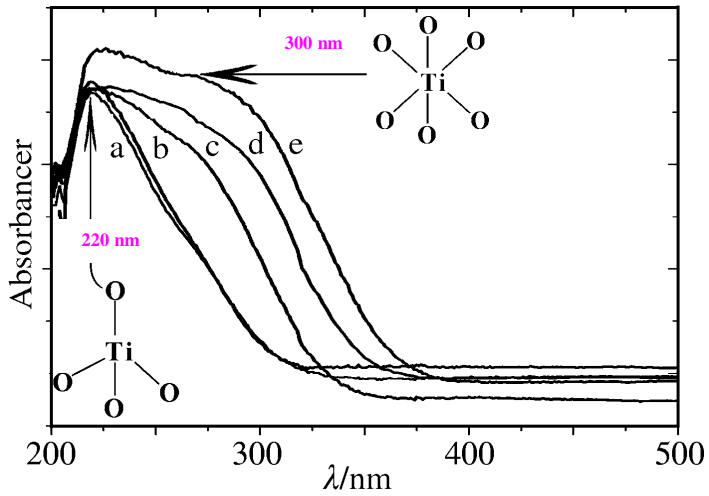

Figure 24 Diffuse reflectance UV–Visible spectra of mesoporous titanosilicates with Si/Ti of (a) 49.9; (b) 34.9; (c) 19.0; (d) 8.3; (e) 1.9.[100]

In the molecule orbital of [TiO_4] (Figure 25), LMCT arises because the absorbed UV radiation causes an electron jumping from *e* orbital at low energy mainly composed of O π-bongding to the *e** orbital in which there is a large contribution from the unoccupied Ti *d* orbitals. The wavelengths (nm) of bands observed in the UV-vis spectra depend on the ease with which an electron can be removed from the ligand. The wavenumber (cm^{-1}) of a particular band increases with an increase in the ionisation energy of the ligand *n*p electrons which normally contribute to the *e* orbital. When the ionisation energy increases, the energy of the *n*p levels decreases, and so the energy gap between the ligand and metal orbitals increases. Therefore the charge transfer $O^{2-} \rightarrow Ti^{4+}$ occurs at the highest energy for the isolated [TiO_4] unit in the silica network, which can attributed to the higher electronegativity from surrounding Si(IV) than from the Ti(IV) in Ti-O-Ti bonds.

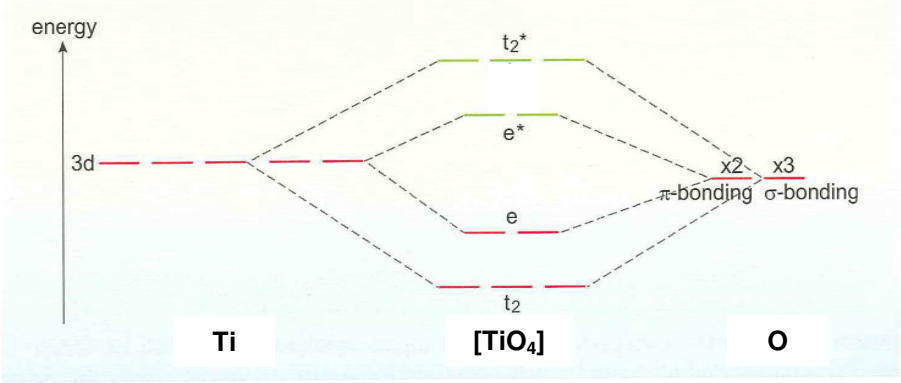

Figure 25 Partial orbital energy-level diagram for the tetrahedral [TiO_4] formed from filled σ-bonding and π-bonding O orbitals.[130]

Mainly based on the theoretical considerations and interpretations of the UV-vis spectra of titanosilicates solid materials, the coordination of Ti species can be assigned generally to an increase of the excitation energy from 42000 cm^{-1} for octahedral coordinated $Ti(OH)_6$, to 48000 cm^{-1} for the tetrahedral one, $Ti(OH)_4$ for perfect symmetries.[131] However, J. Klaas *et al* simulated satisfactory diffuse reflectance UV-vis spectrums (Figure 26, A) for hydrated zeolites Ti-NaY and Ti-NaX, and assumed three different bands with absorption maxima at about 36000 cm^{-1}, 45000 cm^{-1}, and 49000 cm^{-1} with relevance to the Ti monofunctional, bifunctional, or multifunctional bonding manner to the zeolite framework, respectively.[132] L. Bonneviot *et al* deconvolved the UV-vis spectrums of dehydrated TS-1 into three peaks at 50200 cm^{-1}, 44060 cm^{-1} and 40000 cm^{-1} (Figure 26, B) which account respectively for the Ti-OSi, Ti-OH in the tetrahedral open site and Ti-OSi in the stressed tetrahedral closed site.[133]

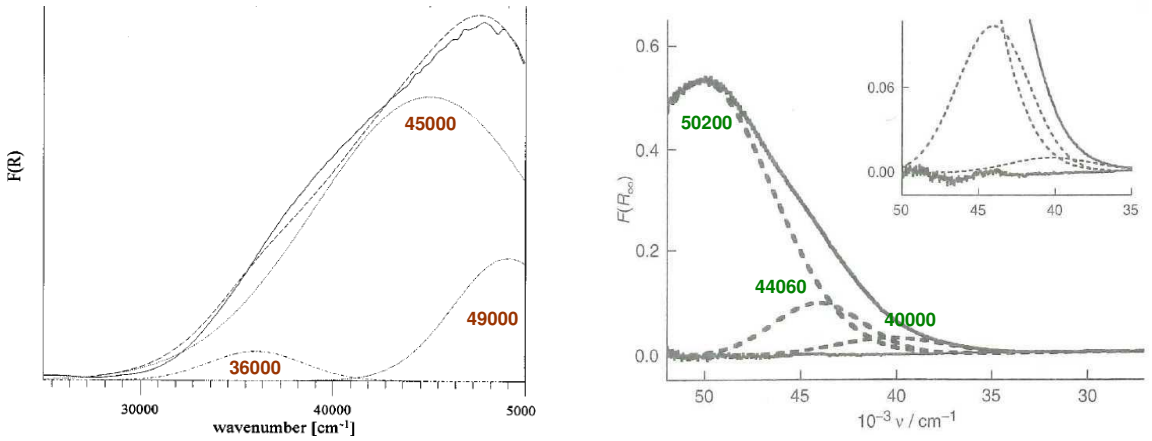

(A) (B)

Figure 26 Normalized diffuse reflectance UV-vis spectrum $F(R)$ of TiO_x species in (A) zeolite NaX (solid line: experimental spectrum; dashed line: silmulated curve; dotted line: fits) and (B) dehydrated TS-1 (solid line: experimental spectrum; dashed line: fits; line on the base: the difference between fits and experimental).

Usually in the UV region, the characteristic bands directly associated with the coordinated transition metal ions, whose wavelength is chosen for the UV laser of resonance Raman spectra (UV-Raman) to enhance the excitation of the ligand to metal charge transfer. It is more efficient to identify the isolated framework metal ions in microporous and mesoporous materials.[134]

For the Ti containing silica materials TS-1 or Ti-MCM-41, the charge transfer transition of tetrahedral Ti-OSi is commonly considered to be observed at 220 nm in the UV-visible diffuse reflectance spectrum (Figure 27, A). The laser line at 244 nm was chosen to excite the electronic transition absorption of the Ti species in Ti containing silica materials for the Raman spectrums. A distinct band appears at 1125 cm^{-1} for TS-1, the microporous titanosilicate, and band at 1110 cm^{-1} are observed for Ti-MCM-41 (Figure 27, B and C). The appearance of these bands is associated with the tetrahedral coordinated Ti but not with silica framework, which are ascribed to the asymmetric stretching vibration of Ti-OSi. When excited by laser at 325 nm and 488 nm, new bands appear at 144, 390, and 637 cm^{-1} which are assigned to the extra-framework Ti clusters (anatase), instead of those in the 1000~1200 cm^{-1} range.[135,136]

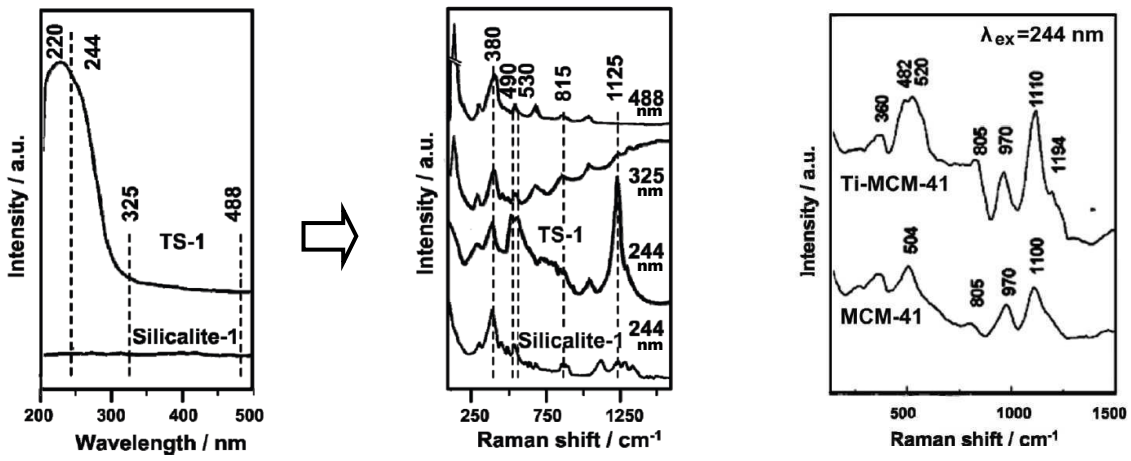

Figure 27 (A) UV-visible diffuse reflectance spectra, (B) Raman spectra excited with different laser lines at 244, 325 and 532 nm of silicalite-1 and TS-1, and (C) UV-Raman spectra of MCM-41 and Ti-MCM-41 (Si/Ti = 200) excited with 244 nm.

According to the subtle dissimilarity between the coordination environments of Ti^{4+} in microporous and mesoporous materials, there is a red shift from 1125 cm^{-1} for rigid tetrahedral Ti-SiO in TS-1 to 1085 cm^{-1} for very flexible site on amorphous SiO_2, which can be used as a figure of merit in assessing the coordination geometry of Ti^{4+} in microporous or mesoporous materials (Figure 28).

Figure 28 Comparison of the three Ti-SiO coordination environments and the corresponding UV Raman bands at 1125, 1100, and 1085 cm^{-1}, respectively, for TS-1, Ti-MCM-41, and Ti/SiO_2.[134]

2.3.2.4 XAS

With high fluxes of penetrating and continuously tunable X-rays (λ = 0.1 nm~100 nm), X-ray absorption spectroscopy (XAS) for fine structure measurements unambiguously establish the atom-specific structure of active centres. It yields electronic information of strictly local, short-range structure concerning bond lengths, coordination numbers, and mean square deviation in bond distances as well as the oxidation state.[137,138,139]

The pre-edge intensity in EXAFS of Ti arising from the transition between core level Ti 1s to the unoccupied $3d^0$ level of Ti(IV), which is known to be sensitive to the symmetry of the coordination environment. Accordingly, the characteristic sharp pre-edge peak at 4967 eV has been ascribed to the Laporte allowed $A_1 \rightarrow E$ characteristic

transition of tetrahedral [TiO_4] units. The structures of analogous Ti-centered silicates can be independently determined as shown in Figure 29 that lack of inversion symmetry for a tetrahedral coordination geometry yields an intense peak, whereas systems with octahedral coordination have small pre-edge intensities. In particular, five-coordinated systems, where there is a double bond as in JDF-L1, have intensities that are intermediate between those of the octahedral and tetrahedral cases. Hence the intensity of this pre-edge peak has been used to estimate the fraction of tetrahedral Ti(IV) by comparing the intensity of the pre-edge peaks of normalized spectra of some samples containing a different proportion between octahedral and tetrahedral Ti(IV).[140]

The change in type of neighbours to the coordinated Ti is identified with the local structural parameters given by EXAFS. G. Sankar *et al* have set out in 1995 the catalyst prepared from $TiCp_2Cl_2$ loaded in MCM-41. The XAFS results offered bonding lengths differing from the free Ti precursor, surface adsorbed molecules, anchored species and calcined Ti state that revealed in the final catalyst isolated Ti(IV)-centered active sites, composed of a tripodally linked titanol groups abound on the mesopores surface, without Ti-O-Ti linkages, nor of any titanyl group (Ti=O), which was active in the epoxidation of cyclohexene with TBHP.[103]

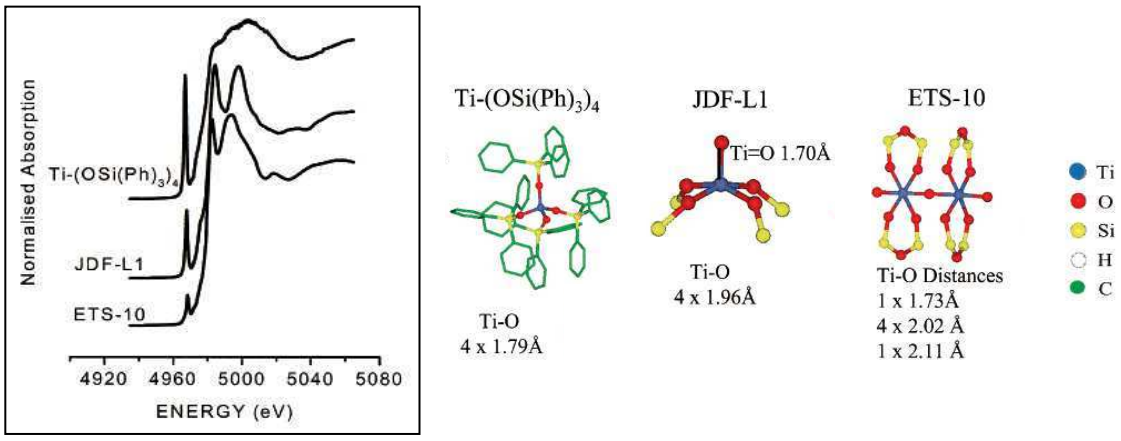

Figure 29 Ti K-edge XANES of three X-ray crystallographically well-defined titanosilicates in which there is four-fold (Ti-$(OSi(Ph)_3)_4$), five-fold (JDF-L1), and six-fold (ETS-10) coordination of oxygens around the central Ti.[98]

2.3.2.5 EPR

The metal ions with an odd number of unpaired electrons are excellent candidate for

electronic paramagnetic resonance studies (EPR). As a consequence that the Ti(IV), either in the precursors or coordinated in the network of solid compound is ESR silent. The reduction of Ti(IV) to Ti(III) with a reductant has been promoted that it helps study in detail the molecular structure or species intermedia of the products generated during the reaction, where the unpaired electron makes the complexes paramagnetic.[141,142,143,144,145]

The structure of titanium incorporated into both MCM-41 and MCM-48 materials were elucidated by EPR spectroscopy in Figure 30. After reduced Ti(III) in Ti-MCM-41 and Ti-MCM-48, species A with $g_{\perp}$ = 1.952 and $g_{//}$ = 1.902, characteristic of titanium atoms in tetrahedral coordination is observed in both materials.

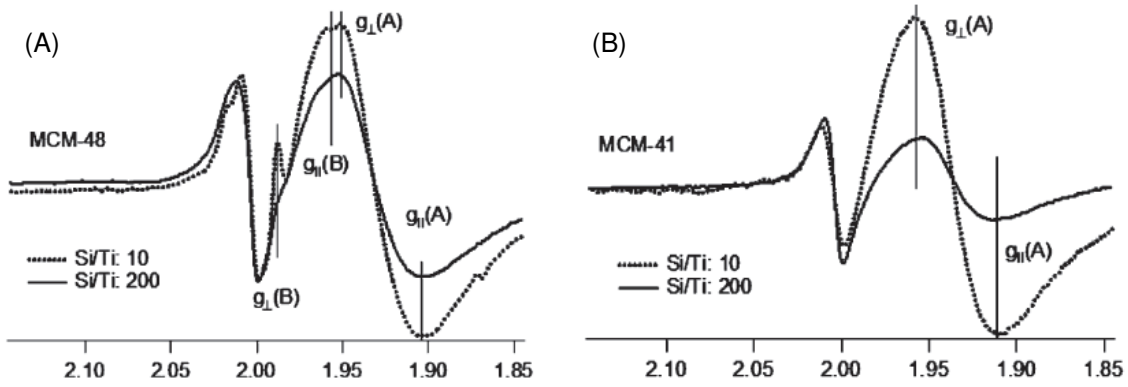

Figure 30 EPR spectra of (A) Ti-MCM-48 and (B) Ti-MCM-41 with different amounts of titanium ions. The spectra were recorded at 5 K after illuminating the samples in the presence of 1 M glycerol under UV irradiation at 77 K for 30 min.[142]

As Ti loading increasing, a second species B with signals $g_{\perp}$ = 1.988 and $g_{//}$ = 1.957 appears in the spectra of Ti-MCM-48 that corresponds to Ti(III) as in bulk anatase.[146,147] The g values indicate presence of both octahedral and/or five-coordinated Ti atoms, which has also been proved in the Ti-SBA-15.[141] A strong signal near g = 2.004 observed in all spectra is due to radicals formed in the reduction as the sacrificial hole scavenger to suppress charge recombination .

A catalytic cycle can be schemed as well by the method of Ti(III) EPR, for example, research reported by C. Petit *et al.* for the reduction of tertiary phosphine oxides (TPO) by hydrosiloxane using titanium alkoxides as catalyst.[145] The ESR spectrum observed two narrow features at g = 1.964 and 1.960 and a shoulder at 1.956 which are

far below the resonance of the free p-type unpaired electron g_e = 2.0023, and silicon, carbon and phosphorus radicals are always reported with values above 2.000. Compared furthermore to a similar isotropic signal of reduced tetraisoamyloxide titanum species which is known not to form any oligomers, the features are finally assigned to the $Ti^{III}(OR)_3$ in solution as a intermedia obtained by reaction between tetramethyldisiloxane and titanium isopropoxide during the reduction of TPO.

2.3.3 Enhancement of catalytic activity

Immobilized either on inert materials, or on functionalized solid supports, the Ti containing heterogeneous catalysts combine the advantages of homogeneous and heterogeneous phases and offer superiorities over homogeneous materials such as, ease of separation from reaction mixture, significant reduction in problems of waste disposal, and reuse applications by recycling, etc.[148,149] Besides to this, however, as to the catalytic behaviour, it is greatly influenced by many other factors like the material preparation route, the support natural characters, the reaction system, and the affinity between the interaction phases, etc.

During the one-pot synthesis, $Ti(OR)_4$ as the common precursor to form homogeneous parent mixture with Si source, has a tendency for oligomeric titano-oxo species or/and anatase cluster leading to low chemical homogeneity and phase segregation. J. El Haskouri *et al.* reported that a complexing polyalcohol was added as the hydrolysis retarding agent of the Ti species which could prepare thermally stable mesoporous titanosilicate molecular sieves with Ti content up to a minimum Si/Ti molar ratio value of 1.9 and the highest amount of tetrahedral Ti-sites was maintained.[100]

Followed by more options of proper Ti source as titanocene dichloride, titanium chelates (as describe in 2.3.1), both of the direct synthesis and post-grating pay more attention to the isolated formation of tetrahedral Ti coordination. However, limited numbers of reports have dealt with Ti-substituted mesoporous silica material. S. Chen *et al.* dealt with a as-made Ti-SBA-15 material with Ti loading up to 10 mol% upon calcination at 600~1000 °C that the extreme high temperature contrary generated

tetrahedrally coordinated Ti(IV) species on the superficial areas of SBA-15 silica framework and acted as more effective catalytic sites in cyclohexene epoxidation compared to that calcined below 600 °C.[150]

Nonetheless, A. Tuel *et al.* have grafted subnanometric monodispersed titanium oxide particles on the surface of SBA-15 via Si-OH using a hexanuclear titanium oxo cluster instead of the conventional $TiCl_4$, $Ti(OR)_4$ sources. TiO_2 nanoparticles formed after calcination to eliminate all the organic ligand and showed active and selective in oxidation reactions using H_2O_2. The novel catalyst with alternate Ti source confirmed that a high activity does not necessarily mean that catalysts are free from TiO_2 particles and contain only tetrahedrally coordinated species and high Ti loading with activity decreasing must not be systematically attributed to the 6-fold coordinated species.[110]

Bi-component metals grafted mesoporous catalysts have been introduced as a significant effect on catalytic activity were observed when a second metal species modifying the silica surface prior to the Ti(IV) grafting. R. D. Oldroyd *et al* announced that Ge compound modified silica leading to large number of Ge-OH groups that would not react with Ti precursor so that it improved the isolation of Ti(IV) and therefore its activity in the epoxidation of cyclohexene with alkyl hydroperoxides, whereas the Sn containing material forms extraframework particles of SnO_2 that act as ineffective supports for Ti(IV) centers, as demonstrated by a separate experiment where $TiCp_2Cl_2$ was grafted onto high surface-area SnO_2.[140] M. Popova *et al.* also synthesized Fe, Ti containing mesoporous silica that increased selectivity of cyclohexanone in the cyclohexanol conversion because of the formation of Fe^{2+} species which acting as strong Lewis acid sites stabilized the adsorbed negatively charged intermediates.[114]

The Ti-substituted mesoporous silica materials with hydrophilic surface usually exhibit bad affinity between catalyst and reagent compared to the zeolite when in the catalytic oxidation of organic molecule. T. Tatsumi *et al.* conducted trimethylsilylation of Ti-MCM-41 and Ti-MCM-48 in order to enhance activity in oxidation with dilute H_2O_2 through increasing their hydrophobicity (as described in Chp. I, Figure 1).[82] The enhancement has been developed after soon as a conventional chemical tool to modify the hydrophobic property of solid catalyst including not only silica but also metal oxide.[151,152,153]

As to the active sites inaccessibility due to the limited pore entrance, both micro-

and meso- structured materials have been made effort to expand their space capability. Based on the remarkable activity of TS-1 zeolite in the oxidation reactions, H. Xin *et al.* presented mesoporous TS-1 with a disordered network of mesopores penetrating the microporous crystalline zeolite framework via a one-pot synthesis using carbon as hard template. The catalytic superiority of meso-TS-1 compared with conventional TS-1 zeolite is mainly attributed to the improved mass transfer by passing with the hierarchical structure.[136] The porosity of mesoporous material has also been tuned by S. Wang *et al.* with employing swelling agents that are hydrophobic in nature. The addition of favorable swelling agents leaded to an increase in pore size from 28.6 Å to 48.3 Å for Ti-MCM-41 accompanied by retaining the mesostructure with a certain decrease of structure ordering. A greatly enhanced catalytic activity of Ti-MCM-41 in the shape-selective transesterification was observed because of pore expansion.[154]

From the viewpoint of hydrophobic issue, there have been two strategies to improve the catalytic activity of Ti-substituted mesoporous silica materials in the epoxidation of olefins: the first approach is the intrinsic enhancement of Ti sites involving silylation on the surface, coordinated with larger ligand, etc, whereas the second approach is based on the reaction process strengthening. A. Corma *et al* concluded that the presence of water is responsible for the ring opening of the epoxide which strongly decreases the catalytic conversion of olefin. Removing water from the reaction media, the non-silylated catalysts display the same activity as those modified.[155] The effects of the method of adding substrates into the reaction system have been underlined as well, especially on the addition of hydrogen peroxide which usually deactivated rapidly on a Ti surface cluster in mesoporous Ti-silica catalysts.[105,156,157] The catalytic behaviour was improved evidently by applying a protocol consisting slow dropwise addition of hydrogen peroxide in the reaction mixture, compared with adding all of the substrates at once.

2.4 Reference

1 M. E. Davis, *Nature*, **2002**, 813.

2 A. Corma, *Chem. Rev.*, **1997**, 97, 2373.

3 M.E. Davis, C. Saldarriaga, C. Montes, J. Garces, C. Crowder, *Nature*, **1988**, 331, 698.

4 M. Estermann, L.B. Mccusker, Ch. Baerlocher, A. Merrouche, H. Kessler, *Nature*, **1991**, 352, 320.

5 T. Kamegawa, N. Suzuki, M. Che, H. Yamashita, *Langmuir*, **2011**, 27, 2873.

6 U. Ciesla, F. Schüth, *Microp. Mesop. Mater.*, **1999**, 27, 131.

7 R.M. Dessau, J.L. Schlenker, J.B. Higgins, *Zeolites*, **1990**, 10, 522.

8 H. van Koningsveid, J.C. Jansen, H. van Bekkum, *Zeolites*, **1990**, 10, 235.

9 B.M. Lok, C.A. Messina, R. Lyle Patton, R.T. Gajek, T.R. Cannan, E.M. Flanigen, *J. Am. Chem. Soc*., **1984**, 106, 6092.

10 T. Yanagisawa, T. Shimizu, K. Kuroda, C. Kato, *Bull. Chem. Soc. Jpn.*, **1990**, 63, 988.

11 J.S. Beck, J.C. Vartuli, W.J. Roth, M.E. Leonowicz, C.T. Kresge, K.D. Schmitt, C. T-W. Chu, D.H. Olson, E.W. Sheppard, S.B. McCullen, J.B. Higgins, J.L. Schlenker, *J. Am. Chem. Soc.*,**1992**, 114, 10834.

12 D.Y. Zhao, J.L. Feng, Q.S. Huo, N. Melosh, G.H. Fredrickson, B.F. Chmelka, G.D. Stucky, *Science*, **1998**, 279, 548.

13 F. Zhang, Y. Meng, D. Gu, Y. Yan, C. Yu, B. Tu, D.Y. Zhao, *J. Am. Chem. Soc.*, **2005**, 127, 13508.

14 Y. Meng, D. Gu, F. Zhang, Y. Shi, H. Yang, Z. Li, C. Yu, B. Tu, D.Y. Zhao, *Angew. Chem. Int. Ed.*, **2005**, 44, 7053.

15 K. Ariga, A. Vinu, J.P. Hill, T. Mori, *Coord. Chem. Rev.*, **2007**, 251, 2562.

16 A. Taguchi, F. Schüth, *Microp. Mesop. Mater.*, **2005**, 77, 1.

17 O.D. Velev, T.A. Jede, R.F. Lobo, A.M. Lenhoff, *Nature*, **1997**, 389, 447.

18 B.T. Holland, C.F. Blanford, A. Stein, *Science*, **1998**, 281, 538.

19 Y. Sakamoto, M. Kaneda, O. Terasaki, D.Y. Zhao, J.M. Kim, G. Stucky, H.J. Shim, R. Ryoo, *Nature*, **2000**, 408, 449.

20 Q.S. Huo, D.I. Margolese, G.D. Stucky, *Chem. Mater.*, **1996**, 8, 1147.

21 Y. Huang, H.Q. Cai, T. Yu, F.Q. Zhang, F. Zhang, Y. Meng, D. Gu, Y. Wan, X.L. Sun, B. Tu, D.Y. Zhao, *Angew. Chem. Int. Ed.*, **2007**, 46, 1089.

22 A.H. Whitehead, J.M. Elliott, J.R. Owen, G.S. Attard, *Chem.Commun.*, **1999**, 331.

23 H. Hatayama, M. Misono, A. Taguchi, N. Mizuno, *Chem. Lett.*, **2000**, 884.

24 D. M. Antonelli, J.Y. Ying, *Angew. Chem. Int. Ed. Engl.*, **1996**, 35, 426.

25 D.M. Antonelli, A. Nakahira, J.Y. Ying, *Inorg. Chem.*, **1996**, 35, 3126.

26 D.M. Antonelli, J.Y. Ying, *Chem. Mater.*, **1996**, 8, 874.

27 F. Schüth, *Chem. Mater.*, **2001**, 13, 3184.

28 R.L. Liu, Y.F. Shi, Y. Wan, Y. Meng, F.Q. Zhang, D. Gu, Z.X. Chen, B. Tu, D.Y. Zhao, *J. Am. Chem. Soc*., **2006**, 128, 11652.

29 S. Jun, S.H. Joo, R. Ryoo, M. Kruk, M. Jaroniec, Z. Liu, T. Ohsuna, O. Terasaki, *J. Am. Chem. Soc.*, **2000**, 122, 10712.

30 S.H. Joo, S.J. Choi, I. Oh, J. Kwak, Z. Liu, O. Terasaki, R. Ryoo, *Nature*, **2001**, 412,169.

31 S. Che, K. Lund, T. Tatsumi, S. Iijima, S.H. Joo, R. Ryoo, O. Terasaki, *Angew. Chem. Int. Ed.*, **2003**, 42, 2182.

32 V. Meynen, P. Cool, E.F. Vansant, *Microp. Mesop. Mater.*, **2009**, 125, 170.

33 C. Sanchez, G.J.A.A. Soler-Illia, F. Ribot, C. Mayer, V. Cabuil, T. Lalot, *Chem. Mater.*, **2001**, 13, 3061.

34 B. Zhu, Y. Chen, J. Liu, W.D. Zhang, H.C. Zeng, *Chem. Mater.*, **2002**, 14, 1391.

35 Q.S. Huo, D.I. Margolese, U. Ciesla, P.Y. Feng, T.E. Gier, P. Sieger, R. Leon, P.M. Petroff, F. Schuth, G.D. Stucky, *Nature*, **1994**, 368, 317.

36 M.C. Orilall, U. Wiesner, *Chem. Soc. Rev.*, **2011**, 40, 520.

37 Y. Wan, D.Y. Zhao, *Chem. Rev.*, **2007**, 107, 2821.

38 H. Kang, Y. Jun, J. Park, K. Lee, J. Cheon, *Chem. Mater.*, **2000**, 12, 3530.

39 S. Tanaka, N. Nishiyama, Y. Egashira, K. Ueyama, *Chem. Commun.*, **2005**, 2125.

40 C. Liang, S. Dai, *J. Am. Chem. Soc.*, **2006**, 128, 5316.

41 G.J.A.A. Soler-Illia, C. Sanchez, B. Lebeau, J. Patarin, *Chem. Rev.*, **2002**, 102, 4093.

42 A. Monnier, F. Schüth, Q.S. Huo, D. Kumar, D. Margolese, R.S. Maxwell, G.D. Stucky, M. Krishnamurthy, P. Petroff, A. Firouzi, M. Janicke, B.F. Chmelka, *Science*, **1993**, 261, 1299.

43 S. Inagaki, Y. Fukushima, K. Kuroda, *J. Chem. Soc., Chem. Commun.*, **1993**, 680.

44 C.Y. Chen, S.Q. Xiao, M.E. Davis, *Microp. Mater.*, **1995**, 4, 1.

45 K. Flodstrom, H. Wennerstrom, V. Alfredsson, *Langmuir*, **2004**, 20, 680.

46 H. Yang, N. Coombs, I. Sokolov, G.A. Ozin, *Nature*, **1996**, 381, 589.

47 Q.S. Huo, D.I. Margolese, G.D. Stucky, *Chem. Mater.*, **1996**, 8, 1147.

48 Q.S. Huo, R. Leon, P.M. Petroff, G.D. Stucky, *Science*, **1995**, 268, 1324.

49 Z.H. Luan, H.Y. He, W.Z. Zhou, J. Klinowski, *J. Chem. Soc., Faraday Trans.*, **1998**, 94, 979.

50 R. Ryoo, S.H. Joo, J.M. Kim, *J. Phys. Chem. B*, **1999**, 103, 7435.

51 R. Schmidt, D. Akporiaye, M. Stocker, O.H. Ellestad, *J. Am. Chem. Soc. Chem. Commun.*, **1994**, 12, 1493.

52 T. Blasco, A. Corma, M.T. Navarro, J.P. Pariente, *J. Catal.*, **1995**, 156, 65.

53 T. Vralstad, G. Oye, M. Stocker, J. Sjoblom, *Micropor. Mesopor. Mater.*, **2007**, 104, 10.

54 J. Rodríguez-Castellón, A. Jiménez-López, P. Maireles-Torres, D.J. Jones, J. Rozière, M. Trombetta, G. Busca, M. Lenarda, L. Storaro, *J. Solid State Chem.*, **2003**, 175, 159.

55 M.H. Nilsen, E. Antonakou, A. Bouzga, A. Lappas, K. Mathisen, M. Stocker, *Micropor. Mesopor. Mater.*, **2007**, 105, 189.

56 E. Ruiz-Hitzky, P. Aranda, M. Dardera, M, Ogawa, *Chem. Soc. Rev.*, **2011**, 40, 801.

57 J. Fan, C.Z. Yu, L.M. Wang, B. Tu, D.Y. Zhao, Y. Sakamoto, O. Terasaki, *J. Am. Chem. Soc.*, **2001**, 123, 12113.

58 R. Xing, N. Liu, Y.M. Liu, H.H. Wu, Y.W. Jiang, L. Chen, M.Y. He, P. Wu, *Adv. Funct. Mater.*, **2007**, 17, 2455.

59 F. Schüth, *Annu. Rev. Mater. Res.*, **2005**, 35, 209.

60 D.W. Sindorf, G.E. Maciel, *J. Phys. Chem.*, **1983**, 87, 5516.

61 C. Lesaint, B. Lebeau, C. Marichal, J. Patarin, *Microp. Mesop. Mater.*, **2005,** 83, 76.

62 L. Mercier, T.J. Pinnavaia, *Chem. Mater.*, **2000,** 12, 188.

63 R. Anwander, *Chem. Mater.*, **2001,** 13, 4419.

64 E. Ruiz-Hitzky, P. Aranda, M. Darder, M. Ogawa, *Chem. Soc. Rev.*, **2011**, 40, 801.

65 M. Vallet-Regí, M. Colilla, B. González, *Chem. Soc. Rev.*, **2011**, 40, 596.

66 F. Hoffmann, M. Cornelius, J. Morell, M. Fröba, *Angew. Chem. Int. Ed.*, **2006**, 45, 3216.

67 L.C. Hu, K.J. Shea, *Chem. Soc. Rev.*, **2011**, 40, 688.

68 N. Mizoshita, T. Taniab, S. Inagaki, *Chem. Soc. Rev.*, **2011**, 40, 789.

69 G.J.A.A. Soler-Illia, O. Azzaroni, *Chem. Soc. Rev.*, **2011**, 40, 1107.

70 F. Hoffmann, Michael Fröba, *Chem. Soc. Rev.*, **2011**, 40, 608.

71 S. Inagaki, S. Guan, Y. Fukushima, T. Ohsuna, O. Terasaki, *J. Am. Chem. Soc.*, **1999**, 121, 9611.

72 T. Asefa, M.J. MacLachlan, N. Coombs, G.A. Ozin, *Nature*, **1999**, 402, 867.

73 M.P. Kapoor, S. Inagaki, S. Ikeda, K. Kakiuchi, M. Suda, T. Shimada, *J. Am. Chem. Soc.*, **2005**, 127, 8174.

74 T. Maschmeyer, F. Rey, G. Sankar, J.M. Thomas, *Nature*, **1995**, 378, 159.

75 M.H. Lim, A. Stein, *Chem. Mater.*, **1999**, 11, 3285.

76 M.H. Lim, C.F. Blanford, A. Stein, *J. Am. Chem. Soc.*, **1997**, 119, 4090.

77 A. Walcarius, M. Etienne, B. Lebeau, *Chem. Mater.*, **2004**, 15, 2161.

78 L. Han, J.F. Ruan, Y.S. Li, O. Terasaki, S.A. Che, *Chem. Mater.*, **2007**, 19, 2860.

79 C.C. Ting, C.H. Chung, H.M. Kao, *Chem. Commun.*, **2011**, 47, 5897.

80 A. Stein, B.J. Melde, R.C. Schroden, *Adv. Mater.*, **2000**, 12, 1403.

81 S.L. Burkett, S.D. Sims, S. Mann, *Chem. Commun.*, **1996**, 1367.

82 T. Tatsumi, K.A. Koyano, N. Igarashi, *Chem. Commun.*, **1998**, 325.

83 C. Sanchez, P. Belleville, M. Popalld, L. Nicoleab, *Chem. Soc. Rev.*, **2011**, 40, 696.

84 N. Igarashi, K. Hashimoto, T, Tatsumi, *Micropor. Mesopor. Mater.*, **2007**, 104, 269.

85 A. Katz, M.E. Davis, *Nature*, **2000**, 403, 286.

86 E.L. Margelefsky, A. Bendjériou, R.K. Zeidan, V. Dufaud, M.E. Davis, *J. Am. Chem. Soc.*, **2008**, 130, 13442.

87 S. Dai, M.C. Burleigh, Y. Shin, C.C. Morrow, C.E. Barnes, Z. Xue, *Angew. Chem. Int. Ed.*, **1999**, 38, 1235.

88 Y. Shin, J. Liu, L.Q. Wang, Z. Nie, W.D. Samuels, G.E. Fryxell, G.J. Exarhos, *Angew. Chem. Int. Ed.*, **2000**, 39, 2702.

89 M.W. McKittrick, C.W. Jones, *Chem. Mater.*, **2003**, 15, 1132.

90 M.W. McKittrick, C.W. Jones, *J. Am. Chem. Soc.*, **2004**, 126, 3052.

91 S. Abry, A. Thibon, B. Albela, P. Delichère, F. Banseb, L. Bonneviot, *New J. Chem.*, **2009**, 33, 484.

92 K. Zhang, B. Albela, M.Y. He, Y.M. Wang, L. Bonneviot, *Phys. Chem. Chem. Phys.*, **2009**, 11, 2912.

93 A. Corma, M.T. Navarro, J.P. Pariente, *J. Chem. Soc., Chem. Commun.*, **1994**, 147.

94 P.T. Tanev, M. Chibwe, T.J. Pinnavaia, *Nature*, **1994**, 368, 321.

95 T. Blasco, A. Corma, M.T. Navarro, J. P. Pariente, *J. Catal.*, **2000**, 189, 40.

96 W.H. Zhang, J.Q. Lu, B. Han, M.J. Li, J.H. Xiu, P.L. Ying, C. Li, *Chem. Mater.*, **2002**, 14, 3413.

97 L. Zhang, H.C.L. Abbenhuis, G. Gerritsen, N. Ni Bhriain, P. Magusin, B. Mezari, W. Han, R.A. van Santen, Q.H. Yang, C. Li, *Chem. Eur. J.*, **2007**, 13, 1210.

98 J.M. Thomas, G. Sankar, *Acc. Chem. Res.*, **2001**, 34, 571.

99 A. Kumar, D.a Srinivas, P. Ratnasamy, *Chem. Commun.*, **2009**, 6484.

100 J. El Haskouri, S. Cabrera, M. Gutierrez, A. Beltrán-Porter, D. Beltrán-Porter, M.D. Marcos, P. Amorós, *Chem. Commun.*, **2001**, 309.

101 P. Wu, T. Tatsumi, *Chem. Mater.*, **2002,** 14, 1657.

102 I.W.C.E. Arends, R.A. Sheldon, *Appl. Catal. A: Gen.*, **2001**, 212, 175.

103 T. Maschmeyer, F. Rey, G. Sankar, J.M. Thomas, *Nature*, **1995**, 378, 159.

104 L. Marchese, E. Gianotti, V. Dellarocca, T. Maschmeyer, F. Rey, S. Coluccia, J.M. Thomas, *Phys. Chem. Chem. Phys.*, **1999**, 1, 585.

105 M. Guidotti, E. Gavrilova, A. Galarneau, B. Coq, R. Psaro, N. Ravasio, *Green Chem.*, **2011**, 13, 1806.

106 U. Schubert, *J. Mater. Chem.*, **2005**, 15, 3701.

107 F. Bérubé, B. Nohair, F. Kleitz, Serge. Kaliaguine, *Chem. Mater.*, **2010**, 22, 1988.

108 M.P. Coles, C.G. Lugmair, K.W. Terry, T.D. Tilley, *Chem. Mater.*, **2000**, 12, 122.

109 R.L. Brutchey, B.V. Morka, D.J. Sirbuly, P.D. Yang, T.D. Tilley, *J. Mol. Catal. A: Chem.*, **2005**, 238, 1.

110 A. Tuel, L.G. Hubert-Pfalzgraf, *J. Catal.*, **2003**, 217, 343.

111 H.L. Xie, Y.X. Fan, C.H. Zhou, Z.X. Du, E.Z. Min, Z.H. Ge, X.N. Li, *Chem. Biochem. Eng. Q.*, **2008**, 22, 25.

112 M. Guidotti, L. Conti, A. Fusi, N. Ravasio, R. Psaro, *J. Mol. Catal. A: Chem.*, **2002**, 182–183, 151.

113 S. Xiang, Y.L. Zhang, Q. Xin, C. Li, *Angew. Chem. Int. Ed.*, **2002**, 41, 821.

114 M. Popova, Á. Szegedi, K. Lázár, A. Dimitrova, *Catal. Lett.*, **2011**, 141, 1288.

115 R.A. Sheldon, M. Wallau, I.W.C.E. Arends, U. Schuchardt, *Acc. Chem. Res.*, **1998**, 31, 485.

116 O.A. Kholdeeva, N.N. Trukhan, *Russ. Chem. Rev.*, **2006**, 75, 411.

117 J.M. Brégeault, *Dalton Trans.*, **2003**, 3289.

118 D.R.C. Huybrechts, P.L. Buskens, P.A. Jacobs, *J. Mol. Catal.*, **1992**, 71, 129.

119 G. Deo, A.M. Turek, I.E. Wachs, D.R.C. Huybrechts, P.A. Jacobs, *Zeolites*, **1993**, 13, 365.

120 W. Zhang, M. Fröba, J. Wang, P.T. Tanev, J. Wong, T.J. Pinnavaia, *J. Am. Chem. Soc.*, **1996**, 118, 9164.

121 M.S. Morey, S. O'Brien, S. Schwarz, G.D. Stucky, *Chem. Mater.*, **2000,** 12, 898.

122 M. Colilla, I. Izquierdo-Barba, S. Sánchez-Salcedo, J.L.G. Fierro, J.L. Hueso, M. Vallet-Regí, *Chem. Mater.*, **2010**, 22, 6459.

123 M.C. Capel-Sanchez, J.M. Campos-Martin, J.L.G. Fierro, *Catal. Today*, **2010**, 158, 103.

124 G. Ricchiardi, A. Damin, S. Bordiga, C. Lamberti, G. Spanò, F. Rivetti, A. Zecchina, *J. Am. Chem. Soc*., **2001**, 123, 11409.

125 A. Shimojima, N. Umeda, K. Kuroda, *Chem. Mater.*, **2001,** 13, 3610,

126 S. Huh, J.W. Wiench, J.C. Yoo, M. Pruski, V.S.Y. Lin, *Chem. Mater.*, **2003,** 15, 4247.

127 S. Inagaki, S.Y. Guan, Y. Fukushima, T. Ohsuna, O. Terasaki, *J. Am. Chem. Soc.*, **1999**, 121, 9611.

128 R. Anwander, I. Nagl, M. Widenmeyer, G. Engelhardt, O. Groeger, C. Palm, T. Röser, *J. Phys. Chem. B*, **2000**, 104, 3532.

129 C. Zapilko, M. Widenmeyer, I. Nagl, F. Estler, R. Anwander, G. Raudaschl-Sieber, O. Groeger, G. Engelhardt, *J. Am. Chem. Soc.*, **2006**, 128, 16266.

130 E. Crabb, E. Moore, L. Smart, *Concepts in Transition Metal Chemistry*, RSC Publishing, **2010.**

131 A.B.P. Lever, *Studies in Physical and Theoretical Chemistry*, Elsevier: Amsterdam, **1984**, 33.

132 J. Klaas, G. Schulz-Ekloff, N.I. Jaeger, *J. Phys. Chem. B*, **1997**, 101, 1305.

133 D.T. On, L.L. Noc, L. Bonneviot, *Chem. Commun.*, **1996**, 299.

134 F.T. Fan, Z.C. Feng, C. Li, *Acc. Chem. Res.*, **2010**, 43, 378.

135 C. Li, G. Xiong, J.K. Liu, P.L. Ying, Q. Xin, Z.C. Feng, *J. Phys. Chem. B*, **2001**, 105, 2993.

136 H.C. Xin, J. Zhao, S.T. Xu, J.P. Li, W.P. Zhang, X.W. Guo, E.J.M. Hensen, Q.H. Yang, C. Li, *J. Phys. Chem. C*, **2010**, 114, 6553.

137 P.E. Sinclair, G. Sankar, C.R.A. Catlow, J.Me. Thomas, T. Maschmeyer, *J. Phys. Chem. B*, **1997**, 101, 4232.

138 S. Bordiga, F. Bonino, A. Damin, C. Lamberti, *Phys. Chem. Chem. Phys.*, **2007**, 9, 4854.

139 J. To, A.A. Sokol, S.A. French, C.R.A. Catlow, *J. Phys. Chem. C*, **2008**, 112, 7173.

140 R.D. Oldroyd, G. Sankar, J.M. Thomas, D. Özkaya, *J. Phys. Chem. B*, **1998**, 102, 1849.

141 Z.H. Luan, L. Kevan, *Microp. Mesop. Mater.*, **2001**, 44-45, 337.

142 R. Peng, D. Zhao, N.M. Dimitrijevic, T. Rajh, R.T. Koodali, *J. Phys. Chem. C*, **2012**, 116, 1605.

143 L. Bonoldi, L. Abis, L. Fiocca, R. Fusco, L. Longo, F. Simone, S. Spera, *J. Mol. Catal. A: Chem.*, **2004**, 219, 47.

144 A. Grassi, S. Saccheo, A. Zambelli, F. Laschi, *Macromolecules*, **1998**, 31, 5588.

145 C. Petit, A. Favre-Reguillon, B. Albela, L. Bonneviot, G. Mignani, M. Lemaire, *Organometallics*, **2009**, 28, 6379.

146 Y. Gao, T.A. Konovalova, T. Xu, L.D. Kispert, *J. Phys. Chem. B*, **2002**, 106, 10808.

147 K. Chaudhari, R. Bal, D. Srinivas, A.J. Chandwadkar, S. Sivasanker, *Microp. Mesop. Mater.*, **2001**, 50, 209.

148 D.E. De Vos, M. Dams, B.F. Sels, P.A. Jacobs, *Chem. Rev.*, **2002,** 102, 3615.

149 H.U. Blaser, B. Pugin, *Chiral Reactions in Heterogeneous Catalysis (Eds.: G. Jannes, V. Dubois)*, Plenum, New York, **1995**, 33.

150 S.Y. Chen, C.Y. Tang, J.F. Lee, L.Y. Jang, T. Tatsumid, S. Cheng, *J. Mater. Chem.*, **2011**, 21, 2255.

151 A. Quintanilla, J.J.W. Bakker, M.T. Kreutzer, J.A. Moulijn, F. Kapteijn, *J. Catal.*, **2008**, 257, 55.

152 A.Y. Fadeev, R. Helmy, S. Marcinko, *Langmuir*, **2002**, 18, 7521.

153 A.R. Almeida, J.T. Carneiro, J.A. Moulijn, G. Mul, *J. Catal.*, **2010**, 273, 116.

154 S.P. Wang, Y. Shi, X.B. Ma, J.L. Gong, *Appl. Mater. Interfaces*, **2011**, 3, 2154.

155 A. Corma, M. Domine, J.A. Gaona, J.L. Jordá, M.T. Navarro, F. Rey, J. Pérez-Pariente, J. Tsuji, B. McCulloch, L.T. Nemeth, *Chem. Commun.*, **1998**, 2211.

156 A. Thangaraj, S. Sivasanker, P. Ratnasamy, *J. Catal.*, **1991**, 131, 394.

157 F. Song, Y.M. Liu, H.H. Wu, M.Y. He, P. Wu, T. Tatsumi, *J. Catal.*, **2006**, 237, 359.

Chapter III

Experimental and Characterization

3.1 Experimental

3.1.1 Chemicals and gases

Table 1 Reagents used in the experiments.

Product	Purity	Provider	cas
Ludox HS-40	40%	Sigma-Aldrich	
Sodium hydroxide	>99%	ACROS	
Cetyltrimethylammonium tosylate (CTATos)	>99%	Merck	
Tetramethylammonium bromid (TMABr)	>99%	Merck	
Hydrochloric acid in water (HCl)	1 N	ACROS	7647-01-1
2,2,5,5-tetramethyl-2,5-disila-1-azacyclopentane (TMDSACP)	9%	ABCR	7418-19-1
Hexamethyldisilazane (HMDSA)	97%	ABCR	999-97-3
Titanium isopropoxide (Ti(O-*i*Pr)$_4$)	distilled	JANSSEN	546-68-9
N-(2-Hydroxyethyl) ethylenediamine (ODA)	99%	Alfa	111-41-1
Diethanolamine (DOA)	99%	ACROS	111-42-2
1-(2-Hydroxyethyl) piperazine (OPE)	>98%	Alfa	103-76-4
Chloromethyl methyl ether	Tech.	Aldrich	107-30-2
Zinc chloride p. a.	98%	ACROS	7646-85-7

Table 2 Gas used in the experiment or characterization.

Gas	Quality	Provider	Utilization	Treatment
Argon	α	Air Liquid	Protection gas for synthesis	Cartridge filtration multifonctions: dehydration, deoxygenation, dehydrocarbon
Nitrogen	U	Air Liquid	Working gas for TGA	No
Air	Industrial	Air Liquid	Working gas for TGA and calcination	No

3.1.2 Preparation of products

3.1.2.1 LUS-CTA & LUS-TMA

MCM-41 type mesoporous silica, LUS-as was prepared using Ludox HS-40 as Si source and hexadecyltrimethylammonium (cetyltrimethylammonium) *p*-toluene sulfonate as surfactant, in the presence of sodium hydroxide solution (Figure 1).

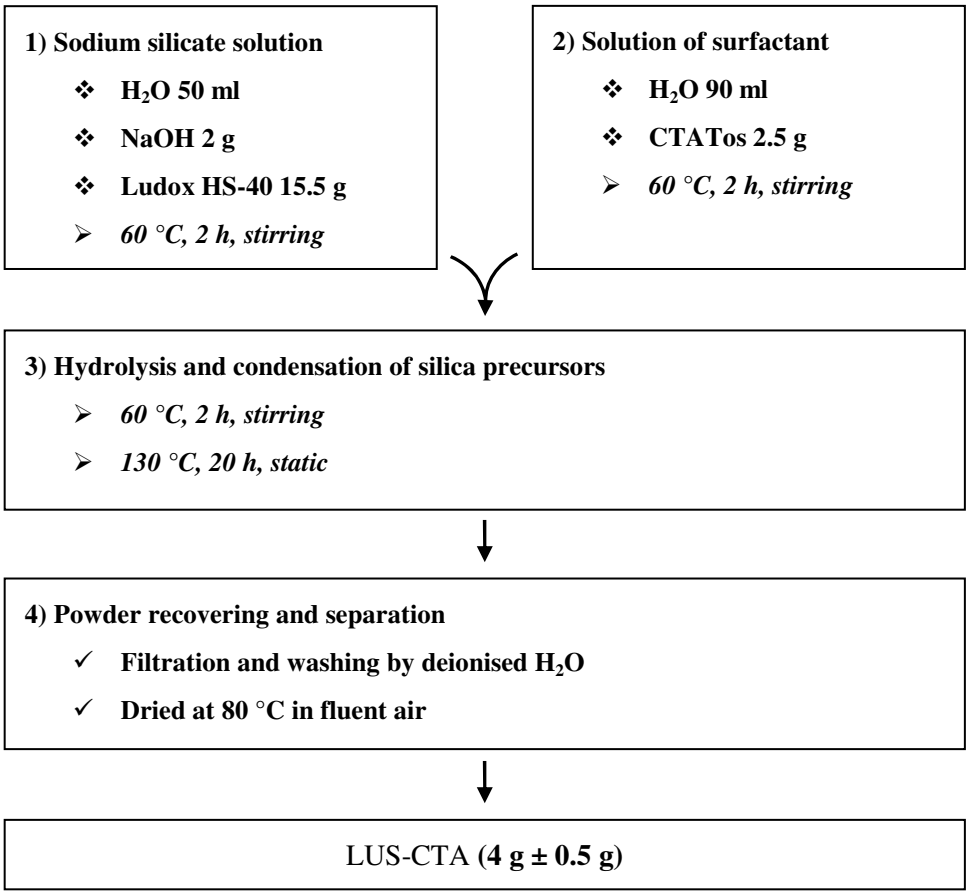

Figure 1 Synthesis of LUS-CTA

Typically, the silica sol was formed by stirring the mixture of Ludox 15.5 g (SiO_2 0.103 mol), NaOH 2 g and H_2O 50 ml at 60 °C for 2 h. Then it was dropwise added into the homogeneous surfactant solution with dissolved CTATos 2.5 g (5.5×10^{-3} mol) in 90 ml deionised H_2O by moderately stirring at 60 °C. The precursor soon producing a cloudy

dispersion was kept stirring at 60 °C during 2 h and subsequently statistic at 130 °C for 20 h. The obtained product was filtered, washed with deionised H_2O and dried at 80 °C overnight, here noted as LUS-CTA (or LUS-as).

The CTA^+ in the as-synthesized solid LUS-CTA was cation-exchanged by TMA^+ obtaining LUS-TMA (Figure 2). 1 g powder was stirred in the 40 ml technical ethanol (96%) solution containing 0.45 g tetramethylammonium bromide (TMABr, 99%, Aldrich) at 60 °C for 30 min, followed the filtration and washing with ethanol and acetone. In this order, the process of ion-exchanging was repeated 2 more times finally getting the white powder LUS-TMA.

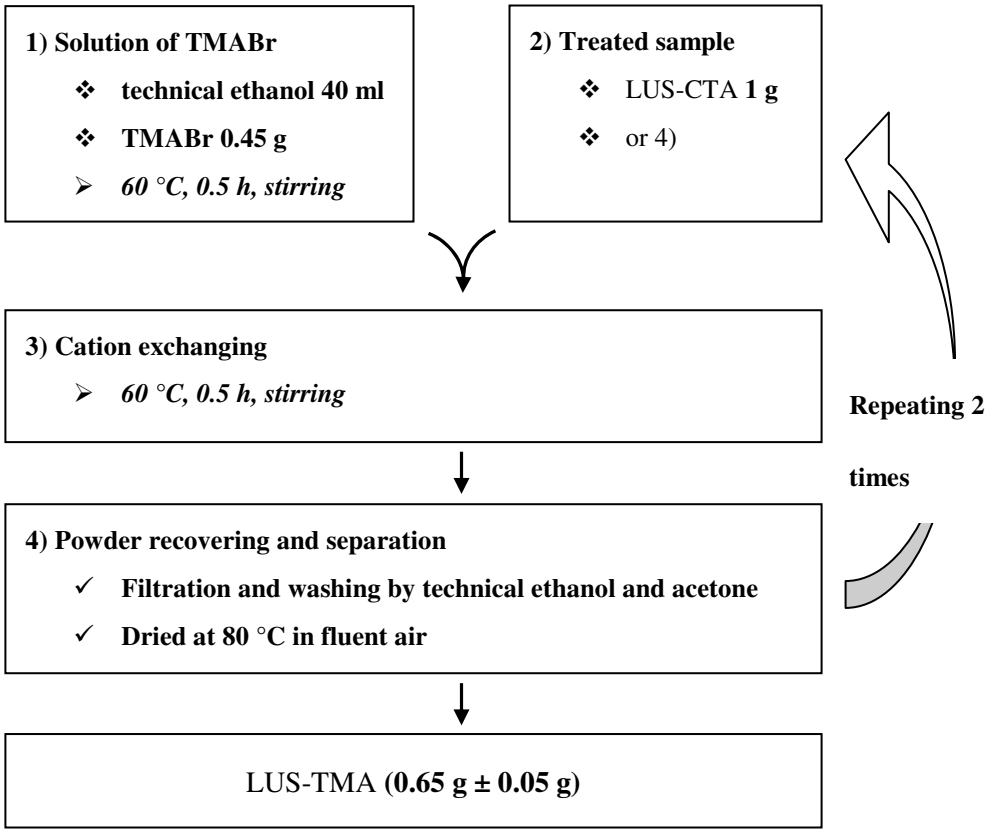

Figure 2 Synthesis of LUS-TMA.

3.1.2.2 LUS-Cx & LUS-Tx

In order to obtain the partial disilyl functionalized silica surface, LUS-CTA or LUS-TMA was partially extracted the cation (CTA^+ or TMA^+) by hydrochloride acid in the technical ethanol solution (Figure 3).

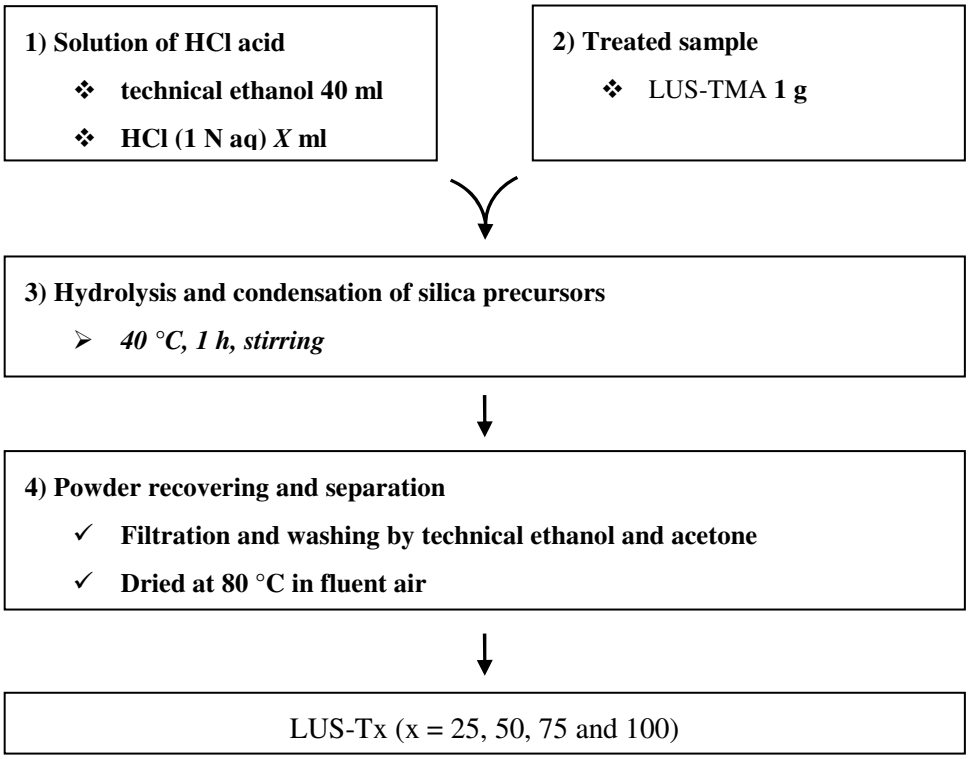

Figure 3 Synthesis of LUS-Tx.

Taking LUS-TMA as an example, 1 g such solid was impregnated in the 40 ml technical ethanol containing *X* ml HCl (1 $mol \cdot L^{-1}$ aq., ACROS). A partial TMA^+ (tetramethylammonium cation, $N^+(CH_3)_4$) would be extracted by stirred at 40 °C for 1 h. The solid was denoted as LUS-Tx after filtered, washed by technical ethanol and acetone, and dried overnight in the air. «x» of LUS-Tx stands for the percentage of extracted TMA^+ out of the total TMA^+ amount in the sample LUS-TMA. Herein, «x» was defined as 25, 50, 75 and 100, meaning that 25%, 50%, 75% and 100% TMA^+ would be

extracted, respectively. The yield by weight percent is 95%, 91%, 88% and 85%, respectively.

The added volume of 1 mol·L^{-1} HCl acid will be determined by the equation as followed:

$$X_{HCl}(mL) = \left(\frac{M\ g \times m\%}{74\ g \cdot mol^{-1}} \times x \times 1.1\ eq \right) \div 1\ mol \cdot L^{-1} \times 1000\ mL \qquad \textbf{Eq (1)}$$

M is the weight of LUS-TMA, which has a mass change *m%* during 150-280 °C in the TG/DTG curves assigned to the dissociation of TMA^+ from framewore silicate SiO^-. From this mass change, a total molar amount of TMA^+ acting as the template in LUS-TMA can be calculated by deviding molecule weight of TMA^+ 74 g·mol^{-1}. If the *x* (25%, 50%, 75% and 100%) TMA^+ is going to be extracted, the equal molar quantity of 1 N HCl acid will be used (1 H^+ for 1 TMA^+). Moreover, the acid amount is usually increased to 1.1 *eq* more considering the extra TMABr adsorbing in the solid.

Concerning to the LUS-CTA sample, the equation (1) will change into:

$$X_{HCl}(mL) = \left(\frac{M\ g \times m'\%}{284\ g \cdot mol^{-1}} \times x \times 1.1\ eq \right) \div 1\ mol \cdot L^{-1} \times 1000\ mL \qquad \textbf{Eq (2)}$$

Here, *m'%* is the mass change of templating CTA^+ appearing in the 150-300 °C region of the TG/DTG curve and 284 g·mol^{-1} is the molecule weight of CTA^+. The long-chain alkyl surfactant cation CTA^+ (cetyltrimethylammonium) is expected to disfavour the CTA^+ displacement, the temperature of acid extraction was increased to 60 °C (Figure 4). To remove 75% and 100% of template, the acid extraction is carried on 2 times to make sure that the equilibrium of protonation will be attained. The yield of LUS-Cx (x = 25, 50, 75 and 100) by weight percent is 86%, 80%, 72% and 58%, respectively. LUS-T100 or LUS-C100 is also named LUS.

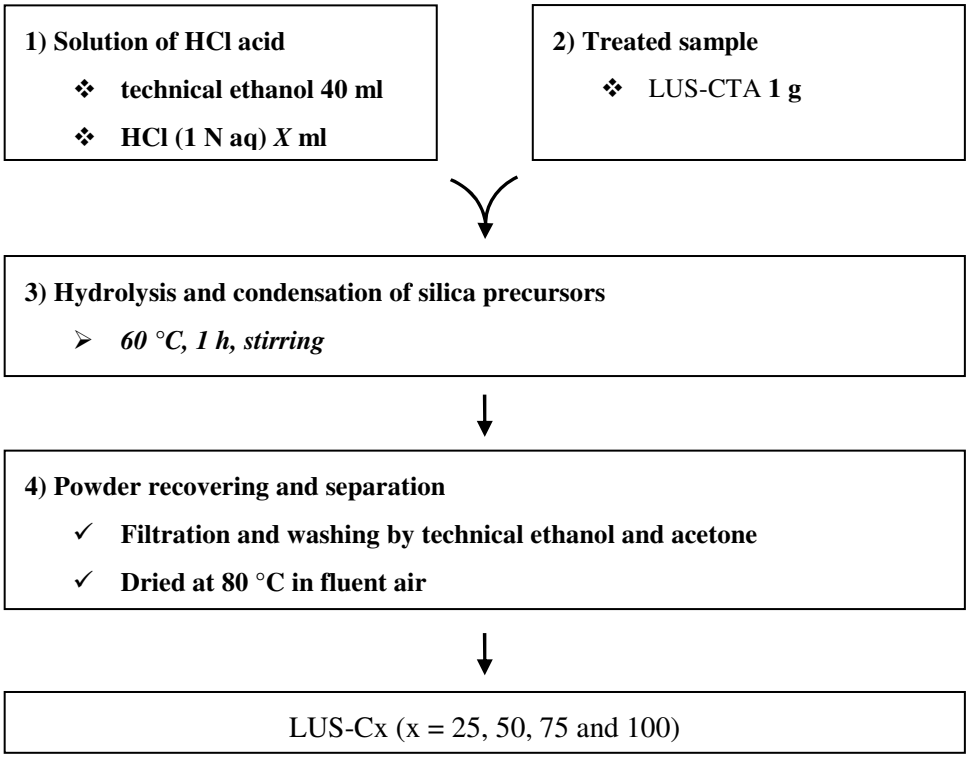

Figure 4 Synthesis of LUS-Cx.

3.1.2.3 LUS-Cx-E & LUS-Tx-E

For the subsequently effective silylation, the samples LUS-Tx or LUS-Cx was further dehydrated at 130 °C under vacuum for 2 h to activate the silanol groups. Taking LUS-Tx as an example, after dehydration, the system was cooled down to room temperature (rt) under Ar gas protection. Dry cyclohexane 40 ml and TMDSACP (2,2,5,5-tetramethyl-2,5-disila-1-azacyclopentane) *Z* mL was added in using a syringe injection. The mixture was stirred 0.5 h at room temperature for the homogeneous liquid-solid diffusion and then refluxed at 80 °C for 16 h to get LUS-Tx-E (EBDMS, ethyl 1, 2-bis(dimethylsilyl)) after filtration, washing with technique ethanol, acetone and drying. For the parent material LUS-Cx, the product is donated as LUS-Cx-E. When the mixture was stirred at room temperature for 16 h, the obtained samples were denoted as LUS-Tx-E_rt and LUS-Cx-E_rt, respectively (Figure 5).

Regarding to the stencil patterning effect from the cation, the dipodal silazane TMDSACP (*Z* ml) adding is given 5 *eq*. exccess to the amount of total silanol groups on the surface of LUS material that has been reported 0.23 molar ratio. As shown in eq. (3):

$$Z_{TMDSACP}\ (mL) = \left(\frac{M\ g \times M'\%}{60\ g \cdot mol^{-1}} \times 0.23 \times 5\ eq \right) \times 159.38\ g \cdot mol^{-1} \div 0.842\ g \cdot mL^{-1} \quad \textbf{Eq (3)}$$

M g is the weight of the treated sample and M'% is the relative residual that refers to the SiO_2 at 1000 °C. 159.38 g·mol-1 and 0.842 g·mL-1 is the formula weight and density of the silazane reagent, respectively.

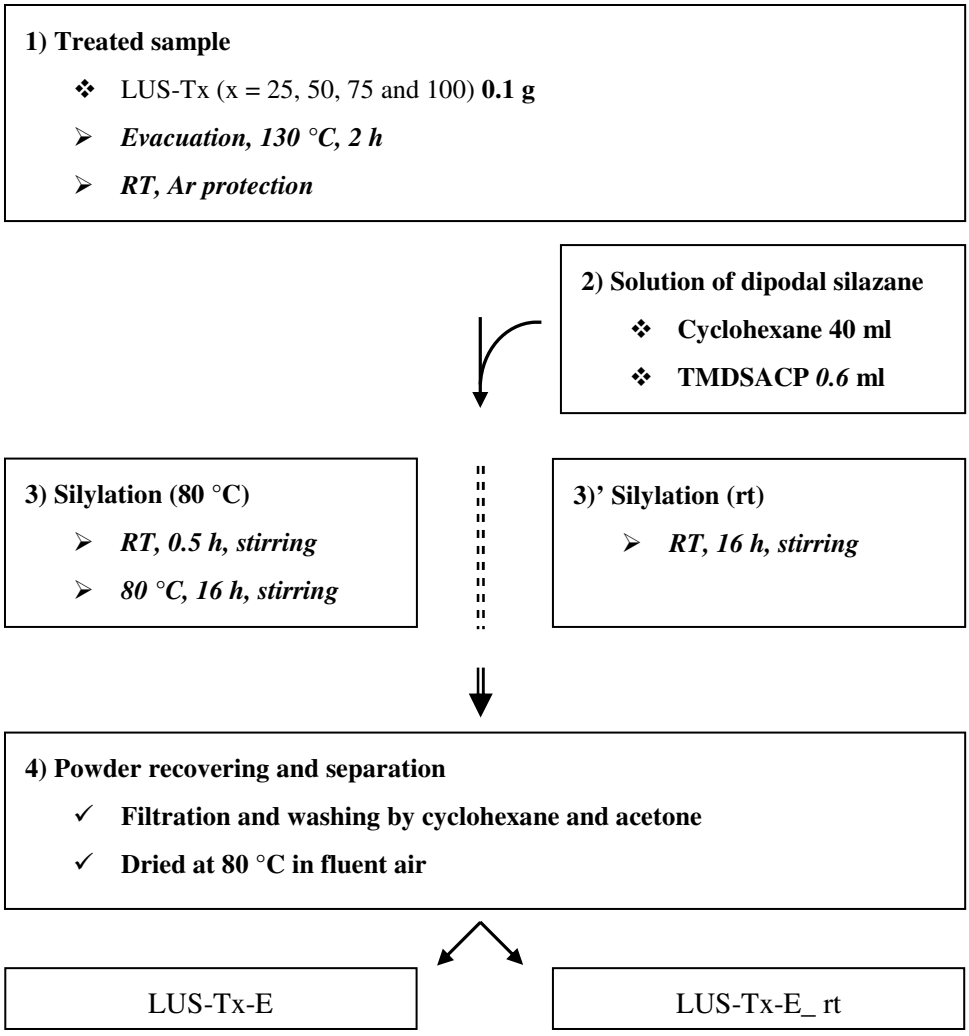

Figure 5 Synthesis of LUS-Tx-E and LUS-Tx-E_rt.

3.1.2.4 LUS-Cx-E-OH & LUS-Tx-E-OH

Subsequently, the materials LUS-Tx-E and LUS-Cx-E (x = 25, 50 and 75) were extracted by 1 N HCl *X'* ml again in the technical ethanol solution to remove the rest template acting as surface protecting group (Figure 3). *X'* ml is determined by the TMA^+ loss in the TG/DTG curve as described in the eq. (1). The obtained product after filtration, washing by technical ethanol and acetone, and drying at 80 °C in fluent air, leads to a hybrid material with both EBDSM function and silanol groups, therefore, denoted as LUS-Tx-E-OH or LUS-Cx-E-OH. The LUS-T100 and LUS-C100grafted by EBDMS group is considered as the full covered, named LUS-T100-E and LUS-T100-E, respectively.

3.1.2.5 LUS-E-Ti-n, LUS-Ti-n & LUS-Ti-E

The sample LUS-T50-E-OH was dehydrated and post-grafted by different adding amount (*Y* ml) of Ti(O-*i*Pr)$_4$ along the same sequence and the same condition as that for LUS-Tx-E. Finally, the product was filtered, washed by cyclohexane and acetone, and dried at 80 °C in the fluent air, denoted LUS-E-Ti-n (Figure 6, Scheme 1). The final mass of the product increases from 1.0 ± 0.05 g to 1.2 ± 0.05 g consistently with the amount of Ti precursor increasing from Si/Ti = 200 to Si/Ti = 20.

The amount (*Y* ml) of Ti precursor Ti(O-*i*Pr)$_4$ compound was calclulated by Ti/Si (t) based on the inorganic Si composition of LUS-T50-E.

$$Y_{Ti} = \frac{N\ g \times n\%}{60\ g \cdot mol^{-1}} \times t \times 159\ g \cdot mol^{-1} \div 0.955\ g \cdot ml \qquad \textbf{Eq. (4)}$$

N g is the weight of LUS-T50-E-OH sample and *n%* is its residual weight at 1000 °C in the TG/DTG curve corresponding to SiO_2.

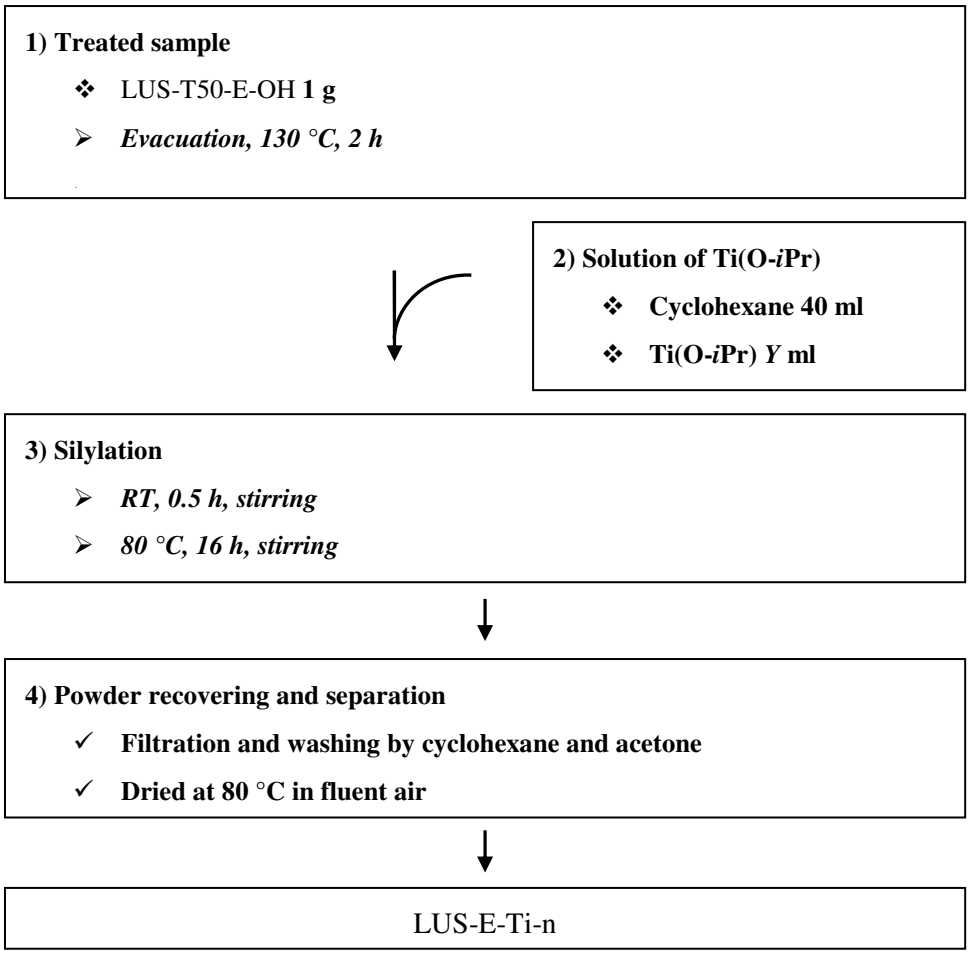

Figure 6 Synthesis of LUS-E-Ti-n.

$Ti(O\text{-}iPr)_4$ was also grafted on a non-modified LUS which had been removed the surfactant CTA^+ or TMA^+, to serve as a comparison for the characterization of the favour materials. All the snythesis were performed in the same condition as that for LUS-T50-E-Ti. LUS-T100 1 g was firstly dehydrated at 130 °C under vacuum for 2 h so that the silica surface full of silanol groups could be effective to the coordination with Ti species. The samples finally gotten were denoted as LUS-Ti-n (Scheme 1). The final mass of the product increases from 1.0 ± 0.05 g to 1.4 ± 0.05 g consistently with the amount of Ti precursor increasing from Ti/Si = 200 to Ti/Si = 20.

LUS-Ti-E was prepared using LUS-T50-E-OH and Si/Ti = 20 in solution, according to the inverted grafting orders of EBDMS and $Ti(i\text{-}OPr)_4$ as that of LUS-E-Ti (Scheme 1).

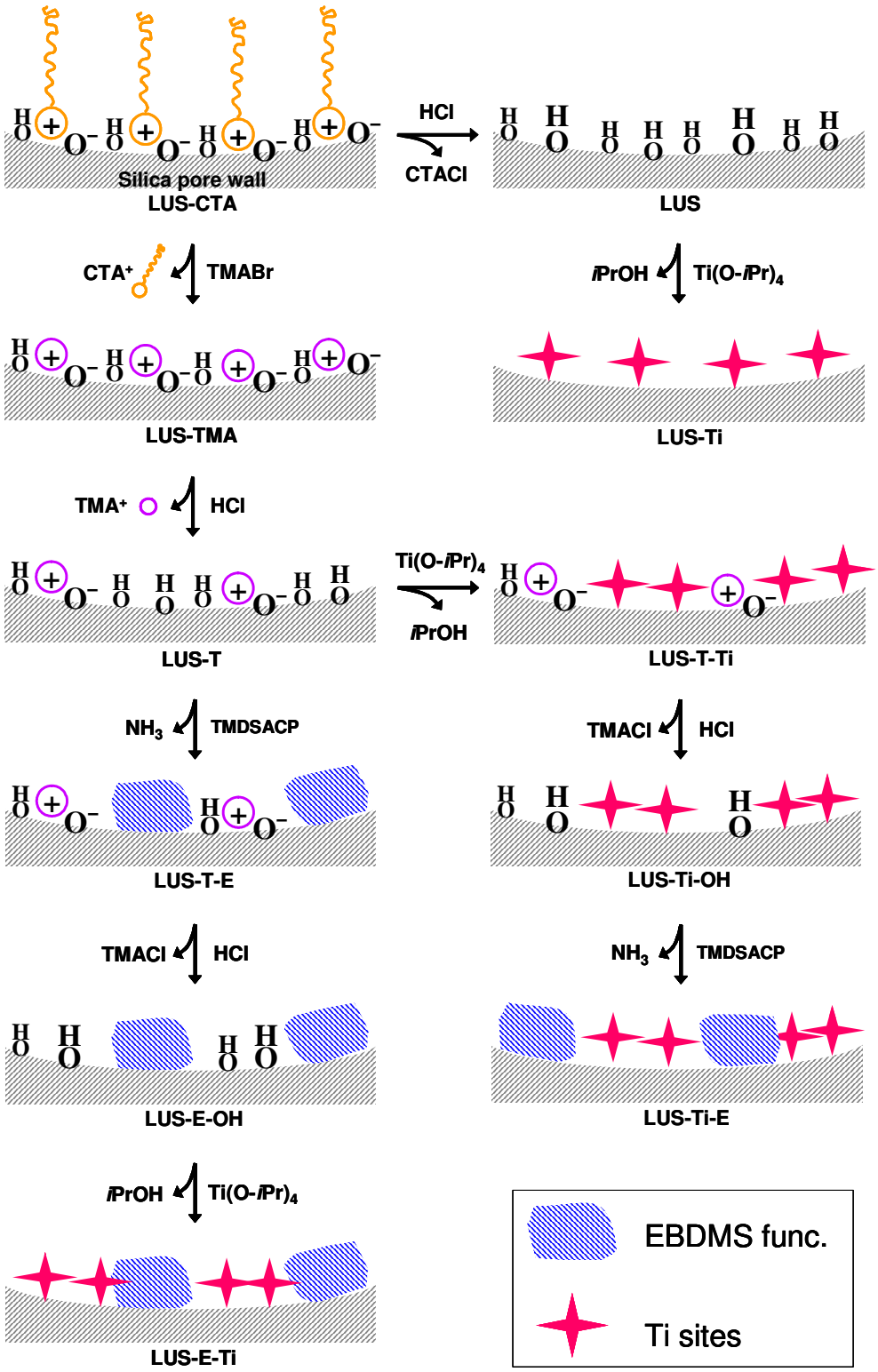

Scheme 1 Schematic presentation for synthesis of LUS-E-Ti, LUS-Ti-E and LUS-Ti.

3.1.2.6 LUS-xTMS

The partially TMS modified materials are prepared according to the same protocle as LUS-Tx-E-OH, denoted as LUS-xTMS (x = 25, 50, 75 and 100) (Figure 5). Silane precursor HMDSA is added by volume of 4:1 to the weight of sample (g), which is at least 10 *eq* exccess to the amount of active silanol groups on the surface of the LUS samples.

3.1.2.7 LUS-xE-cal & LUS-xTMS-cal

The thermal treatment was carried on in a tube furnace where the air goes through the tube during the calcination and the final gas was absorbed by H_2O (Figure 1). When the calcination temperature was < 500 °C, a glass tube was used and if temperature > 500 °C, a tube in quartz was required (Figure 7A).

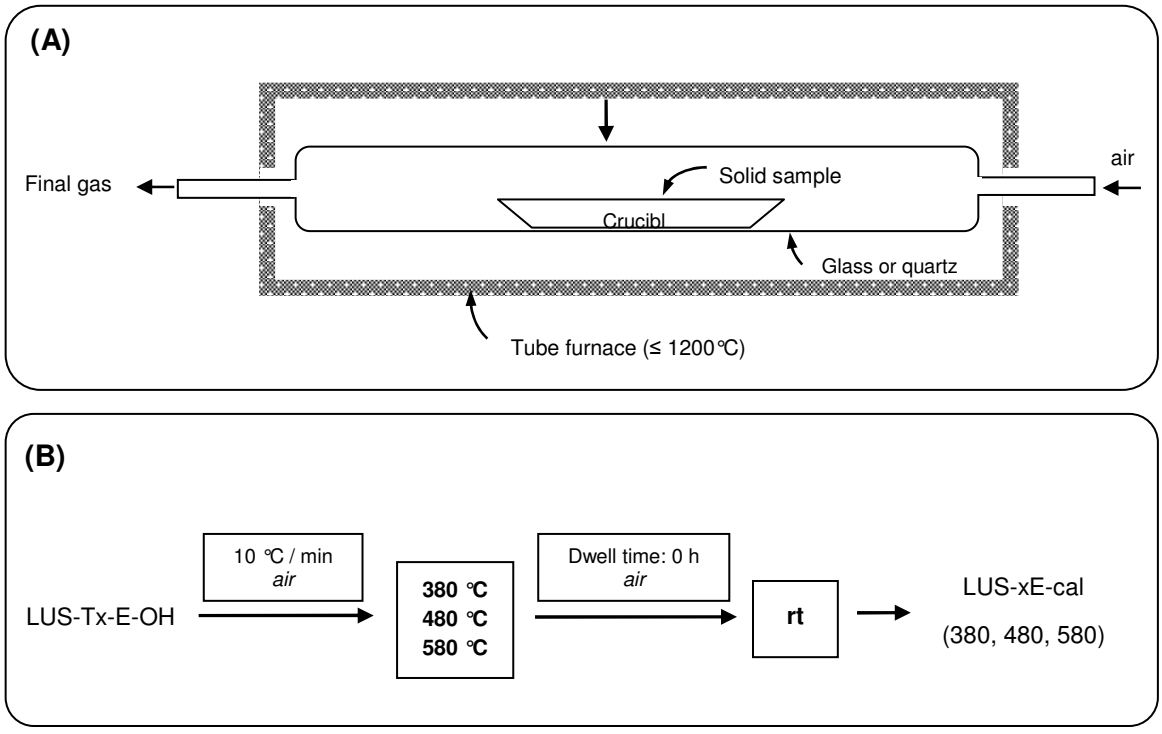

Figure 7 (A) Tube furnace for calcination of silica materials LUS-T100-E and (B) calcination protocol.

The treatment conditions were determined from the TG analysis. Heating temperature starts from room temperature ~25 °C, rising by 10 °C/min until the target temperature, then ends without dwelling segment. The EBDMS modified materials LUS-Tx-E-OH (x = 50 and 100) were calcined at 380 °C, 480°C, 580 °C (Figure 7B), noted as LUS-xE-cal (x = 50 and 100; cal: 380, 480 and 580), respectively. While for TMS modified ones, LUS-xTMS were treated at 400 °C, 500°C and 600 °C to get LUS-xTMS-cal (x = 0, 25, 50, 75 and 100; cal: 400, 500 and 600). LUS was calcined at 550 °C for 10 h to be a reference, named *LUS-550*.

3.1.2.8 LUS-xE-cal-E & LUS-xTMS-cal-TMS

The subsequently re-capping on the calcined materials was carried out according to the same protocol as that for samples LUS-Tx-E or LUS-Cx-E (Figure 3). TMS and EBDMS functions were grafted into the materials, respectively. The volume of HMDSA was added by 4:1 (mL) ratio related to the weight of the calcined samples and TMDSACP was added in a 6:1 ratio. Both of the precursors were 10 eq excess to the accessible silanol groups that the materials possess. The final products were noted as LUS-xE-cal-E and LUS-xTMS-cal-TMS, respectively.

3.1.2.9 LUS-xE-cal-Ti & LUS-xTMS-cal-Ti

$Ti(O\text{-}iPr)_4$ could be grafted into the calcined materials with adding Ti/Si varied from 20-200. Herein, the $Ti(O\text{-}iPr)_4$ was grafted in a ratio of Ti/Si=200 according to the same experimental protocol as described in 2.3 (Figure 6).

3.2 Characterization

Low angle X-ray powder diffraction (XRD) experiments were carried out using a Bruker (Siemens) D5005 diffratometer using CuKα monochromatic radiation.

Thermogravimetric analyses were performed using a DTA-TG Netzsch STA 409 PC/PG instrument. Samples (7-10 mg) placed in 70 μL alumina crucible were heated in air flow (40 ml/min) up to 1000 °C at a heating rate of 10 °C/min with N_2 as supporting gas (15 ml/min).

Nitrogen adsorption-desorption isotherms at 77 K were determined at BELSORP-max (BEL Japan, INC.). In all cases, 30-50 mg samples were degassed at 80 °C for 12 h and then at 130 °C for 2 h under a vacuum lower than 0.01 kPa before the analysis. The specific surface area was calculated according to the BET method in the 0.05-0.25 range of relative pressure. The mesopore diameter evaluated by the pressure of the mesopore-filling step of the isotherm (D_{BdB} (Å)= 14.60994 + 74.67812 * x – 81.96198 * x^2 + 155.8457 * x^3, X = P/P_0 ($0.11 \leq P/P_0 \leq 0.50$)).[1,2]

Fourier transform infrared spectra (FT-IR) were recorded using a JASCO FT/IR-4200 (JASCO) spectrometer with ATR PRO470-H accessory, on which about 1 mg sample was measured by reflectance (%R). IR peak intensities were height normalized for the sake of quantitative monitoring using the peak at 460 cm^{-1} as internal reference (bending mode of the [SiO_4] tetrahedral units).[3]

To confirm the amount of silanol groups in the synthesized materials ^{29}Si NMR analyses was operated in a Bruker AVANCE III 500 spectrometer at 99.362 MHz. Solid samples were tested in a 4 mm zirconia rotor and recorded by magic angle spinning (MAS) at 5 kHz. Chemical shifts (δ) of ^{29}Si were externally referred to trimethyl silane (TMS) at δ=0.0 ppm. Solid-state ^{13}C CPMAS NMR measurements were collected also on a Bruker AVANCE III 500 spectrometer. For both cross polarization (CP) was performed

at 100.6 MHz with 6 ms (h = p/2) pulses and a repetition time of 3 s. The spinning rate of the rotor was about 5 kHz and the number of scans was 10000.

Solid UV-visible spectra were recorded using a JASCO V-670 (JASCO) spectrophotometer in the diffuse reflectance mode. The selected recording parameters comprised a spectral bandwidth of 5.0 nm, a scan speed of 400 nm·min^{-1}, and a data interval of 1 nm. The powders were filled in a hole (20 mm in diameter and 2 mm deep) of a sample holder, and the surface was smoothed and the layer can be regarded as infinitely thick. The standard spectroteflon from JASCO with 82% reflectivity was used as a reference (Figure 8).

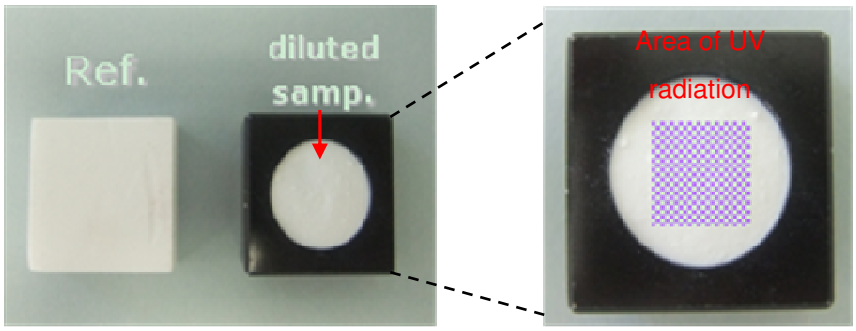

Figure 8 Sample holder of JASCO V-670 spectrophotometer in the diffuse reflectance mode.

The samples were stored under normal conditions, and spectra were recorded directly in air with no further pre-treatment. When showing an absorbance of F(R) > 1.0 samples were diluted with LUS-cal which was calcined at 550 ºC for 10 h after the removal of surfactant. Since the Kubelka-Munk theory predicts that F(R) is proportional to the concentration *c* of the absorbing species as long as the assumptions of the theory are fulfilled, namely, that the absorbance of the sample is not too high (Figure 9). $F(R)_{max}$ = 1.0 is limited to be sure that the absorbance is linear, if not, a higher absorption causes a change that is observed as a blue shift in the F(R) spectrum.[4] The minor absorbance of

diluent is 0.15. All spectra presented in this work are corrected for the absorbance of the support and diluent.

The absorption per Ti can be calculated regarding to the F(R) and the Ti molar amount in one unit, as eq. (5):

$$Total\ Abs/Ti\,(mmol\cdot cm^{-2}) = \frac{F(R)}{\frac{26mg\cdot cm^{-2} * dilution\% * Ti\,wt\%}{48g\cdot mol^{-1}}} \qquad \textbf{Eq. (5)}$$

Here, the 26 mg·cm^{-2} was obtained by a test that increasing the thickness of pure silica under the UV radiation until the absorption was completely full by the powder. Dilution% is the weight ratio between the diluant and Ti-contained sample and Ti wt% was given by elemental analysis.

Unpolarized Raman spectra were excited with 514.5 nm and 244 nm of an argon-ion laser and recorded by the Horiba Jobin-Yvon Labram HR800 visible spectrometer in backscattering geometry at room temperature. This Raman system consists of a microscope with 100* objective lens, which allows a spot size of ~1μm.

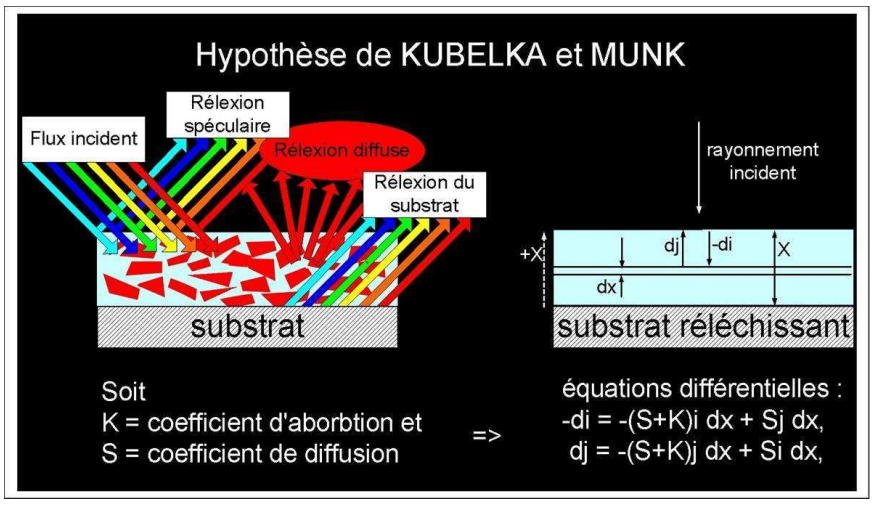

Figure 9 Hypothesise of Kubelka-Munk theory.

3.3 Catalytic Reaction.

A typical heterogeneous catalytic epoxidation experiment was conducted at 60 °C for 2 h by using 50 mg catalyst stirred in a mixture of 10 mmol cyclohexene (>98%), 10 mmol *tert*-butyl hydroperoxide (TBHP, 30%) and 10 ml acetonitrile as solvent. After the catalyst powder was removed from the reaction system by centrifugal separation, the products were analyzed on a gas chromatograph Shimadzu GC-2014 with a FID detector. All the chemicals for catalytic characerization were commercial from China National Medicines Corporation Ltd.

The conversion of products was calculated according to the GC peak area (S) percentage of each products and the reactant:

$$Conv.\%_{product} = \frac{\sum_{n=4} S(product_n)}{S(reactant) + \sum_{n=4} S(product_n)} \times 100\% \qquad \textbf{Eq. (6)}$$

Concomitantly, the turnover number (TON) of the catalyst is:

$$TON_{product_1}(mol^{-1} - Ti \cdot h^{-1}) = \frac{Conv.\%_{product} \times 10mmol}{(50mg \times Tiwt\% \div 48g \cdot mol) \times 2h} \qquad \textbf{Eq. (7)}$$

The products of epoxidation of cyclohexene mainly include (1) cyclohexene epoxide, (2) 1,2-cyclohexanediol obtained by hydrolysis of (1), (3) 2-cyclohexen-1-ol and (4) 2-cyclohexen-1-one both obtained by side redox reactions. Therefore, the selectivity of the product (1) is:

$$Selec.\%_{product_1} = \frac{S(product_1)}{\sum_{n=4} S(product_n)} \times 100\% \qquad \textbf{Eq. (8)}$$

3.4 Reference

1 A. Galarneau, D. Desplantier, R. Dutartre, F. DiRenzo, *Microp. Mesop. Mater.*, 1999, 27, 297.

2 J. IAPICHELLA, thesis « Structuration hiérarchique des particules et des monolithes siliciques pour la chromatographie », l'Université Montpéllier II, 2006.

3 K. Zhang, B. Albela, M.Y. He, Y.M. Wang, L. Bonneviot, *Phys. Chem. Chem. Phys.*, 2009, 11, 2912.

4 J. Klaas, G. Schulz-Ekloff, N.I. Jaeger, *J. Phys. Chem. B*, 1997, 101, 1305.

Chapter IV

Titanium Dispersion Control using Organic patterning of the silica surface

4.1 Introduction

Titanium substituted zeolites such as TS-1, Ti-beta and Ti-MWW are reported to be efficient oxidation catalysts, in particular for olefin epoxidation [1-3]. The discovery of Ti-incorporated mesoporous molecular materials such as Ti-MCM-41, Ti-HMS, Ti-MCM-48 and Ti-SBA-15 greatly expanded the capability to catalyze reaction involving bulky reactant molecules that were not able to access embedded Ti sites in the framework of microporous zeolites [4-9]. Unfortunately, the activity and selectivity of such materials is lower than that of TS-1 so far. In particular, in the case of olefin epoxidation, adsorption of the epoxide on the hydrophilic silica surface often leads to ring opening and therefore to the formation of diols [10-11].

Modification of Ti-containing mesoporous materials with organic groups can both increase the stability of the material and modify the catalytic activity. These functions can be introduced either by post-grafting using organosilanes functions [12-15] or by direct synthesis where the organic function and the titanium precursors are added in the initial gel [16-18]. In particular, hydrophobic agents such as hexamethyldisilazane (HMDSA) trimethylchlorosilane (TMCS), hexametyldisiloxane (HMDSO), N-methyl-N-(trimethylsilyl) trifluoroacetamide (MSTFA) [19], and N-trimethylsilyl-imidazole (TMSI) [20] are often reported as capping agent replacing silanol by trimethylesilyl groups (TMS). Tatsumi *et al.* grafted the highly reactive HMDSA on the surface of Ti-MCM-41 and Ti-MCM-48, respectively, to achieve the maximum degree of silylation of 2.35 and 2.06 trimethylsilyl groups per nm^2 [14].Such highly hydrophobic samples present an outstanding conversion on the oxidation of cyclododecene even in the presence of a high amount of water.

Direct synthesis presents the advantage of affording a homogeneous distribution of both Ti species and hydrophobic functions in the material. In addition, the pore size is not obstructed affording higher molecular diffusion. However, the coordination environment

of the Ti sites is difficult to control. Indeed, Ti species with 4-, 5-, and 6-fold coordination as well as TiO_2 oligomers may coexist depending on the experimental conditions [18,21]. The post-grafting approach is proposed as a viable alternative although titanium oxide clusters either on the internal channel or on external silica surface are sometimes formed when unstable titanium alkoxydes or titanium chloride are used as precursors [22-23]. To improve the catalytic performance of the material, several attempts have been reported to optimize both the synthesis protocol [24-26] and the titanium precursors [27-29] in order to favour isolated tetrahedral Ti sites, which are the active species.

Many hydrophobic functions such as TMS are linked onto the silica surface by a single covalent Si-O-Si bridge and, are likely liable to leaching often observed during recycling or even during a stepwise synthesis protocole. Instead of the monopodal TMS moieties, we propose in this study the use of a dipodal hydrophobic agent, ethyl-1,2-bis(dimethylsilyl) (-$SiMe_2CH_2CH_2Me_2Si$-, EBDMS) [30-32] that eventually forms two Si-O-Si bridges less prone to a double cleavage and to leach out of the catalyst. To our knowledge, this is the first time that such dipodal hydrophobant agent is used in heterogeneous catalysis. This dipodal function has been reported once in the presence of other grafted function but was added after the first function as a mere hydrophobic agent [33]. Here, the hydrophobic function is introduced prior the incorporation of the Ti species to also act as a dispersant as described according to molecular stencil pattering (MSP) technique [32].

4.2 Masking the surface by TMA^+ or CTA^+

The temperature of silylation is often reported at the refluxing temperature of toluene, *ca.* 110°. Here, the use of cyclohexane which is much less toxic imposes at most, 80 °C which is expected to be high enough to graft the dipodal EBDMS function quantitatively. This were tested first on a silica surface free of any cationic surfactant or organic moieties and then applied on modified surfaces with masking agents such as those used in the MSP technique.

4.2.1 Characterization of template free LUS capped with EBDMS

The LUS-C100 and LUS-T100 are intermediate materials in the MSP sequential treatment, they still contain either the CTA^+ templating agent (as-synthesized LUS) or TMA^+ when the latter is exchanged for the former. After acidic extraction of the ammonium, they are called ammonium free LUS-C100 and LUS-T100, respectively. The presence of organic matter is evaluated first from mass loss measured using TGA as it will be systematically done in the actual thesis. To better underline the temperature at which particular losses may occur, the derivatives (DTG) are also reported (Figure 1).

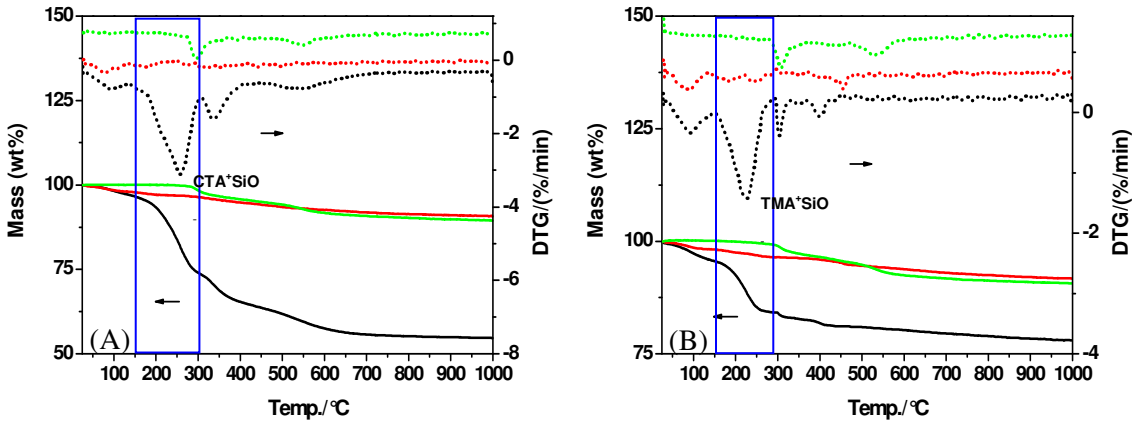

Figure 1 TG/DTG profiles of materials; in A, starting material containing CTA, LUSC0 (black line), 100% surfactant extracted material, LUS-C100 (red line) and, EBDMS grafted materials, LUS-C100-E (green line); In B, as in A except that the series starts with the fully TMA^+ exchanged material, LUS-T0 (black line), followed by the fully extracted TMA material, LUS-T100 (red line), and the EBDMS grafted material, LUS-T100-E. (Note that letter C as CTA stands for the first series and the letter T as TMA stands for the second series.

The as-synthesized LUS-C0 exhibits three weight loss regions dominated by the water release (<150 °C), the surfactant decomposition (150-450 °C) and the silanol condensation (450-1000 °C) (Figure 1A). The weight loss between 150 °C and 300 °C accounting about 23 wt% have been noted as the decomposition of CTA^+ linked to the surface silanol, SiO^-. The latter are typical of the electrical $\{S^+, I^-\}$ electrical interface characteristic of LUS, MCM-41or MCM-48 materials. The following loss between 300-450 °C are attributed also to CTA^+ that are still associated with their anionic counterions (here tosylate, Tos) and remaining trapped in the channel and accounting for as much as 20%. Their weaker interaction with the interface may explain the delay (or higher temperature) observed for their decomposition.

Like LUS-C0, LUS-T0 presents similar weight loss regions. Between 150 and 290 °C TMA^+ decomposition accounts for *ca.* 11 wt% (Figure 1B). The region 290-450 °C is slightly different and characterized by a first narrow peak ca. 310 °C and a second one at ca. 400°C. The first one is assigned to the decomposition of TMA^+ associated to bromide ion (Br^-). The origin of the second peak near 400°C is not yet clear. However, it reasonable to think that carbonaceous residue of the surfactant decomposition might stick to the surface and finally decompose at such high temperature. For CTA, such a peak does not show up clearly since a larger range of decomposition temperature is expected with a larger diversity of carbonaceous residues than for TMA. Anyhow, these residue accounts for less than 1% mass loss. After extraction of the ammonium, both materials (LUS-C100 and LUS-T100) exhibit similar and rather flat TG/DTG curves (Figure 1A-B, red lines). Nonetheless, some physically adsorbed water molecules are detected below 100°C and water produced by silanol condensation between 300 and 500°C, for a total loss of less than 5 wt%.

Then, the surfactant-free materials were fully silylated using 2,2,5,5-tetramethyl-2,5-disila-1-azacyclopentane (TMDSACP) yielding LUS-C100-E and LUS-T100-E

materials. The latter are distinctively hydrophobic according to the absence of any mass loss below 100°C showing that there is no adsorbed molecular water molecules (Figure 1A-B, green lines). The discontinuities of the TGA curves better seen on the DTG curves reveal two new weight loss peaks, one rather sharp at around 320 °C and the other broader in the region 450-600 °C. The first one is doubtlessly due to EBDMS while the second one is probably due to carbonaceous residues of the EBDMS combined with silanol condensation.

At this stage, a better understanding of the surface species evolution is necessary , justifying the use of our quantitative ^{29}Si MAS NMR and ^{13}C CPMAS NMR study. The material after calcination at 380 °C which used the exact heating programme as that in TG measurement was also characterized (Figure 2).

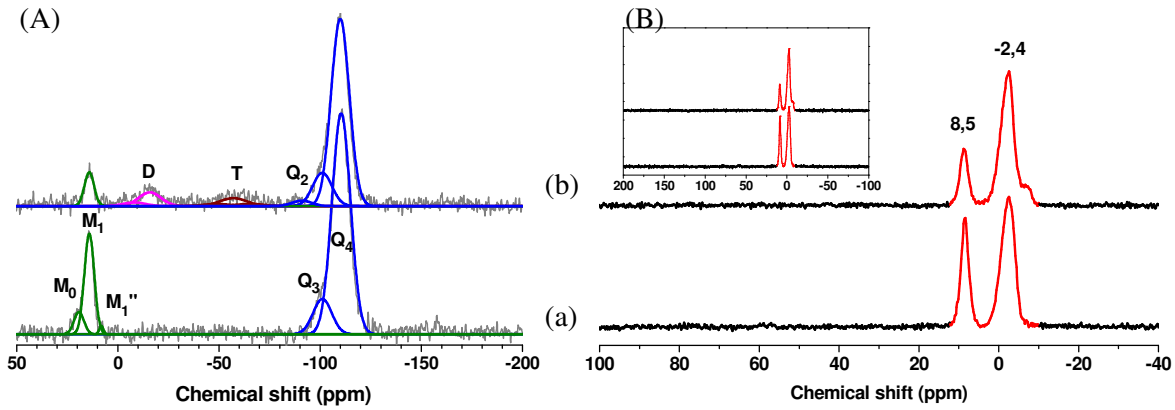

Figure 2 Quantitative ^{29}Si MAS NMR (A)and ^{13}C CP MAS NMR spectra of the materials (B, the insert shows all the spectral range investigated); a) LUS-T100-E and b) after calcination at 380 °C. The chemical shifts in the ^{29}Si MAS NMR spectra are : Q_4 = -111.0 ± 0.3, Q_3 = -101.9 ± 0.3, Q_2 = -91.8 ± 0.4; M_1 = 14.1 ± 0.1, M_0 = 18.6 ± 0.4, M_1'' = 6.7 ± 0.1, T_3 = -65.4 ± 0.2; T_2 = -57.1 ± 0.1; T_1 = -49.0 ± 0.1; D_2 = -15.4 ± 0.4; D_1 = -8.2 ± 0.1. Linewidths are the same for all Q_n species and equal to 9.21 ppm in spectrum "a" and 9.45 ppm in spectra "b", respectively; M species are treated similarly with a single linewidth of 4.90 ppm in "a" and 4.78 ppm in "b"; in spectrum "b", the linewidths of all D_n and T_n species are equal to 11.00 ppm. The lineshape is the same for all signal with a Gaussian/Lorentzian ratio of 1.00.

The ^{29}Si MAS NMR spectrum for LUS-T100-E (Figure 2A, a) exhibits the characteristic signals at -110.8 (intense, Q_4) and -101.9 ppm (Q_3) assigned to the [SiO_4] tetrahedral connected fto four or to three other tetrahedral units, respectively. There is also three smaller signals, arising on the low field side at 6.7, 14.1 and 18.6 ppm that can be ascribed to silicon atoms in [$R_3SiOSiR_3$] units (M_1"), [$R_3SiO(SiO_3)$] unit (M_1), and [R_3SiOH] unit (M_0) (R = -CH_3 or -CH_2-) respectively. The small signal M_1" indicates than some EBDMS species have condensed together into dimers or oligomers. However in most of the cases this signal remains small. The dominant species M_1 at 14.1 ppm is the fingerprint of the grafting of EBDMS on the silica surface. However, the presence of species M_0 shows that not all organosilyl function are grafted suggesting that single grafted EBDMS are also produced. Meanwhile, in the ^{13}C CPMAS NMR spectrum two signals appear at -2.4 and 8.5 ppm attesting for the presence of methyl and methylene carbon atoms (R = -CH_3 or -CH_2-) in the EBDMS moieties, respectively, (Figure 2B, a) without signals at high chemical shift region, related to the other C species (Figure 2B, insert).

Among the possible surface EBDMS species according to R. Anwander *et al*, the dipodal silazane is digrafted in the ring siloxyl group (E2), the bulkier siloxyl bridged dimer (E1-E1) and the monopodal siloxyl group (E1) on the surface of dehydrated LUS-T100 as presented in scheme 1. Note that the digrafted E2 function affords M_1 groups only while monografted species E1 is characterized by M_0 and M_1' neighbouring groups. M_1 and M_1' are similar groups that are not resolved, since they differ only by different next neighbours (Scheme 1). Therefore, the relative intensities between M_0, M_1+ M_1' and M_1" is directly related to the relative distribution among E1, E2 and E1-E1 grafted species.

The ^{29}Si NMR spectra of LUS-T100-E material calcined at a temperature corresponding to the second mass loss corresponds i. e., 380 °C does not exhibit M_1'' nor

M_0 species anymore. Concomitantly, the methylene ^{13}C NMR signal (8.5 ppm) diminishes consistently with a partial decomposition of the digrafted E2 EBDMS moieties and a total disappearance of the monografted E1 and the grafted dimer E1-E1 (Figure 2B, b). The appearance of D and T species shows that the residue of EBDNS decomposition still contains organic silicon species that are linked by two or three covalent bond to the surface instead of one in EBDMS. This will be described in detail later.

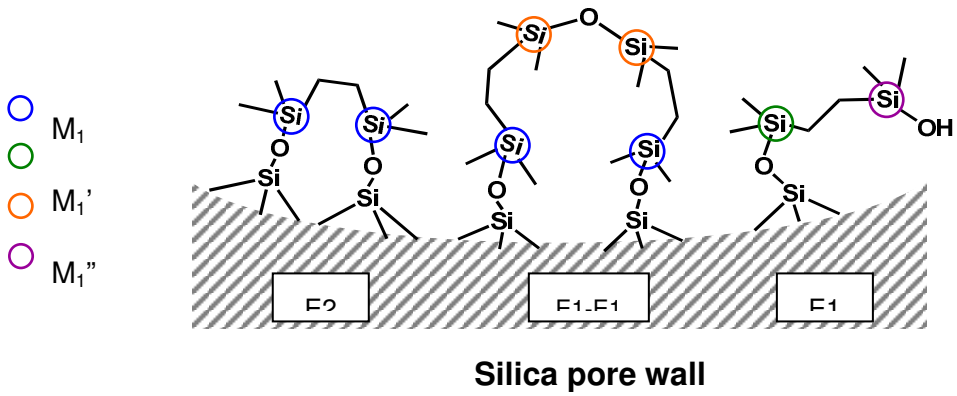

Scheme 1 Possible EBDMS surface species generated upon silylation of dehydrated mesoporous silica LUS using silazane 2,2,5,5-tetramethyl-2,5-disila-1-azacyclopentane (TMDSACP, HN(SiMe2CH2-)2); M_1, M_1', M_1'', and M_0 refer to the Si signals observed in ^{29}Si-NMR.

4.2.2 EBDMS Grafting in the presence of surface masking ammonium agent

The retention of ammonium cations adsorbed on the surface is expected to limit and control the coverage of grafted organosilane. This masking role of adsorbed ammonium is investigated in the following.

4.2.2.1 Monitoring of the grafting sequence using FT-IR

All the solids were characterized at different step of the surface treatments including XRD, TGA, Nitrogen isotherms and NMR techniques. However, the daily monitoring was based on the FT-IR technique that is fast and simple. It has been also

found easier to rely first on this technique to described all the stages of the surface modification before to get through all the other complementary techniques.

4.2.2.1.1 Preparation of the ammonium mask: LUS-Cx & LUS-Tx

On the basis of MSP technique, when partial template is removed, the self-repulsion between the cation (CTA^+ or TMA^+) is meant to provide a regular pattern homogeneously distributed all through the channel. This step also depends on the diffusion of the organosilane to be grafted. A large molecule for masking agent such as CTA^+ may have a negative effect on the diffusion of the organosilane all along the channel (Scheme 2). The replacement of CTA^+ by TMA^+ as masking agent, which was shown to applied to the MSP technique for the control of the TMS coverage is applied also here (Scheme 2).

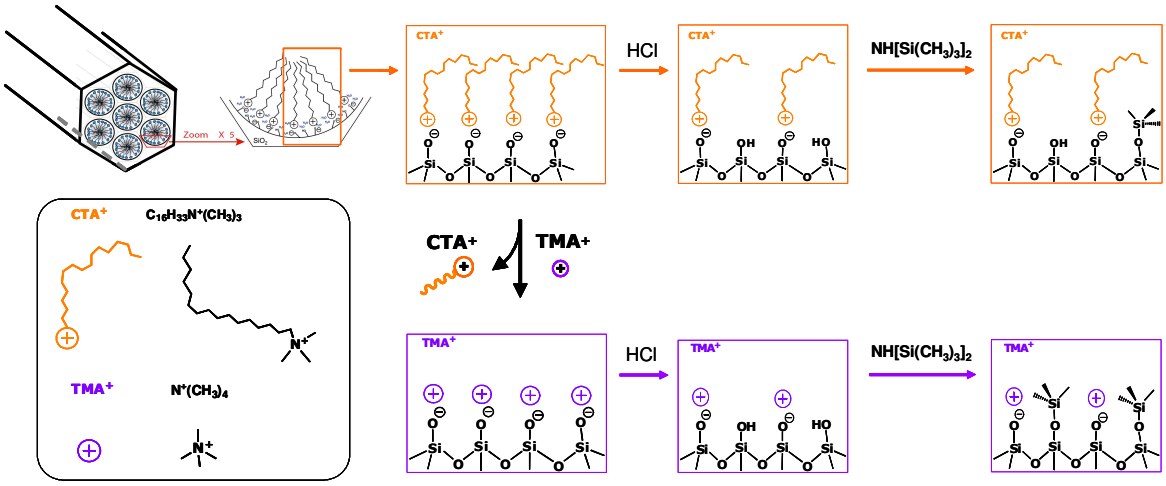

Scheme 2 Synthetic steps for TMS partial grafting in the nano channels of mesoporous silica surface templated by CTA^+ or TMA^+.

The masking efficiency of CTA^+ or TMA^+ onto the grafting of EBDMS were compared using LUSC0 and LUS-T0 extracted at 0%, 25%, 50% and 75%.

In the high frequency region (2400-4000 cm^{-1}), the bands centered at *ca.* 1490 cm^{-1} (Figure 3, a). They are assigned to C-H stretching (ν_{C-H}) and bending (δ_{C-H}) vibrations,

respectively. As expected, the intensity of those bands decreases drastically after partial removal of CTA^+ in LUS-C50.

The characteristic IR bands of CTA^+ are replaced by those of TMA^+, after exchanging the former by the latter (Figure 2A, c). A sharp single peak rises up at 1490 cm^{-1} replacing the much broader set of peaks assigned to C-H bending vibration of CTA^+ in LUSC0. This single peak of TMA assigned to the C-H bending vibration of $-CH_3$ compared to. Consistently, the former peak decreases further in proportion with the level of TMA^+ extraction (Figure 2A, d-g). Therefore, the band of C-H bending is noted as a characteristic of the phenomenon that a part of silanol groups have been protonated while the rest TMA^+ protecting the silicate surface.

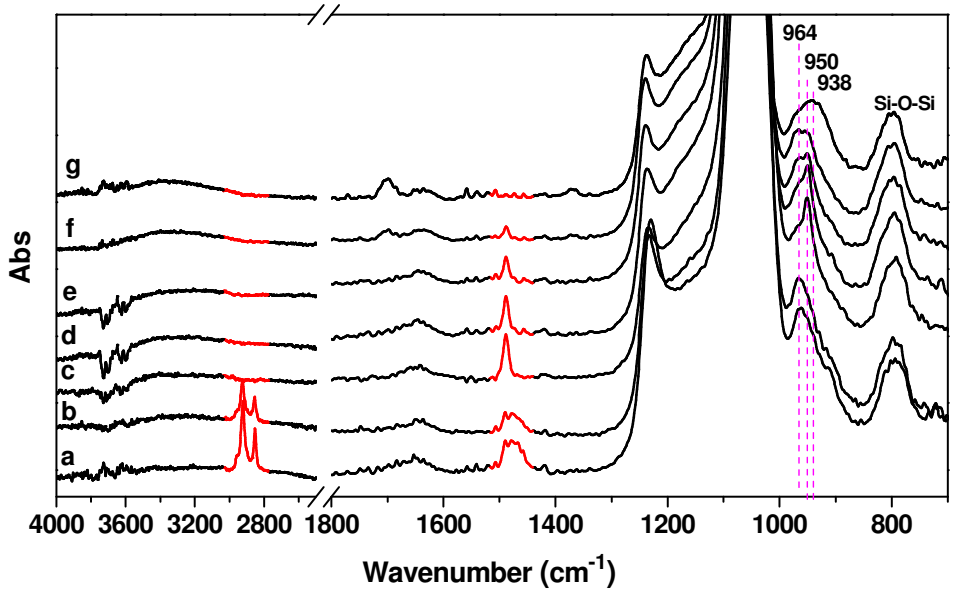

Figure 3 FT-IR monitoring of partial removal of CTA^+ or TMA^+. a, starting LUSC0; b, 50% extracted leading to LUS-C50; c, starting LUS-T0; d, 25% extracted leading to LUS-T25; e, 50% extracted, LUS-T50; f, 75% extracted, LUS-T75; g,100% extracted, LUS-T100. C-H stretching vibrations of $-CH_3-$ and $-CH_2-$ in the range of 2850~2960 cm^{-1} and C-H bending vibration at ~1490 cm^{-1}; Si-O stretching vibration of $Si-O^-$ at 964 cm^{-1} and of Si-OH at 938 cm^{-1}; C-N stretching of TMA^+ at 950 cm^{-1}.

Note that the narrow band arising at 950 cm^{-1} also is due to the presence of TMA^+ and may be assigned to N-C vibration mode or to another type of Si-O stretching mode

specific of the presence of TMA (vide infra). It diminished with the removal of TMA^+ (Figure 2, d-g). The Si-O stretching mode of the surface $Si-O^-$ units paired with either CTA^+ or TMA^+ ions appear at 964 cm^{-1} (Figure 3, a~f). By comparison, the corresponding mode of the Si-OH covering surface of the fully extracted LUS-T100 and LUS-C100 materials is broad and centred at 938 cm^{-1} (Figure 3, g; LUS-C100 not shown).

4.2.2.1.2 EBDMS grafting in the presence of the mask: LUS-Cx-E & LUS-Tx-E

The LUS-Cx-E materials obtained after grafting EBDMS show similar FT-IR spectra before and after silylation in the range 1000-4000 cm^{-1}. In particular the IR band assigned to C-H stretching and bending modes are still there at about the same intensity than before grafting, showing that CTA^+ was retained in the pore. The main evolution are observed at lower wavenumbers where two bands appear at 758 and 834 cm^{-1} both assigned to the Si-C stretching (Figure 4A). The former strongly overlaps with the band at 800 cm^{-1} due to the symmetric stretching mode of the $[SiO_4]$ units. The latter (red line) is emphasized since this band is a fingerprint of the EBDMS moieties that can be used for quantification. By contrast to CTA^+, EBDMS can hardly be detected in the region 2800-2900 cm^{-1} where the C-H stretching bands remain very weak (Figure 4A, e′). Nonetheless, the retention of the peak due to SiO^- at 950 cm^{-1} in LUS-C100-E and the drastic decrease of the Si-O stretching mode at 938 cm^{-1} assigned to the SiOH group is consistent to the grafting of EBDMS by reaction of the unmasked silanol groups and the protection of the silanolate groups.

Basically, the same evolution of the FT-IR spectrum is observed in LUS-Tx-E materials in comparison to LUS-Cx-E indicative for the success of EBDMS grafting onto a silica surface partly protected by ammonium ions (Figure 3, c; Figure 4B, a). The main difference with CTA^+ lies on the 940-960 cm^{-1} region where in the presence of TMA^+ no other band than that at 950 cm^{-1} remains. This is questioning the attribution of the latter

to any N-C vibration mode and supporting instead an assignment to a Si-O stretching specific of $Si\text{-}O^-$ counterbalanced by TMA^+. Moreover, it is clear that EBDMS grafted in the presence of TMA masking group react with a larger number of silanol groups .

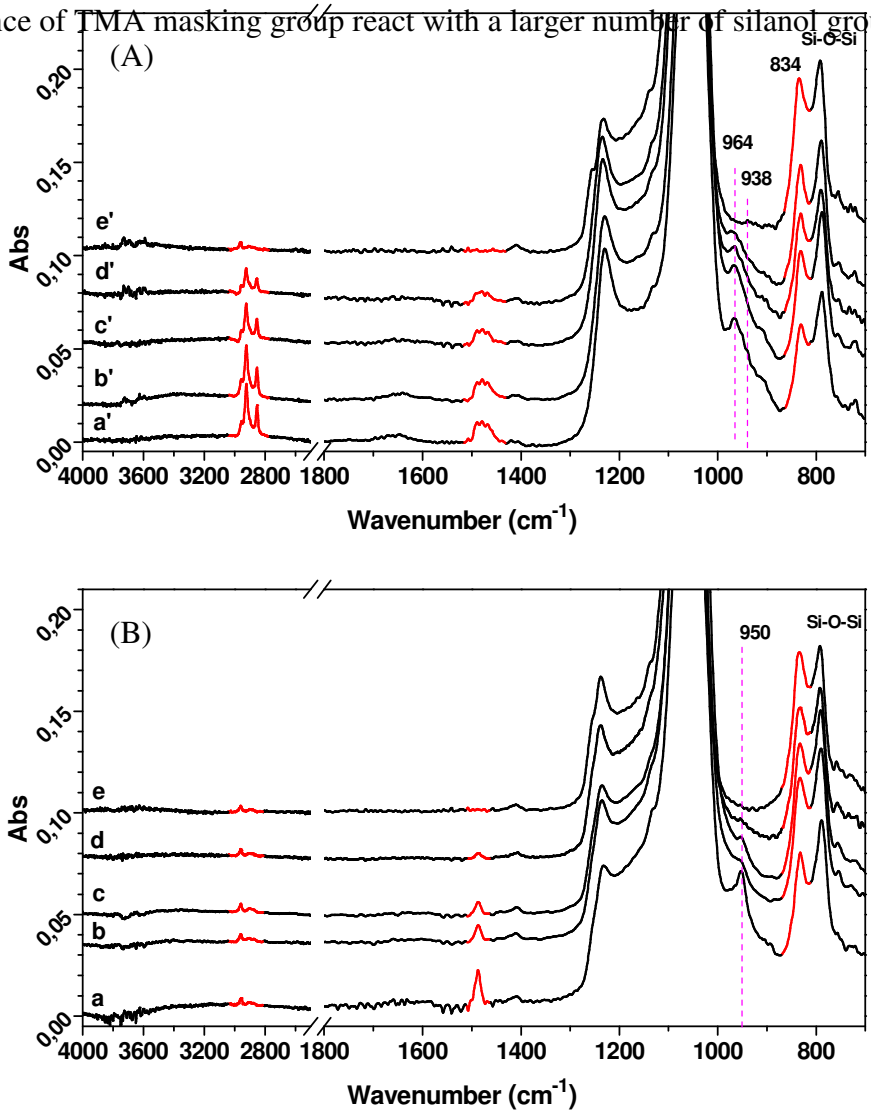

Figure 4 FT-IR spectra for the materials after EBDMS grafting in the presence of partially extracted masking ammonium cations: A) CTA^+ and B) TMA^+; a′, LUSC0-E; b′, LUS-C25-E; c′, LUS-C50-E; d′, LUS-C75-E; e′, LUS-C100-E. a, LUS-T0-E; b, LUS-T25-E; c, LUS-T50-E; d, LUS-T75-E; e, LUS-T100-E. The red lines point out the spectral ranges of C-H stretching (left), C-H deformations (middle) and one of the Si-C stretching (834 cm^{-1}) modes.

4.2.2.1.3 Elimination of masking ammonium layer: LUS-Cx-E-OH & LUS-Tx-E-OH

The EBDMS grafted materials were treated using 1N HCl acid ethanol solution in order to titrate the remaining silanol groups and remove the masking ammonium. 1.1 *eq.* HCl per ammonium was used to avoid any excessive acidity. Regarding to the difficulty in ion-exchanging CTA^+ with long alkyl chain, the acid extraction to LUSC0-E was monitored using FT-IR spectra (Figure 5).

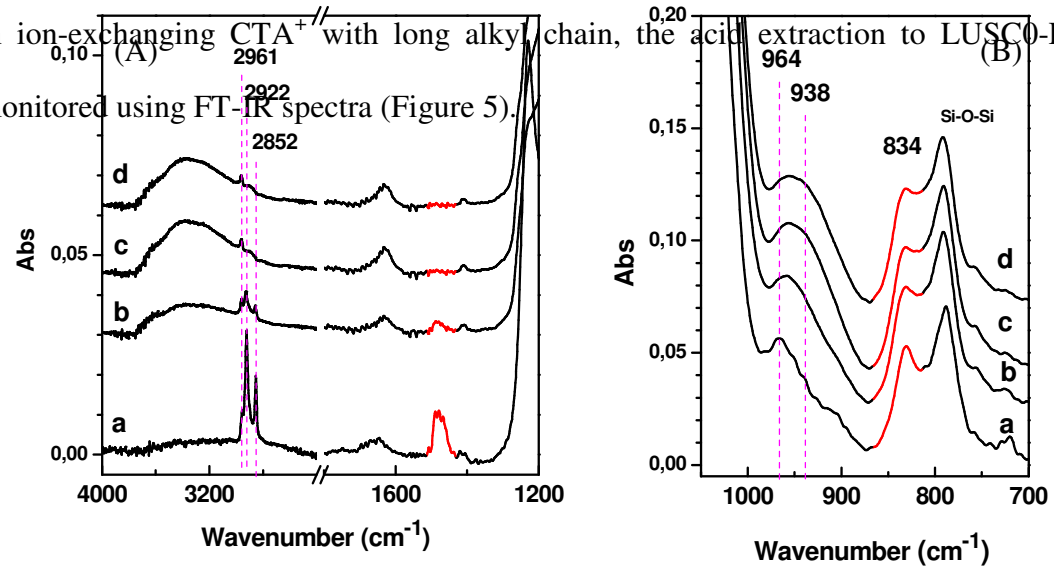

Figure 5 FT-IR spectra of the material after extraction of the masking CTA^+ammonium agent: A) high and B) low wavenumber regions; a) before extraction LUSC0-E b) after first extraction, LUSC0-E-OH_1st, c) after second extraction, LUSC0-E-OH_2rd and d) after the third extraction, LUSC0-E-OH_3rd (= LUSC0-E-OH).

The FT-IR monitoring leads us to proceed three consecutive acid washing to achieve an appropriate removal. Indeed, the 1450-1500 cm^{-1} range was used to follow the removal of CTA^+, which is almost completed at the first washing (Figure 5A, a-b). At the third washing, the only C-H stretching left arise at 2961, 2922 cm^{-1} and belong to EBDMS (Figure 5A, d). The normalized intensity of 834 cm^{-1} Si-C stretching band changes from 0.19 ± 0.01 for LUS-C0-E to 0.21 ± 0.01 for LUS-C0-E-OH, indicating that EBDMS species remain stable under such weak acid condition (Figure 5B).

The other ammonium masked and EBDMS grafted materials were also extracted following the same acid treatment yielding LUS-Cx-E-OH or LUS-Tx-E-OH (Figure 6).

Very similar spectral evolution is observed except the relative intensities of the FT-IR band following the expected trend, i. e., less masking agent for more grafted EBDMS. Additionally, the protected silanolate groups (band at 950 cm^{-1}) in both LUS-Cx-E and LUS-Tx-E materials are converted into silanol groups (band at 938 cm^{-1}, Figure 6A, b′-d′; B, b-d). As to the fully EBDMS covered samples LUS-C100-E and LUS-T100-E, no Si-OH stretching is observed (Figure 6-A, e; B, e′).

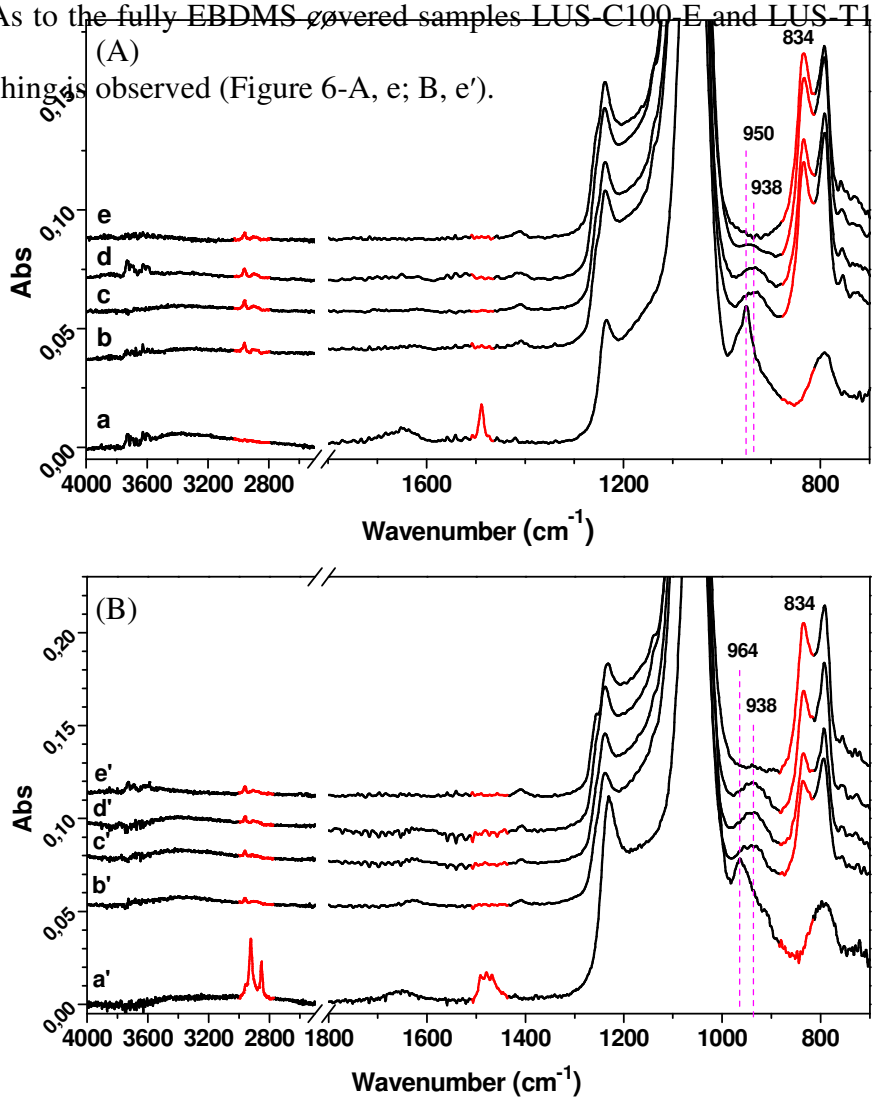

Figure 6 FT-IR spectra for EBDMS grafted materials after removing the template: A) CTA^+ and B) TMA^+ masking agent; a′) LUSC0, b′) LUS-C25-E-OH, c′) LUS-C50-E-OH, d′) LUS-C75-E-OH, e′) LUS-C100-E. a, LUS-T0; b, LUS-T25-E-OH; c, LUS-T50-E-OH; d, LUS-T75-E-OH; e, LUS-T100-E.

4.2.2.2 Complementary investigations using various techniques

In complement to the FT-IR investigations presented above, the meso-structures of materials were characterized by X-ray diffraction and nitrogen sorption isotherm, TGA and solid state NMR throughout all the synthetic sequences.

4.2.2.2.1 Structure of LUS-Cx-E-OH & LUS-Tx-E-OH

Like the genuine CTA^+ templated material, LUS-T0 and its derivatives exhibit the same typical 2D-hexagonal XRD patterns with a *p6mm* point group (Figure 12). The weaker peak intensity of the [100], [110] and [200] reflections for LUSC0 compared to those of LUS-T0, is due to the high channel filling factor by the long alkyl chain of CTA^+ (Figure 12, a-b). Both of acid washing and EBDMS grafting bring no change to the reflection peaks, suggesting that the meso-structure was retained during the patterning sequences (Figure 12, c-f).

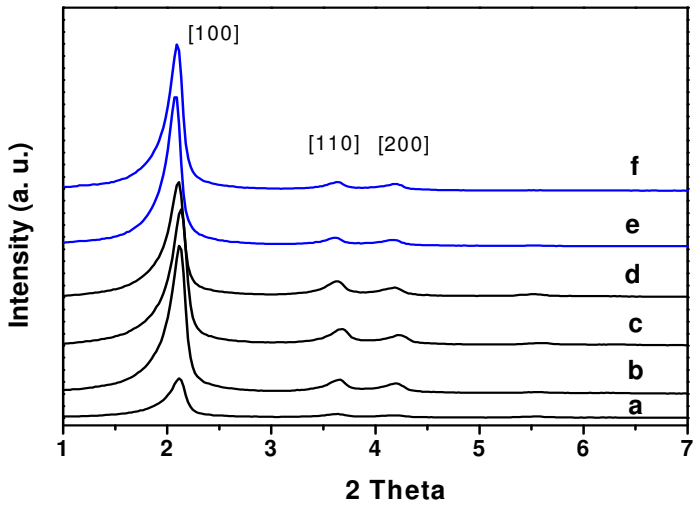

Figure 12 Small-angle powder XRD pattern of materials: a) LUSC0, b) LUS-T0, c) LUS-T50, d) LUS-T100, e) LUS-T50-E-OH and f) LUS-T100-E.

Consistently, the N_2 adsorption isotherms are typical of MCM-41 type of materials for either template extracted or EBDMS grafted ones. For instance, LUS-T100, LUS-T50-E-OH and LUS-T100-E exhibit all a characteristic type IV sorption profile (Figure 13). For the fully extracted TMA LUS-T100, a steep step of adsorption branch at P/P_0= ~ 0.4 indicates a narrow mesopore size distribution centred at 4.0 nm for a surface area of 1025 m^2/g and a pore volume of 1.0 cm^3/g (Figure 13A-B, black line; Table 4, entry 2). Similarly, LUS-C100 is characterized by 1063 m^2/g and 1.0 cm^3/g, respectively (Table 4, entries 1-2). This demonstrates that the exchange of TMA for CTA followed by a full chemical extraction affects the surface area for less than 5%, i. e., within the experimental error. As expected, the EBDMS grafted LUS-T100-E and LUS-T50-E-OH material with a corresponding nominal surface masking level of 0 and 50 % exhibit a lower capillary condensation pressure at P/P_0 = ~ 0.25-0.3 that correspond to 3.4 ± 1 and 3.2 ± 1 nm pore diameters, respectively (Figure 13A-B, red and green lines; Table 4, entries 4-5).

More precisely, after masking by TMA^+ groups with nominal coverages of 100 %, 50% and 0%, LUS-T0-E-OH and EBDMS sylilation, LUS-T50-E-OH, and LUS-T100-E materials are characterized by a reduction of specific surface areas of 70, 67, and 59%, and smaller pore volumes of 58%, 56% and 53% in comparison of the genuine material LUS-T100, respectively. Moreover, the C parameter, which represents the affinity between the absorbant and the absorbate, decreases from 111 for LUS-T100 down to 35, 32 and 29, respectively. The evolution of all these parameters is consistent with 1D nano channels covered by the hydrophobic EBDMS functions (Table 4, entries 3-5). By comparison, materials with CTA^+ protected surfaces at similar masking coverage in LUS-C0-E-OH, LUS-C50-E-OH, and LUS-C100-E exhibit a reduction of 84, 68, and 59% of the specific area and 70, 63 and 53% of the pore volume of LUS-C100, respectively for C parameters decreasing from 121 of LUS-C100 to 41, 37 and 28, respectively (Table 4, entries 1, 6-8).

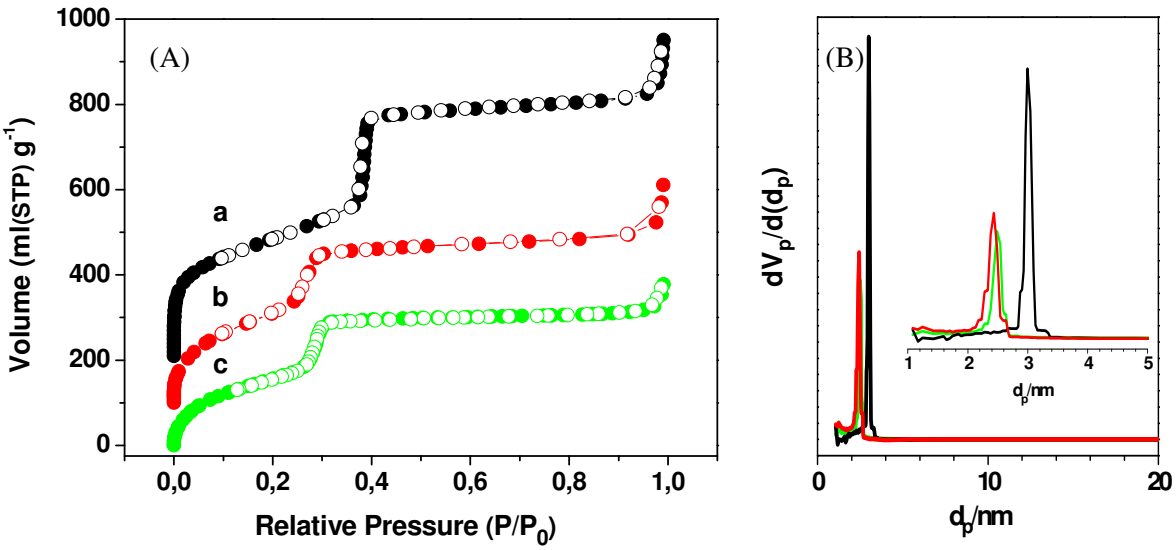

Figure 13 A) N_2 ads-desorption isotherms and B) pore size distribution from BJH analysis (add *ca.* 0.7 nm for more precise BdB equivalent) of a) LUS-T100 (offset of +200 ml (STP) g^{-1}), b) LUS-T50-E-OH (offset of +100 ml (STP) g^{-1}) and c) LUS-T100-E.

Noteworthy, the fully extracted LUS-C100-E and LUS-T100-E are rather similar and possesses the characteristic of the conventional calcined LUS or MCM-41 materials (Table 4). Therefore, exchanging CTA for TMA does not modify the material. Therefore, the reduction of pore volume and surface area after grafting are assigned the layer of EBDMS grafted in the internal surface of the materials. Moreover, LUS-Tx-E-OH samples possess slightly smaller surface area, pore volume and C value than LUS-Cx-E-OH materials consistently with more grafted EBDMS. So concerning to the MSP technique, herein, CTA^+ has a higher protecting effect against EBDMS grafting than TMA^+. By comparison, the coverage of TMS in similar masking conditions was smaller than EBDMS, matching a full coverage of the unmasked surface and no significant difference was noted between both ammonium masking properties. The higher coverage observed with EBDMS (more pronounced for TMA^+ masking ammonium) clearly

indicated that the dual grafting properties favors in some extent the displacement of the ammonium away from the surface. This effect remains partial since the coverage of EBDMS is smaller in the presence of both masking ammonium ions. Both a lower hindrance or a higher mobility may favor the partial displacement of TMA that needs to be confirmed by chemical analysis.

Table 4 N_2 adsoption isotherm data for LUS-C100 and LUS-T100 materials and after EBDMS functionalization.

Entries	Samples	S_{BET} (m^2 g^{-1}) % vs ref[a]	V_{total}[b] (cm^3 g^{-1})	D_{BdB}[c] (nm)	C[d]
1	LUS-C100	100	1.0	4.0	121
2	LUS-T100	100	1.0	4.0	111
3	LUS-C0-E-OH	*84*	*70*	3.5	41
4	LUS-C50-E-OH	*68*	*63*	3.2	37
5	LUS-C100-E	*59*	*53*	3.3	28
6	LUS-T0-E-OH	*70*[e]	*58*	3.3	35
7	LUS-T50-E-OH	*67*	*56*	3.2	32
8	LUS-T100-E	*59*	*53*	3.4	29

a, In the $0.05< P/P_0 <0.25$ range , LUS-C100 and LUS-T100 surface areas of 1063 and 1024 m^2/g are taken as references for each series; b, Total pore volume measured at $P/P_0 = 0.92$; c, Y (BdB Pore Diameter, Å) $=14.60994+74.67812*x–81.96198*x^2+155.8457*x^3$, $X=P/P_0$ ($0.11\leq P/P_0\leq 0.50$); d, BET-plot parameter, ± 2; e, S_{BET}(sample)/S_{BET}(LUS support)*100%; V_{total} (sample)/V_{total}(LUS support)*100%.

4.2.2.2.2 Chemical analysis

The chemical composition of the EBDMS modified samples were characterized by TG/DTG, elemental analysis and quantitative ^{29}Si MAS NMR. Typical TG/DTG curves are shown in Figure 7 for genuine and intermediate materials of the sequential grafting of EBDMS with 0% and 50% extraction of CTA or TMA.

The material LUS-C50 exhibits a weight loss of 15.29 wt% between 150-320 °C assigned to the decomposition of the CTA^+SiO^- surface ion pairs that has to be compared with 22.57 wt% mass loss in the genuine material, LUSC0. Note that is only 32% less than 50% planned. The weight loss in the same temperature range rises up to 18.09 wt% when EBDMS is grafted (LUS-C50-E) showing that the decomposition of EBDMS occurs at least partially at this temperature when the surfactant is still present. The second peak near 340 °C due to CTA^+Tos^- decreases (Figure 7, a). This shows that there is a redistribution of the surfactant upon the grafting effect of EBDMS

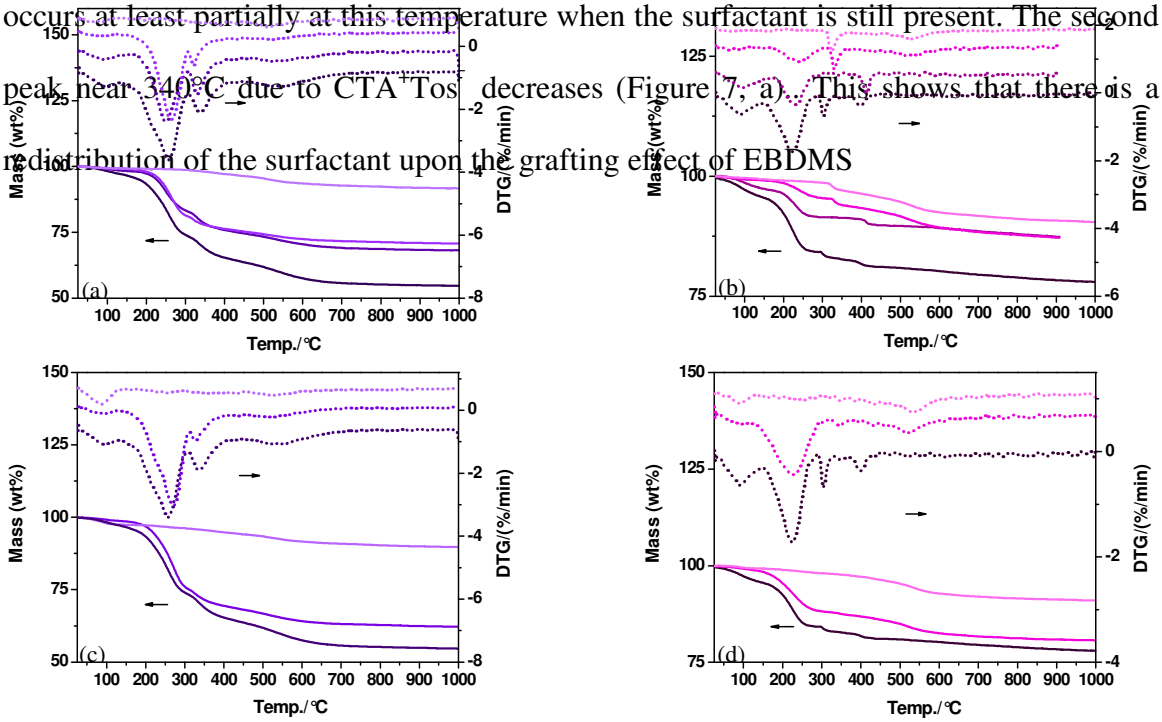

Figure 7 TG (solid line) with related DTG (dot line) curves for templated materials functionalized by EBDMS with 50% ammonium extraction (a,b) or no extraction (c,d) with CTA (righ) or TMA (left) as masking agent : a) LUSC0, LUS-C50, LUS-C50-E and LUS-C50-E-OH; b) LUS-T0, LUS-T50, LUS-T50-E and LUS-T50-E-OH; c) LUSC0, LUSC0-E and LUSC0-E-OH; d) LUS-T0, LUS-T0-E and LUS-T0-E-OH.

In the range 150-290 °C, the weight loss of LUS-T50-E is about twice less than for LUS-T0, i. e., 5.44 instead of 10.91 wt%. This temperature range is assigned to the mass loss occurring during the decomposition of TMA^+SiO^-. This is consistent with the

expectation showing in this case that the removal has efficiently taken place contrary to the above observation for CTA^+. Another difference with the CTA masked surface, resides in a reduction of the mass loss down to 3.81 wt% in the same temperature range when EBDMS is grafted. It suggests that some TMA^+ cations have leached out during the grafting process. Above this range, a sharp peak at 320 °C in the DTG curve is present LUS-T0 and is shifted up to 340°C. This evolution already observed by Zhang Kun in his thesis was attributed to different salt of TMA^+ retained in the channel after exchange and partial extraction. The first salt is TMABr that is the salt used to exchange CTA for TMA and the second one is TMACl produced during the extraction using HCl (Figure 7, b). Anyhow these DTG peaks are small details here since they correspond to a very small mass losses. TG/DTG curves confirms that the partial surface masking using the MSP technique lead to a control of the amount of grafted EBDMS function. This technique show further that the masking power (ammonium retention) is lower against EBDMS grafting than against TMA grafting and that CTA^+ has better masking capabilities than TMA^+ (Table 2).

CTATos acting as a surfactant remains in the channel of the as-synthesized LUSC0 in two different situations as ions pairs $\{SiO^-, CTA^+\}$ surface ion pairs or $\{Tos^-, CTA^+\}$ free ion pairs filling the voidin the channe left by the surface ions pairs. As a results, the $\{Tos^-, CTA^+\}$ pairs can be replaced by any other molecular filling agent such as grafted EBDMS. This is monitored here using the N element to calculate the amount of ammonium retained in the materials. Indeed, comparing LUSC0 and LUS-C-E with N/Si of *ca.* 0.150 and 0.121 for a decrease of ca. 0.3 N/Si, i. e., about 20% of CTA^+ . This matches the the proportion of $\{Tos^-, CTA^+\}$ pairs expected in such materials according to previous reports Table 2, entry 1).[34] A comparable removal occurs during the exchange of CTA for TMA where the none electrostatically retained ammonium are washed out.[32] However, for the present cation exchange, a stronger N/Si decreases down to 0.102 was

produced may be because of harsher conditions than those of ref. 32 (Table 2, entry 1, LUS-T0). Anyhow, the most stricking results of the first line is the drastic EBDMS grafting reaching up to 57 and even 71% of coverage in the presence of CTA^+ or TMA^+. In fact removing 25% or 50% of the surfactant does increase the coverage by EBDMS but not as much as expected since about 64 and 66% of EBDMS coverage is produced in the presence of CTA^+, respectively. For TMA^+ masking agent, the EBDMS coverage is systematically higher than in the case of CTA^+ as already anticipated from FT-IR, and N2 isoterm investigations. One of the difference comes from already from the cation exchange that yield from 20 to 46% lss ammonium in the channel while the second is the higher loss of TMA during EBDMS grafting evolving from 13 to 18% from CTA and about 45% for TMA. This allows to generate a series of surfaces that are covered from 57 to 92 %, i.e., in the range of interest for site isolation (> 66%).

Table 2 Elemental analysis of materials via sequential EBDMS grafting

Entries	Samp.	CTA^+				TMA^+			
		CTA^+/Si_{tot}			EBDMS/$Si_{tot.}$ *(LUS-Cx-E)*	$TMA^+/Si_{tot.}$			EBDMS/$Si_{tot.}$ *(LUS-Tx-E)*
	x[a]	N/Si[b] *(LUS-Cx)*	N (wt%) *(LUS-Cx-E)*	C (wt%)	Si_E/Si_{tot} %[c] (coverage %)[d]	N/Si *(LUS-Tx)*	N (wt%) *(LUS-Tx-E)*	C (wt%)	Si_E/Si_{tot} %[c] (coverage%)[e]
1	0	0.150	0.121	6.58	0.13 (*57*)[d]	0,102	0.099	7.84	0.15 (*68*)[e]
2	25	0.097	0.084	7.75	0.15 (*65*)	0.078	0.045	10.82	0.20 (*91*)
3	50	0.076	0.065	7.91	0.15 (*65*)	0.056	0.036	9.33	0.17 (*77*)
4	75	0.057	0.047	9.68	0.19 (*83*)	0.031	0.017	10.89	0.20 (*91*)
5	100	0.002	0.002	11.84	0.23 (*100*)	0.005	0.003	11.74	0.22 (*100*)

a) nominal extraction level based on a HCl/ammonium extraction ratio of 1:x = 0, 25, 50, 75 and 100; x = 0 stands for LUSC0 and LUS-T0

b) molar ratio: N/Si_{tot} = [(N wt%/14 g mol^{-1})]/(Si wt%/28 g mol^{-1}) * 100%, from EA

c) molar ratio: Si_F/Si_{tot} = [(C wt%/12 g mol^{-1})/3]/(Si wt%/28 g mol^{-1}) * 100%, from EA

d) The relative EBDMS coverage considering LUS-C100-E as 100% coverage reference

e) The relative EBDMS coverage considering LUS-T100-E as 100% coverage reference

To further investigate the effect of different masking properties of TMA and CTA for the grafting of EBDMS, the intensity of IR peak at 834 cm^{-1} has been monitored quantitatively by normalization to the IR peak at 450 cm^{-1} (scissor bending mode of the O-Si-O angle of the [SiO_4] units). This band is a local vibration mode of the [$SiOC_3$] units characterizing silicon atoms of EBDMS denoted also as Si_{org}. Both types of ammonium masking and both temperatures of grafting are compared.what we call the organic silicon and its intensity is related to the number of grafted function assuming as we will see below from NMR that most EBDMS are digrafted. The figure 8 collect all the data for both LUS-Cx-E-OH and LUS-Tx-E-OH series of materials where the masking agent is either TMA or CTA for EBDMS grafting using in one case TMS grafting as a reference. As expected from previous report and announced before, it is found that tetramethylsilyl function coverage follows in excellent accordance the surface left by the masking TMA^+ (Figure 8, green bar). By contrast EBDMS function follows this trend only above 50% CTA extraction. Below the the EBDMS coverage is much higher than expected > 50%. The coverage is even higher when TMA is the masking agent with a coverage remaining above 80% for TMA^+ extraction of 25% or higher. The quantification is in full agreement with the chemical analysis and confirms the conclusion that TMA+ is a poor masking agent for the grafting of EBDMS while CTA^+ remains effective for partial extraction above 50%.

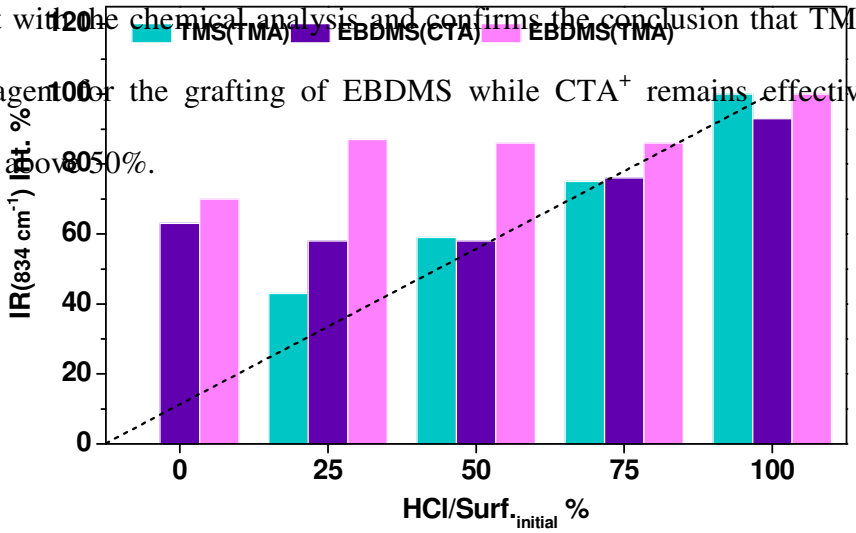

Figure 8 Evolution of the specific IR band of TMS or EBDMS depending on the nominal masking level and the type of ammonium after grafting at 80 °C and mask removal. (Dot line: y = x)

Further analysis of samples by quantitative ^{29}Si MAS NMR were performed to assess the chemical grafting of the dipodal silyl group to the silica network. In all the spectra, the resonances at ca. -111, -102 and -92 ppm represent Q_4 [***Si***$(SiO)_4$], Q_3 [***Si***$(SiO)_3(OR)$], and Q_2 [***Si***$(SiO)_2(OR)_2$] silicon sites, respectively (R = H, C). The supporting materials LUS-C100 and LUS-T100 are observed in the $Q_4/Q_3/Q_2$ relative populations of 63/33/4 and 61/36/3, respectively, revealing no significant changes to the SiO_4 connectivity when exchanging CTA^+ for TMA^+ (Figure 9, a-b; Table 3, entries 1-2). After calcination in air at 550 °C for 10 h, the samples LUS-C100-cal550 and LUS-T100-cal550 exhibit also very similar $Q_4/Q_3/Q_2$ relative populations of 59/37/4 and 60/35/5, respectively. Both calcined materials presents more Q_3 or Q_2 species indicating a higher cocnetration of silanol groups certainly due to a restructuration of the surface to maintain a stable framework (Figure 9, c-d; Table 3, entries 3-4).

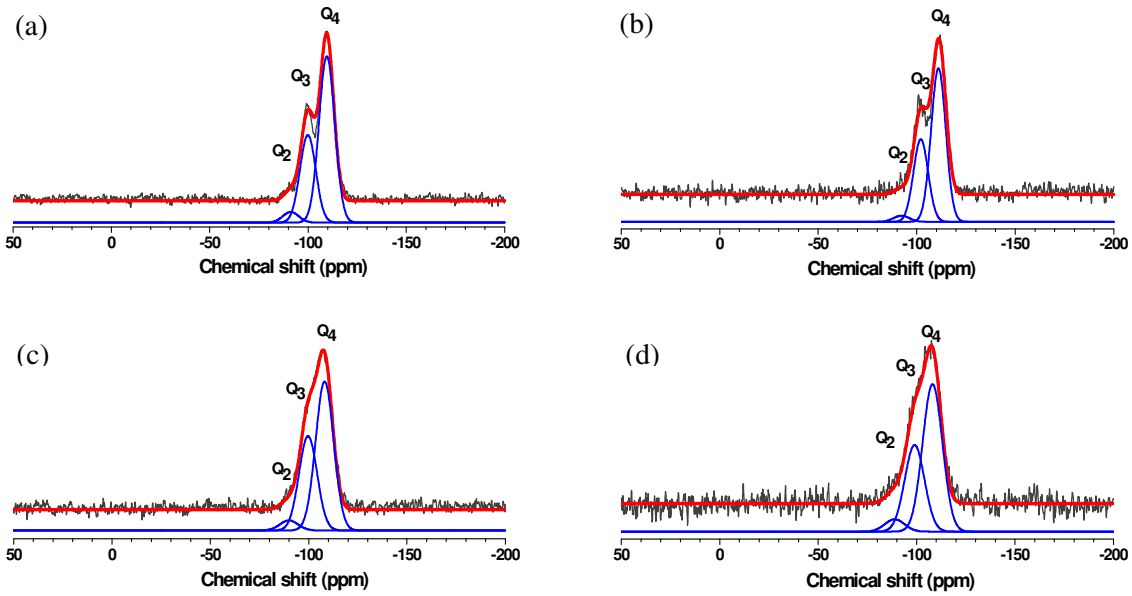

Figure 9 Single echo ^{29}Si MAS NMR spectra of the materials (a) LUS-C100, (b) LUS-T100, (c) LUS-C100-cal550, (d) LUS-T100-cal550. Gray line: raw curve, red line: cumulative curve, blue lines: fits of Q_n species silicon.

After EBDMS grafting, the resulting LUS-Tx-E and LUS-Cx-E (x = 0 or 50) materials present two additional peaks at 7.0 and 13.0 ppm. The former is narrow and can be ascribed to a silicon atom (M_1'') of [R_3***Si***O***Si***R_3] moieties characteristic of monografted pairs, E1-E1. Strikingly, there is no M_0 signal precluding the formation of any single grafted EBDMS species, E1. The signal at 13 ppm is likely due to a M_1 type silicon atom of [R_3***Si***(OSi)] moieties in bigrafted E2 or monografted pairs E1-E1 species (Figure 10, a-b; Scheme 1). Interestingly, the width of M_1 peak is 0.3 ppm broader when TMA^+ or CTA^+ ammoniums are present comparing LUS-C50-E-OH or LUS-T50-E-OH) to LUS-C50-E or LUS-T50-E (Figure 10a and 10b versus 10c and 10d). Similar observation are made when grafting is performed without partial extraction of the masking ammonium comparing LUS-C0-E-OH or LUS-T0-E-OH to LUS-C0-E or LUS-T0-E (Figure 11a and 11b versus 11c and 11d). The narrow signal appears much less abundant when the Carl-Purcel cross polarization technique is applied (CP-MAS). The poor CP magnetization transfer is consistent with free rotation species that do not follow the MAS rotation rate contrary to the grafted species for which the transfer is optimized. Another qualitative information is for most of the appearance of a broader and less intense (in most of the cases) M_1'' peak at the expense of the narrow one after extraction of the ammonium masking agent. This is further support the hypothesis that at least some non-grafted molecular dimeric species are retained in the channel and removed only during the extraction of the masking ammonium ions.

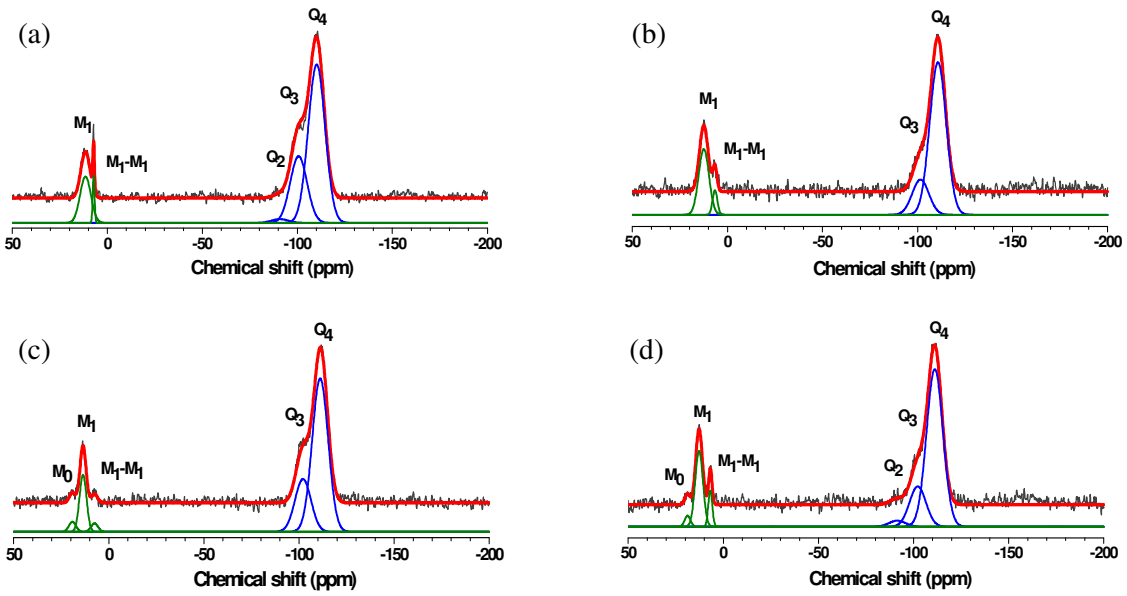

Figure 10 Single echo ^{29}Si MAS NMR spectra of the materials (a) LUS-C50-E, (b) LUS-T50-E, (c) LUS-C50-E-OH, (d) LUS-T50-E-OH. Gray line: raw curve, red line: cumulative curve, blue lines: fits of Q_n silicon species, green lines: fits of M_n silicon species.

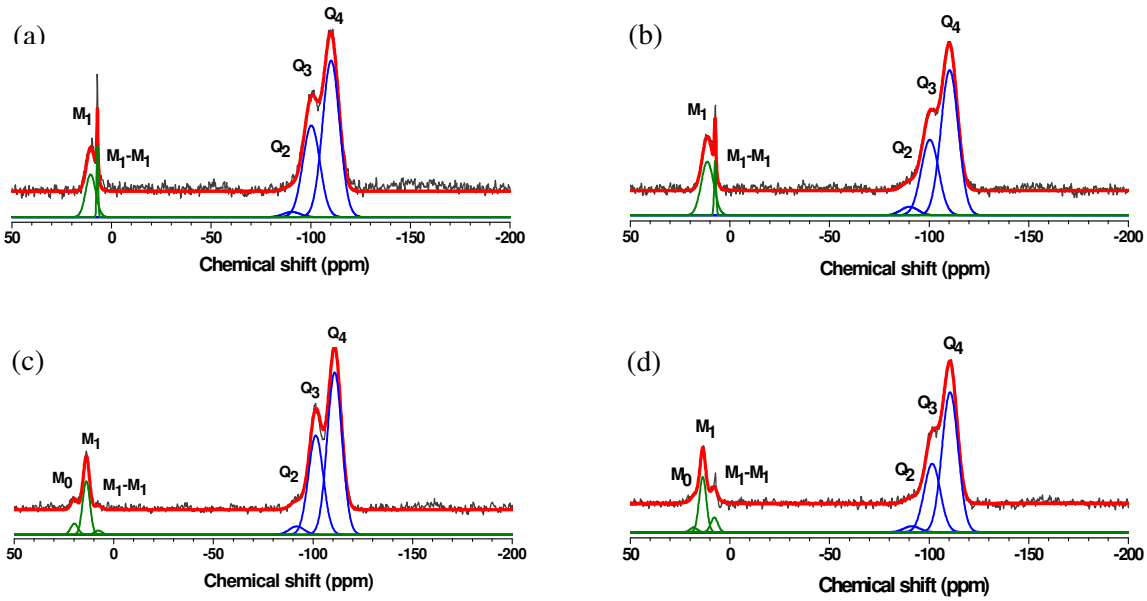

Figure 11 Single echo ^{29}Si MAS NMR spectra of the materials (a) LUS-C0-E, (b) LUS-T0-E, (c) LUS-T0-E-OH, (d) LUS-T0-E-OH. Gray line: raw curve, red line: cumulative curve, blue lines: fits of Q_n species silicon, green lines: fits of M_n species silicon.

Table 3 Percentage of Q_n, M_n obtained from ^{29}Si NMR and related grafted species after different grafting steps and for different masking coverages by CTA^+ or TMA^+ for grafting at 80°C.

Entries	Sample	Q_2 %	Q_3 %	Q_4 %	Si_{inorg} %	M_1 %	M_0 %	M_1'' %	Si_{org} [a] %	E2 [b] %	E1 [c] %	(E1-E1) [d] %
1	LUS-C100	4[e]	33	63	*100*	—	—	—	—	—	—	—
2	LUS-T100	3	36	61	*100*	—	—	—	—	—	—	—
3	LUS-C100-cal550	4	37	59	*100*	—	—	—	—	—	—	—
4	LUS-T100-cal550	5	35	60	*100*	—	—	—	—	—	—	—
5	LUS-C0-E	2	32	52	*86*	9	0	3	*12*	*67*	*0*	*33*
6	LUS-C0-E-OH	3	33	53	*89*	9	2	0	*11*	*64*	*36*	*0*
7	LUS-T0-E	2	26	52	*80*	15	0	5	*20*	*67*	*0*	*33*
8	LUS-T0-E-OH	1	25	57	*83*	12	2	3	*17*	*50*	*29*	*21*
9	LUS-C50-E	2	27	57	*86*	12	0	2	*14*	*83*	*0*	*17*
10	LUS-C50-E-OH	1	26	59	*86*	12	2	0	*14*	*71*	*29*	*0*
11	LUS-T50-E	0	15	65	*80*	17	0	3	*20*	*82*	*0*	*18*
12	LUS-T50-E-OH	2	16	63	*81*	14	2	3	*19*	*56*	*25*	*19*
13	LUS-C100E	0	17	61	*78*	15	6	1	*22*	*38*	*57*	*5*
14	LUS-T100E	0	11	68	*79*	16	4	1	*21*	*55*	*40*	*5*

a, percentage of Si_{org} obtained from $P_{Siorg} = \Sigma P_{Mi} = P_{M0} + P_{M1} + P_{M1''}$

b, percentage of E2, $P_{E2} = 100 \times (P_{M1} - P_{M0} - P_{M1''}) / [P_{M0} + P_{M1}]$; percentage of M1 type of signal belonging to E2 is proportional to $P_{M1}(E2) = P_{M1} - P_{M0} - P_{M1''}$,i.e., $P_{E2} = k \cdot P_{M1}(E2) /2$ ($k = 200/[P_{M0} + P_{M1}]$ according to $\Sigma P_{Ej} = P_{E2} + P_{E1} + P_{E1\text{-}E1} = 100$ and to P_{E1} and $P_{E1\text{-}E1}$ expressions provided in c and d (notice that E2 possesses 2 S_{iorg})

c, percentage of monografted $P_{E1} = 200 \times M_0 / [P_{M0} + P_{M1}]$; $P_{E1} = k \cdot P_{M0}$

d, percentage of dimer $P_{E1\text{-}E1} = 100 \times M_1'' / [P_{M0} + P_{M1}]$; $P_{E1\text{-}E1} = k \cdot P_{M1''}/2$

e, Analytical integral error by noise of baseline (± 2)

Considering now quantitative aspects of the ^{29}Si signal, it appears that in all the cases the concentration of organosiloxane species, grafted or non-grafted, seems unchanged after extraction of the ammonium according to the fraction of Si_{org} species in accordance with previous conclusion from FT-IR (Table 3). The maximum Si_{org} coverage achieved here is 0.28 obtained from Si_{org} / Si_{inorg} molar ratio (Table 3, ratio between column 6 & 10, entries 13 & 14). It compares well with 0.22-0.23 molar ratio for full coverage of monopodal TMS species taking into account that most of the species are monografted in these samples and only part of the Si_{org} are grafted.[32, 34] Consequently, the non-grafted species (non grafted dimers) present before ammonium extraction are mostly converted into grafted species. Those non-grafted dimers are at the highest concentration for the highest ammonium masking coverage, evolving from *ca.* 30 down to 5% of the all grafted species in the present series of materials (Table 3, last three columns). Their grafting into dimers is maximum when TMA is the masking agent. Conversely when the masking agent is CTA, few or none of them survive to the acidic extraction and end up as grafted monomeric and monografted E1 species. The data of column 1 of table 3 reveals also that part of the digrafted species E2 are converted into monografted E1 species particularly when the masking agent is TMA. This insight into the distribution of the grafted species confirms that TMA does not protect the surface as efficiently as CTA. However it is not clear whether it comes from an additional steric hindrance due to the long chain of CTA or merely from a different dynamic effect. In the following both hypotheses are confronted with respect to the temperature dependence of grafting.

4.3 Masking by CTA^+ and TMA^+ at room temperature (rt)

For efficient silanol capping, chlorosilanes, $SiCl_xR_{(4-x)}$ and alkoxysilanes $Si(OR)_xR_{(4-x)}$, are reacted in refluxing solvent, i.e., ca. 80°C in cyclohexene as here or 110°C in toluene often used even in the presence of catalytic (e.g., H_2O) or stoichiometric amounts of additives (e.g., pyridine). In addition, these silylating reagents often display multifunctional surface reactions producing (undesired) by-products such as alcohols and alkylammonium halides which are difficult to separate. In contrast, silazane-based silylation precursors were reported for (i) mild reaction conditions, (ii) a relatively slow surface reaction, (iii) monografted surface reaction, (iv) favourable for atom economy, and (v) ease of thermal desorption of the by-product ammonia.

For the MSP technique, the reaction performed at 80 °C led to excellent capping for TMS. [32-34] However it has been found in the case of EBDMS that grafting leads to a mixture of species with variable stability upon ammonium removal and titanium grafting (see below when titanium grafting will be at stake). Then EBDMS grafting at room temperature was investigated.

4.3.1 FT-IR for monitoring the grafting sequence

The same type of analyses has been applied as above starting first with the FT-IR investigation. As before, LUSC0(or T0), LUS-C(or T)50, and LUS-C(or T)100 were submitted to similar grafting conditions except for the temperature maintained at 25°C instead of 80°C. The first important information is the evidence of a significant EBDMS grafting at room temperature according to the C-H stretching bands appearing in the range 2860-2950 cm^{-1} and the Si-C stretching at 834 cm^{-1} for both of LUS-Cx-E_rt and LUS-Tx-E_rt. In addition as above the masking ammonium remains during grafting according to the characteristic bands of C-H bending in the 1400-1500 cm^{-1} range (Figure 14A-B, a-b).

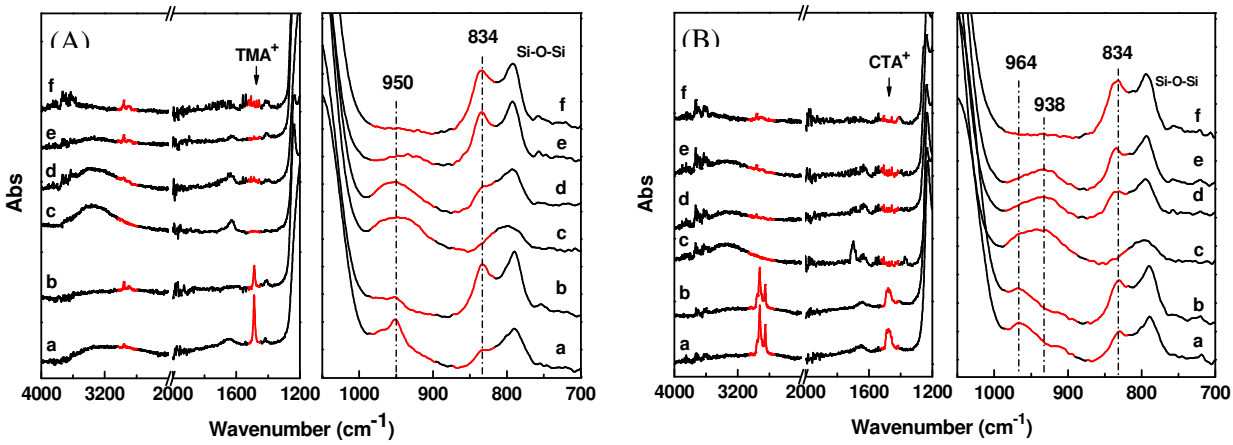

Figure 14 FT-IR spectra for monitoring the synthesis of materials using (A) CTA^+ and (B) TMA^+ as surface protecting groups to silylation at room temperature. In (A): a, LUS-T0-E_rt; b, LUS-T50-E_rt; c, LUS-T100; d, LUS- TMA-E_rt-OH; e, LUS-T50-E_rt-OH; f, LUS-T100-E_rt; a, LUSC0-E_rt; b, LUS-C50-E_rt; c, LUS-C100; d, LUS- CTA-E_rt-OH; e, LUS-C50-E_rt-OH; f, LUS-C100-E_rt.

As previously observed, the extraction of the masking agent using an acid solution is evidenced by the disappearance the C-H stretching bands and preservation of the grafted organosilyl species with unmodified Si-C stretching band intensities. In addition, the decrease of intensity of the Si-OH stretching band in the range 938-964 cm^{-1} is corresponds to a higher EBDMS grafting rate in relation with the extent of masking produced by TMA or CTA. Indeed, the fully extracted LUS-C(T)100 materials exhibit the most intense band associated to EBDMS. Moreover, the broad band of O-H stretching in the 2800-3400 cm^{-1} range diminishes to almost no absorption from LUSC0(TMA)-E_rt-OH to LUS-C(T)100-E_rt-OH in agreement with a complete silylation of all IR-detectable silanol group (Figure 14A-B, c-f).

4.3.2 Chemical characterization

The weight loss of EBDMS modified LUS-T50-E_rt and LUS-C50-E_rt materials are shown by the TG/DTG curves (Figure 15). LUS-C50-E_rt exhibits TG-DTG curves with 22.93 wt% loss in 150-300 °C range to be compared with 15.33 wt% before grafting for LUS-C50 for a higher temperature. As stated before for EBDMS grafting at 80°C, this is related to a rearrangement of the electrostatically retained CTA^+ cations likely due to the removal of the CTA ammonium not retained by silanolate SiO- groups and remaining in the channel as void filling agent under the form of a CTATos (Figure 15A, a-b). This is also consistent with less organic matter despite the grafting with respect to the smaller weitgh loss at 1000°C. When the TMA is the masking agent there is no excess of TMA^+ in comparison of SiO^- groups and consistently, no loss of TMA was observed during grafting with respect to the weight in the 120-300°C range (5.37% weight loss after grafting in LUS-T50-E_rt for 5.62 wt% before grafting in LUS-T50; (Figure 15B, a-b). In this case, the gain of organic matter can be evidenced by the weight loss at 1000 °C which is consistently larger.

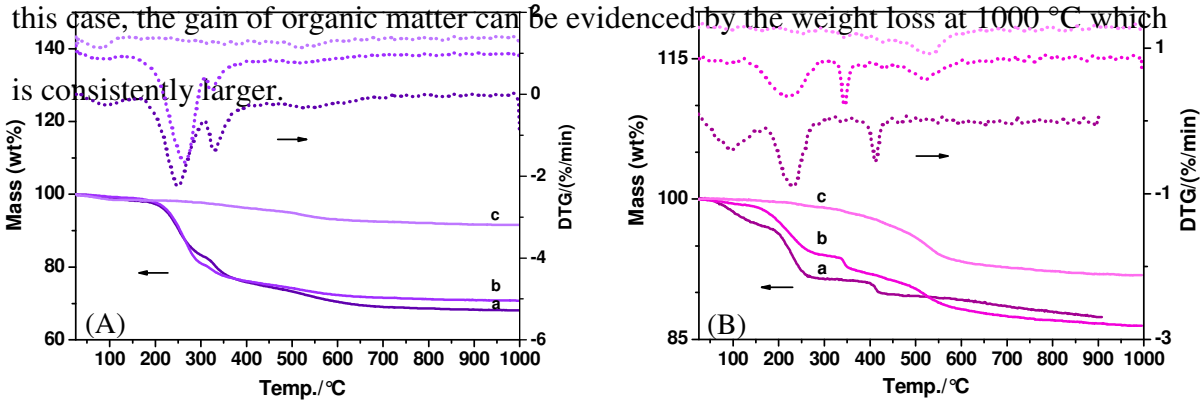

Figure 15 TG-DTG traces of materials functionalized by EBDMS at room temperature with (A) CTA^+ and (B) TMA^+ as protecting group. In (A): a, LUS-C50; b, LUS-C50-E_rt; c, LUS-C50-E_rt-OH; In (B): a, LUS-T50; b, LUS-T50-E_rt; c, LUS-T50-E_rt-OH.

Elemental analysis has also been performed to compare EBDMS grafting at R.T. versus 80 °C (Table 5). The N/Si atom ratio calculated from N wt% show that the ammonium mask resists at RT as well as at 80°C which is logical for a lower temperature.

Table 5 Elemental analysis of materials via sequential EBDMS grafting

Entries	Samp.	CTA^+				TMA^+			
		N/Si[c]		EBDMS/$Si_{tot.}$ *(LUS-Cx-E_rt-OH)*		N/Si[c]		EBDMS/$Si_{tot.}$ *(LUS-Cn-E_rt-OH)*	
		LUS-Cx	*LUS-Cx-E_rt*	C (wt%)	Si_E/Si_{tot}[d] (*coverage %*)[e]	*LUS-Tx*	*LUS-Tx-E_rt*	C (wt%)	Si_E/Si_{tot}[d] (*coverage %*)[f]
1[a]	0	0.150	0.097	6.10	0.012 (*57*)	0.102	0.095	4.66	0.09 (*36*)
2[b]	0	0.150	0.105	6.58	0.013 (*57*)	0,102	0.099	7.84	0.015 (*68*)
3[a]	50	0.068	0.070	7.10	0.013 (*62*)	0.054	0.048	9.99	0.019 (*76*)
4[b]	50	0.068	0.065	7.91	0.015 (*65*)	0.056	0.036	9.33	0.017 (*77*)
5[a]	100	0.002	0.001	11.47	0.021 (*100*)	0.001	0.001	12.79	0.025 (*100*)
6[b]	100	0.002	0.002	11.84	0.023 (*100*)	0.005	0.003	11.74	0.022 (*100*)

a) grafting at 80 °C

b) grafting at 25 °C

c) molar ratio : N/Si = [(N wt%/14 g mol^{-1})]/(Si wt%/28 g mol^{-1})*100%

d) molar ratio: Si_F/Si_{tot} = [(C wt%/12 g mol^{-1})/3]/(Si wt%/28 g mol^{-1})*100%

e) The relative EBDMS coverage considering LUS-C100-E as 100% coverage reference

f) The relative EBDMS coverage considering LUS-T100-E as 100% coverage reference

Considering a grafting yield based on the carbon content, there is only little change in comparison with the grafting at 80°C when CTA^+ is the masking agent (LUS-Cx-E_rt°). The main change is a better retention of TMA during grafting as evidence comparing LUS-Tx-E_rt-OH with the LUS-Tx-E-OH. Consistently, the grafting yield is lower consistent with a better masking efficiency for TMA^+ at 25°C in comparison with 80°C. since no changes are found for CTA^+, the role of the long organic chain is

negligible other wise a higher masking efficiency would have been observed. Since the ammonium head is the main effect for CTA, and TMA^+ produces the same hindrance, the rational for a lower masking efficiency is likely due to the molecular dynamics. Indeed, TMA^+ is expected to move more freely than CTA and cover less efficiently the surface. A quantitative IR is necessary since it is more function specific than an overall chemical analysis that can be affected by solvent trapped in the material. The trend is depicted in figure 16 using as a probe, the IR band at 834 cm^{-1}, which is a local vibration mode of the [$SiOC_3$] units characterizing silicon atoms of EBDMS. Both types of ammonium masking and both temperatures of grafting are compared.

As before, the quantification is based on the normalized intensity of IR peak at 834 cm^{-1}. There is systematically less grafting at room temperature than at 80°C. The difference is the largest when the ammonium is not extracted. Therefore, one cannot invoke the steric hindrance of the CTA^+ long chain since the effect is observed with the same amplitude when TMA^+ is the masking agent for none partially extracted samples (LUSC0-E-OH or LUS-T0-E-OH). Finally, FT-IR quantification confirms that the masking efficiency increases for TMA^+ at room temperature. The FT-IR quantification that is function provides a much better evaluation of the grafting yield shows that TMA is still a not as good as CTA for masking the surface particularly when the ammonium masking coverage is set at 50%. A better insight on the binding mode of EBDMS is required as above and was investigated also using ^{29}Si Solid State NMR.

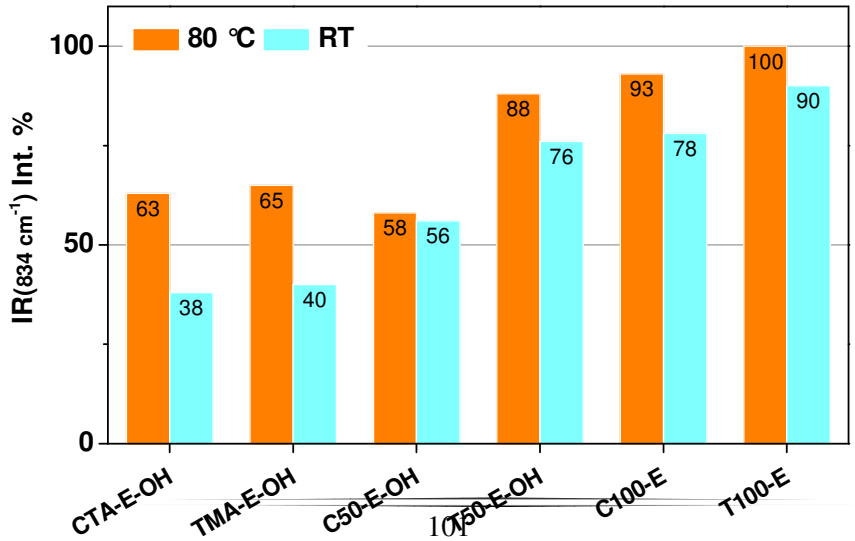

Figure 16 Evolution of the normalized IR band at 834 cm^{-1} depending on the nominal masking level and the type of ammonium after EBDMS grafting at 25 or 80 °C and mask removal.

Figures 17 and 18 depict the ^{29}Si NMR spectra of materials grafted at room temperature without extraction of the masking ammonium or after a nominal extraction of 50%. The materials exhibit very similar spectra than those obtained for materials grafted at 80°C. The simulation of the different peaks was also performed according to the same technique. Both M_1 and M_1" signals are indeed observed before extraction of the masking ammonum and M_0 signal appears after extraction at the expense of M_1". As expected, the

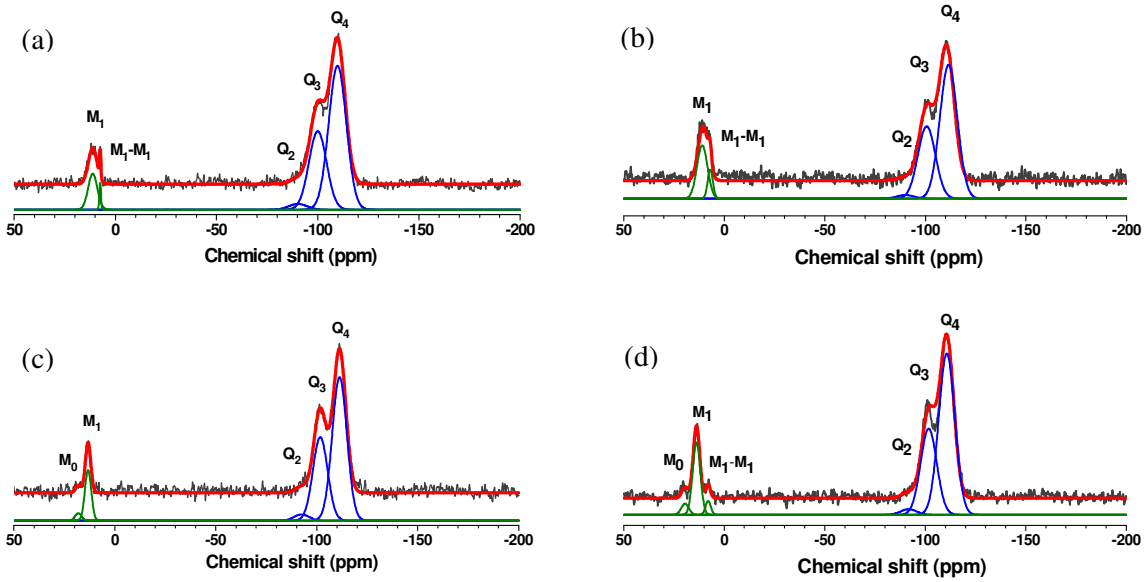

Figure 17 ^{29}Si MAS NMR spectra of the materials (a) LUSC0-E_rt, (b) LUS-T0-E_rt, (c) LUSC0-E_rt-OH, (d) LUS-T0-E_rt-OH; M1-M1 stands M_1" at at 7 ppm at the right hand side of the M_1 signal.

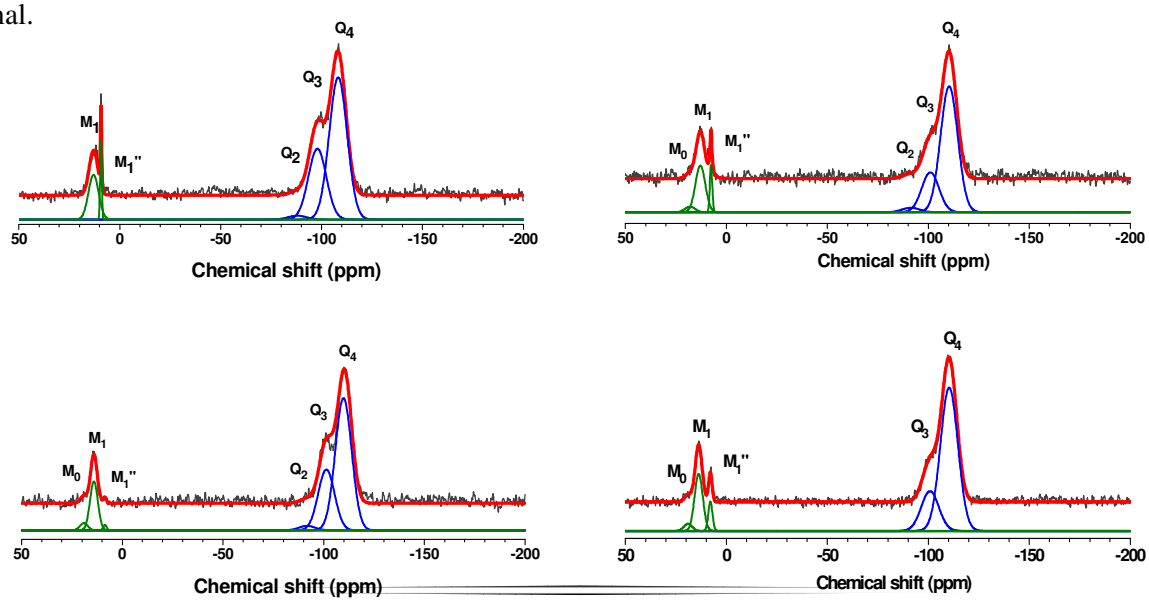

Figure 18 ^{29}Si MAS NMR spectra of materials (a) LUS-C50-E_rt, (b) LUS-T50-E_rt, (c) LUS-C50-E_rt-OH, (d) LUS-T50-E_rt-OH.

same E1, E1-E1 and E2 species are all present. The same trend is also observed upon ammonium extraction. Sole the relative concentration of species are different in some cases particularly when the surface is partially masked by TMA.

Table 6 Percentage of Q_n, M_n obtained from ^{29}Si NMR and related grafted species after different grafting steps and for different masking coverages by CTA^+ or TMA^+ for grafting at 80°C

Entries	Sample	Q_2	Q_3	Q_4	Si_{inorg}	M_1	M_0	M_1''	Si_{org} [a]	E2% [b]	E1% [c]	(E1-E1)% [d]
1	LUS-T100	3[e]	36	61	*100*	—	—	—	—	—	—	—
2	LUS-C100	6	40	54	*100*	—	—	—	—	—	—	—
3	LUS-C0-E	0	31	60	*91*	8	0	1	*9*	*88*	*0*	*12*
4	LUS-C0-E-OH	2	32	56	*90*	7	1	0	*8*	*75*	*25*	*0*
5	LUS-T0-E	1	29	53	*83*	13	0	4	*17*	*69*	*0*	*31*
6	LUS-T0-E-OH	2	29	54	*85*	12	2	1	*15*	*64*	*28*	*8*
7	LUS-C50-E	2	28	57	87	10	0	3	13	*70*	*0*	*30*
8	LUS-C50-E-OH	2	27	60	*89*	11	2	1	*14*	64	29	7
9	LUS-T50-E	2	20	59	*81*	13	0	5	*18*	*62*	*0*	*18*
10	LUS-T50-E-OH	0	19	64	*83*	11	2	4	*17*	*38*	*31*	*31*
11	LUS-C100E	2	18	61	*81*	12	7	0	*19*	*26*	*74*	*0*
12	LUS-T100E	1	16	62	*79*	14	6	1	*21*	*35*	*60*	*5*

a, percentage of Si_{org} obtained from $P_{Siorg} = \Sigma P_{Mi} = P_{M0} + P_{M1} + P_{M1''}$

b, percentage of E2, $P_{E2} = 100 \times (P_{M1} - P_{M0} - P_{M1''}) / [P_{M0} + P_{M1}]$; percentage of M1 type of signal belonging to E2 is proportional to $P_{M1}(E2) = P_{M1} - P_{M0} - P_{M1''}$,i.e., $P_{E2} = k \cdot P_{M1}(E2) /2$ ($k = 200/[P_{M0} + P_{M1}]$ according to $\Sigma P_{Ej} = P_{E2} + P_{E1} + P_{E1\text{-}E1} = 100$ and to P_{E1} and $P_{E1\text{-}E1}$ expressions provided in c and d (notice that E2 possesses 2 S_{iorg})

c, percentage of monografted $P_{E1} = 200 \times M_0 / [P_{M0} + P_{M1}]$; $P_{E1} = k \cdot P_{M0}$

d, percentage of dimer $P_{E1\text{-}E1} = 100 \times M_1'' / [P_{M0} + P_{M1}]$; $P_{E1\text{-}E1} = k \cdot P_{M1''}/2$
e, Analytical integral error by noise of baseline (± 2)

Concerning species E1-E1 characterized by the signal M_1'' it disappears completely after ammonium extraction when CTA is the masking agent (Figure 17 c) which is not the case when TMA is the masking agent. After extraction, the M_1'' signal is broader as already observed after grafting at 80°C and this is also assigned to grafted dimers (Figure 17 d). Therefore, some non-grafted dimers are removed and some are grafted (if not grafted already) as observed when the grafting temperature is 80°C. A quantitavive ^{29}Si NMR investigation was done to further comment the transformation of the grafted species on the surface under the ammonium extracion and reported in Table 6.

At first sight, it appears that the surface masking properties of CTA are not much affected by the grafting temperature while obvious differences are observed for TMA. A thorough synthesis of the data provided in Table 3 and 6 is needed to get a better insight on the subtle effects. First, the quantitative NMR analysis shows that extraction of the masking ammonium causes a systematic though rather small loss of Si_{org} species (10 to 15% at most) whatever the grafting temperature. The rational is the loss of a part of the free rotating and non-grafted species dimers during extraction of the masking ammonium. in both CTA and TMA masked surfaces for grafting performed at 25°C. When TMA is the masking agent, there is apparently more grafted dimeric species that remains grafted after removal of the masking ammonium. This is more obvious for grafting at 80°C than for grafting at 25°C where both CTA of TMA produces very similar distribution of species with the stricking exception of LUS-T50. Indeed, the latter materials is the only one that exhibit a high yield of grafted dimers E1-E1 (LUS-T50-E-OH, Table 6, entry 10). This is not related to the large quantity of non-grafted dimers before extraction since LUS-T0-E with similar dimer concentration yield a LUST0-E-OH relatively poor in E1-

E1 grafted species (8 for 31% for the former, Figure 17d & 18d). Moreover, a higher content of dimer after removal of the mask support the idea that part of the grafted dimers are generated from bigrafted E2 species as suggested before looking at the distribution of species in LUS-T0-E-OH and LUS-T50-E-OH grafted at 80°C in Figure 10 d, table 3, entries 8 & 12 of Table 3). Therefore, it appears that at half coverage, the masking properties of TMA is les effective than at full coverage with respect to the quantity of grafted dimers. In a lesser extent, this is also true for CTA. This can be rationalize rather by the mobility of the ammonium heads that is higher for TMA than CTA and higher at 80°C than 25°C.

All the characterization techniques applied here show consistently that EBDMS can be grafted at room temperature and the molecular stencil patterning using ammonium masking agent can be applied using either CTA and TMA. It appears that the masking properties of TMA are improve at low temperature and approach those of CTA ammonium as masking agent. Previous data clearly show that the long chain of CTA is not acting via its potential steric hindrance since for monopodal TMS there is no difference between TMA and CTA masking effect.[34] Therefore, the a dipodal siloxyl moieties like EBDMS make a difference because it moves away TMA^+ more easily than CTA^+ as evidence with a higher grafting yield than monopodal grafting but also from its capacity to generate E1-E1 grafted pairs. Nonetheless it is demonstrated that TMA can be successfully used as masking agent if the grafting temperature is lowered (Scheme 3A). A too dynamic molecular mask favors the formation of grafted pairs. The very low content of grafting dimers in absence of masking agent reveals that despite the mobility at half masking coverage there is still a surface confinement that favors dimers grafting versus monomer digrafting.

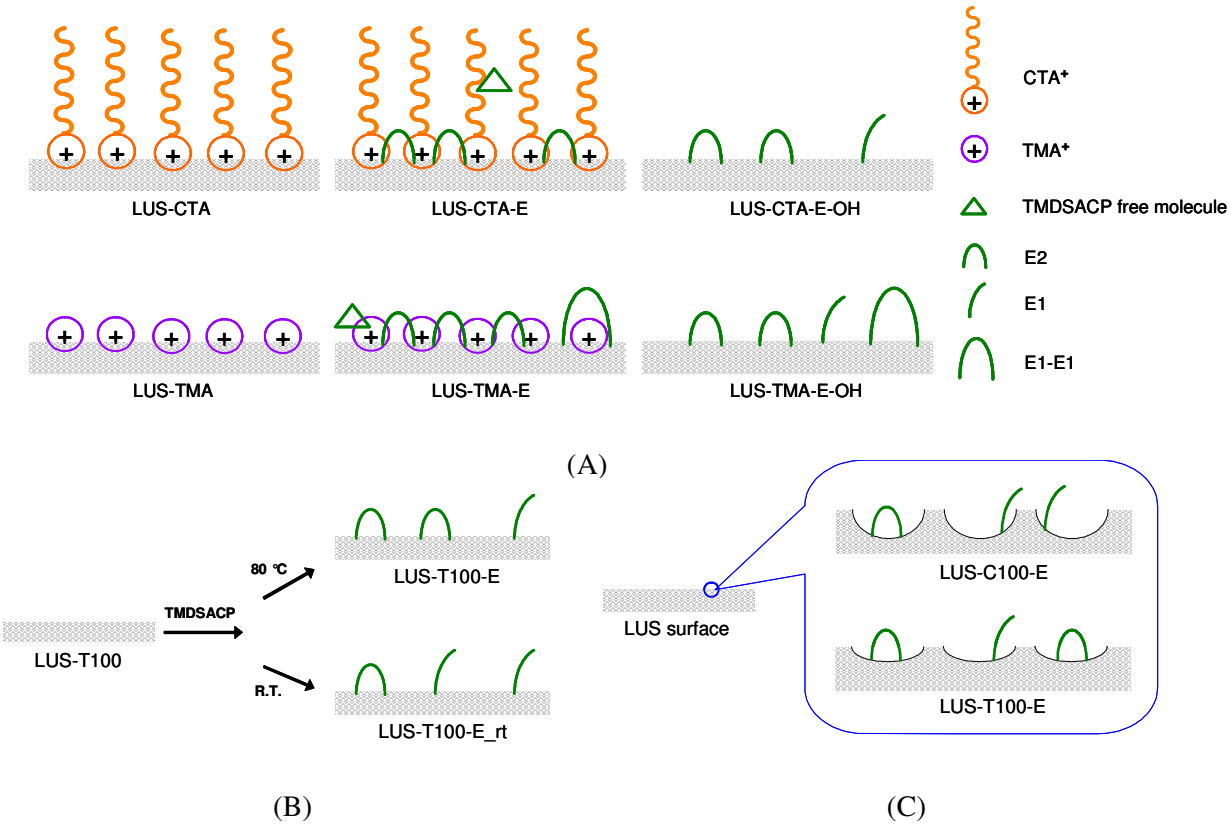

Scheme 3 Three effects of (A) template, (B) silylation temperature and (C) silica surface property on the grafting of EBDMS.

It is shown also that the temperature of grafting and the nature of the masking ammonium agent can be used to tune the distribution of grafted species (Scheme 3B). More grafted species are favoured at high temperature formation of grafted pairs is favored by TMA at intermediate masking coverage. As a consequence, dipodal EBDMS provides novel grafting possibilities for grafting a second function in comparison to monopodal capping agent like TMS. The size of the surface silanol patches that remain for further grafting should scale the size of the ammonium head that is about 0.7 nm

diameter. The effect of the molecular roughness of the surface that is close to such very small islands remains an open question. Nonetheless, to go further in the design of a catalysts, the effect of such novel surface on the nuclearity of grafted Ti species has been investigated below.

4.4 Incorporation of Ti into mesoporous silica (LUS-E-Ti-n & LUS-Ti-n)

4.4.1 Characterization

The Ti amount in the final material was checked by elemental analysis and the coordination of Ti sites in the solid samples was characterized by DR-UV spectroscopy without any pre-treatment.

Twelve different Ti catalysts were generated starting from LUS-T50-E-OH treated with various amounts of Ti(O-*i*Pr)$_4$ in an excess of solvent cyclohexane for 16 h, noted LUS-E-Ti-*n*. The Ti amount in the final material ranges from 0.6 to 5.5 wt %, which corresponds to 0.0082 and 0.086 Ti/Si molar ratio, respectively (Table 7, entries 1-12).

For comparison, eight catalysts using unmodified mesoporous silica (LUS-T100) was prepared by incorporation of Ti(O-*i*Pr)$_4$ resulting in LUS-Ti-*n*, the Ti incorporation yield is total up to Ti/Si molar ratio of 0.2 (Table 7, entries 13-20). By contrast, on the mesoporous silica modified by EBDMS grafting, LUS-E-Ti-*n*, the maximum incorporated was found for Ti/Si = 0.08 (Table 7, entry 8). At this step also, EBDMS functions were not removed, as shown by ^{29}Si NMR and by the IR according to the peak intensity at 833 cm^{-1}, which correspond to the Si-C stretching that remains unaltered (Figure 19). In addition, the shift of a local asymmetric stretching vibration mode of the [SiO_3(OH)] units from 964 down to 935 cm^{-1} usually assigned to the formation of [SiO_3(Ti)] unit where at least one Si-O-Ti covalent bridge is formed. This is consistent with a direct bonding of the metal to surface accessible silanol groups.

Again, nitrogen sorption isotherms are consistent with a preserved channel structure with a characteristic sharp adsorption step typical of such mesoporous silica after the titanium grafting. Consistently with the titanium incorporation, a decrease of specific surface, pore volume and pore diameter was observed (Table 8, LUS-E-OH and LUS-E-Ti-n). Furthermore, the Ti incorporation followed the same trend with an increasing effect

Table 7 Ti content in the initial gel and in the final solid, UV characteristics of LUS-E-Ti-n and LUS-Ti-n series of materials.

Entries	Sample	Ti/Si			γ_{max}/nm[c]	γ_{infl}/nm[c]
		Solution[a]	Solid[a]	Solid [b]		
1	LUS-E-Ti-1	0.009	0.008	0.58	217	257
2	LUS-E-Ti-2	0.017	0.015	1.0	223	266
3	LUS-E-Ti-3	0.019	0.018	1.27	222	264
4	LUS-E-Ti-4	0.038	0.033	2.26	235	272
5	LUS-E-Ti-5	0.062	0.065	4.27	251	295
6	LUS-E-Ti-6	0.080	0.078	5.08	256	300
7	LUS-E-Ti-7	0.081	0.086	5.51	255	299
8	LUS-E-Ti-8	0.10	0.083	5.43	259	305
9	LUS-E-Ti-9	0.12	0.046	3.1	242	276
10	LUS-E-Ti-10	0.12	0.045	3.01	238	273
11	LUS-E-Ti-11	0.20	0.035	2.45	237	272
12	LUS-E-Ti-12	0.33	0.033	2.3	234	271
13	LUS-Ti-1	0.002	0.003	0.17	250	275
14	LUS-Ti-2	0.005	0.007	0.46	248	280
15	LUS-Ti-3	0.01	0.012	0.84	251	285
16	LUS-Ti-4	0.02	0.024	1.55	253	288
17	LUS-Ti-5	0.04	0.049	3.01	253	287
18	LUS-Ti-6	0.10	0.105	5.85	255	290
19	LUS-Ti-7	0.20	0.216	10.65	264	304

20	LUS-Ti-8	0.30	0.150	8.67	255	299

a) Molar ratio; determined in the solid by elemental analysis, accuracy ± 0.001

b) Ti loading in wt% including both organic and inorganic matter

c) λ_{max} wavelength at band maximum or λ_{infl} at inflexion point as shown in Figure 21A

for higher metal loading (Table 8, LUS-E-Ti-n (n = 3-4, 8)). In the ^{29}Si MAS NMR spectra, apparently some of the monografted and dimeric species disappear at the expense of digrafted ones. The rational is likely that Ti may bind both silanol groups of the silicasurface and those of the pending monografted EBDMS, E1 (Table 8, E1%, E2%). Similarly, the decrease of the grafted dimeric species, E1-E1, can be explained by Si-O-Si opening and formation of Ti-O-Si bridges (Table 8, E1-E1%). This evolution is in consistent with the Ti loading (3.5 mol%) and the quantity of grafted EBDMS implied (~ 2 molar %).

Within the measurement accuracy (± 5%), a total yield of Ti incorporation is observed up to the maximum of *ca.* 0.08 and 0.21 Ti/Si molar ratios for organically modified and for the unmodified supports, LUS-Ti-n and LUS-E-Ti-n, respectively (Figure 20). This is consistent with a 68% decrease access to free silanol species on organically modified surfaces, consistent with the organic surface coverage of 71% (Table3, entry 10). Strikingly, for higher Ti concentration in solution, the Ti incorporation decreases drastically instead of reaching a plateau. This is a fingerprint of a drastic decrease of surface accessibility. Since the structure has not collapsed, the rational is a fast deposition of titanium at the channel entrance favoured by high Ti concentration resulting in pore plugging and strong diffusion limitation for the titanium precursor. Nonetheless, the channel blockage occurs at higher Ti loading when the surface presents higher Ti incorporation capacity showing that both diffusion and grafting rates a comparable .

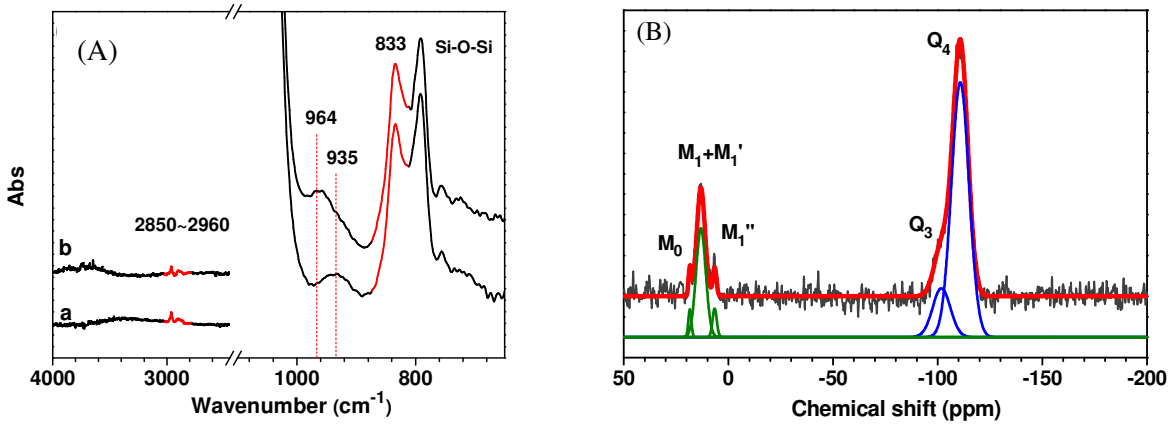

Figure 19 (A) FT-IR spectra of materials (a) LUS-E-OH, (b) LUS-E-Ti-11and (C) ^{29}Si MAS NMR of LUS-E-Ti-11. Normalized intensity of 833 cm^{-1} ν_{Si-C} peak: (a) 0.28 ± 0.01, (b) 0.31 ± 0.01.

Table 8 textural analysis, Ti , Si_{org} contents and grafted species distribution in materials LUS, LUS-E-OH and LUS-E-Ti-n

Sample	Ti/Si[a]	S_{BET}[b] ($m^2\ g^{-1}$)	V_p[c] ($cm^3 g^{-1}$)	D_{BdB}[d] (nm)	Si_{org}/Si_{inorg}[e]	E1%[f]	E2%[g]	E1-E1%[h]
LUS-E-OH	—	644	0.51	3.27	0.20	25	56	19
LUS-E-Ti-3	0.018	621	0.48	3.17	—	—	—	—
LUS-E-Ti-4	0.033	600	0.46	3.13	0.20	35	53	12
LUS-E-Ti-8	0.083	582	0.43	3.11	0.20	30	61	9
LUS-E-Ti-11	0.035	603	0.46	3.17	0.21	32	53	15

a) Elemental analysis as in Table 2

b) accuracy ± 5%

c) total pore volume measured at $P/P_0 = 0.92$, accuracy ± 0.01

d) $Y = 14{,}60994 + 74{,}67812 * X + 81{,}96198 * X^2 + 155{,}8457 * X^3$, $X = P/P_0$ ($0.11 \leq P/P_0 \leq 0.45$), Y = pore diameter (in Å), accuracy ± 0.1

e-h) calculation made as in Table 3 and 6

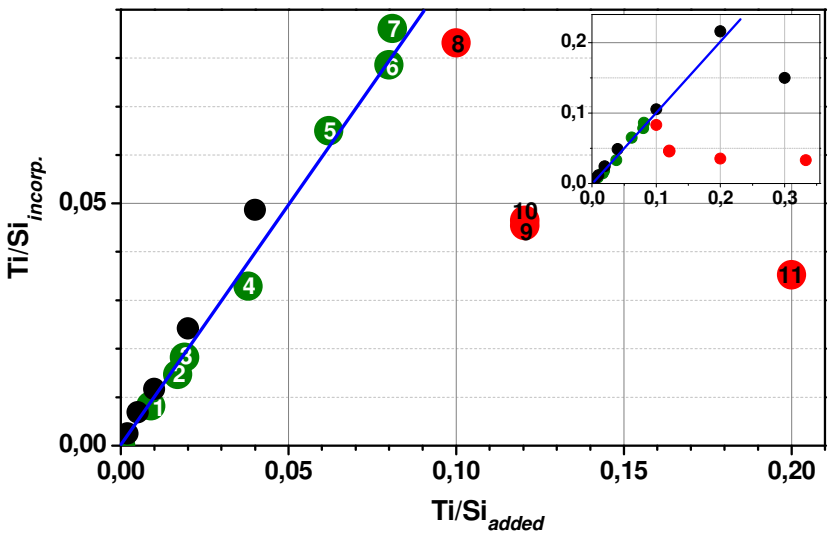

Figure 20 Correlation between Ti in the solution and Ti in the material for LUS-Ti-n (black circle) and LUS-E-Ti-n (green and red circles) materials; numbers refer to n of the sample name. Inset for full scale. The blue straight line stands for 100% yield Ti incorporation.

In addition to a much lower capacity for grafting Ti(*i*PrO)$_4$, the oxide deposits exhibit very different UV characteristics depending on titanium and the type of surface. For equivalent Ti loadings, the UV band is much more red shifted on the unmodified surface up to the maximum loading incorporation pointed above (Figure 21). For instance compare LUS-E-Ti-1 (Ti/Si = 0.009) with LUS-Ti-2 (Ti/Si = 0.005) (Figure 22A). LUS-E-Ti-1 and LUS-E-Ti-3 are characterized by bands centred at 217 and 222 nm, respectively (Figure 21A, a-b; Table 7, entries 1 and 3). With the similar Ti loading on unmodified surface, LUS-Ti-2 and LUS-Ti-4 display boarder spectra with maximum

absorption centred at 248 nm and 253 nm, respectively (Figure 21B, f-g; Table 7, entries 2 and 4).

Moreover, the red shift increases when the Ti content increases in both series (Figure 22B). Then, a similar band position is reached at much higher Ti loading on organically modified with LUS-E-Ti-5 (Ti/Si = 0.0 65) or LUS-E-Ti-9 (Ti/Si = 0.046) with a loading that is ca. 10 times larger (Figure 22A, Table 7, entries 5, 9 & 14). Then the band positions converge towards similar values at maximum incorporation in LUS-E-Ti-8 Ti/Si = 0.0083 or 5.43 wt% Ti) and LUS-Ti-7 (Ti/Si = 0.216 or 10.65 wt% Ti; see Figure 22B).

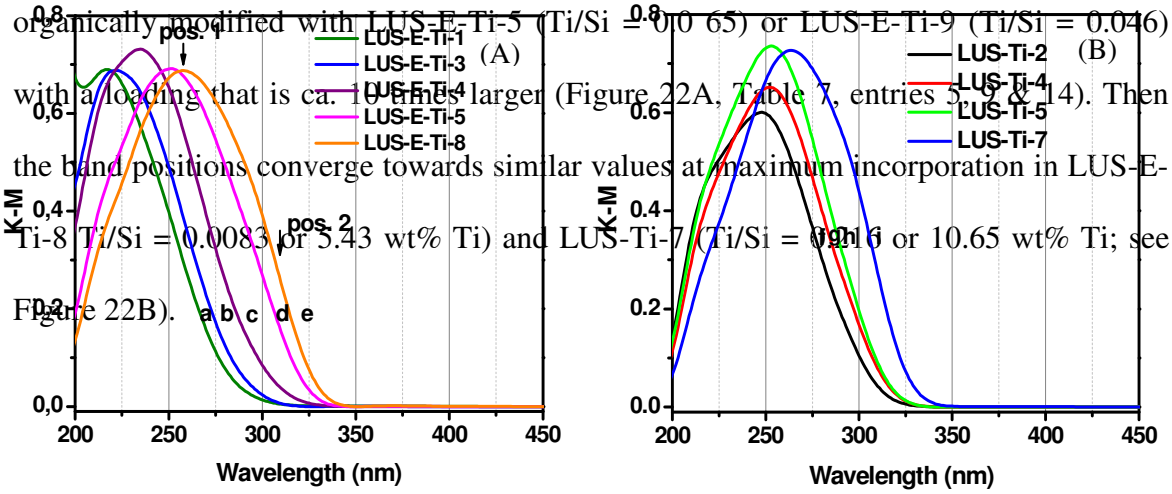

Figure 21 UV-vis spectra for (A) LUS-E-Ti and (B) LUS-Ti with incorporated Ti/Si ratio of (a) 0.0082 (0.58 wt%), (b) 0.0180 (1.27 wt%), (c) 0.0323 (2.26 wt%), (d) 0.0628 (4.27 wt%), (e) 0.0831 (5.43 wt%), (f) 0.0072 (0.46 wt%), (g) 0.0240 (1.55 wt%), (h) 0.0487 (3.01 %), (i) 0.2160 (10.65 wt%), respectively. Note that all the curves fall into the same range of intensity expressed according to the Kubelka-Munk theory developed for quantitative exploitation of diffuse reflectance spectra; this was obtained by trial and error dilution of the solid (see experimental part).

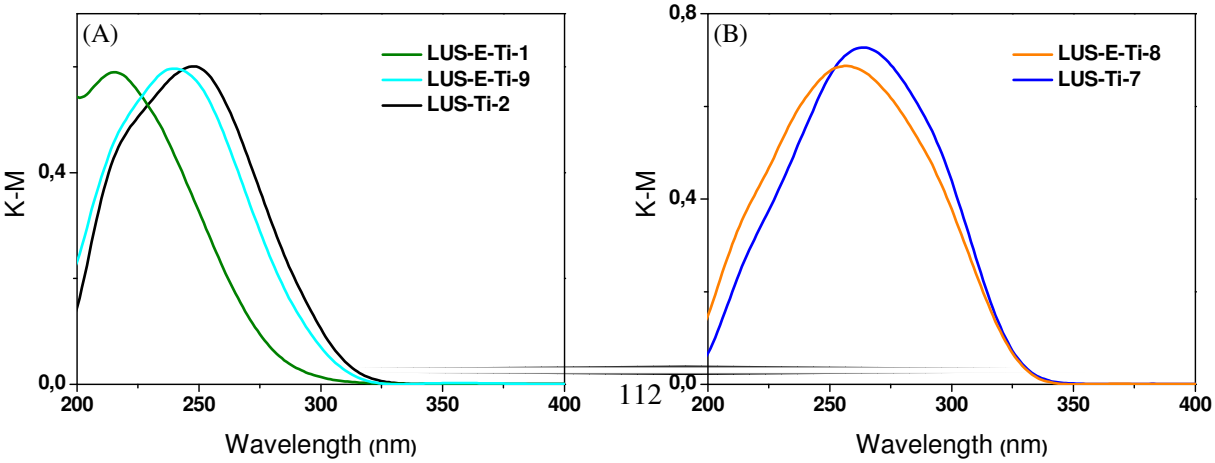

Figure 22 UV-vis spectra for (A) the similar Ti incorporation loading and (B) the same UV-vis spectra for the different Ti incorporation loading on the LUS-TiPr and LUS-E-TiPr.

Another general feature of the spectrum is the shape that is not purely Gaussian nor purely Lorentzian. Its deformation upon increasing Ti loading denotes the presence of a mixture of several species with different spectral characteristics. This has been observed in the literature where the red shift has been described by mere increase of coordination number in TS-1 materials.[35] In monomeric species like in metal complexes these UV bands are related to the so-called ligand to metal transition, LMCT. The band is blue shifted particularly for strong ligands or short bond lengths; this is the case for tetrahedral species. A red shift is expected for octahedral species since its generate longer bonds. In addition, bridged ligand, like oxo O^{2-} ligand in oxides, provides even longer bond lengths. When the number of metal centers in an oxide cluster increases for larger clusters, the number of molecular orbitals increases and the LUMO-HOMO energy splitting decreases leading to lower LMCT transition progressively evolving towards physicist call the band gap characterized at the inflexion point (position 2 in Figure 21). Then, the red shift is even more pronounced when TiO_2 oxide clusters are present and further increases when the size of these cluster increases up to the position of bulk TiO_2 arising at 330-350 nm (effect known as the quantum size effect).[36] Here, the band at 200 nm are assigned to tetrahedral Ti site like in TS-1.[35] Monomeric species pentahedral or octahedral ones may lies in the 250 range but other band belong to dimers where hydroxo or oxo bridges are at stake or eventually to larger clusters. Nonetheless, The absence of absorption above 325 nm precludes the existence of bulk TiO_2.

Therefore here the variation of the UV absorption, is interpreted as a fingerprint for the formation of dimeric or other higher oligomeric Ti(IV) species. To better visualized the trend the shift of the wavelength at the peak maximum (position 1) as well as the peak at the inflexion point (position 2) are provided in Figure 23. Knowing that there is a mixture of species, position 1 will better probe the center of the distribution of species in terms of size and coordination while position 2 will be more sensitive to the largest TiO_2 clusters. Consequently, according to the position 1 below Ti/Si = 0.05, more octahedral site and larger oligomers are formed on the silica free surface (LUS-Ti-n series). By contrast, more monomeric tetra-, and penta- and hexacoordinated Ti sites are formed in the in LUS-E-Ti-n The proportion of which is more sensitive to the Ti Loading (Figure 23A). Note also that above the maximum Ti incorparation, the average TiO_2 cluster size decreases since the loading decreases. The position of the maximum is very slightly red shifted in comparison with the materials obtained with comparable Ti loading and obtained with less Ti in solution (LUS-E-Ti-n, n = 11 &12 in comparison to LUS-E-Ti-4, with a Ti/Si molar ration of *ca.* 0.033, i.e., 2.3 Wt% Ti).

The most sensitive position for clustering is position 2 as anticipated above. Figure 23 B depicts the trend extracted from the inflexion point. As expected, this is close to the maximum of Ti incorporation that differences are evidenced. Indeed, one observed a higher red shift for the organically modified surface in LUS-E-Ti-n, n =5-8 while for the same loading the free surface is far from saturation. The shift for both surface is maximum and the same at the saturation for LUS-E-Ti-8 and LUS-E-Ti-7 for Ti/Si = 0.0083 and 0.216 (i.e., for 5.35 and 10.65 wt%Ti).

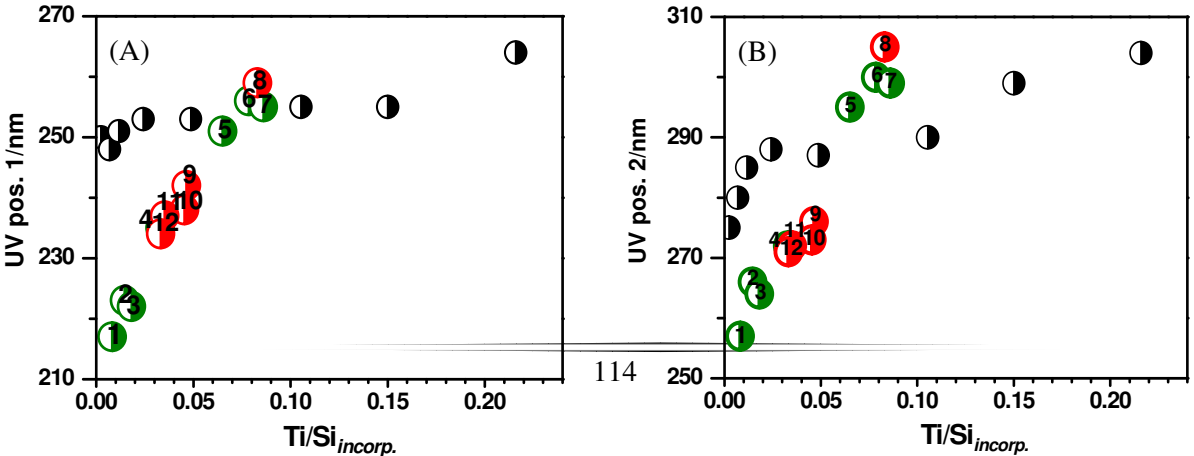

Figure 23 The relevance between the incorporation amount of Ti and UV absorption at (A) pos. 1 and (B) pos. 2 (black circle: LUS-Ti-n; green and red circles: LUS-E-Ti-n).

In conclusion, capping of the silica surface inside the channels using EBDMS as capping agent and the MSP technique to reach a patterned organic coverage of ca. 70% leads to new surface for grafting metal ions such as titanium. In comparison to non-capped surface, a much higher metal dispersion, i. e., high concentration of monomeric Ti sites, are obtained for metal loadings smaller than 2.5 wt%Ti. To further probe these isolated sites that seems scarce on non-capped surface, reactivity of such materials were compared in catalytic epoxidation reaction known to run on isolated Ti sites.

4.4.2 Catalytic reaction

Expoxidation of cyclohexene in CH_3CN was performed on materials LUS-E-Ti-n and LUS-Ti-n using *t*-butyl hydroperoxide (TBHP 30 wt% in water) as oxidant. These conditions were chosen to better probe the hydrophobic surface generated in the present series of materials.

The epoxidation generate the cylohexane-1-2-epoxide and the cylohexane-1-2-epoxidediol. The latter is obtained as a side hydrolysis reaction of the former. In addition, hydroxylation in beta position of the double bond (allylic position) produces 2-cyclohexen-1-ol and by consecutive oxidation 2-cyclohexen-1-one. Therefore, both activity (cyclohexene transformation) expressed in turnover number (TON after 2 hours) and selectivity in peroxide was ploted versus Ti/Si molar ratio in the catalysts (Figure 24). Green symbols are related to the LUS-E-Ti-n series modified using EBDMS while black symbols provides the catalytic characteristic of the free silica surface and all the data are available in Table 9.

The drastic decrease of TON per Ti for higher metal loading indicates that the proportion of active site decreases (Figure 24A). The minimum of catalytic activity is found at the maximum incorporation level for the EBDMS grafted surface. More precisely, the decrease is not linear showing that among the species certainly several are not active. In addition, when the Ti concentration is too high (Ti/Si > 0.08), the lower Ti loaded materials do not exhibit TON as high as the materials synthesized with the appropriate Ti concentration (Ti/Si < 0.08). This is fully consistent with the hypothesis that a lower yield of Ti incorporation for Ti/Si > 0.08 is due to diffusion problem that indeed should generate concentration profile and a larger distribution of grafted Ti species, i. e., less isolated active species; compare LUS-Ti-7 or LUS-Ti-8 that are *ca.* 40% less active than LU-E-Ti- 4 (Table 9, entries 3, 5 & 6). Confirmation of the UV investigation is further supported by the catalytic activity of materials synthesized without organic patterning.

Table 9 The TON and selectivity of epoxidation of cyclohexene on the Ti/Si incorporated ratios of LUS-E-Ti and LUS-Ti

Entries	Sample	Ti/Si_{added}	Ti/Si_{incorp}	Conv. (mol%)	TON (mol(mol-Ti h^{-1}))	Product selec. (mol%)		
						Epoxide[a]	Allylic[b]	Diols[c]
1	LUS-E-Ti-1	0.009	0.008	14.7	122	91	8	1
2	LUS-E-Ti-3	0.019	0.018	22.6	85	95	5	0
3	LUS-E-Ti-4	0.038	0.033	23.1	49	94	5	1
4	LUS-E-Ti-5	0.062	0.065	26.5	30	94	4	2
5	LUS-E-Ti-7	0.081	0.086	10.5	9	94	4	2
6	LUS-E-Ti-8	0.10	0.083	16.1	15	89	7	4
7	LUS-E-Ti-11	0.20	0.035	15.3	30	88	10	2
8	LUS-E-Ti-12	0.33	0.033	16.2	34	91	4	5
9	LUS-E-Ti-13	0.050	0.045	18.5	28	93	5	2
10	LUS-T50-Ti-E	—	0.044	3.9	8	79	20	2
11	LUS-Ti-1	0.002	0.003	1.5	41	46	54	0

12	LUS-Ti-2	0.005	0.007	2.3	24	66	32	1
13	LUS-Ti-3	0.01	0.012	2.1	12	72	26	2
14	LUS-Ti-4	0.02	0.024	2.7	8	80	18	3
15	LUS-Ti-5	0.04	0.049	7.4	12	82	12	6
16	LUS-Ti-6	0.10	0.105	5.9	5	89	7	5
17	LUS-Ti-7	0.20	0.216	10.8	5	73	10	16
18	LUS-Ti-8	0.30	0.150	5.4	3	72	16	11
19	LUS-Ti-9	0.050	0.047	5.5	9	47	50	3

a) Cyclohexene epoxide , b) 2-cyclohexen-1-ol and 2-cyclohexen-1-one, c) 1,2-cyclohexanediol and d) $Si_{org}/Si_{inorg} = 0.176$

Indeed, the drop down of activity observed at low Ti loadings (< 2.5 wt%) is so important that for similar Ti loadings of ca. 0.5 wt% Ti, in LUS-E-Ti-1 and LUS-Ti-2, the activity is about six times lower on the silica free of organic. This confirms the UV investigation showing that the organically patterned silica surface inhibit the formation of clusters.

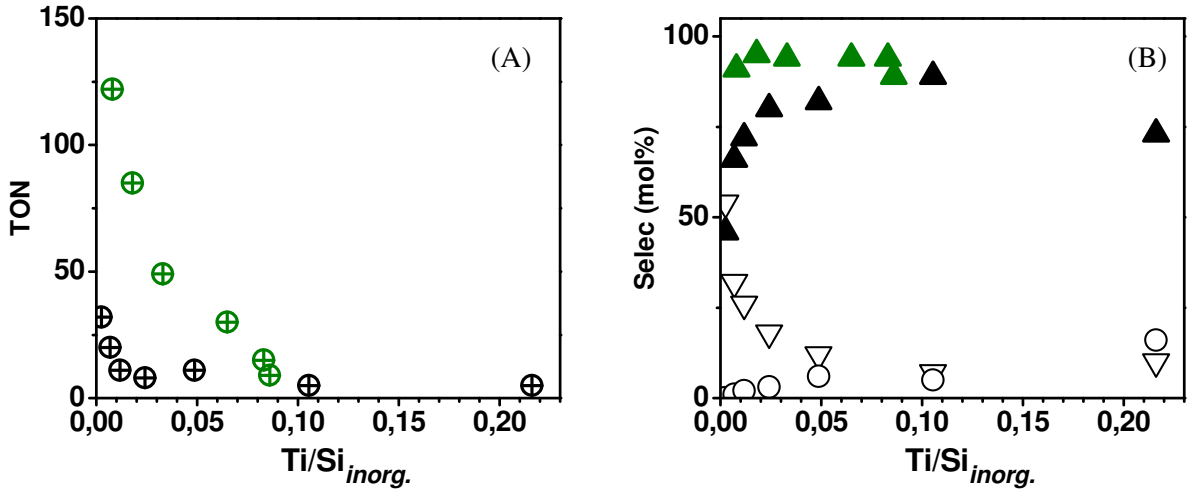

Figure 24 (A) The TON per Ti atom and (B) selectivity of epoxidation of cyclohexene on the Ti/Si incorporated ratios of LUS-E-Ti and LUS-Ti. In (A), green circles: LUS-E-Ti-n (n = 1, 3-5, 7-8); black circle: LUS-Ti-n (n = 1-7). In (B), green solid triangle: epoxide product on LUS-E-Ti-n; black solid triangle: epoxide product on LUS-Ti-n, black inverted triangles: allylic by-products on LUS-Ti-n, black circle: diol by-products on LUS-Ti-n.

It has been observed that inverting EBDMS and Ti graftings generates much less active catalysts for the same Ti loading; compare LUS-T50-Ti-E (Table 9, entry 10) with LUS-E-Ti-13 (Table 9, entry 9) that is *ca.* 5 times less active (Figure 25). Note that the EBDMS grafting upon a surface where Ti has been already grafted does not displace the grafted Ti species (LUS-T50-Ti; Table 9, entry 19). All these observations consistently support the idea that the patches of silanol groups are small enough to enforce site isolation upon Ti alkoxydes grafting.

In addition to conversion, selectivity is also affected be the grafting EBDMS partly due to the increase surface hydrophobicity. In fact in most of the case investigated here, hydrophobization using EBDMS capping moieties favours high selectivity into epoxide (> 90%) at relatively high conversion (up to 26 %) and high TON (> 30 % up to 120%) to the expense of hydroxylation in allylic position. By contrast, formation of diols (> 10%) is favours at relatively high Ti loadings (Ti/Si molar ratio > 15%) for rather low TON (< 11) showing that Ti clusters favours the formation of diol according to a rather low reaction rate.

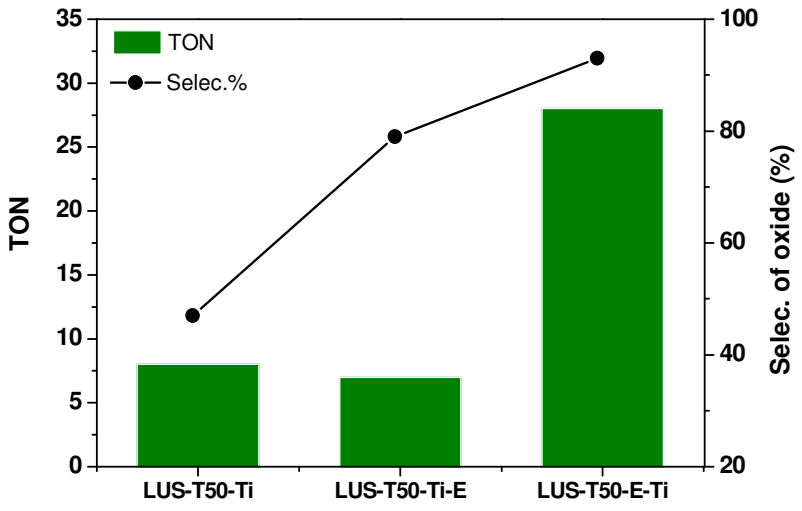

Figure 25 TON and selectivity in cyclohexene epoxidation on LUS-T50-Ti, LUS-T50-E-Ti and LUS-T50-Ti-E materials possessing *ca.* 0.5wt% Ti loading.

4.5 Conclusion

Using a convergence of proves based on different physical characterization techniques and the catalytic reactivity in cyclohexene epoxidation, it has been shown that the dipodal EBDMS organosiloxyl grafting is compatible with the molecular patterning technique like the monopodal tetramethylsiloxyl capping agent using both CTA or TMA as surface masking agents. The temperature of grafting and the nature of the masking ammonium agent can be used to tune the distribution of grafted species. More grafted species are favoured at high temperature formation of grafted pairs is favored by TMA at intermediate masking coverage. As a consequence, dipodal EBDMS provides novel grafting possibilities for grafting a second function in comparison to monopodal capping agent like TMS. The size of the surface silanol patches that remain for further grafting should scale the size of the ammonium head that is about 0.7 nm diameter. The subnano silanol islands of such organically modified surfaces favours site isolation of titanium during Ti(i-PrO)$_4$ alkoxide grafting. Much more active and selective epoxidation catalysts have been synthesized according to this technique. Nonetheless, the best catalysts still contains mixtures of species leaving some room for further improvement. In addition some clarification is needed on the participation of monografted EBDMS E1 species in the fixation of the Ti sited. This technique of dispersion can be applied to many other metals or non-metal as far as silanol are involved for covalent fixation of the element.

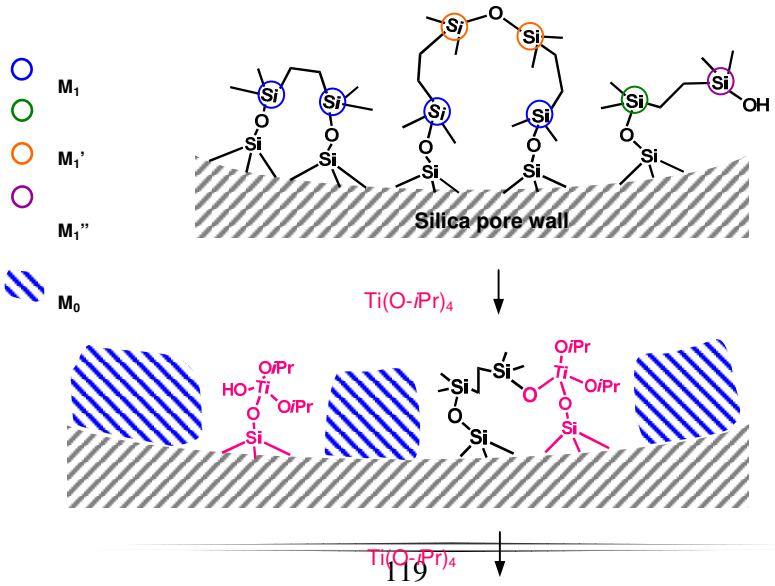

Scheme 4 Possible heterogeneous surface functionalized by EBDMS group and Ti species. M_1 and M_1'' refer to the Si signals observed in ^{29}Si-NMR.

4.6 Reference

1 B. Notari, *Adv. Catal.*, 1996, **41**, 253.

2 P. Wu, T. Tatsumi, T. Komatsu, T. Yashima, *J. Catal.*, 2001, **202**, 245.

3 L. Wang, Y. Liu, W. Xie, H. Zhang, H. Wu, Y. Jiang, M. He, P. Wu, *J. Catal.*, 2007, **246**, 205.

4 P.T. Tanev, M. Chibwe, T.J. Pinnavia, *Nature*, 1994, **368**, 321.

5 A. Corma, M.T. Navarro, J.P. Pariente, *J. Chem. Soc., Chem. Commun.*, 1994, 147.

6 W. Zhang, J. Lu, B. Han, M. Li, J. Xiu, P. Ying, C. Li, *Chem. Mater.*, 2002, **14**, 3413.

7 T. Maschmeyer, F. Rey, G. Sankar, J.M. Thomas, *Nature*, 1995, **378**, 159.

8 M.S. Morey, S. O'Brien, S. Schwarz, G.D. Stucky, *Chem. Mater.*, 2000, **12**, 898.

9 M. Guidotti, I. Batonneau-Gener, E. Gianotti, L. Marchese, S. Mignard, R. Psaro, M. Sgobba, N. Ravasio, *Microp. Mesop. Mater.*, 2008, **111**, 39.

10 T. Blasco, A. Corma, M.T. Navarro, J.P. Pariente, *J. Catal.*, 1995, **156**, 65.

11 A. Corma, M. Domine, J.A. Gaona, J.L. Jordá, M.T. Navarro, F. Rey, J. Pérez-Pariente, J. Tsuji, B. McCulloch, L.T. Nemeth, *Chem. Commun.*, 1998, 2211

12 T. Tatsumi, K.A. Koyano, N. Igarashi, *Chem. Commun.*, 1998, **3**, 325.

13 P. Wu, T. Tatsumi, T. Komatsu, T. Yashima, *Chem. Mater.*, 2002, **14**, 1657

14 N. Igarashi, K. Hashimoto, T. Tatsumi, *Microp. Mesop. Mater.*, 2007, **104**, 269.

15 R.R. Sever, R. Alcala, J.A. Dumesic, T.W. Root, *Microp. Mesop. Mater.*, 2003, **66**, 53.

16 A. Bhaumik, T. Tatsumi, *J. Catal.*, 2000, **189**, 31.

17 A. Bhaumik, T. Tatsumi, *Catal. Lett.*, 2000, **66**, 181.

18 N. Igarashi, S. Kidani, R. Ahemaito, K. Hashimoto, T. Tatsumi, *Microp. Mesop. Mater.*, 2005, **81**, 97.

19 J. Bu, H. Rhee, *Catal. Lett.*, 2000, **65**, 141.

20 J. Bu, H. Rhee, *Catal. Lett.*, 2000, **66**, 245.

21 W. Zhang, M. Fröba, J. Wang, P.T. Tanev, J. Wong, T.J. Pinnavaia, *J. Am. Chem. Soc.*, 1996, **118**, 9164.

22 D. Zhao, J. Sun, Q. Li, G.D. Stucky, *Chem. Mater.*, 2000, **12**, 275.

23 M. Iwamoto, Y. Tanaka, J. Hirosumi, N. Kita, S. Triwahyono, *Micropor. Mesopor. Mater.*, 2001, **48**, 217.

24 L. Barrio, J.M. Campos-Martín, M.P. de Frutos-Escrig, J.L.G. Fierro, Micropor. Mesopor. Mater., 2008, **113**, 542.

25 F. Bérubé, A. Khadhraoui, M.T. Janicke, F. Kleitz, S. Kaliaguine, *Ind. Eng. Chem. Res.*, 2010, **49**, 6977.

26 S.-Y. Chen, C.-Y. Tang, J.-F Lee, L.-Y. Jang, T. Tatsumi, S. Cheng, *J. Mater. Chem.*, 2011, **21**, 2255

27 L. Marchese, E. Gianotti, V. Dellarocca, T. Maschmeyer, F. Rey, S. Coluccia, J.M. Thomas, *Phys. Chem. Chem. Phys.*, 1999, **1**, 585.

28 A. Tuel, L.G. Hubert-Pfalzgraf, *J. Catal.*, 2003, **217**, 343.

29 F. Bérubé, B. Nohair, F. Kleitz, S. Kaliaguine, *Chem. Mater.*, 2010, **22**, 1988.

30 R. Anwander, I. Nagl, M. Widenmeyer, *J. Phys. Chem. B*, 2000, **104**, 3532.

31 C. Zapilko, M. Widenmeyer, I. Nagl, F. Estler, R. Anwander, G. Raudaschl-Sieber, O. Groeger, G. Engelhardt, *J. Am. Chem. Soc.*, 2006, **128**, 16266.

32 K. Zhang, B. Albela, M. He, Y. Wang, L. Bonneviot, *Phys. Chem. Chem. Phys.*, 2009, **11**, 2912.

33 M.A. Camblor; M. Costantini; A. Corma; L. Gilbert; P. Esteve; A. Martinez; S. Valencia, *Chem. Commun.*, 1996, 1339.

34 A.-R. Badiei, S. Cantournet, M. Morin, L. Bonneviot, *Langmuir*, 1998, *14*, 7087-7090.

35 D. Trong On, L. Le Noc and L. Bonneviot, *J. Chem. Soc., Chem. Comm.,* 299-300,1996

36 D. Trong On, S. Kaliaguine and L. Bonneviot, *J. Catal.,* 157, 235-243, 1995

Chapter V

Thermal Treatment of Organically Patterned surface and effect on subsequent grafting

5.1 Introduction

The molecule stencil patterning technique allows a post modification with vicinity control of multiple functions on the mesoporous silica surface. As we described in the «Chapter IV», a dipodal group 1-2-ethanebis(dimethylsilyl) (EBDMS) is less flexible in patterning thus leading to a difficulty in surface coverage control compared to the monopodal trimethylsilyl (TMS) group [1-4], but it is more stable to anchor on the silica surface and furthermore favours Ti site isolation. Nonetheless, a way to make the organic grafted layer on silica starting from TMS function is to create more linkage of the silicon atoms directly with the silica surface. This implies that Si-C bonds should be connected into Si-O bond in the grafted organic moieties. Moreover, the coverage can be more flexible in full range of ex. 25%, 50% and 75% according to the MSP technique [5]. TMS as to do, it is proposed in this chapter to investigate the effect on a controlled thermal treatment to benefit both of the controlled organic covering and the stable grafting.

Herein, the mesoporous silica functionalized by EBDMS or TMS are thermally treated at proper temperatures. A thermal gravity analysis (TGA) profile has curve table to find the appropriate temperatures. Therefore, the same temperature ramp as in TGA is applied to the samples up to the desired temperature then the temperature drops down. To check the effective stable of the organic grafted moieties, a set of FT-IR spectra as well as ^{29}Si MAS NMR in solid state is applied. A FT-IR spectra simulation profiles the evolution of Si-C and Si-O-Si bonds at different calcination temperatures with Gaussian function fitting independently for the bands which are assigned to the symmetric ν_{Si-C} and symmetric $\nu_{Si-O-Si}$, then those corresponding organic moieties can be identified and quantified by ^{29}Si MAS NMR. In order to probe the new isolated space opened by calcinations and the extra silanol groups converted from Si-C, a re-capping of EBDMS, TMS or Ti species has been applied.

5.2 Temperature of thermal treatment

The TG-DTG-DTA curves where the LUS-100E and LUS-100TMS change their mass within the heating temperature between 25-1000 °C supply the condition of post-thermal treatment (Figure 1). LUS-100E has two distinguished DTG peaks due to the weight loss at around 300 °C and 450-600 °C (Figure 1, blue solid line). The former is probably the thermo-decomposition of the cyclic dimer bridge (M_1"-M_1", Scheme S1) and methylene in the EBDMS group according to the results of ^{29}Si MAS NMR and ^{13}C CP MAS NMR (Chp. IV, Figure 2, A), thus characterized a sharp step, so-called thermal decomposition segment. While the latter displays broader resulting from the combustion of alkyl moieties, so-called combustion segment (Figure 1, black solid line). Moreover, a small exothermic peak occurs at 800 °C in the DTA curve for LUS-100E revealing a silica crystallization (Figure 1, red solid line). Accordingly, a choosing of calcination temperatures at 380 °C, 480 °C and 580 °C observes the convertion of EBDMS to the inorganic silica subsequently with a C-C bond cutting, Si-C bond oxidation to Si-OH, etc (Figure 1, arrows 1-3).

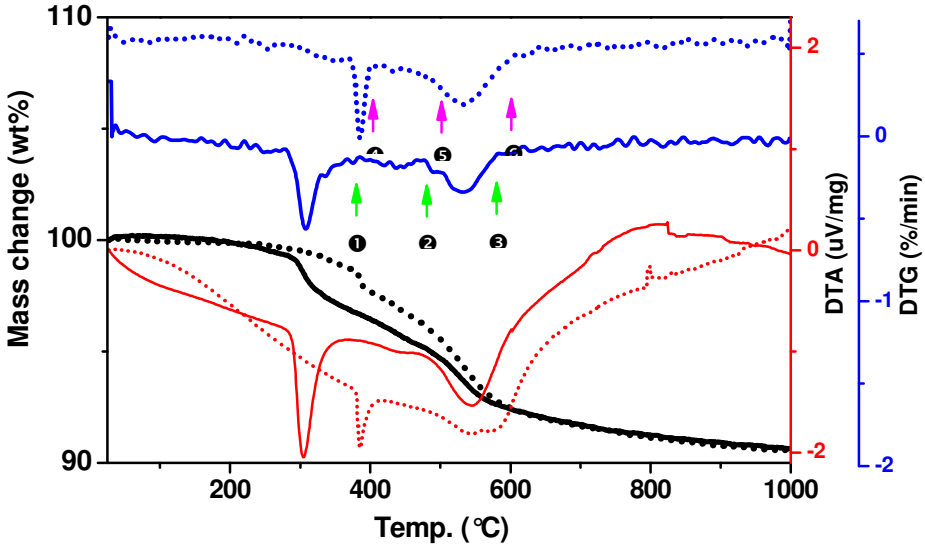

Figure 1 TG-DTA-DTG traces of LUS-100E (solid line) and LUS-100TMS (dot line). The arrows (1) 380 °C, (2) 480 °C, (3) 580 °C, (4) 400 °C, (5) 500 °C and (6) 600 °C; (1)-(2), (4)-(5): thermal decomposition segment; (2)-(3), (5)-(6): combustion segment.

LUS-100TMS has the similar TG-DTG curves (Figure 1, black&blue dot lines) that a sharp mass change step at around 380 °C probably due to the decomposition of free TMS molecule (Chp. IV, Figure 2, B). Nonetheless, a large endothermic peak is observed between 100-800 °C in the DTA curve corresponding to the unstable monopodal group compared to the EBDMS (Figure 1, red lines). Consistently, the temperatures at 400 °C, 500 °C and 600 °C are selected for the calcination of TMS modified materials to find a proper thermal point for both of organic covering and the stable grafting (Figure 1, arrows 4-6).

5.3 Characterization

5.3.1 Structure of material

The mesostructure of the solids after post-thermal treatment is checked at each step of the synthesis using X-ray diffraction and nitrogen sorption isotherms. For instance, XRD pattern of LUS-100E displays the typical MCM-41 profiles of 2D-hexagonal structure with *p6mm* plain group and even after calcination at 580 °C, the structure of LUS-100E-580 maintains as parent's indicating the harmfulness of calcination at each defined temperature can be ignorable to the meso-structure of materials (Figure 2, a-b).

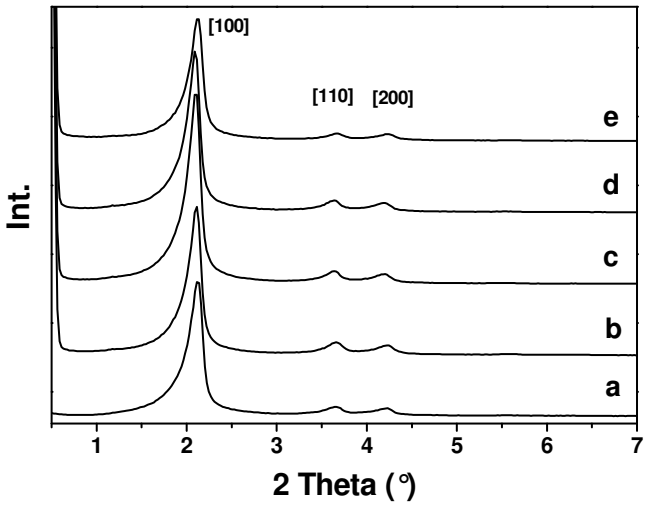

Figure 2 Small-angle powder XRD of materials (a) LUS-100E, (b) LUS-100E-580, (c) LUS-100E-380-E, (d) LUS-100E-480-E, (e) LUS-100E-580-E.

Again, nitrogen sorption isotherms are consistent with a preserved channel structure for the calcined materials (Figure 3). The LUS-550 shows a slight decrease of pore volume due to an unsurprisingly structure shrink at the conventional calcination condition (Figure 3, a-b; Table 1, entries 1-2). Moreover, LUS after fully covered by TMS then followed calcination at 600 °C, the meso-structure of LUS-100TMS-600 has not only maintained indicating its thermal stability, but also recovered to the same structure as that of LUS-550, with continuously surface area increasing and pore volume decreasing due to the extra introduced organic Si (Figure 3, c; Table 1, entry 5). By contrast, the incomplete structure recovering of LUS-100E-580 with specific area and pore volume diminished to 719 $m^2 \cdot g^{-1}$ and 0.58 $cm^3 \cdot g^{-1}$ respectively reveals the superior thermal stability of EBDMS at such high temperature (Figure 3, c; Table 1, entry 4). In addition, the C parameter, which represents the affinity between the adsorbant and the adsorbate, evolved from 111 ± 3 of LUS to 99 ± 2 of LUS-550, as a consequence of the hydrophobization of the surface due to the thermal condensation of the silanol groups. As to the LUS-100TMS-600 and LUS-100E-580, the C parameter has decreased to 74 and 71, respectively indicating the presence of organo group causes more Si-O-Si linkage on the pore wall surface.

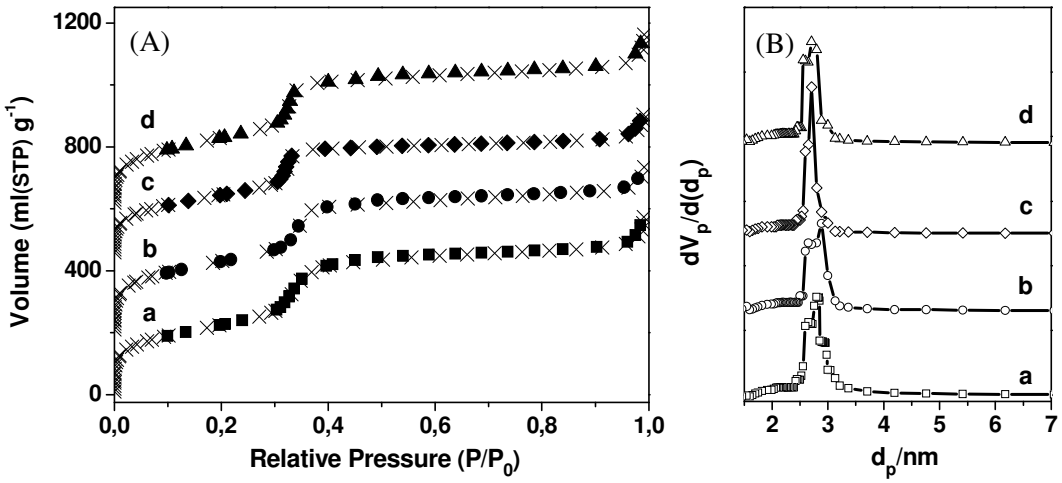

Figure 3 (A) N_2 sorption isotherms and (B) pore size distribution of (a) LUS, (b) LUS-550 (offset of + 200 ml (STP) g^{-1}), (c) LUS-100E-580 (offset of + 450 ml (STP) g^{-1}) and (d) LUS-100TMS-600 (offset of + 600 ml (STP) g^{-1}).

The thermal effect to the structure of materials calcined at different temperatures has been summarized in the Table 1. Normally, a full coverage of EBDMS or TMS function to the LUS-T100 causes the specific area reducing to ~80% and pore volume ~70% (Table 1, entries 1, 3 and 7). Whereas, the calcinations after the first thermal decomposition segment (RT-480 °C for LUS-100E, and RT-500 °C for LUS-100TMS) to LUS-100E or LUS-100TMS would continue to decreasing the specific area and pore volume (Table 1, entries 3-5 and 7-9). It may result in the new intermedia species occupying the space of the material.

Table 1 N_2 sorption isotherm analysis for the materials

Entry	Sample	S_{BET} ($m^2\ g^{-1}$)	V_{total}[a] ($cm^3\ g^{-1}$)	Pore distribution (nm)		C[c]
				D_{BdB}[b]	D_{BJH}	
1	LUS	824	0.75	3.6	2.8	111
2	LUS-550[d]	837	0.72	3.7	2.9	99
3	LUS-100E	663	0.52	3.2	2.5	27
4	LUS-100E-380	648	0.53	3.3	2.5	31
5	LUS-100E-480	638	0.52	3.5	2.6	33
6	LUS-100E-580	719	0.58	3.6	2.7	71
7	LUS-100TMS	667	0.53	3.3	2.5	27
8	LUS-100TMS-400	655	0.55	3.5	2.6	26
9	LUS-100TMS-500	605	0.54	3.3	2.5	34
10	LUS-100TMS-600	843	0.71	3.6	2.7	74
11	LUS-50TMS-500-TMS	594	0.66	3.3	2.5	27
12	LUS-100TMS-500-TMS	447	0.39	3.2	2.4	24

a, Total pore volume measured at $P/P_0 = 0.92$;

b, $Y = 14{,}60994 + 74{,}67812*x - 81{,}96198*x^2 + 155{,}8457*x^3$, $X = P/P_0$ ($0.11 \leq P/P_0 \leq 0.50$), Y = Pore Diameter (Angstrom, Å);

c, BET-plot parameter.

d, Calcined at 550 °C for 10 h

While after the combustion segment, the structures of LUS-100E-580 and LUS-100TMS-600 materials were conserved well with a characteristic adsorption step typical of such mesoporous silica (Figure 3A-B, c-d). Compared to LUS-550, LUS-100E-580 recovered 86% specific surface, 80% pore volume, and almost the same pore diameter. And LUS-100TMS-600 recovered to the same structure as that of LUS-550. It indicates that the high temperature calcinations returned the organic surface of LUS-100E and LUS-100TMS to the inorganic one without any harmfulness, and moreover, an extra framework was generated from EBDMS function but no effect from TMS group (Table 1, entries 2, 6 and 10). In addition, the C parameters of the both materials decreased to 71 ± 2, consistently with the more composition of orgranic part in the hybrid material resulting in more hydrophobic Si species, Si-O-Si.

The structure of calcined materials maintains after further re-capping EBDMS or TMS. LUS-100E-cal re-capped with EBDMS leading to LUS-100E-cal-E exhibits again the regular array of meso-channel as well as the retention of the cell parameters evincing a homogeneous dispersion of EBDMS on the surface of LUS-100E-cal (Figure 2, c-e). Nonetheless, the specific surface area, pore volume and pore diameter consistently decreases with introducing the extra organic function. For instance, LUS-100TMS-500 losses 10% surface area due to the new intermediate produced while the pore volume and pore diameter keeps constant compared to LUS-100TMS (Table 1, entries 7 and 9). After re-capping, LUS-100TMS-500-TMS possesses a diminished structure indicating a full channel decoration by the organic moieties in particular which leads to the C parameter decreasing to 24 more hydrophobic than LUS-100TMS and LUS-100TMS-500 (Table 1, entry 12).

5.3.2 Chemical properties

5.3.2.1 LUS-100E-cal and LUS-100E-cal-E

The FT-IR spectra monitored the calcination of LUS-100E under 380 °C, 480 °C and 580 °C, respectively. The distinct bands centred at 833 cm^{-1} and 757 cm^{-1} assigned to the Si-C stretching and appearance of C-H stretching in the 2860-2950 cm^{-1} region indicates a strong signal of the EBDMS group anchored on the surface of the original LUS-100E material (Figure 2A-C, a). Increasing the temperature of calcination, the Si-C band diminishes gradually as well as the C-H bands announcing the consumption of the alkyl part on the EBDMS group (Figure 2A, C, b-c). After the 580 °C calcination, the C-H bands totally disappeared and Si-C band became a slight shoulder on the band of Si-O-Si bending at 800 cm^{-1} (Figure 2(A, C), d). At the same time, the Si-O-Si band reduced correspondingly suggesting a cut of the Si-O bond.

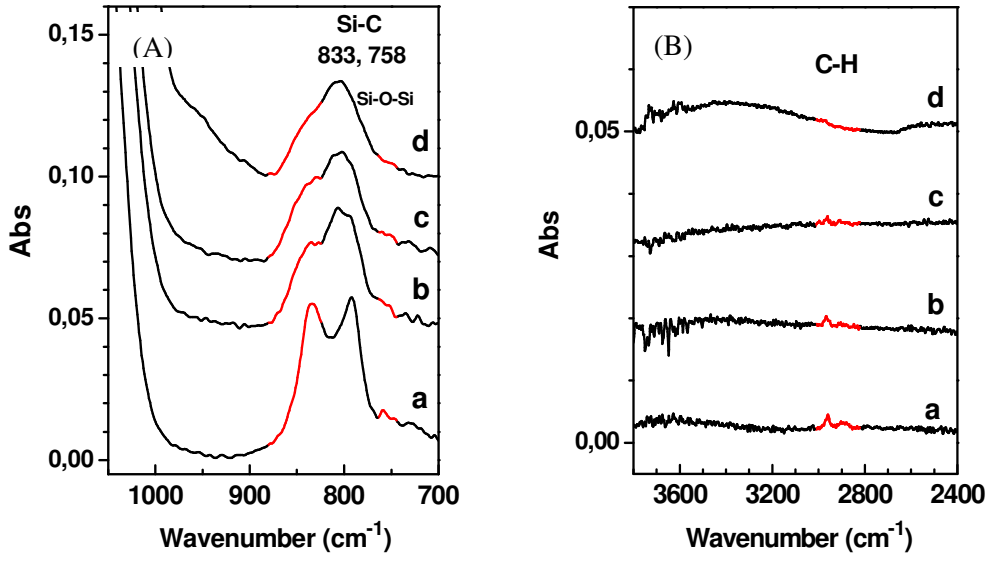

Figure 4 FT-IR spectra monitoring the thermal treatment to the materials LUS-100E in the (A) inorganic region and (B) organic region, respectively. a, LUS-100E; b, LUS-100E-380; c, LUS-100E-480; d, LUS-100E-580.

The deconvoluted FT-IR spectra of LUS-100E-cal materials, show three bands centred at 758, 834 and 870 cm^{-1} that are associated with Si-C stretching modes of –

$Si(CH_2)_2CH_3$ in EBDMS function. In addition to these peaks, a band at 800 cm^{-1} is generally attributed to symmetric stretching vibration of Si-O-Si in the mesoporous silica framework (Figure 5A). The Si-C stretching bands diminish with the calcination temperature increasing among which the main band at 834 cm^{-1} has reduced to 1/5 in the LUS-100E-580. As to the Si-O-Si symmetric stretching band, it keeps stable until 480 °C, then it is reduced (Figure 5B-C). It probably because the first connected layer of surface silica was destroyed by a varity of the new species generated during the combustion of organic group, thus the evolution of the organic group directly linked to the surface Si decreases the symmetry of Si-O-Si revealing a surface property modification by the thermal treatment like the transformation of Si-C into Si-OH, the Si-O-Si linkage fracture, etc (Figure 5D).

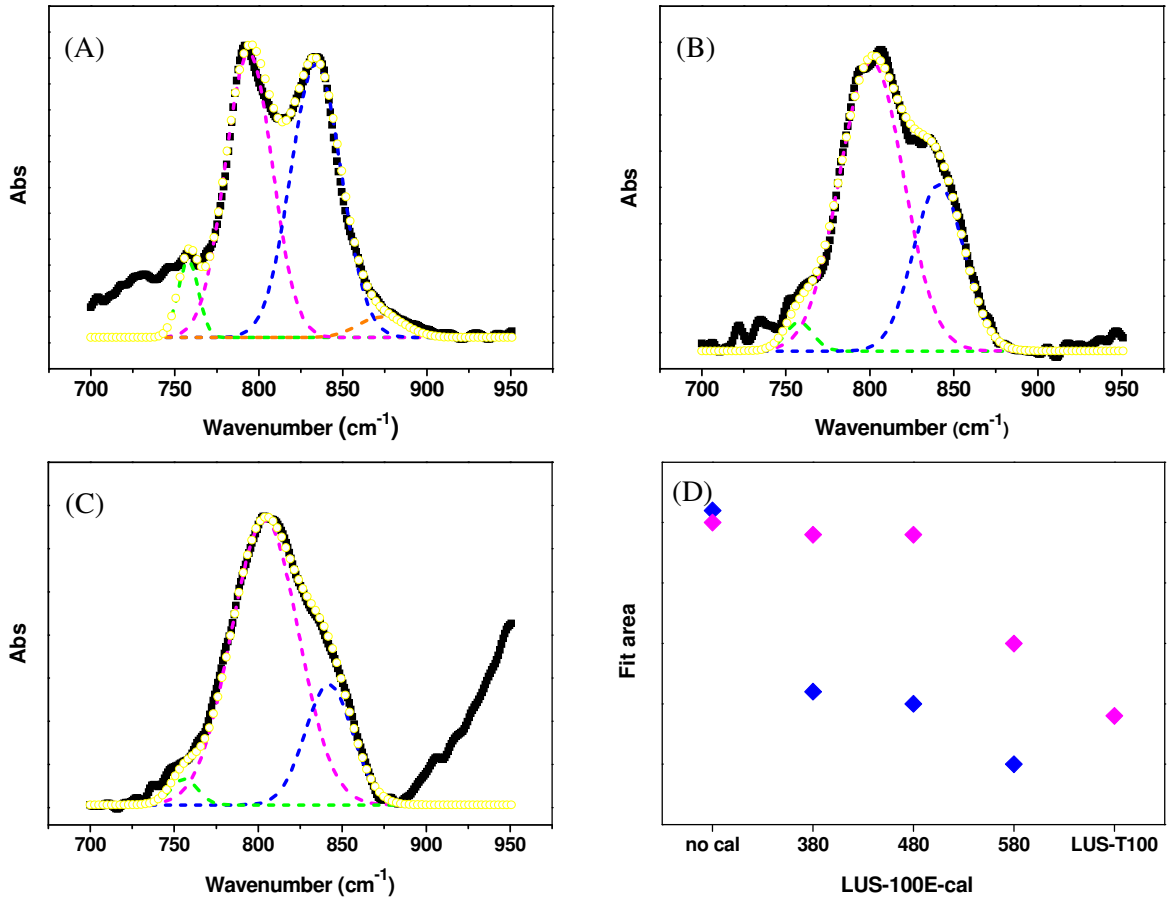

Figure 5 Simulated IR spectra of (A) LUS-100E, (B) LUS-100E-380 and (C) LUS-100E-580, and (D) the revelance of peak intensity and calcination temperature. In (A-C), black square line: raw

spectrum; green dash line: fit of 758 cm^{-1}, width 8 cm^{-1}; pink dash line: (A) fit of 794 cm^{-1}, width 14 cm^{-1}, (B) fit of 801 cm^{-1}, width 19 cm^{-1}, (C) fit of 804 cm^{-1}, width 20 cm^{-1}; blue dash line: (A) fit of 834 cm^{-1}, width 15 cm^{-1}, (B) fit of 841 cm^{-1}, width 15 cm^{-1}, (C) fit of 842 cm^{-1}, width 14 cm^{-1}; orange dash line: (A) fit of 873 cm^{-1}, width 14 cm^{-1}; yellow circle line: cumulative line. In (D), blue diamond: blue fit; pink diamond: pink fit.

The question remains about the regenerated surface with new silicon species during the calcination and the more detail is discriminate by the quantitative ^{29}Si MAS NMR. As shown in the Figure 6A, M_0, M_1 and M_1'' that are characteristic of C_3-Si-OH (monografted), C_3-Si-O-Si-O_3 (bigrafted) and C_3-Si-O-Si-R_3 (grafted dimers) type of groups, arising at 18.6, 14.1 and 6.7 ppm, respectively. As expected, LUS-100E material possesses mainly bigrafted EBDMS (~80%) and some grafted dimeric species (Table 2, entry 2).

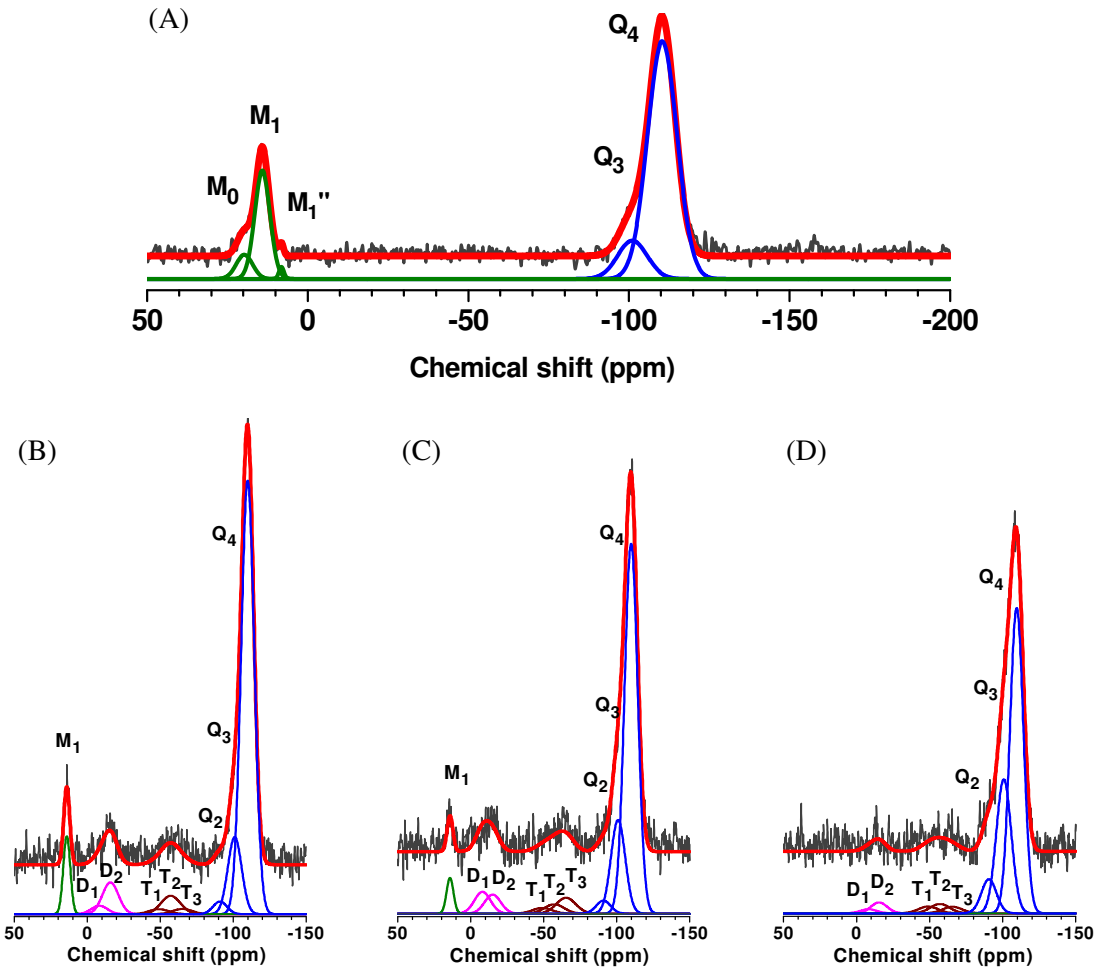

Figure 6 ^{29}Si MAS NMR spectra of the materials (A) LUS-100E, (B) LUS-100E-380, (C) LUS-100E-480, and (D) LUS-100E-580. Peak position (ppm): Q_4 = -111.0 ± 0.3, Q_3 = -101.9 ± 0.3, Q_2 = -91.8 ± 0.4; M_1 = 14.1 ± 0.1, M_0 = 18.6 ± 0.4, M_1'' = 6.7 ± 0.1, T_3 = -65.4 ± 0.2; T_2 = -57.1 ± 0.1; T_1 = -49.0 ± 0.1; D_2 = -15.4 ± 0.4; D_1 = -8.2 ± 0.1.
Fits width for Q species is 9.21 ppm in (a), 9.45 ppm in (b), 9.73 ppm in (c), and 10.22 ppm in (d). Fits width for M species is 4.90 ppm in (a), 4.78 ppm in (b), and 4.70 ppm in (c). Fits width for T species is 13.21 ppm and D species 11.00 ppm in (b-d). Analytical integration accounts for the same G/L ratio 1.00.

After 380 °C calcination, the signals of M_0 and M_1'' disappear and Q_2 species rises at -91.8 ± 0.4 ppm again. Simultaneously, several new signals appear in the 0~-20 ppm and -40~-70 ppm regions declaring the generation of D and T species of Si atoms (Figure 6B). With the calcination temperature continuingly rising, the M_1 species weakens gradually until the disappearance of LUS-100E-500 (Figure 6C-D; Table 2, entry 5).

Table 2 ^{29}Si MAS NMR deconvolution results for the materials LUS-100E calcined by different temperature and followed grafted EBDMS group again.

Entry	Sample	Q_4	Q_3	Q_2	Si_{inor}	T_3	T_2	T_1	D_2	D_1	M''	M_1	M_0	T	D	M^a	$Si_{org}{}^b$
1	LUS	63[c]	34	3	*100*	—	—	—	—	—	—	—	—	—	—	—	—
2	LUS-100E	69	11	0	*80*	—	—	—	—	—	1	16	3	—	—	*20*	*20*
3	LUS-100E-380	67	12	2	*81*	1	4	1	6	2	0	6	0	*6*	*7*	*6*	*19*
4	LUS-100E-480	64	16	2	*83*	4	2	1	5	2	0	3	0	*7*	*7*	*3*	*17*
5	LUS-100E-580	60	27	7	*94*	1	2	2	1	0	0	0	0	*5*	*1*	*0*	*6*
6	LUS-100E-380-E	68	11	0	*79*	3	2	1	4	2	1	7	2	*5*	*6*	*10*	*21*
7	LUS-100E-480-E	68	12	1	*81*	2	2	1	5	1	1	6	1	*5*	*6*	*8*	*19*
8	LUS-100E-580-E	59	18	3	*80*	2	2	1	2	1	3	8	1	*5*	*3*	*12*	*20*
		Q_4'[d]	Q_3'	Q_2'	—	T_3'	T_2'	T_1'	D_2'	D_1'	$(M_1'')'$	$(M_1)'$	$(M_0)'$	T'	D'	M'	$Si_{org}{}'$
9	LUS-100E	86	14	0	—	0	0	0	0	0	0	20	5	*0*	*0*	*25*	*25*
10	LUS-100E-380	83	15	2	—	2	5	1	7	2	0	8	0	*8*	*9*	*8*	*25*
11	LUS-100E-480	77	20	3	—	4	3	2	6	2	0	4	0	*9*	*8*	*4*	*21*
12	LUS-100E-580	65	28	7	—	2	2	2	1	0	0	0	0	*6*	*1*	*0*	*7*
13	LUS-100E-380-E	86	14	0	—	3	2	1	5	2	1	9	3	*6*	*7*	*13*	*26*
14	LUS-100E-480-E	84	15	1	—	3	3	1	6	2	1	8	1	*7*	*8*	*10*	*25*
15	LUS-100E-580-E	74	22	3	—	3	2	1	2	1	4	11	2	*6*	*3*	*17*	*26*

a, $M_i = M_1'' + M_1 + M_0$

b, $Si_{org} = T_i + D_i + M_i$

c, Analytical integral error by noise of baseline (± 1)

d, $Q_i' = Q_i / \Sigma Q_i$; $T_i' = T_i / \Sigma Q_i$; $D_i' = D_i / \Sigma Q_i$; $M_i' = M_i / \Sigma Q_i$; $Si_{org}' = \Sigma Si_{org\text{-}i} / \Sigma Q_i$. Error ± 0.5

After 380 °C calcination, the signals of M_0 and M_1'' disappear and Q_2 species rises at -91.8 (±0.4) ppm again. Simultaneously, several new signals appear in the 0 ~ -20 ppm and -40 ~ -70 ppm regions declaring the generation of D and T species of Si atoms (Figure 6B; Scheme 1). According to the integral intensities of each species illustrated in Table 2, D is the first generated from M species, converting to T species soon afterwards. Nonetheless, D and T species acing as the intermedias are considered to be produced simultaneously without distinguishable order along the whole process.

Obviously, the T and D species silicon increases in the calcined materials while M species decreases consistent with the calcination temperature rising. Up to the LUS-100E-480, most of the organic groups are conserved including 7% T, 7% D and 3% M species, among which the latters two correlated to di- or tripodal of one silicon atom indicating a more stable linkage. Besides to the organic moieties, a considerable amount of silanol groups retain, isolated by the organic Si nucleis (Table 2, entry 4; Scheme 1).

The M_1 species finally disappears in LUS-100E-580 that 94% inorganic silicon representing in Si-O is recovered from the organic moieties Si-C (Figure 6C; Table 2, entries 8 and 15). Strikingly, the Q_2 and Q_3 species are strengthened to 27% and 7% respectively, by contrast of Q_4 decreasing compared to the LUS-100E revealing a drastic hydrophobic/hydrophilic property conversion on the surface. Therefore, the conversion is presumable that Q_2 was the main species generated from the organic moieties, in the meanwhile, assuming a 1:1 pending Q_2:Q_2 stoichiometry for the condensation of silanol it would consequently lead to the same amount of Q_3 (Scheme 1).

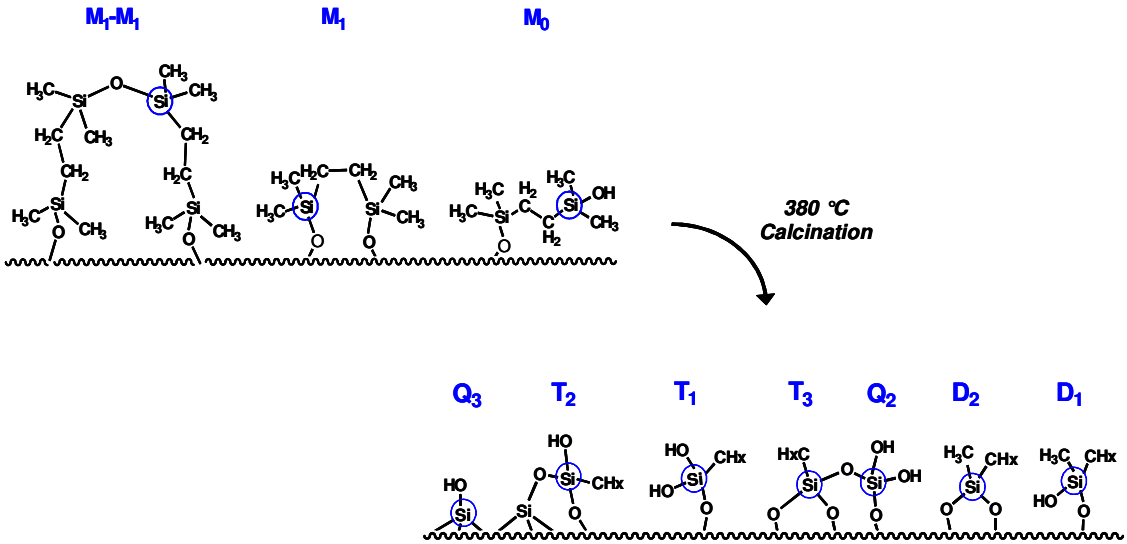

Scheme 1 Evolution of the organic function in the calcination.

The calcined surface tested by re-capping EBDMS function on LUS-100E-cal materials is characterized by FT-IR spectra. Both of the Si-C band at 834 cm^{-1} and C-H bands in the 2860-2950 cm^{-1} have been enhanced showing the successful EBDMS capping on the thermal treated surface (Figure 4, b-d; Figure 7, b'-d'). However, the Si-C band could not reach the same intensity as that of LUS-100E, reflecting the calcined samples are irreversible compared to the initial material LUS even after the complete calcination at 580 °C.

As displayed in the 2600-3800 cm^{-1} region, the hydrophobicity on the surface due to the initial EBDMS function had weakened when calcinations temperature increased, which is especially represented by the LUS-100E-580 with a broad H-O stretching band (Figure 7B, a, d and d'). But the re-capping of EBDMS made it disappear emphasizing the hydrophobizing property of the dipodal function and moreover, the reversibility of hydrophobic/hydrophilic properties of the organically modified silica surface realized by the alternative ways concerning calcination and grafting.

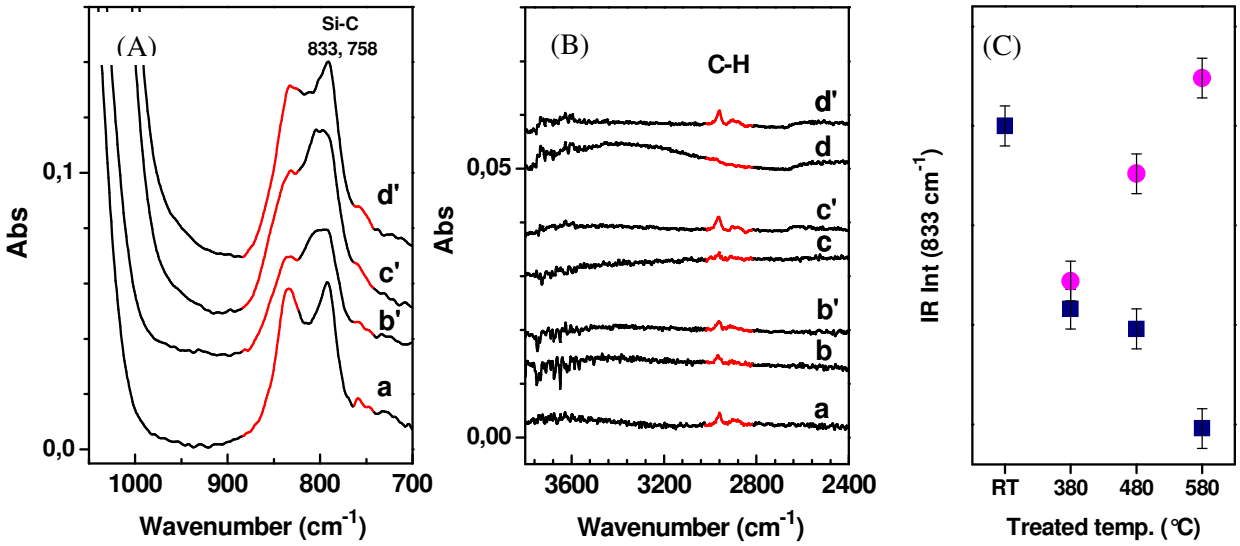

Figure 7 FT-IR spectra of materials LUS-T100-E-cal-E in the (A) inorganic region and (B) organic region, respectively and (C) the evolution of EBDMS coverage vesus the calcination temperature present in IR intensity of peak 833 cm^{-1}. a, LUS-100E; b, LUS-100E-380; c, LUS-100E-480; d, LUS-100E-580; b', LUS-100E-380-E; c', LUS-100E-480-E; d', LUS-100E-580-E.

The normalized intensity of IR 834 cm^{-1} peak before and after re-capping EBDMS group on the calcined materials is illustrated in the Figure 7C. Calcination causes the intensity of Si-C decreasing by 60%, while the re-capping EBDMS made it increase. Compared with LUS-100E-380-E, LUS-100E-480-E and LUS-100E-580-E have the double and triple intensity of EBDMS, respectively, due to the abundant silanol groups derivate from the D and T species as well as the re-generated Q_3 and Q_2 species.

The re-capping materials were characterized by the solid ^{29}Si MAS NMR to vertify the grafted Si species on the calcined surface. The M species including M_0, M_1 and M_1'' appear again in the samples LUS-100E-380-E, LUS-100E-480-E and LUS-100E-580-E (Figure 8).

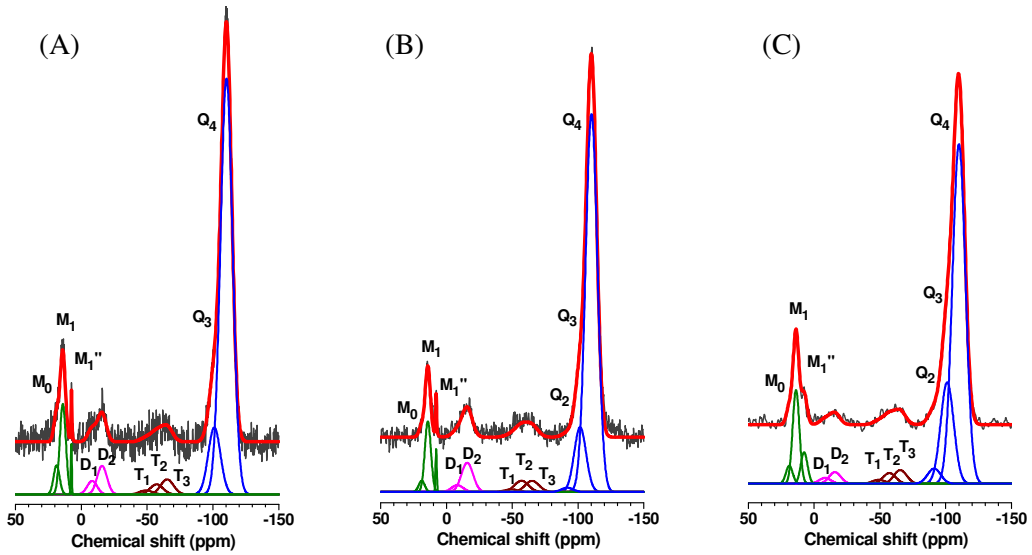

Figure 8 ^{29}Si MAS NMR spectra of the materials (A) LUS-100E-380-E, (B) LUS-100E-480-E, and (C) LUS-100E-580-E. Peak position (ppm): Q_4 = -111.0 ± 0.3, Q_3 = -101.9 ± 0.3, Q_2 = -91.8 ± 0.4; M_1 = 14.1 ± 0.1, M_0 = 18.6 ± 0.4, (M_1'') = 6.7 ± 0.1, T_3 = -65.4 ± 0.2; T_2 = -57.1 ± 0.1; T_1 = -49.0 ± 0.1; D_2 = -15.4 ± 0.4; D_1 = -8.2 ± 0.1. Fits width for Q species is 9.26 ppm in (A), 9.02 ppm in (B), and 9.91 ppm in (C). Fits width for M species is 4.58 ppm in (A), 4.57 ppm in (B), and 5.10 ppm in (C) while for M_1-M_1 species is 0.78 ppm in (A), 0.97 ppm in (B), and 5.10 ppm in (C). Fits width for T species is 9.77 ppm in (A), 10.57 ppm in (B), and 9.65 ppm in (C). Fits width for D species is 7.48 ppm in (A), 8.84 ppm in (B), and 8.82 ppm in (C). Analytical integration accounts for the same G/L ratio 1.00 except for that of M_1'' species 0.5.

A set of distinct M species appear at 7-19 ppm region with the coexistence of T and D species. However, the Q_2 species in LUS-100E-580-E was not exhausted as that in LUS-100E revealing some of the silanol groups generated by thermal pyrolysis of EBDMS function are non-accessible.

As the integral intensity illustrated in the Figure 9, the M species of the three materials increse to 13%, 10% and 17%, respectively, compared to the 8%, 4% and 0% before re-capping. At the same time, the Q_3 and Q_2 species decrease with Q_4 increasing indicating the silanol groups were consumed as the grafting sites (Figure 8A-B; Table 2, entries 10-15). The amount of organic Si contained in all the re-capping materials recovered to the same level as that of LUS-100E, but it composites of M, T, and D species silica, which would supply a varity of organic functions to the surface properties.

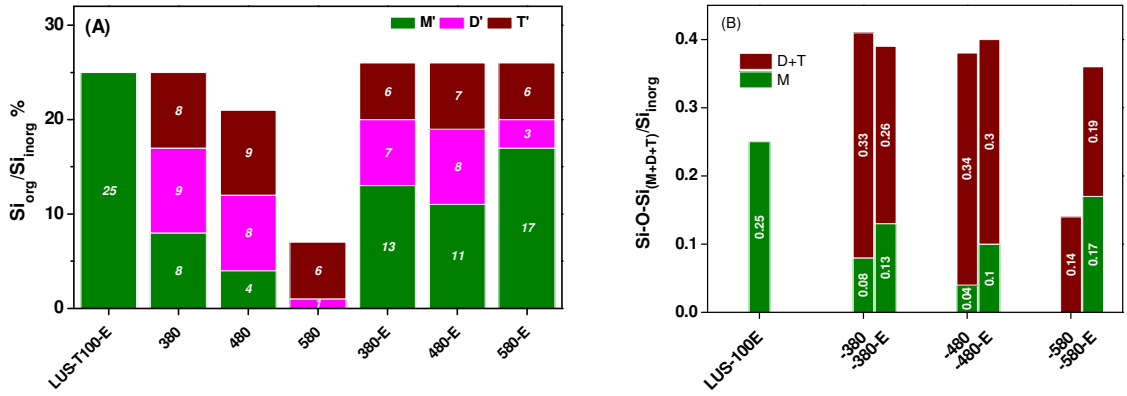

Figure 9 Quantitative ^{29}Si MAS NMR spectra for the comparison of (A) organic Si and (B) its Si-O-Si linkage contained in the materials LUS-100E, LUS-100E-cal and after EBDMS re-capping LUS-100E-cal-E. In (A), Si_{org}/Si_{inorg} % = ΣSi_{org-i} / ΣQ_i * 100%, ΣSi_{org-i} = T+D+M; In (B), $Si\text{-}O\text{-}Si_{(M+D+T)}/Si_{inorg}$ = $\Sigma[1*(M_1+D_1+T_1)+2*(D_2+T_2)+3*T_3] / \Sigma Q_i$ (i = 2-4).

A slight change in total amount of D or T species during the re-capping proves not only the stability of the related organic groups but also the di- or tripodal firmly anchoring on the surface (Figure 9). Calcined at 380-480 °C produces more Si-O-Si from T or D species as well as offering silanol group to induce an internal transformation from D to T during the re-capping (Scheme 1). In these cases, the position of M_1 species is considered to shift to M_1'' because of the linkage of $R_xO_{3-x}Si\text{-}O\text{-}\boldsymbol{Si}C_3$ (X=1-2) between EBDMS and D or T species Si atom (Figure 8C).

5.3.2.2 LUS-100TMS-cal and LUS-100TMS-cal-TMS

The same calcination processes were carried on the LUS-100TMS shown in the FT-IR spectra (Figure 10). Compared with LUS-100E, the bands assigned to Si-C stretching in TMS function appears at 847 cm^{-1} and 757 cm^{-1} as well as the typical C-H stretching bands in the 2880-2950 cm^{-1} region. Moreover, another accompanied band centred at 760 cm^{-1} due to the C-H out-of-plan bending mode (Figure 10A-B, a). The organic group was consumed with increasing calcinations temperature to the samples and from LUS-

100TMS-500 to LUS-100TMS-600, the bands, especially of the Si-C stretching and C-H bending, disappeared at once revealing the stability of TMS group limited in the 500 °C-600 °C region (Figure 10A, b-d).

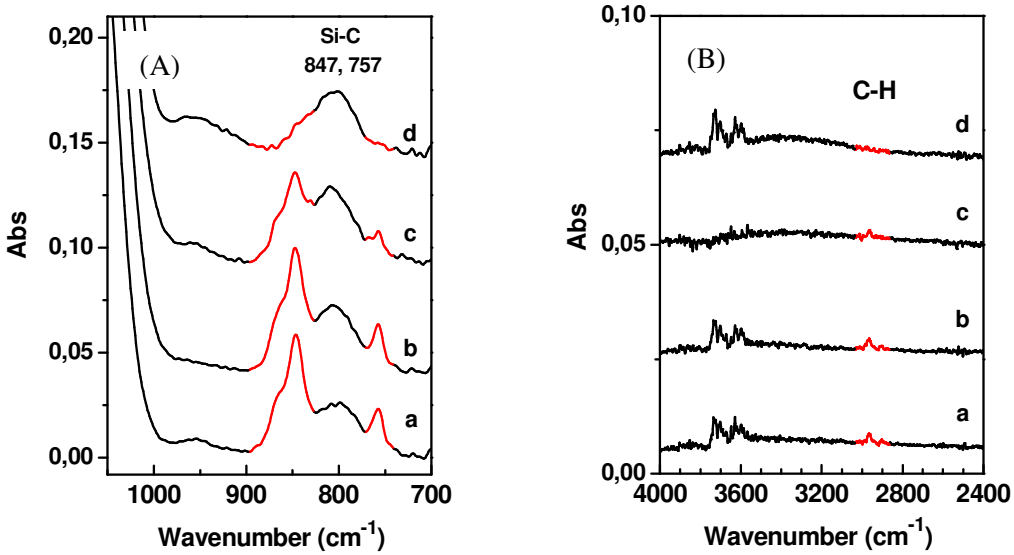

Figure 10 FT-IR spectra monitoring the different calcination temperatures to LUS-100TMS presented in (A) inorganic region and (B) organic region. a, LUS-100TMS; b, LUS-100TMS-400; c, LUS-100TMS-500; d, LUS-100TMS-600. Si-C stretching vibration in TMS at 847 cm^{-1}.

The same three bands due to Si-C stretching and one band of Si-O-Si symmetric stretching are shown in the deconvoluted FT-IR spectra of LUS-100TMS and its calcined products (Figure 11A-C). The thermal treatment made the intensity of Si-C stretching bands decrease correlatively. The Si-O-Si symmetric stretching band, by the contrast it increases to the maximum at 500 °C then decreases (Figure 11D). Therefore, it can be presumable that the symmetry of Si-O-Si connectives were improved when partial methyl group in the TMS function was burned, turning $-Si(CH_3)_3$ into $=Si(CH_x)_2$. With continuous calcination to 600 °C, the organic groups disappeared leading to more inorganic silica that caused the surface silica structure more asymmetric.

Consistently, LUS-100TMS-cal materials show the similar change for the Si-C bands with temperature increasing (Figure 10, b-d). Nonetheless, the LUS-100TMS presents less relative intensity of the Si-O-Si symmetric stretching compared with LUS-

100E (Figure 11, A). However, the calcination of TMS group causes Si-O-Si symmetric stretching strengthened until 500 °C that turning partial -$Si(CH_3)_3$ into -$Si(CH_x)_2OR$ or -$Si(CH_x)_1(OR)_2$ (R = H or Si) in the TMS function can improve the symmetry of Si-O-Si connectives (Figure 11, B-D). While continuous calcination to 600 °C, the organic groups are burned leading to the silica surface rich in silanol groups that makes silica structure more asymmetric as the initial status of LUS.

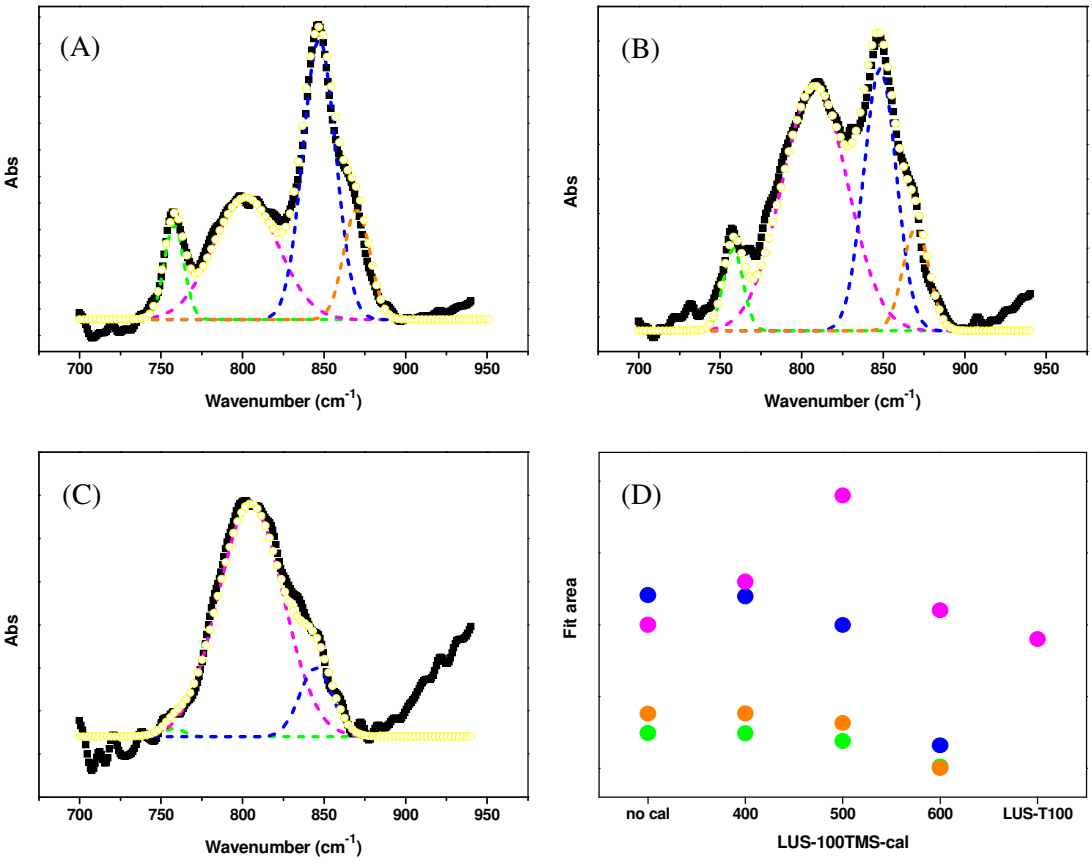

Figure 11 Simulated IR spectra of (A) LUS-100TMS, (B) LUS-100TMS-500 and (C) LUS-100TMS-600, and (D) the revelance of peak intensity and calcination temperature. In (A-C), black square line: raw spectrum; green dash line: fit of 758 cm^{-1}, width 6 cm^{-1}; pink dash line: (A) fit of 802 cm^{-1}, width 20 cm^{-1}, (B) fit of 808 cm^{-1}, width 20 cm^{-1}, (C) fit of 805 cm^{-1}, width 20 cm^{-1}; blue dash line: (A) fit of 847 cm^{-1}, width 10 cm^{-1}, (B) fit of 848 cm^{-1}, width 10 cm^{-1}, (C) fit of 845 cm^{-1}, width 10 cm^{-1}; orange dash line: fit of 870 cm^{-1}, width 8 cm^{-1}; yellow circle line: cumulative line. In (D), circles are corresponding to fits with the same color.

Compared with LUS-100E-cal materials, the LUS-100TMS-cal ones are simpler observed in the solid ^{29}Si MAS NMR spectra (Figure 12). The material with full coverage of TMS (LUS-100TMS) exhibits M_1 and M_0 Si species at 13.4 and 19.0 ppm, respectively (Figure 12A). M_1 is also the characteristic of Si in TMS function (C_3-*Si*-O-Si_3) and M_0 indicates an excess addition of TMS precursor that causes a C_3-*Si*-OH free species adsorbed in the solid after filtration and washing by technical ethanol and acetone. 15% organic Si was introduced in leading to the structure with inorganic Si of 63% Q_4, 34% Q_3 and 3% Q_2 adjusting to 81% Q_4, 19% Q_3 and 0% Q_2, respectively (Table 3, entry 1).

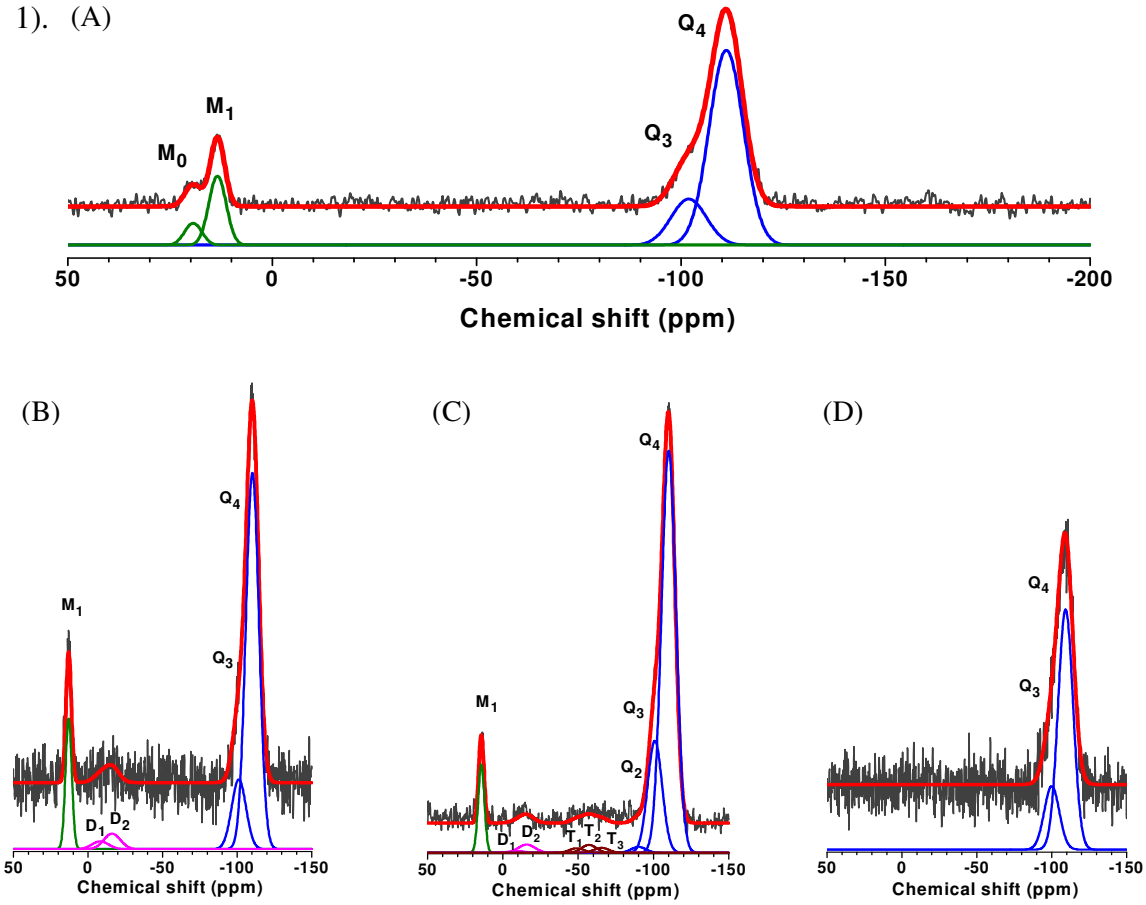

Figure 12 ^{29}Si MAS NMR spectra of the materials (A) LUS-100TMS, (B) LUS-100TMS-400, (C) LUS-100TMS-500 and (D) LUS-100TMS-600. Peak position (ppm): Q_4 = -111.0 ± 0.3, Q_3 = -101.9 ± 0.3, Q_2 = -91.8 ± 0.4; M_1 = 13.4 ± 0.4, M_0 = 19.0 ± 0.4 ; T_3 = -65.4 ± 0.2; T_2 = -57.1 ± 0.1; T_1 = -49.0 ± 0.1; D_2 = -16.0 ± 0.2, D_1 = -10.0 ± 0.1. Fits width for Q species is 8.90 ppm in (A), 9.58 ppm in (B) and (C), 11.54 ppm in (D). Fits width for M species is 4.21 ppm. Fits width

for T species is 9.68 ppm. D species is 11.00 ppm in (A) and (B). Analytical integration accounts for the same G/L ratio 1.00.

LUS-100TMS-400 shows only 4% new generated D species silicon atom that leading to 84% Q_4 and 16% Q_3 compared to 81% and 19% in LUS-100TMS, revealing more Si-O-Si linkage of organic moieties direct to the surface is produced (Figure 12B; Table 3, entries 2 and 6). The T species appear in LUS-100TMS-500 with Q_4 decreasing and Q_3 increasing indicating part of silanol is released by the thermal treatment besides to a novel ultra-stable surface (Figure 12C; Table 3, entries 3 and 7). Up to 600 °C, all the organic Si had been cleaned off leading to a inorganic structure consisting of 79% Q_4 and 21% Q_3, by contrast, LUS-100TMS-cal produce few Q_2 as LUS-100E-cal having due to the monopodal grafting (Figure 12D; Table 3, entries 4 and 8).

Table 3 ^{29}Si MAS NMR deconvolution results for the materials LUS-100TMS calcined by different temperature.

Entry	Sample	Q_4	Q_3	Q_2	Si_{inor}	T_3	T_2	T_1	D_2	D_1	M_1''	M_1	M_0	*T*	*D*	*M*[a]	Si_{org}[b]
1	LUS-100TMS	69[c]	16	0	85	—	—	—	—	—	0	11	4	—	—	*15*	*15*
2	LUS-100TMS-400	72	13	0	85	0	0	0	3	1	0	11	0	*0*	*4*	*11*	*15*
3	LUS-100TMS-500	69	19	1	89	0.8	1.4	0.8	1.6	0.3	0	6	0	*3*	*2*	*6*	*11*
4	LUS-100TMS-600	79	21	0	100	0	0	0	0	0	0	0	0	*0*	*0*	*0*	*0*
		Q_4[d]	Q_3'	Q_2'	—	T_3'	T_2'	T_1'	D_2'	D_1'	$(M_1'')'$	$(M_1)'$	$(M_0)'$	*T'*	*D'*	*M'*	Si_{org}'
5	LUS-100TMS	81	19	0	—	—	—	—	—	—	0	13	5	—	—	*18*	*18*
6	LUS-100TMS-400	84	16	0	—	0	0	0	3	1.7	0	13	0	*0*	*5*	*13*	*18*
7	LUS-100TMS-500	78	21	1	—	1	2	1	2	0.3	0	7	0	*4*	*2*	*8*	*14*
8	LUS-100TMS-600	79	21	0	—	0	0	0	0	0	0	0	0	*0*	*0*	*0*	*0*

a, $M = M_1'' + M_1 + M_0$

b, $\Sigma Si_{org\text{-}i} = T + D + M$

c, Analytical integral error by noise of baseline (± 0.5)

d, $Q_i' = Q_i / \Sigma Q_i$; $T_i' = T_i / \Sigma Q_i$; $D_i' = D_i / \Sigma Q_i$; $M_i' = M_i / \Sigma Q_i$; $Si_{org}' = \Sigma Si_{org\text{-}i} / \Sigma Q_i$. Error ± 0.5

Accordingly, the combustion of TMS functionalized material is more clearly than that of EBDMS modified ones. It displays a procedure containing transition of M to D species firstly, then from D to T species, and finally the complete conversion from organic Si (D or T) species to inorganic ones Q_i. The M species Si atom changed from 15% in LUS-100TMS to 11%, 6% and 0% in the corresponding three calcined materials, respectively. At the same time, Q_3 decreased from 16% to 13% in LUS-100TMS-400 and increases to 19% in LUS-100TMS-500 meaning that the silanol groups were involved in the transition between organic Si species but re-generated in the conversion from organic to inorganic (Table 3, entries 1-4).

The relative composition of each Si atom species is shown as entries 5-8 in the Table 3. Q_4 and Q_3 reached 84% and 16% in LUS-100TMS-400 compared to 81% and 19% in LUS-100TMS. While M_0 disappeared and M_1 kept no changed indicating that there was a grafting between the adsorbed C_3-***Si***-OH (M_0) free species and ***Si***-OH (Q_3) when M_1 transited to D species (Table 3, entries 5-6). With the calcinations temperature increasing, C-H continues to be oxidized into OH group. On the other hand, the oxidation was trend to opening the Q_4 ring to be helped to form D_2, T_2 or T_3 species (Scheme 2). Thus, Q_4 decreases in the LUS-100TMS-500 and LUS-100TMS-600 materials with the contrast of the Q_3 increasing (Table 3, entries 7-8). Not like LUS-100E-cal, LUS-100TMS-cal produced few Q_2 due to the monopodal function on the silica surface.

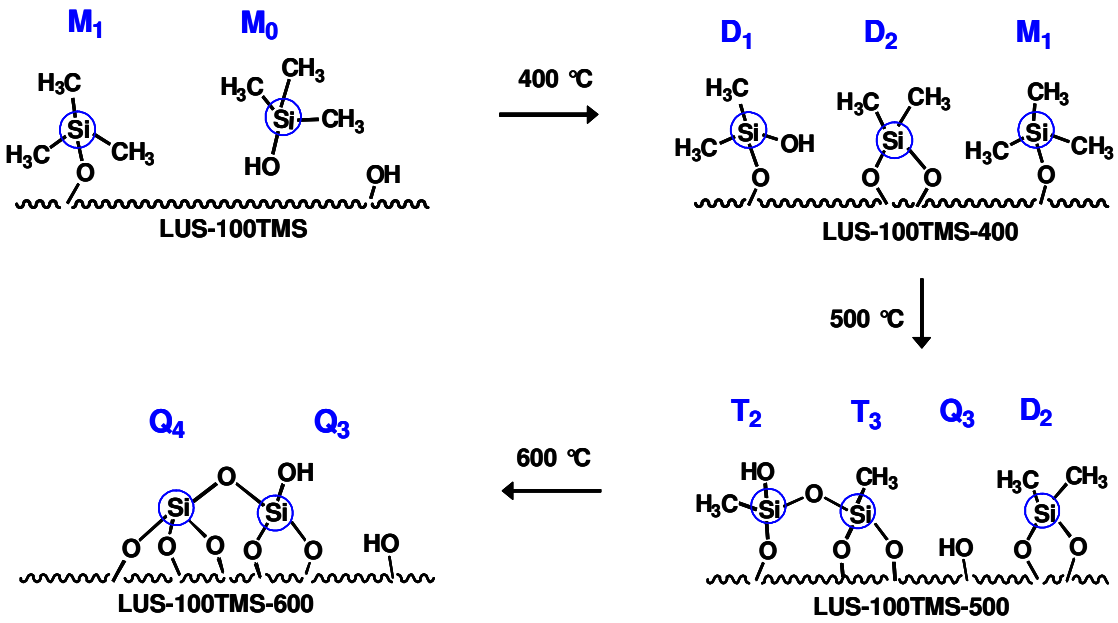

Scheme 2 Evolution of the TMS function modified material in the calcination.

5.3.2.3 LUS-xTMS-cal & LUS-xTMS-cal-TMS

Accordingly, the proper calcination temperature can be determined at 500 °C for the surface improvement to the other LUS-xTMS materials (x = 0, 25, 50 and 75) because of the stable surface generated with dipoal or tripodal linkage of organic moieties as well as the kept properties of metal or new organic species dispersion. The obtained samples are characterized by FT-IR spectroscopy and ^{29}Si MAS NMR for a overview of the novel surface

The FT-IR spectra of LUS-xTMS-OH (x = 25, 50, 75 and 100) display a regular intensity increasing of Si-C band at 847 cm^{-1} with decreasing template TMA^{+} (Figure 13A). It proved the excellent templating effect of TMA^{+} during the TMS function grafting in good accordance with the work reported by K. Zhang.[5] Whereas, the intensity of 847 cm^{-1} band decreases to a certain extent after calcinations at 500 °C (Figure 13B; Figure 14).

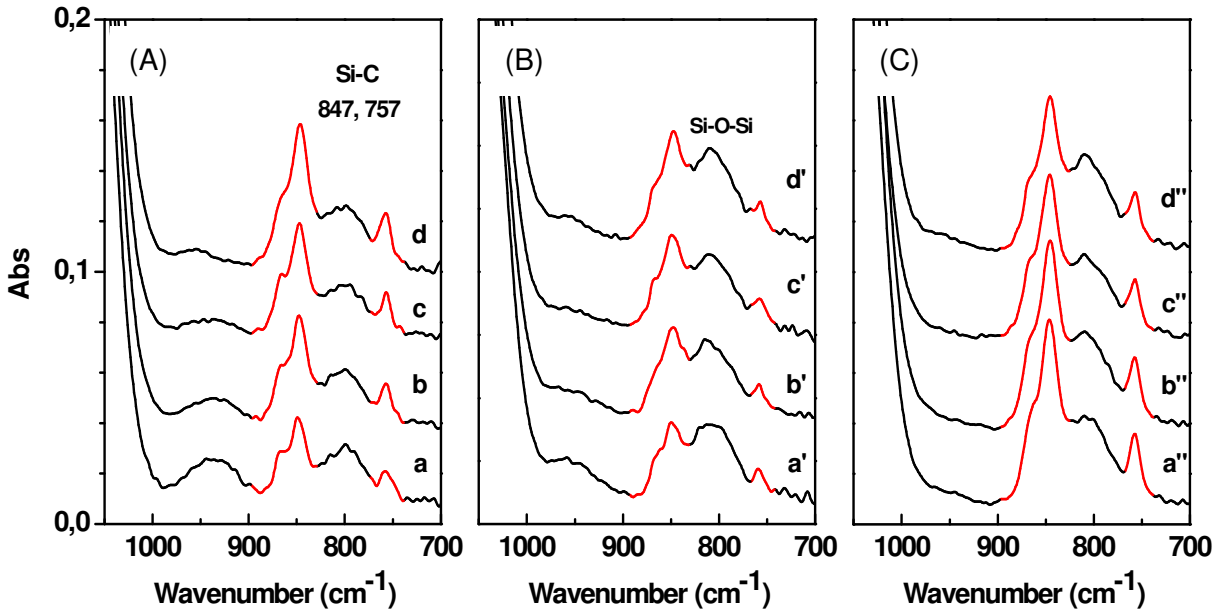

Figure 13 FT-IR spectra for monitoring (A) the partially TMS group covered materials (B) thermally treated at 500 °C and (C) grafted by TMS function again. In (A): a, LUS-25TMS; b, LUS-50TMS; c, LUS-75TMS; d, LUS-100TMS. In (B): a', LUS-25TMS-500; b', LUS-50TMS-500; c', LUS-75TMS-500; d', LUS-100TMS-500. In (C): a'', LUS-25TMS-500-TMS; b'', LUS-50TMS-500-TMS; c'', LUS-75TMS-500-TMS; d'', LUS-100TMS-500-TMS.

Detected by ^{29}Si MAS NMR, the relative integral intensity of each Si atom species in the calcined materials are listed in Table 4. Compared to the inorganic Si structure of LUS which contains 63% Q_4, 34% Q_3 and 3% Q_2, the LUS-100TMS exhibits the situation of 81% Q_4, 19% Q_3 and 0% Q_2 where all the accessible silanol groups were consumed by the monopodal group (Table 4, entry 8).

As to the LUS-xTMS, some of the silanol groups were left with existence of TMS function such as LUS-50TMS who owns 22% (Q_3+Q_2) and 12% Si_{org} (Table 4, entry 1). They were calcined at 500 °C leading to LUS-xTMS-cal materials (x = 25, 50, 75 and 100) possessing 4%, 7%, 9% and 5% (D_i+T_i) from the reduced M species, respectively, as well as the slightly changed (Q_3+Q_2) species (Table 4, entries 3-6). Moreover, the structure of inorganic Si was preserved well after calcinations (Table 4, entries 7 and 10, 8 and 12).

Table 4 ^{29}Si MAS NMR deconvolution results for the materials LUS-xTMS (x = 25, 50, 75 and 100) calcined at 500 °C.

Entry	Sample	Q_4	Q_3	Q_2	Si_{inorg}	T_3	T_2	T_1	D_2	D_1	M_1''	M_1	M_0	*T*	*D*	*M*[a]	Si_{org}[b]
1	LUS-50TMS	66[c]	21	1	88	—	—	—	—	—	0	11	1	—	—	*12*	*12*
2	LUS-100TMS	69	16	0	85	—	—	—	—	—	0	11	4	—	—	*15*	*15*
3	LUS-25TMS-500	62	26	3	92	1	1	0	1	1	0	5	0	*2*	*2*	*5*	*9*
4	LUS-50TMS-500	66	19	2	87	2	1	1	2	1	0	6	0	*4*	*3*	*6*	*13*
5	LUS-75TMS-500	66	18	1	85	2	2	1	2	2	0	6	0	*5*	*4*	*6*	*15*
6	LUS-100TMS-500	69	18	1	89	0.8	1.4	0.8	1.6	0.3	0	7	0	*3*	*2*	*7*	*12*
7	LUS-50TMS-500-TMS	66	17	0	83	1.5	1	0	2	0.5	0	10	2	*2.5*	*2.5*	*12*	*17*
8	LUS-100TMS-500-TMS	66	18	1	85	2	1	0.5	2	0.5	0	8	1	*3.5*	*2.5*	*9*	*15*
		Q_4[d]	Q_3'	Q_2'	—	T_3'	T_2'	T_1'	D_2'	D_1'	$(M_1'')'$	$(M_1)'$	$(M_0)'$	*T′*	*D′*	*M′*	Si_{org}'
7	LUS-50TMS	75	24	1	—	—	—	—	—	—	0	13	1	—	—	*14*	*14*
8	LUS-100TMS	81	19	0	—	—	—	—	—	—	0	13	5	—	—	*18*	*18*
9	LUS-25TMS-500	68	29	4	—	1	1	0	1	1	0	6	0	*2*	*2*	*6*	*10*
10	LUS-50TMS-500	76	22	2	—	2	2	1	3	1	0	6	0	*5*	*4*	*7*	*15*
11	LUS-75TMS-500	77	21	2	—	3	2	1	3	2	0	7	1	*6*	*5*	*7*	*18*
12	LUS-100TMS-500	78	21	1	—	1	2	1	2	0.3	0	7	0	*4*	*2*	*8*	*14*
13	LUS-50TMS-500-TMS	80	20	0	—	2	1	0	2	1	0	13	2	*3*	*3*	*15*	*21*
14	LUS-100TMS-500-TMS	78	21	1	—	2	1	1	2.5	0.5	0	10	1	*4*	*3*	*11*	*18*

a, $M = M_1'' + M_1 + M_0$

b, $\Sigma Si_{org\text{-}i} = T + D + M$

c, Analytical integral error by noise of baseline (± 0.5)

d, $Q_i' = Q_i / \Sigma Q_i$; $T_i' = T_i / \Sigma Q_i$; $D_i' = D_i / \Sigma Q_i$; $M_i' = M_i / \Sigma Q_i$; $Si_{org}' = \Sigma Si_{org\text{-}i} / \Sigma Q_i$. Error ± 0.5

Evolution of TMS coverage versus HCl/TMA% is presented by the intensity of IR 847 cm^{-1} peak. It increases upon the more removal of TMA^+ (Figure 14A, black square) and further decreases (Figure 14A, red circle) due to the combustion of organic moieties under the subsequent thermal treatment. Nonetheless, re-capping TMS groups on the calcined materials results in a strengthened intensity of the IR 847 cm^{-1} peak due to the growth in number of Si-C (Figure 13C; Figure 14A, green triangle). It indicates the

successful grafting of TMS function on the novel Si surface as well as an effective thermal activation to the surface silanol.

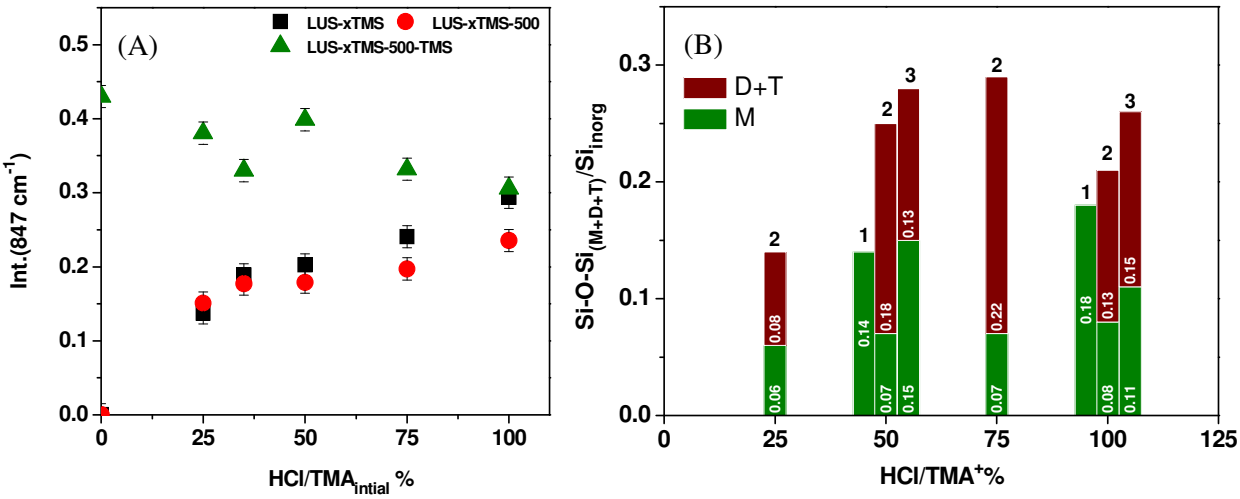

Figure 14 Evolution of TMS coverage versus HCl/TMA% reported in molar ratio by (A) the IR intensity of peak at 847 cm^{-1} and (B) the quantitative ^{29}Si MAS NMR spectra. In (B), Si-O-$Si_{(M+D+T)}/Si_{inorg}$ = $\Sigma[1*(M_1+D_1+T_1)+2*(D_2+T_2)+3*T_3] / \Sigma Q_i$ (i = 2-4); bar marked 1: LUS-xTMS, marked 2: LUS-xTMS-500, marked 3: LUS-xTMS-500-TMS.

However, the amount of re-capping group decreases consistent with increasing the TMS coverage before calcination. Indeed, LUS-500-TMS shows 1.5 more coverage of TMS compared to LUS-100TMS-500-TMS. Assuming a 1:1 pending TMS/Si-OH stoichiometry in the former, the moieties TMS in the latter is not only monopodal but also di- and/or tripodal linkage direct with the surface silanol group which causes the available silanol decreasing. Consistently, the dipodal and tripodal can be presumed to increase by 0-20% upon the increasing of TMS coverage before calcination which leads to an ultra-stable surface.

Further information about the dipodal and tripodal Si-O-Si linkage is obtained from the quantitative ^{29}Si MAS NMR (Figure 14B). The amount of M silicon atom in LUS-xTMS is reduced more than half after 500 °C calcinations (Figure 14B, bar marked 1; Table 4, entries 7-8, 10 and 12). Instead, D and T species silicon is generated in principle

leading to double and triple Si-O-Si directly linked to the surface, respectively. The factors which determine the results of new species silicon are investigated when comparing LUS-50TMS-500 and LUS-100TMS-500. The latter produces more Si-O-Si linkage although it possesses more TMS revealing the presence of the residual silanol group is promotive to the conversion. Accordingly, LUS-75TMS-500 producing more than LUS-50TMS-500 proves the amount of TMS is also a way to tune the linkage (Figure 14B, bar marked 2). The re-capping causes the Si-O-Si decreasing in consistence with the reduced D and T species indicating a further conversion between the species (Figure 14B, bar marked 3; Table 4, entries 13-14).

5.4 Ti post-grafting and catalytic reaction

The novel Si surface after calcinations was detected by post-grafting of Ti(*i*-*O*Pr)$_4$ as well. And UV spectra were utilized to characterize the coordination of Ti species in the calcined materials. With increasing the calcination temperature, the incorporation of Ti led to more penta- or octahedral species that cause red-shift in the UV spectra (Figure 15A-B; Figure 16).

On the other side, LUS-50E-380-Ti absorbed at 232 nm maximum compared to the LUS-50E-Ti centred at 215 nm, possessing half Ti loading (Ti: 0.26 wt%) than that of the latter (Ti: 0.58 wt%). And the material without organically modification LUS-T100 was incorporated 0.17 wt% Ti but has more red-shift in the UV spectrum (Figure 15C). The organically modified surface of the materials became more hydrophilic under the thermal treatment, due to the loss of organic function and the generated silanol groups.

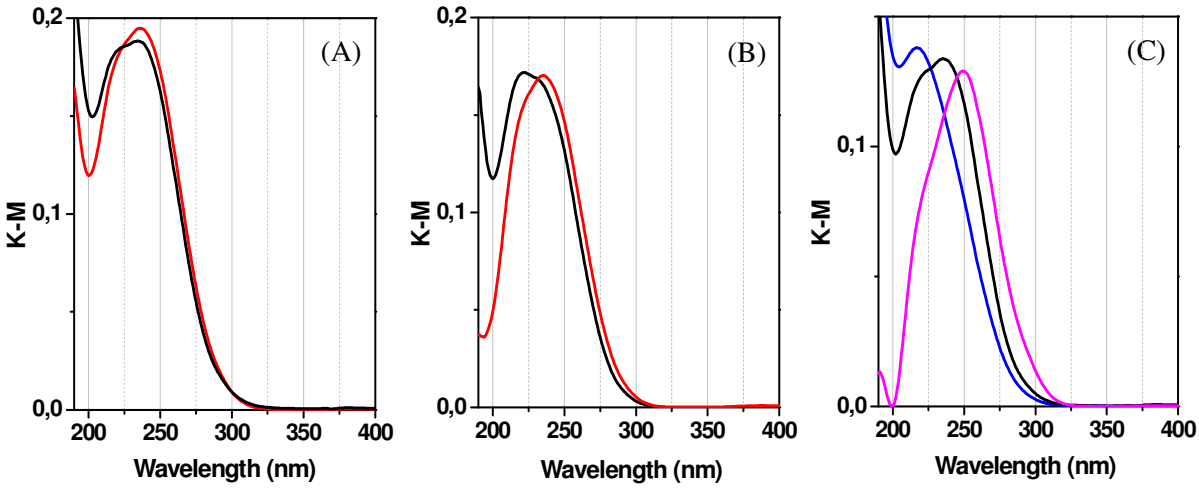

Figure 15 UV-vis spectra for Ti post-grafted on (A) LUS-50E and (B) LUS-100E after calcined at 380 °C (black line) and 480 °C (red line) and (C) the comparison of LUS-50E-Ti (Ti: 0.58 wt%; blue line), LUS-50E-380-Ti (Ti: 0.21 wt%) and LUS-Ti (Ti: 0.17 wt%; pink line).

Nonetheless, the TMS function modified materials have more hydrophilic surface than that of LUS-xE. The LUS-xTMS-cal-Ti absorbed less energy in the 200-220 nm region which is assigned to the absorption position of tetrahedral species (Figure 16, black lines). Furthermore, the LUS-xTMS-600-Ti displayed the same UV spectrum as that of LUS-Ti when after calcined at 600 °C (Figure 16A, red line and pink line). It means the LUS-xTMS-600 material was totally recovered into the initial pure mesoporous silica by the thermal treatment with accordance in the results of N_2 adsorption.

The thermal treatment made the silica surface rich in silanol groups as well as the considerable organic functions. Therefore, the former supplies chances to accommodate other groups via using the silanol groups, and the latter can not only hydrophobized the surface but also isolated the new introduced groups, such as Ti species.

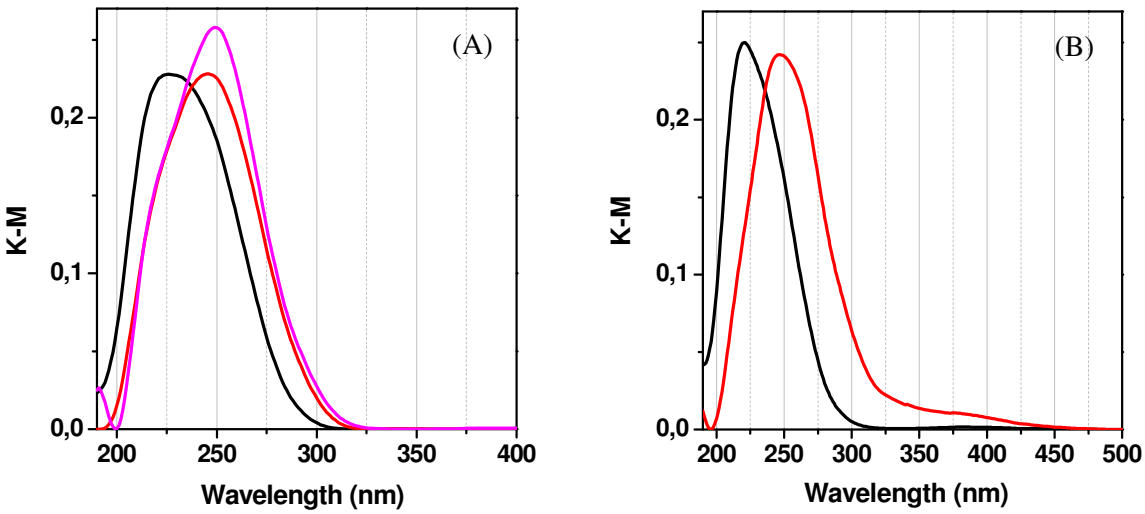

Figure 16 UV-vis spectra for Ti post-grafted (A) LUS-50TMS and (B) LUS-100TMS after calcined at 500 °C (black line) and 600 °C (red line) and the comparison of LUS-50TMS-400-Ti (Ti: 0.21 wt%) and LUS-Ti (Ti: 0.17 wt%; pink line).

Compared to the no-capped LUS-500-Ti, the LUS-xTMS-500-Ti catalysts shows considerable activity in epoxidation of cyclohexene although low Ti loading leads to weak conversion (Figure 17A, green bar; Table 5). Obviously, the TON reaches the top at LUS-75TMS-500-Ti in good consistence with the result of Si-O-Si from quantitative ^{29}Si MAS NMR (Figure 17A, red symbol). Note that the activity is optimized with the ultra-stable surface that the retention of organic moieties has been improved by dipodal and tripodal anchoring on the surface. Nonetheless, the selectivity of epoxide gets the highest point at LUS-50TMS-500-Ti probably due to the optimized hydrophobicity and accessible metal sites, and then decreases with increasing by-products of allylic and diols because of the reduced reaction area and less hydrophobic moities (Figure 17B).

As to the LUS-xE-cal-Ti catalysts, LUS-50E-380-Ti and LUS-50E-480-Ti showed nearly no difference in the catalytic activity, in the well accordance with the UV spectra (Table 5, entries 7-8; Figure 15A). The LUS-100E-cal-Ti catalysts display a slightly decreasing difference on both of the TON and epoxide selectivity with calcination

temperature increasing owning to the less tetrahedral Ti incorporation (Table 5, entries 9-10; Figure 15B).

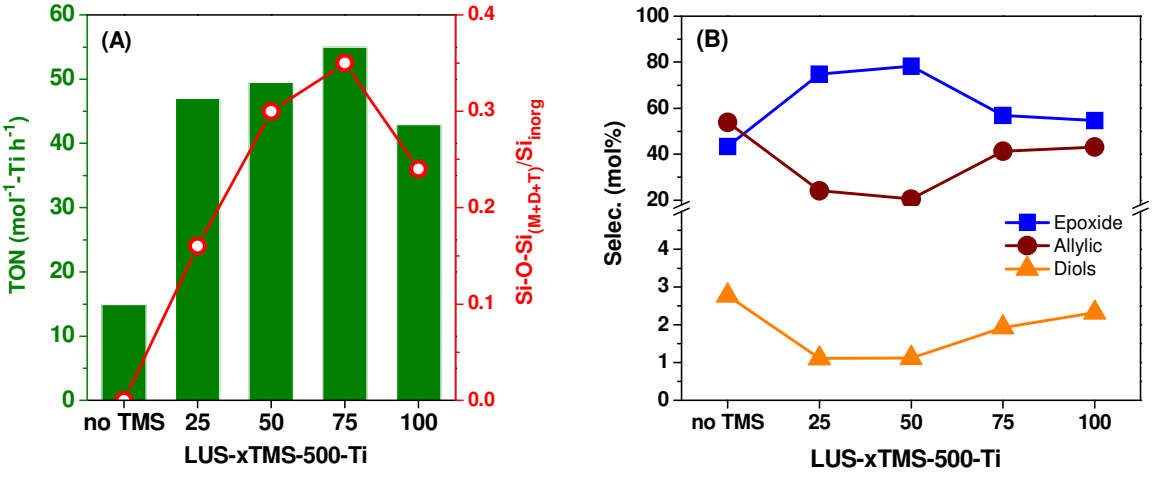

Figure 17 Dependence of (A) the TON consistent with Si-O-Si linkage from organic moieties and (B) the products selectivity on the LUS-xTMS-500-Ti (x = 0, 25, 50, 75 and 100).

Table 5 Epoxidation of cyclohexene with TBHP over LUS-xTMS-cal-Ti and LUS-xE-cal-Ti.

Entries	Sample	Ti/Si_{total}	Convn (mol%)	TON (mol(mol-Ti·h^{-1}))	Selec. (mol%)		
					Oxide	Allylic	Diols
1	LUS-500-Ti[a]	0.009	2,7	15	43	54	3
2	LUS-25TMS-500-Ti	0.003	2,0	47	75	24	1
3	LUS-50TMS-500-Ti	0.003	2,1	50	78	21	1
4	LUS-75TMS-500-Ti	0.003	2,3	55	57	41	2
5	LUS-100TMS-500-Ti	0.003	1,8	43	55	43	2
6	LUS-50TMS-600-Ti	0.003	0,8	19	23	73	4
7	LUS-50E-380-Ti	0.003	1,1	27	56	43	1
8	LUS-50E-480-Ti	0.003	1,2	29	50	47	2
9	LUS-100E-380-Ti	0.003	1,7	40	60	38	3
10	LUS-100E-480-Ti	0.003	1,3	31	51	46	3

a, Catalyst weight: 25 mg.

5.5 Conclusion

The organic functionalized mesoporous silica treated thermally is shown a stable structure as well as keeping the initial organic groups in a controlled distribution. Moreover, the surface calcined at a proper temperature favours grafting extra new silane groups such as EBDMS, TMS etc. or Ti species with an excellent isolating effect.

The calcination temperatures are chosen 380 ºC, 480 ºC and 580 ºC for the EBDMS modified materials and 400 ºC, 500 ºC and 600 ºC for the TMS modified materials from the TGA curve tables. Calcined at superior temperatures, the structure of the materials with either EBDMS or TMS have been preserved with the approximate specific surface area, pore volume and pore diameter as those of LUS-T100 according to the nitrogen sorption isotherm. Note that calcined at 600 ºC LUS-T100-TMS material can be recovered to the initial meso-structure although full TMS coverage before.

The evolution of the organic surface is profiled by FT-IR spectra that the Si-C moieties in EBDMS groups loss half below 380 ºC then retains until 480 ºC, whereas they stay stable in the TMS groups up to 400 ºC and begin to loss consistently with continuously temperature increasing. Additionally, the Gaussian fitting reveals that the symmetry of [SiO_4] moieties in the siliceous pore wall has been increased drastically by the graft of TMS function, while EBDMS has no such effect. The symmetry decreases with the organic species burning into Si-OH, but there is an increasing ramp consistently with temperature rising to 500 ºC in the TMS covered surface probably due to the generation of D_2 intermediate [$(SiO)_2SiC_2$] rather than other species.

Abundant ultra-active silanol groups as well as di- or tripodal organic moieties generated after calcinations are detected by means of solid state ^{29}Si MAS NMR, taking advantage of which, EBDMS, TMS and Ti species have stably been re-capped on with isolated dispersion. Note that the presence of some initial silanol groups on the organic modified surface can cooperatively promote the conversion of Si-C into extra Si-O-Si. As a result, the calcined surface which had been covered with 75% TMS (LUS-75TMS-500)

is probed an ultra-stable organic surface leading to a superior TON in epoxidation of cyclohexene.

The calcined samples containing organic groups with a vicinity control also display as an ultra-stable catalyst that favors the Ti site isolation in comparison to non-modified silica surface. Consequently, they perform the superior activity and selectivity in the epoxidation of cyclohexene using *tert*-butyl peroxide as oxidant.

5.6 Reference

1 T. Tatsumi, K.A. Koyano, N. Igarashi, *Chem. Commun.*, **1998**, 3, 325.

2 N. Igarashi, K. Hashimoto, T. Tatsumi, *Microp. Mesop. Mater.*, **2007**, 104, 269.

3 A. Corma, M. Domine, J.A. Gaona, J.L. Jordá, M.T. Navarro, F. Rey, J. Pérez-Pariente, J. Tsuji, B. McCulloch, L.T. Nemeth, *Chem. Commun.*, **1998**, 2211

4 J.M. Fraile, J.I. García, J.A. Mayoral, E. Vispe, *J. Catal.*, **2000**, 189, 40.

5 K. Zhang, B. Albela, M. He, Y. Wang, L. Bonneviot, *Phys. Chem. Chem. Phys.*, **2009**, 11, 2912.

Chapter VI

Assignment and quantification of grafted Ti species using UV-Visible Spectroscopy

6.1 Introduction

As described in the *Chapter III* and *IV*, the silyl groups including monopodal e.g. trimethylsilyl (TMS), and dipodal e.g. 1-2-ethanebis(dimethylsilyl) (EBDMS) partially capping the mesoporous silica surface via a controlled grafting technique or a thermal treatment before Ti grafting can both hydrophobize the silica surface and isolate the Ti sites.

It is well known that the Ti-substituted silica catalysts, such as TS-1,[1-5] Ti-β,[6-7] Ti containing ordered mesoporous silica,[8-10] amorphous xerogels,[11-12] and Ti-supported silica[13-16] have exhibited a remarkably high efficiency and molecular selectivity in the catalytic reactions thanks to the different types of isolated or bulky active sites loaded in the support silica. Note that those reactions include photodegradation,[17-19] aromatic hydroxylation,[20] alkane oxidation,[21] olefin epoxidation,[22-23] cyclohexanone ammoximation,[24-25] oxidation of ammonia to hydroxylamine,[26-27] and the conversion of secondary amines to dialkylhydroxylamines[28] and secondary alcohols to ketones.[29]

Currently, thus, the UV spectroscopy is generally used as a simple means to predict or verify the coordination environment around a titanium center in the solid state. It shows an absorption associated with the ligand to metal charge transfer (LMCT) from the oxygen atom to the Ti(IV) ion, namely $Ti^{4+}O^{2-} \rightarrow Ti^{3+}O^{-}$. Band appears in the λ = 200-220 nm region arising from the LMCT of oxygen to titanium(IV) in the tetrahedral sites. When the tetrahedral Ti is coordinated by the inserted water (or ammonia) molecules, absorption band shifts at λ = 220-260 nm, indicating the pentahydral or octahedral species.[30] A broader band besides to the formers exhibits in the range of λ = 260-320 nm assigned to an incipient oligomerization of Ti tetrahedral species like TiO_x nanocluster, bulky anatase, etc.

Numerous experimental and theoretical studies using UV spectroscopy have advanced the detail about the coordination of Ti in the solid silica materials and its active sites for the heterogeneous catalysis.[31-36] Normally, the tetrathedral Ti site demonstrates highly catalytic activity in the oxidation with H_2O_2 or tert-butyl peroxide as oxidant[37-38] and the penta- or octahedral Ti species will generate Brönsted acid sites due to the hydroxyl groups or water in their coordination sphere.[39-40] Moreover, the TiO_2 has been widely studied for the removal of several types of organic pollutants particularly owing to its excellent photocatalytic activity.[17-18] Nonetheless, to our knowledge no study concerns the quantification of Ti sites that would relate to the 'real' turnover number (TON) of Ti-loaded catalysts.

Herein, each Ti sites including tetrahedral, octahedral and TiO_x oligomer in the catalysts LUS-E-Ti-n which were applied in the *Chapter III* are quantified. The quantification method processes several steps: first, using diffuse reflectance UV spectroscopy (DR UV) to characterize the samples in solid state, then the UV spectra are simulated independently by a set of Gaussian function that correlates to each Ti site. Since the absorption area of fit is proportional to the measured Ti content, based on the Kubelka-Munk theory,[41] the extinction coefficient constant (ε) of each Ti site in the TiO_2-SiO_2 solid state can be calculated. Thus the coefficient constant of Ti site can furthermore amend the virtual amount of active Ti nucleus involved in the catalytic epoxidation of cyclohexene that relates to the real TON.

6.2 Calculation of extinction coefficient constant (ε)

6.2.1 DR-UV spectroscopy for Ti deposits on the surface of silica

The Ti deposits were characterized using diffuse reflectance UV spectroscopy (DR-UV). During the measurment, the samples were stored under normal conditions, and spectra were recorded directly in air with no further pretreatment. According to Kortüm, the absolute reflectance R_∞ of an infinitely thick layer must be used to calculate Kubelka-Munk spectra. The theory predicts that $F(R)$ is proportional to the concentration c of the absorbing species as long as the assumptions of the theory are fulfilled, namely, that the absorbance of the sample is not too high (eq. 1).

$$F(R_\infty) \equiv \frac{(1-R_\infty)^2}{2R_\infty} \approx c \qquad \text{Eq. (1)}$$

The standard form spectroteflon with the absolute reflectivity R_{std} = 80% was used as reference. The reflectivity of the sample R_{samp} which is related to the measured intensity of both standard reference J_{std} was corrected according to $R_{samp} = \sigma_{std} J_{samp}/J_{std}$. After K-M calculation, $F(R)$ spectra were found to be linear up to $F(R)_{max}$ = 1.0. A higher absorption causes a change in the spectrum that is observed as a blue shift in the $F(R)$ spectrum (Figure 1A, black line).

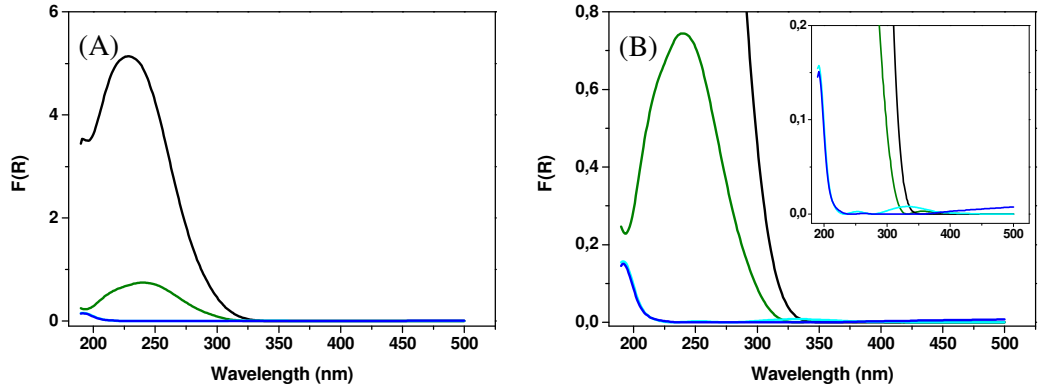

Figure 1 UV spectra of Ti incorporated silica materials and after dilution using LUS-cal as diluent. Black line: initial sample; green line: initial sample after dilution; blue line: LUS without surfactant calcined at 550 °C for 10 h; cyan line: LUS with surfactant TMABr calcined at 550 °C for 10 h.

In our case, samples showing an absorbance of $F(R)>1$ were diluted with 550 °C calcined LUS (Figure 1A, green line). The diluent exhibits an absorbance of 0.15 centred at 190 nm and LUS with surfactant TMABr calcined at 550 °C for 10 h still exists several bands in the 250-350 nm region (Figure 1B, insert). Therefore, the obtained $F(R)$ is the Kubelka-Munk spectrum calculated with the reflectance of the sample relative to an absorbing diluent LUS-cal.

During the measurement, although the layer of powder in the holder can be regarded as infinitely thick, at least 5 times repeating to get the approximate K-M absorption of the real sample. For example, the error from measurements of 6 times repeating can actually reach ± 8.0% of the final average K-M absorption (Figure 2). Therefore, the total absorption usually results from the average value of 5 times measurement.

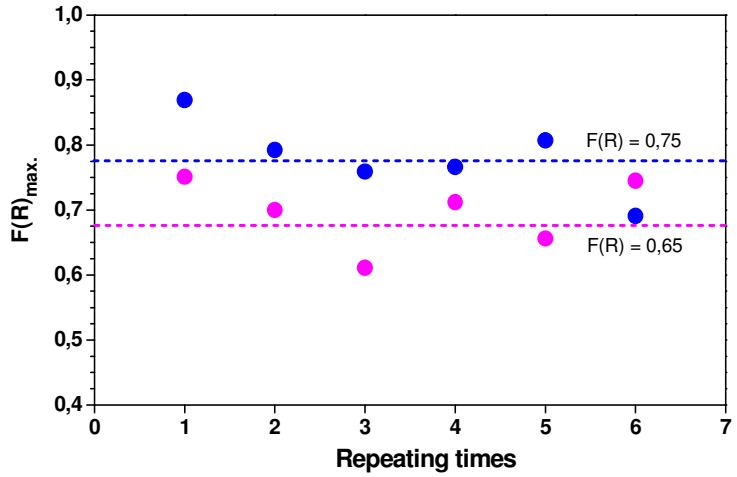

Figure 2 Repeating times of the UV spectra measurement.

It is known that tetrahedral Ti species, which are mostly contained by catalysts such as TS-1 (Figure 3, black line), Ti-β, i.e. present a O→Ti ligand-metal charge transfer band centered at 200-220 nm. The tetrahedral sites has been reported to be active in the catalytic reactions, for example the epoxidation of olefin, for the -O-O- in oxidants such as H_2O_2, tert-butyl hydroperoxide i.e. can coordinated within the coordination sphere of

the tetrahedral Ti sites. While the introduction of water molecule leads to the penta-coordianted or octahedral sites, these bands appear between 225-260 nm. Upto the saturated coordaination of TiO_x, the nanoclusters and bulky TiO_2 phases the maximum arises at 280-320 nm like the anatase (Figure 3, red line), rutile titanium oxides.

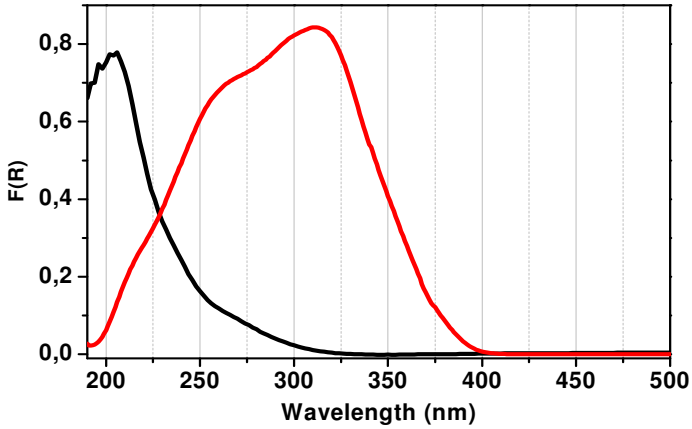

Figure 3 UV-vis spectra for diluted TS-1 (black line) and anatase (red line).

6.2.2 Simulation of UV spectra

The excitation energy of the charge transfer transitions (LMCT) between the O^{2-} and the empty *d* orbital of Ti^{4+} can be estimated from the optical electronegativities χ of ligand O and Ti^{4+} by the following equation:

$$\bar{\upsilon}\left(cm^{-1}\right) = 300000\left[\chi_{opt}(O) - \chi_{opt}(Ti)\right] \qquad \text{Eq. (2)}$$

The χ_{opt}(Ti) varied from 1.85 to 2.05 with the increase of the coordination of Ti from tetrahedral to octahedral. Moreover, the published χ_{opt}(O) are quite arbitrary due to the different second coordination sphere such as $\chi_{opt}(Si\text{-}O^-)$=3.17, $\chi_{opt}(H\text{-}O^-)$=2.9-3.45, $\chi_{opt}(O^{2-})$=3.45, and $\chi_{opt}(H_2O)$=3.5, etc. Therefore, the energy change is not only due to the coordination of Ti but also is accompanied by a change in the second coordination sphere

of ligand.[42] For perfect symmetries, an increase of the excitation energy from 49000 cm^{-1} for the tetrahedral one [$Ti(OSi)_4$], to 44000 cm^{-1} for octahedral coordination [$Ti(OSi)_6$] is calculated (Figure 4A).

Actually, for TiO_x species bonded to supports such as zeolites, mesoporous silica i.e., a strong deviation from perfect symmetries can be expected so that exact calculations of excitation energies will not be possible. However, the basic conclusion that the energies will increase with decreasing coordination number should be applicable for an assignment. The assignments of the absorption maximum at around 49000, 45000, and 36000 cm^{-1}, gleaned from the spectra analysis, to the different $TiOx$ species bonded in a tetrahedral, penta- or octahedral, TiO_2 nano- or bulk phases in the general manner of the silica framework is mainly based on theoretical considerations and interpretations of the UV-vis spectra of TS-1 and anatase.[33]

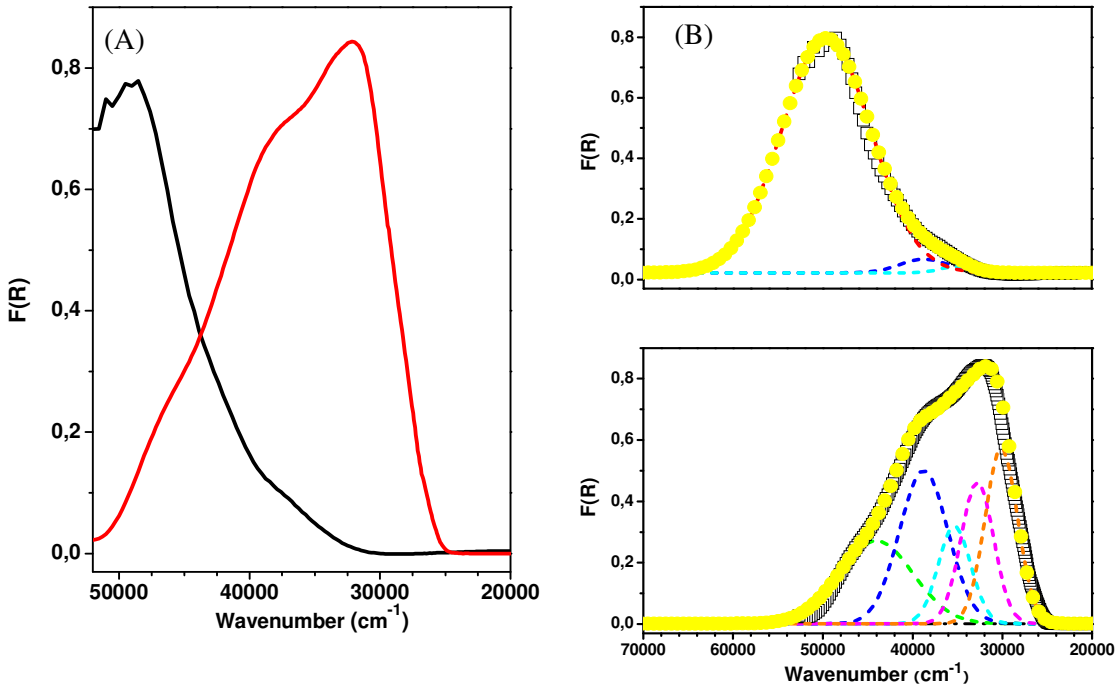

Figure 4 (A) UV-vis spectra and (B) Gaussian fits for diluted TS-1 and anatase. In (A), black line: TS-1, red line: anatase. In (B), square: experimental data, yellow solid circle: cumulative data, colourful dash line: fits (detail, Table 1)

The UV-vis spectra of the Ti incorporated samples which had been explored in the air, are dominated by the overall absorption of each species. For TS-1, the spectrum demonstrates narrow and concentrated at 49000 cm^{-1}. The mainly Gaussian fits can consist of a strong band at 49000 cm^{-1} and two slight shoulders at 39000 cm^{-1} and 35000 cm^{-1}, respectively (Figure 4B, upper). While that for anatase is broad and red shifted in the lower energy region, those fits are more interpreted in the way that a fraction of penta-coordinated species at the 44000 cm^{-1} and octacoordinated one at the 39000 cm^{-1}. Moreover, the growing bands related to the TiO_x nano-oligomer and TiO_2 bulky clusters appear at 35000 cm^{-1}, 33000 cm^{-1} and 30000 cm^{-1}, respectively (Figure 4B, lower). These observations are generally consistent with previous findings except that the dehydrated species without oligomer and clusters of TiO_2 at low wavenumber were reported.[33]

The fits with the defined centre are cumulated in the simulation of UV spetra curves by using the the Gaussian equation (eq. 3).

$$y = y_0 + A \cdot e^{-\frac{1}{2}\left(\frac{x-x_c}{w}\right)^2} \qquad \text{Eq. (3)}$$

Where the $\boldsymbol{y_0}$ is related to the spectrum baseline, usually equals 0, and $\boldsymbol{e}$ is *Euler's number* 2.718281828. $\boldsymbol{A}$ is the intensity of each fit determined by the cumulative need. $\boldsymbol{x_c}$ will use the centre parameter in wavenumber (cm^{-1}) and $\boldsymbol{w}$ stands for the width of each Gaussian peak (cm^{-1}). According to the definition of Gaussian function, the fit will be symmetric and represent each independent Ti species. Six fits have been defined corresponding to the coordinated Ti sites of tetrahedral, pentahedral, octahedral, two types of oligomers, and TiO_2 cluster (Table 1).

Table 1 Parameters of Gaussian fits for deconvolving the UV spectra

	Fit 1	Fit 2	Fit 3	Fit 4	Fit 5	Fit 6
Coordination	*Tetrahedral*	*Pentahedral*	*Octahedral*	*Oligomer 1*	*Oligomer 2*	*Cluster 1*
Centre/cm^{-1}	*49000±500*	*44248±400*	*39063±300*	*35088±250*	*32787±200*	*30120±150*
Centre/nm	*204±2*	*226±2*	*256±2*	*285±2*	*305±2*	*332±2*
Width/cm^{-1}	*5000*	*4100*	*2700*	*1800*	*1800*	*1800*
Color of line	*red*	*green*	*blue*	*cyan*	*pink*	*orange*

The appearance of the oligomers bands at 35000 cm^{-1} and 33000 cm^{-1} with rising Ti loading corresponds to the presumed intermedia species which contain the growing molecules of the octahedral species, nonetheless smaller than the anatase TiO_2.

With the six defined fits, the UV spectra of samples LUS-E-Ti-n are well simulated by the cumulative Gaussian curves (Figure 5). The relative content of the tetrahedral species presented by the red dash line in Figure 6, has been decreased with the increasing amount of the incorporated Ti. While the octahedral species was strengthened gradually indicating the conversion between the two sites. However, the pentahedral species, acting as an intermedia from tetrahedral to octahedral sites, increased from the Ti/Si of 0.0082 to 0.0465 (Figure 5, a-d; Table 5, entries 1, 3, 4 and 7) and decreased when Ti/Si ≥ 0.0628 (Figure 5, e-f; Table 2, entries 11 and 13). The trend reflects the saturated coordination of tetrahedral sites leading a conversion to the pentahedral ones, and the latter also forced the generation of the octahedral sites simultaneously.

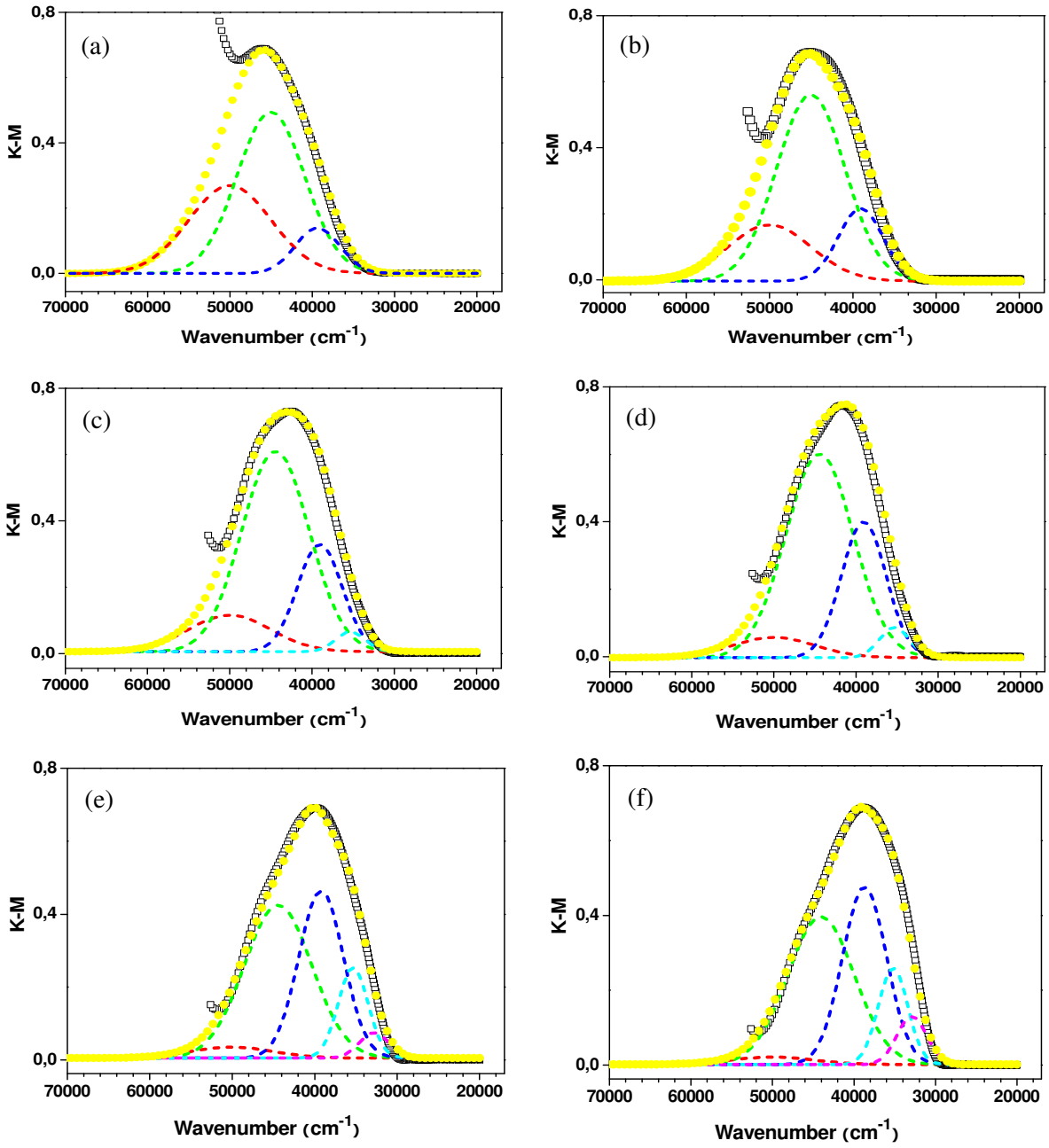

Figure 5 UV-vis spectra deconvolution for LUS-E-TiPr with the Ti/Si ratio of (a) 0.0082 (0.58 %), (b) 0.0180 (1.27 %), (c) 0.0323 (2.26 %), (d) 0.0465 (3.10 %), (e) 0.0628 (4.27 %), (f) 0.0831 (5.43 %), Ti weight percentage in the parentheses. Hollow square for the experimental curve, yellow solid circle for the cumulative curve, dash lines for fits (detail in Table 2)

When up to the 2.26 wt% Ti incorporated, the oligomer 1 appeared and until 4.27 wt% Ti, the oligomer 2 emerged, which reveals the growing procedure of the Ti species from the monomer to the polymer. Both of the oligomers increased (Figure 5, c-f; Table 2, entries 4, 7, 11 and 13) with more Ti loading in the accordance with the trend in the

Figure 4B. The oligomers have been reported as a non-favorable species in the catalysis, where the H_2O_2 or TBHP will be inactivated by the consumption of -O-O- when bonded with the Ti sites in oligomers.[35]

As to the UV spectra of LUS-Ti-n samples without organic modification have a distinguished difference with those of the modified ones. After deconvolution, all the spectra consist of the fits of penta-, octahedral and oligomers with a disappearance of the tetrahedral species (Figure 6). Impregnating in the excess cyclohexane solution, the Ti precursor was able to distribute along the mesoporous channels. However, the coordination of Ti was much faster in the pure silica surface than that with the EBDMS group and tetrahedral sites were active and less stable that it is easier to become the pentahedral or more ones.

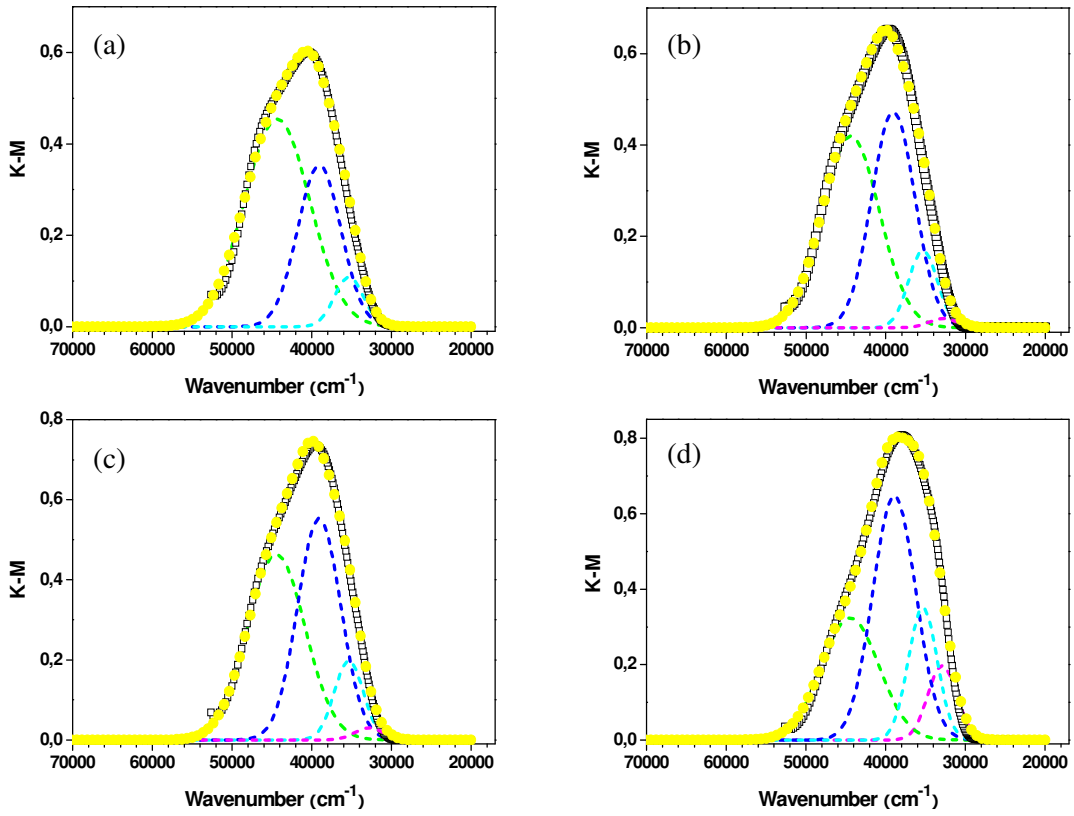

Figure 6 UV-vis spectra deconvolution for LUS-Ti with Ti/Si ratio of (a) 0.0072 (0.46 wt%), (b) 0.0240 (1.55 wt%), (c) 0.0487 (3.01 %), (d) 0.2160 (10.65 wt%), Ti weight percentage in the parentheses. Hollow square for the raw curve, yellow circle for the cumulative curve, dash lines for fits (detail in Table 1).

The species with more coordination number were developed by the increasing the Ti loading as well as that in the LUS-E-Ti-n samples. Surprisingly, the oligomer 1 appeared when Ti incorporated in for 0.46 wt% and the oligomer 2 formed in the sample containing Ti ≥ 1.55 wt%, which are almost 5 times and 3 times more in the LUS-E-Ti, respectively (Figure 6, a-b; Table 2, entries 4 and 19, 11 and 21).

Table 2 Analytical results of UV spectra for Ti incoordinated mesoporous silica

Entries	Ti wt%	Abs%						Total abs./Ti
		200 nm	225 nm	255 nm	285 nm	305 nm	330 nm	
1[a]	0.58	35	55	10	0	0	0	1,90E+06
2	1	34	47	19	0	0	0	2,52E+06
3	1.27	22	61	17	0	0	0	2,48E+06
4	2.26	15	59	24	3	0	0	2,26E+06
5	2.45	13	62	24	2	0	0	1,97E+06
6	3.01	15	58	25	2	0	0	—
7	3.1	5	62	30	3	0	0	1,85E+06
8	3.28	12	52	29	6	1	0	2,00E+06
9	3.8	4	55	32	7	2	0	1,24E+06
10	4.18	41	40	12	6	0	0	1,76E+06
11	4.27	2	48	35	11	3	0	1,43E+06
12	5.08	0	44	38	12	6	0	1,38E+06
13	5.43	0	41	38	14	7	0	1,01E+06
14	5.51	0	47	36	11	5	0	8,31E+05
15	5.77	5	51	34	8	2	0	1,06E+06
16	7.03	0	56	34	9	1	0	7,42E+05
17	8.67	0	46	36	11	7	0	8,60E+05
18[b]	0.17	0	39	58	3	0	0	—
19	0.46	0	62	32	7	0	0	—
20	0.84	0	55	35	9	1	0	—
21	1.55	0	48	41	10	1	0	—
22	3.01	0	47	42	10	2	0	—
23	5.85	0	46	41	11	2	0	—
24	10.65	0	30	45	16	9	0	—
Anatase	60	0	23	28	12	17	20	—
TS-1	1	96	0	3	1	0	0	4.80E+06

a, Entries 1-17: LUS-E-Ti-n

b, Entries 18-24: LUS-Ti-n

The area of each fit is obtained by the giving full width at half maximum (FWHM) and height (*A* in eq. 3). Compared to the total area of the spectrum, the relative area (Abs.%) is considered as the absorption energy proportion for each Ti species. Moreover, it also stands for the probability of the possible formation for one Ti atom since the total area of the spectrum is normalized by the amount of Ti atoms (Table 2).

6.2.3 Extinction coefficient constant (ε) of different Ti sites

The results derivative from UV spectra deconvolution, was put into multiple linear regression to get the extinction coefficient constant ε_n. In the equation (4), «abs_n%» is related the proportion of Ti species with tetrahedral, octahedral or clusters coordination which would contribute to the total absorption. And «ε_n» (n=1-5) stands for the extinction coefficient constant of each Ti species that was simulated in fit-n.

$$\mathbf{E} = abs_1\% * \varepsilon_1 + abs_2\% * \varepsilon_2 + abs_3\% * \varepsilon_3 + abs_4\% * \varepsilon_4 + abs_5\% * \varepsilon_5 \qquad \text{Eq. (4)}$$

There are two ways to calculate the ε_n. One is to put the «E» and «abs_n%» into calculation by the analysis tool «*multiple linear regression*» in the Excel or Origin software. The constants ε_1, ε_2, and ε_3 related to the absorption of Ti coordinated monomer, including tetrahedral, pentahedral and octahedral, are about several times intensive than the ε_4 and ε_5 of clusters.[32] Thus the multiple linear equation contained only ε_1, ε_2, and ε_3 three polynomials assumed ε_4 and ε_5 having no effect (eq. 5). Then ε_4 and ε_5 can be calculated by multiple linear regression again using the obtained $\varepsilon_{1\text{-}3}$ to eliminate the influences of Ti monomer (eq. 6-7). The other calculation of $\varepsilon_{1\text{-}5}$ was carried out by defined programme applying *linear least-squares fit* method. It gives the optimized $\varepsilon_{1\text{-}5}$ that matches the results from the first way well (Table 3, A).

$$\mathbf{E} \approx abs_1\% * \varepsilon_1 + abs_2\% * \varepsilon_2 + abs_3\% * \varepsilon_3 \qquad \text{Eq. (5)}$$

$$\mathbf{E'} = abs_1\% * \varepsilon_1 + abs_2\% * \varepsilon_2 + abs_3\% * \varepsilon_3 \qquad \text{Eq. (6)}$$

As expected that the ε_1 due to the tetrahedral site is nearly 4 times to the constants of pentahedral and octahedral sites and 10-10^2 times to the ε_4 and ε_5, which are assigned to the extinction coefficient constants of small TiO_x polymer and bulky TiO_2 cluster, respectively (Table 3). These spectral differences are related to different Ti-OSi bonding length and bond angle of the Ti sites. With more insert ligands, such as H_2O or -OTi, the Ti-O bonding length increases and O-Ti-O angle decreases. Therefore it will weaken the π bonding between the *p* orbital of O and unoccupied *d* orbital of Ti, leading to less electrons jumping from the bonding *e* molecular orbital to the anti-bonding *e**.

Table 3 Extinction coefficient constant for Ti species in the hydrated mesoporous silica material

Cons. ($mmol \cdot cm^{-2}$)	ε_1	ε_2	ε_3	ε_4	ε_5
A	(250±22) E+04	(70±34) E+04	(80±60) E+04	(2±2) E+04	(11±8) E+04
B[a]	230 E+04	60 E+04	75 E+04	4 E+04	17 E+04

a, Calculated by computerial programme using linear least-squares fit.

The comparasion between the UV absorption of one Ti unit (tot. abs/Ti) in the solid material «E» and calculated «E''_a» and «E''_b» using $\varepsilon_{1\text{-}5}$ is presented in Figure 7. It contains 10% error considering the influences resulting from the UV spectra measure, curves simulating, i.e. Most of the calculated results E'' fit the UV absorption. While increasing the Ti loading, the tetrahedral species gradually transfer to the penta-, octa-hedral and clusters (Table 1), and consequently the absorption decreases due to the much smaller constants of latters.

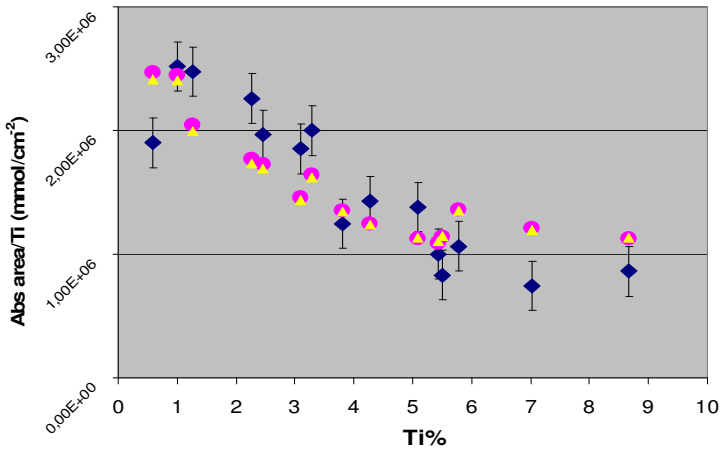

Figure 7 Fitness between the UV spectra deconvolution and the calculation for Ti incorporated mesoporous silica. Blue diamond: experimental E; pink circle: calculated E''_a; yellow triangle: calculated E''_b.

It is worthing to note that the samples applied in the simulation using Gaussian function represent a sort of material which are hydrophobized by organic group and hydrated. The LMCT may be affected by the micro-environtment around the metal centres. Thus a series of dehydrated Ti-MCM-41 should be investigated in the further study.

6.2.4 DFT simulation

As described in the experimental section, the independently deconvolved tetra-, penta-, octahedral and dimer species has been employed to the DFT method using SiH_3 as coordination ligand to simulate the Ti(IV) sites in the mesoporous silica and to study its interaction with added H_2O molecules (Table 4).

Table 4 Geometrically optimized features of the Ti tetra-, penta-, octahedral and dimer moieties.

	Tetrahedral	Pentahedral	Octahedral	Dimer
Structure	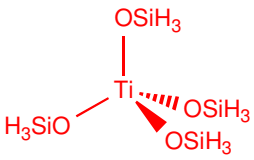	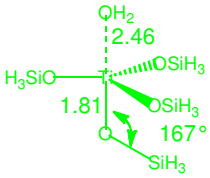	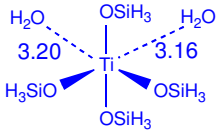	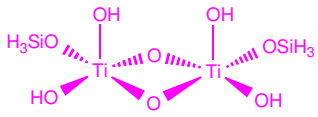
Abs_{max}/nm	194	208	207	218-260
Bonding length/Å	TiO = 1.80	TiO = 1.80-1.84	TiO = 1.80-1.84	TiO = 2.00 TiOH = 1.80 TiOSi = 1.81
Ti-O-Si Angle/°	140	151, 167	130, 160	164, 166
Stability	—	-40.56 kJ/mol	+5.6 kJ/mol	—

A single tetrahedral coordinated with four $–SiH_3$ is reported in the optimized bonding length TiO = 1.80 Å with Ti-O-Si angle 140°. After inserting a H_2O molecule leading to pentahedral causes an elongation of the Ti-O bond to TiO = 1.80-1.84 Å, averaged over the five framework atoms. In the meanwhile, the angles in pentahedral coordination have been widen to 151° and 167° related to the horizontal and vertical Ti-O-Si, respectively. Apparently, the insertion of H_2O molecule has two effects compared with the tetrahedral: 1), decreasing the electron density around the Ti center due to the electrophile O atom; 2), distorting site geometry thus the Ti-O-Si angle enlarging. The former one results in the weaker interaction thus the longer bonding length, while the latter suggests an probability of a π donation from O to the electronic empty d orbital of Ti via the more opening Ti-O-Si bond.[31-32] As to inserting two H_2O molecules in octahedral, the change of Ti-O bond distance is too slight to observe but the angles

showing 130° and 160° indicate a more distorted structure by force. Note that the octahedral is calculated less stable than pentahedral with the final binding energy +5.6 kJ/mol compared to -40.56 kJ/mol of the latter.

As far as the species with geometrically optimized features is concerned, their absorption in UV radiation region is shown in Figure 8. The introduction of H_2O molecule within the coordination sphere of the tetrahedral Ti site leads to a red-shift of the electronic transition calculated by DFT to a greater wavelength (Figure 8, red, green and blues lines). This finding agrees with the experimental observation that an increase in the coordination number of the titanium center causes the wavelength of the LMCT transition to shift. However, it is difficult to distinguished the pentahedral and octahedral upon the absorption energy which corresponds to the similar bonding length.

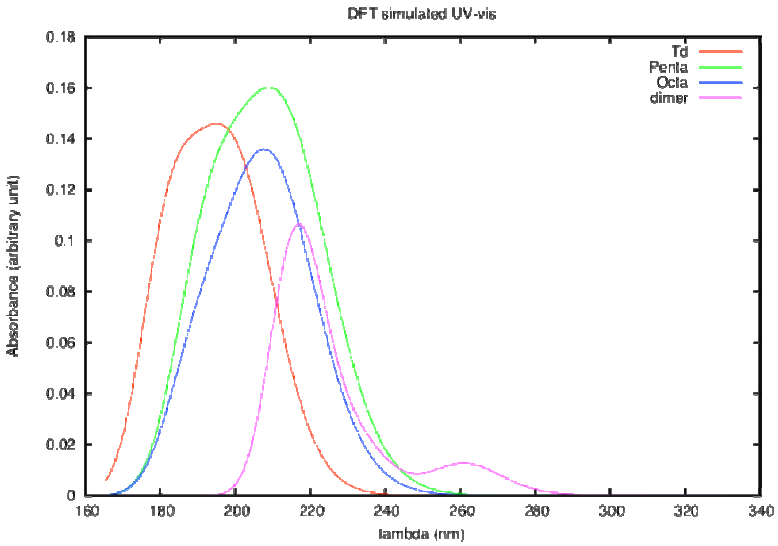

Figure 8 Calculated UV spectra of Ti coordination species.

A spectrum with multiple bands at the right side indicating a fastest red-shift from the tetrahedral species is attributed to the three main transitions in the dimer (Figure 8, pink line). As shown in Table 3, Ti-O = 2.00 Å in the Ti-O-Ti bridge is longer than Ti-OH =1.80 Å and Ti-OSi = 1.81 Å in the outer sphere since the electron donation is stronger in the latter two than in the Ti-O-Ti bridge. Therefore, the band centred at λ =

220 nm probably concludes the transitions of Ti-OH and Ti-OSi while the most right band centred at λ = 220 nm should be attributed to the bridge Ti-O.

These attributions reached show two markedly differences as those obtained from experimental simulation. 1), It is difficult to separate the pentahedral and octahedral species in the hydrated samples and moreover, the former is more stable than the latter revealing the impossibility of transformation from the penta- to octa-. 2), The absorption scale is large for dimer that overcrosses ~40 nm including three types of Ti-O transitions (Table 4). Therefore, as defined in Table 1 the Gaussian fits for deconvolving the UV spectra should be adjusted that fit 2 used to be attributed to pentahedral actually contains octahedral and fit 3 used to be the octahedral is supposed to combine with fit 4 and fit 5 for the dimer transitions (Table 1').

Table 1' Parameters of Gaussian fits modified with DFT results for deconvolving the UV spectra after DFT tuning

	Fit 1	Fit 2	Fit 3	Fit 4	Fit 5	Fit 6
Coordination	*Tetrahedral*	*Penta + Octa*	*Dimer*			*Cluster*
Centre/cm^{-1}	*49000±500*	*44248±400*	*39063±300*	*35088±250*	*32787±200*	*30120±150*
Centre/nm	*204±2*	*226±2*	*256±2*	*285±2*	*305±2*	*332±2*
Width/cm^{-1}	*5000*	*4100*	*2700*	*1800*	*1800*	*1800*
Color of line	*red*	*green*	*blue*	*cyan*	*pink*	*orange*

6.3 Active Ti sites in the epoxidation of cyclohexene and the real TON

Normally, the activity of Ti incorporated silica materials in the catalytic reaction which is presented by turn over numbers of the active sites (TON). The tetrahedral site is usually considered as the active role. However, TON is under estimate because the numbers of the actual active sites use the total loading Ti amount. The coefficient constants ε_n represent the capability of the energy absorption for the ligand-metal charge

transfer of Ti-O. Each site can be deconvolved using the $\varepsilon_{1\text{-}5}$. One Ti atom in the tetrahedral site contributes more absorption under the UV radiation compared to another one in the other coordinated sites. It means the material even has sharply absorbed UV spectrum centred at 200-220 nm region which could possess small amount of tetrahedral Ti sites.

The TON of the epoxidation of cyclohexene on the LUS-E-Ti-n materials has been recalculated using the coefficient constant ε_n. According to the increasing of Ti loading in the catalysts, the TON decreases if total Ti amount was accounted (Figure 9, black circle). However, the new content of Ti site at 200 nm result in nearly a plat of TON except a linear increasing due to the trades of tetrahedral species after Ti/Si = 0.03 in the EBDMS modified catalysts (Figure 9, red circle). Note that the TON refined to 1000 to 2000 is similar to that of classic TS-1 which is uniquely tetrahedral Ti incorporated in the framework. As to the sites at 225 and 250 nm absorption, the former shows a slight change to the raw TON and the latter drops largely with non-ignorable error, both offer the weak supportiveness to the identification of active Ti sites in the reaction.

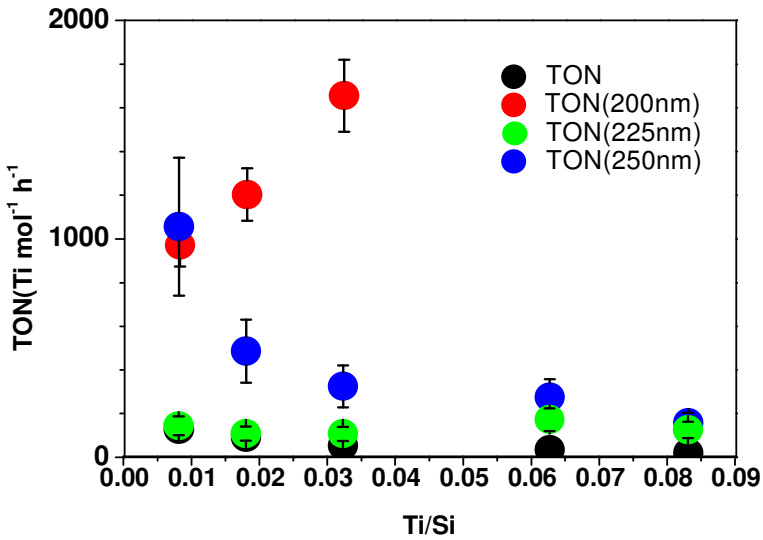

Figure 9 Recalculated TON of the epoxidation of cyclohexene on the LUS-E-Ti-n materials has been recalculated using the coefficient constant ε_n. Black square line: TON; pink square line: TON/(200+225 nm) Ti mol%; green triangle line: TON/(225 nm) Ti mol%; TON/(200+225+255 nm) Ti mol%.

6.4 Conclusion

Since the UV spectra of LUS-E-Ti-n samples were recorded in ambient air containing water the coordination of Ti is more or less saturated producing penta-/octahedral or oligomer coordination states and intermediate red-shifts with the inserted molecules H_2O, or Ti species.

The spectra are fitted independently by a set of Gaussian functions centred at 50000, 44000, 40400, 36000 and 32000 cm^{-1} assigned to the tetrahedral, pentahedral, octahedral, TiO_x nanoparticle and bulky anatase, respectively. Indeed, this is consistent with the observation that tetrahedral TiO_4 become less simultaneously with the increase octahedral and oligomers when loading more Ti species. And the pentahedral Ti sites as defined, is actually an intermediate in the transformation from tetrahedral to octahedral. Consequently, the extinction coefficient constants (ε) of each Ti sites are calculated (250±22)E+04, (70±34)E+04, (80±60)E+04, (2±2)E+04, (11±8)E+04 $mmol \cdot cm^{-2}$ for tetrahedral, pentahedral, octahedral, TiO_x nanoparticle and bulky anatase, respectively. Note that the tetrahedral absorbs ca. 4-5 times more energy than octahedral, and 2 magnitude orders more than TiO_x nanoparticle or bulky anatase.

Accordingly, the 'real' TON has been improved strikingly applying these ε to calculate the active Ti centres which had been used to employ the total Ti loading. The real TON turns out to be a constant for the reactions with a target catalyst, regardless of the kinetic factors. Note that the tetrahedral and pentahedral species are considered as the active sites for the epoxidation of cyclohexene using LUS-E-Ti as catalyst.

6.5 Reference

1 M. Taramasso, G. Perego, B. Notari, US Pat. 4410501, **1983**

2 B. Notari, *Adv. Catal.* **1996**, 41, 253

3 M.G. Clerici, G. Bellusi, U. Romano, *J. Catal.* **1991**, 129, 159

4 M.G. Clerici, P. Ingallina, *J. Catal.* **1993**, 140, 71

5 M.C. Capel-Sanchez, J. M. Campos-Martin, J.L.G. Fierro, *Appl. Catal. A* **2003**, 246, 69

6 R. Hutter, D. C.M. Dutroit, T. Mallat, T.M. Schneider, A. Baiker, *J. Chem. Soc. Chem. Commun*. **1995**, 163

7 P.J. Saxton, W. Chester, J.G. Zajacek, G.L. Crocco, K.S. Wijesekera, US Patent 5621122, **1997**

8 G. Sankar, F. Rey, J.M. Thomas, G.N. Greaves, A. Corma, B.R. Dobson, A.J. Dent, *J. Chem. Soc. Chem. Commun.* **1994**, 2279

9 P.T. Tanev, M. Chibwe, T. J. Pinnavaia, *Nature* **1994**, 368, 321

10 T. Maschmeyer, F. Rey, G. Sankar, J. M. Thomas, *Nature* **1995**, 378, 159

11 R. Hutter, T. Mallat, A. Baiker, *J. Catal.* **1995**, 153, 177

12 R. van Grieken, J.L. Sotelo, C. Martos, J.L.G. Fierro, M. Kpez-Granados, R. Mariscal, *Catal. Today* **2000**, 61, 49

13 J.M. Fraile, J. I. GarcLa, J.A. Mayoral, L. C. de MMnorval, F. Rachdi, *J. Chem. Soc. Chem. Commun.* 1995, 539

14 E. Jorda, A. Tuel, R. Teissier, J. Kerneval, *J. Chem. Soc. Chem. Commun.* **1995**, 1775

15 M.C. Capel-Sanchez, J.M. Campos-Martin, J.L.G. Fierro, M.P. de Frutos, A. Padilla Polo, *Chem. Commun.* **2000**, 855

16 M.C. Capel-Sanchez, J.M. Campos-Martin, J.L.G. Fierro, *J. Catal.* **2003**, 217, 195

17 M.S. Sadjadi, N. Farhadyar, K. Zare, *Supperlatices Microstruct.* **2009**, 46, 266

18 A. Orlov, Q.Z. Zhai, J. Klinowski, *J. Mater. Sci.* **2006**, 41, 2187

19 A.K. Aboul-Gheit, S.M. Abdel-Hamid, S.A. Mahmoud, R.A. El-Salamony, J. Valyon, M.R. Mihályi, A. Szegedi, *J. Mater. Sci.* **2011**, 46, 3319

20 T. Yokoi, P. Wu, T. Tatsumi, *Catal. Commun.* 2003, 4, 11

21 J.J. Bravo-Suárez, K. K. Bando, T. Fujitani, S. T. Oyama, *J. Catal.* **2008**, 257, 32

22 L. Cumaranatunge, W.N.J. Delgass, *Catal.* **2005**, 232, 38

23 T. Liu, P. Hacarlioglu, S.T. Oyama, M.F. Luo, X.R. Pan, J.Q. Lu, *J. Catal.* **2009**, 267, 202

24 T. Sooknoi, V.J. Chitranuwatkul, *Mol. Catal. A* **2005**, 236, 220.

25 S. Saxena, J. Basak, N. Hardia, R. Dixit, S. Bhadauria, R. Dwivedi, R. Prasad, A. Soni, G.S. Okram, A. Gupta, *Chem. Eng. J.* **2007**, 132, 61

26 M.A. Mantegazza, G. Leofanti, G. Petrini, M. Padovan, A. Zecchina, S. Bordiga, *Stud. Surf. Sci. Catal.* **1994**, 82, 541

27 M.A. Mantegazza, G. Petrini, G. Spanó, R. Bagatin, F. Rivetti, *J. Mol. Catal. A* **1999**, 146, 223

28 B.S. Lane, K. Burgess, *Chem. Rev.* **2003**, 103, 2457

29 B. Notari, *Adv. Catal.* **1996**, 41, 253

30 S. Bordiga, S. Coluccia, C. Lamberti, L. Marchese, A. Zecchina, F. Boscherini, F. Buffa, F. Genoni, G. Leofanti, G. Petrini, G. Vlaic, *J. Phys. Chem.* **1994**, 98, 4125

31 D. Trong On, L. Le Noc, L. Bonneviot, *Chem. Commun.* **1996**, 299

32 L. Le Noc, D.T. On, S. Solomykina, B. Echchahed, F. Béland, C. Cartier dit Moulin, L. Bonneviot, *Stud. Surf. Sci. Catal.* **1996**, 101, 611

33 J. Klaas, G. Schulz-Ekloff, N. I. Jaeger, *J. Phys. Chem. B* **1997**, 101, 1305

34 V.A. de la Pena O'Shea, M. Capel-Sanchez, G. Blanco-Brieva, J.M. Campos-Martin, J.L.G. Fierro, *Angew. Chem. Int. Ed.* **2003**, 42, 5851

35 J. To, A.A. Sokol, S.A. French, C. R.A. Catlow, *J. Phys. Chem. C* **2008,** *112,* 7173

36 S. Yuan, H. Si, A. Fu, T. Chu, F. Tian, Y. Duan, J. Wang, *J. Phys. Chem. A* **2011**, 115, 940

37 C. Lamberti, S. Bordiga, A. Zecchina, A. Carati, A.N. Fitch, G. Artioli, G. Petrini, M. Salvalaggio, G.L. Marra, *J. Catal.* **1999**, 183, 222

38 T. Blasco, M. Camblor, A. Corma, J. Pérez-Parriente, *J. Am. Chem. Soc.* **1993**, 115, 11806

39 T. Kataoka, J.A. Dumesic, *J. Catal.* **1988**, 112, 66

40 M. Popova, Á. Szegedi, K. Lázár, A. Dimitrova, *Cata.l Lett.* **2011**, 141, 1288

41 G. Kortüm, Reflexions spektroskopie; Springer: Berlin, **1969**

42 X.Gao, I.E. Wachs, *Catal. Today* **1999**, 51, 233

Chapter VII

Conclusion and Perspective

Silica supported titanium are often reported as heterogeneous catalyst for oxidation reaction and particularly for epoxidation of alkenes where isolated titanium sites are known to be the active species. However, site isolation on a refractory surface like silica remains a challenge since most metals like titanium tend to aggregate into oxide clusters. The strategy adopted here consists to graft titanium isopropoxide by reaction with surface silanol groups, the quantity of which has been decreased at low temperature by chemical capping instead of high temperature thermal condensation. The originality resides in the molecular control of such operation using the so-called molecular stencil patterning (MSP) specifically developed for cationic templated silicas in the laboratory. Indeed, these silicas presents very high surface areas and very well calibrated cylindrical 1D nanochannel in the range 2.5 to 10 nm that is favorable for high metal dispersion and for post organic modification without loss of accessibility for reactants. Indeed, MSP overcome the diffusion problem for metal dispersion using a surface masking method based on the templating surfactant kept at a controlled filling factor inside the channels. After the removal of the masking surfactant, the silanol left available are located on isolated spots where in principle any metal can be grafted.

It is shown here that MSP can be applied to graft metal directly to these isolated silanol spots. The Ti-contained mesoporous silica catalyst was prepared using a novel post-hydrophobization agent, a dipodal 1-2-ethanebis(dimethylsilyl) (EBDMS) group via partially capping the silanol groups before the titanium isopropoxide grafting. EBDMS moieties are mostly bigrafted by quantitative ^{29}Si NMR and FT-IR, thus more stable than the monopodal trimethylsilyl moieties (TMS) and was tested and found applicable but less convenient for surface coverage control. Nonetheless, the templated mesoporous silicas capped with dipodal organosilyl EBDMS groups contain as planned more isolated sites than the unmodified silica. Part of EBDMS is directly linked to grafted Ti sites likely via the formation of a direct Ti-O-Si bridge during the sequent Ti post-grafting. This

advantage depends on the titanium loading and it is more pronounced at low Ti loading where site isolation is at the best. A drastic blue shift of the ligand to metal UV transition attest for a profound effect on Ti dispersion in strongly correlated with the activity in epoxidation of cyclohexene with *tert*-butyl hydroperoxide (TBHP) as oxidant.

The organosilazane precursor of the quite stable grafted EBDMS is much more expensive and less convenient than that of TMS. Therefore stabilization of the grafted monopodal TMS moieties was studied using a thermal treatment. The goal was to convert TMS into di-or trigrafted species using TGA profile as an indicator for the best choice of temperature. Thanks to a quantitative ^{29}Si NMR monitoring, the highest temperature to avoid a loss of grafted organosilyl moieties was determined (500 °C). An ultra-stable organically modified surface was obtained and the hydrophobic/hydrophilic surface properties could be tuned. Furthermore, a post modification at least for TMS, EBDMS and Ti can be available on the calcined surface.

To quantify the grafted Ti species that are always present as a mixture, it was necessary to determine their molar coefficient of extinction. It was found that five different Gaussian only was necessary to deconvolve and simulate the quite large number of UV spectra obtained from the different syntheses. The Gaussian fits centred at 50000, 44000, 40400, 36000 and 32000 cm-1 are assigned to the tetrahedral, pentahedral, octahedral, TiOx nano-oligomer and bulky TiO_2 particle respectively. Based on the K-M theory, the extinction coefficient constant (ε) of each Ti sites in the solid state of TiO2-SiO2 is calculated (250 ± 22) E+04, (70 ± 34) E+04, (80 ± 60) E+04, (2 ± 2) E+04 and (11 ± 8) E+04 mmol·cm^2, respectively. It was found for the first time on a surface that this coefficient decreases along the above series over representing isolated and tetrahedral species by far. The ε of the tetrahedral site is nearly 6 times than that of octahedral, and two order of magnitude higher than that of TiO_x oligomers. The success of ε calculation helps quantify the Ti sites in the solid silica state for the first time. Consequently, with ε

of tetrahedral and pentahedral Ti sites, the turnover number (TON) of active Ti centre in the catalytic epoxidation of cyclohexene is refined to be unchangeable consistently with the same one kind of catalysts, revealing the real active Ti centre.

The results in this thesis focus mainly on the surface study of the hydrophobized Ti-contained mesoporous silica material. Some can be suggested such as:

1), the dipodal function may apply to other metals not only for catalysis or separation but also for imaging by tuning fluorescence, etc;

2), the thermal treatment offers a simple way for the sustainable modification on the silica or the other organic-inorganic hybrid materials, as well the silica surface study after treatment in this dissertation can be cited as a basic reference;

3), the quantification of Ti sites in the solid silica state using extinction coefficient constant ε can be applied in almost the Ti-substituted silica materials and the coordinated sites of other metals like V, Cu, etc, can also be calculated by the spectroscopy method as we used herein;

4), the results of reaction catalyzed by Ti-Si heterogeneous materials will be more precise with relation to the quantification of Ti sites and the TON will be fixed and well predicted referring to the same type of materials, which use same synthesis condition despite of varying the Ti ratio, in the same reaction mediate.